UNIVERSITÀ DEGLI STUDI DI TRENTO
UNIVERSITÀ DEGLI STUDI DI BRESCIA

DOCTORAL THESIS

Comprehensive study of identified hadron spectra, $\pi^{\pm}$, $K^{\pm}$ and $p(\bar{p})$ in PbPb collisions at $\sqrt{s_{NN}}$ = 5.36 TeV with the ALICE detector at CERN

Author:
Rohaan DEB

Supervisor:
Dr. Ramona LEA

A thesis submitted in fulfillment of the requirements for the degree of
Doctorate of National Interest
on
Space Science and Technology

January 22, 2026

Finanziato dall'Unione europea NextGenerationEU
Ministero dell'Università e della Ricerca
Italiadomani PIANO NAZIONALE DI RIPRESA E RESILIENZA

Declaration of Authorship

I, Rohaan DEB, declare that this thesis titled, "Comprehensive study of identified hadron spectra, $\pi^{\pm}$, $K^{\pm}$ and $p(\bar{p})$ in PbPb collisions at $\sqrt{s_{NN}}$ = 5.36 TeV with the ALICE detector at CERN" and the work presented in it are my own. I confirm that:

- This work was done wholly or mainly while in candidature for a research degree at this University.
- Where any part of this thesis has previously been submitted for a degree or any other qualification at this University or any other institution, this has been clearly stated.
- Where I have consulted the published work of others, this is always clearly attributed.
- Where I have quoted from the work of others, the source is always given. With the exception of such quotations, this thesis is entirely my own work.
- I have acknowledged all main sources of help.
- Where the thesis is based on work done by myself jointly with others, I have made clear exactly what was done by others and what I have contributed myself.

Signed: Rohaan Deb

Date: 11.10.2025(dd.mm.yyyy)

Abstract

Rohaan DEB

Comprehensive study of identified hadron spectra, $\pi^{\pm}, K^{\pm}$ and $p(\bar{p})$ in PbPb collisions at $\sqrt{s_{\rm NN}}$ = 5.36 TeV with the ALICE detector at CERN

In ultra-relativistic heavy-ion collisions, the Large Hadron Collider (LHC) at CERN recreates, for a brief instant, the conditions that existed microseconds after the Big Bang. Under such extreme conditions, ordinary nuclear matter transitions into a deconfined state of strongly interacting quarks and gluons, the fundamental degrees of freedom of **Quantum Chromodynamics (QCD)**, forming what is known as the **Quark Gluon Plasma (QGP)**. One of the central goals of modern nuclear physics and a primary objective of the **ALICE (A Large Ion Collider Experiment)** experiment at the LHC, is to comprehend the properties of this primordial state of matter, including its evolution, expansion, and eventual hadronization into the particles we observe. With its exceptional tracking and particle identification (PID) capabilities, ALICE offers a unique opportunity to measure identified hadron spectra and explore the microscopic characteristics of this medium.

By investigating how matter responds to heating to trillions of degrees and compression to energy densities significantly higher than those found in atomic nuclei, this thesis presents a precision study of identified hadron production, specifically pions ($\pi^{\pm}$), kaons ($K^{\pm}$), and protons (p, $\bar{p}$) in lead–lead (PbPb) collisions at a center of mass energy per nucleon pair of $\sqrt{s_{\rm NN}} = 5.36$ TeV. A dedicated analysis framework was developed to extract particle yields by employing information from the Time Projection Chamber (TPC) and Time of Flight (TOF) detectors, enabling robust particle species separation over a broad range of transverse momenta ($p_{\rm T}$) and collision centralities.

Exploiting the high-stat dataset from the LHC Run 3, high precision $p_{\rm T}$ spectra across several centrality intervals are obtained by reconstructing, calibrating, and correcting raw particle yields. Each stage of the analysis, from PID using TPC and TOF signals to the evaluation of efficiency and acceptance corrections was rigorously validated to ensure stability and reliability throughout the entire $p_{\rm T}$ range. The corrected spectra provide a quantitative foundation for future physics studies and serve as essential benchmarks for theoretical models describing the transport properties, collective dynamics, and hadronization mechanisms of strongly interacting QCD matter.

In addition to the PbPb study, this thesis applies the same analysis strategy to **oxygen–oxygen (OO)** collisions at $\sqrt{s_{\rm NN}} = 5.36$ TeV, recorded during the first light-ion run at the LHC. As the smallest genuine nucleus–nucleus system ever collided at the LHC, OO provides a unique link between proton-induced (pp, p–Pb) and heavy-ion (Xe–Xe, Pb–Pb) reactions. Using identical reconstruction and correction procedures, the OO spectra allow a direct and unbiased comparison of particle production across a wide range of system sizes. When the results are expressed as a function of charged-particle multiplicity ($\mathrm{d}N_{\mathrm{ch}}/\mathrm{d}\eta$), the OO measurements align smoothly with established PbPb trends, reinforcing the emerging picture that many bulk observables scale primarily with final-state multiplicity rather than the mass number of the colliding nuclei. By combining PbPb and OO results, this thesis provides new insight into final-state collectivity, strangeness production, baryon enhancement, and kinetic freeze-out dynamics in light-ion collisions.

Acknowledgements

I wish to express my sincere gratitude to all those who have supported and accompanied me throughout my doctoral research, especially my supervisor Dr. Ramona Lea for her scientific advice and continuous encouragement. I am deeply thankful to the ALICE Collaboration and to CERN for providing the unique scientific environment, computing infrastructure, and data that made this work possible. I am especially grateful to my colleagues at CERN for their continuous guidance, stimulating discussions, and day-to-day collaboration, which significantly enriched both the technical and scientific quality of this project.

I gratefully acknowledge the Data Processing Group (DPG) for their sustained efforts in data production, calibration, and reconstruction, without which this analysis could not have been carried out. I also wish to thank the University of Trento and the University of Brescia for their academic support, resources, and the opportunity to pursue this research within an inspiring and collaborative environment. My sincere thanks extend to the PhD office and administrative staff, whose consistent assistance and efficiency ensured that all practical aspects of my doctoral work proceeded smoothly.

Finally, I am deeply appreciative of the friendship and encouragement of my friends and acquaintances, who offered constant support, motivation, and balance throughout the challenges of the research journey. Their presence has been invaluable, both personally and academically.

Contents

List of Figures

List of Tables

List of Abbreviations

ALICE	A Large Ion Collider Experiment (CERN).
LHC	Large Hadron Collider.
CERN	European Organization for Nuclear Research.
SM	Standard Model of particle physics.
QCD	Quantum Chromodynamics.
QGP	Quark–Gluon Plasma.
EoS	Equation of State.
μ_B	Baryochemical potential.
$\sqrt{s_{\mathrm{NN}}}$	Nucleon–nucleon center-of-mass energy.
Pb–Pb	Lead–lead collisions.
pp	Proton–proton collisions.
p–Pb	Proton–lead collisions.
TPC	Time Projection Chamber.
ITS	Inner Tracking System.
TOF	Time-of-Flight Detector.
FT0	Fast Timing Detector (event time in Run 3).
EMCal	Electromagnetic Calorimeter.
TRD	Transition Radiation Detector.
HMPID	High-Momentum Particle Identification Detector.
PID	Particle Identification.
dE/dx	Specific energy loss in the TPC.
n_σ	Normalized PID deviation.
p_{T}	Transverse momentum.
y	Rapidity.
η	Pseudorapidity.
MC	Monte Carlo simulation.
AOD	Analysis Object Data (Run 3 format).
QA	Quality Assurance.
N_{ev}	Number of events.
Primaries	Particles produced at the interaction vertex.
Secondaries	Particles from decays or material interactions.
Feed-down	Contribution from weak decays.
Eff.	Efficiency (tracking + acceptance + PID).
Unfolding	Correction for detector resolution effects.
BGBW	Boltzmann–Gibbs Blast-Wave model.
T_{kin}	Kinetic freeze-out temperature.
β_{max}	Maximum transverse flow velocity.
$\langle\beta\rangle$	Average transverse flow velocity.
c_s	Speed of sound in the medium.
v_n	Flow coefficients.
R_{AA}	Nuclear modification factor.
EPOS	Hydrodynamics-based event generator.

HIJING	Heavy-ion event generator.
O2	ALICE Run 3 Online–Offline computing framework.
CTF	Compressed Time Frame (Run 3 data format).
DPG	Data Processing Group.
TFC	Time Frame Coordinator.
NDF	Number of degrees of freedom in a fit.
χ^2	Chi-square fit statistic.
Stat.	Statistical uncertainty.
Syst.	Systematic uncertainty.

Chapter 1

Introduction

1.1 The Fundamental Human Quest

Since the very beginning of scientific history, mankind has sought to understand the fundamental nature of the universe. The instinct to look out to the horizon, to try to figure out the code of nature, to ask the **WHY** and **HOW** questions of the world around us, has guided the progress of physics from natural philosophy to modern particle theory. Over millennia, this pursuit has led to the discovery that all visible matter is made up of progressively elementary building blocks that are governed by a set of universal laws.

At the tiniest scales, these constituents are quarks and gluons that interact via the fundamental force defined by Quantum Chromodynamics (QCD) [1, 2]. Quarks and gluons are normally confined within hadrons such as protons and neutrons, but at sufficiently high temperatures and energy densities, they can exist in a deconfined state known as the Quark-Gluon Plasma (QGP) [3, 4]. Understanding the features of this medium, its origin, development, and hadronization; is one of the most significant challenges in modern nuclear and particle physics [5].

In order to investigate such extreme conditions, scientists make use of complex experimental facilities such as the Large Hadron Collider (LHC) at CERN [6] and its dedicated heavy-ion experiment, ALICE (A Large Ion Collider Experiment) [7]. These instruments enable us to recreate, in a controlled laboratory environment, the conditions that existed microseconds after the Big Bang. By colliding heavy nuclei at ultra-relativistic energies, one can investigate how strongly interacting matter behaves when pushed far beyond the limitations of regular atomic nuclei.

This thesis adds to this collaborative effort by investigating the production of identified hadrons in PbPb collisions at $\sqrt{s_{\mathrm{NN}}} = 5.36$ TeV

1.2 The Big Questions: Matter Under Extreme Conditions

At its heart, this thesis seeks to answer questions that lie at the boundary between the known and the unknown:

- What happens when atomic nuclei collide at energies comparable to those just after the Big Bang?
- How does ordinary matter transform when subjected to such extraordinary conditions?
- Can we recreate, for a brief instant, and understand the primordial soup, the QGP, from which all matter in the universe emerged?

These questions are not merely of particle physics; they also connect to cosmology and the early-universe evolution [8, 9]. They link our understanding of the smallest building blocks of nature to the macroscopic behavior of the cosmos itself.

1.3 The Context: Heavy-Ion Collisions at the LHC

To address these questions, physicists study ultra-relativistic heavy-ion collisions: smashing heavy ions together at such high energies that protons and neutrons are themselves broken down into fundamental quarks and gluons [10]. The LHC at CERN reaches energies unprecedented in the laboratory, effectively acting as a time machine to recreate the conditions of the universe few microseconds after the Big Bang [11].
At the heart of this effort is the ALICE detector [7, 12], a complex instrument designed to explore the emergent properties of strongly interacting matter at the extreme energy densities achieved in ultra-relativistic collisions. By measuring the spectra of identified particles (pions, kaons, protons, etc.), we obtain crucial information about the system's temperature, expansion, and hadronization dynamics.

1.4 Why Pions, Kaons, and Protons?

The emphasis on pions, kaons, and protons is intentional and fundamental. These are the lightest and most abundantly produced hadrons, and their spectra contain key information about:

- **Collective properties of the medium:** the shapes of p_{T} spectra and flow patterns reflect the degree of collective expansion and hydrodynamic behavior [13, 14].
- **Particle production and hadronization:** differences between mesons (π and K) and baryons (p) provide insight into quark recombination and fragmentation mechanisms [15, 16].
- **Freeze-out conditions:** yields and spectra encode the conditions at chemical and kinetic freeze-out [17].
- **Matter-antimatter balance:** proton and antiproton production probe baryon transport and net-baryon density at midrapidity [18].
- **Signatures of deconfinement:** ratios such as p/π and K/π serve as sensitive indicators of a transition from confined hadronic matter to deconfined QGP [**Adam2016Spectra**, 19].

In many ways, studying these spectra closely is like reading the DNA of the collision: each particle carries the memory of the hot and dense medium often referred to as the fireball, formed immediately after the impact, encoding it's temperature, expansion, and chemical composition.

1.5 Structure of the Thesis

This thesis is organised to guide the reader from the general physics motivation to the detailed analysis strategy and final physics interpretation:

- **Chapter 1: Introduction** - Outlines the scientific context and motivation of ultra-relativistic heavy-ion collisions, introduces the role of pions, kaons and protons as soft probes of the QGP, and summarises the main goals of the thesis.
- **Chapter 2: Theoretical Framework** – Reviews the Standard Model and Quantum Chromodynamics, the QCD phase diagram and the concept of the QGP. It describes the space–time evolution of heavy-ion collisions, the definition of centrality, and the main classes of hard and soft observables used to characterise the medium.
- **Chapter 3: Light-Flavour Hadron Production** – Discusses production mechanisms for light-flavour hadrons in pp, p–Pb and Pb–Pb collisions. Thermal and statistical models, strangeness enhancement and the role of canonical suppression are introduced, together with collective flow and the Boltzmann–Gibbs Blast–Wave (BGBW) description.
- **Chapter 4: The ALICE Experiment** – Presents the LHC and the ALICE detector, with emphasis on the subsystems relevant for this work (ITS, TPC, TOF, FIT) and on the Run 3 upgrades, reconstruction chain and computing framework.
- **Chapter 5: Data Samples & Analysis Strategy** – Describes the Pb–Pb and O–O data sets and corresponding Monte Carlo samples, event and track selection, PID strategy, yield-extraction methods, correction procedures and the overall analysis workflow.
- **Chapter 6: PbPb Analysis & Results** – Details the extraction of raw yields in PbPb, the determination of efficiencies and primary fractions, and the construction of fully corrected spectra. It presents particle-to-pion ratios, TPC–TOF comparisons, Blast–Wave fits and integrated yields for PbPb collisions at $\sqrt{s_{\mathrm{NN}}} =$ 5.36 TeV.
- **Chapter 7: Light-Ion Collisions: OO Analysis & Results** – Applies the same analysis chain to OO collisions at $\sqrt{s_{\mathrm{NN}}} = 5.36$ TeV. It discusses TOF-based yield extraction, efficiency and feed-down corrections, corrected spectra, and the corresponding K/π and p/π ratios, as well as Blast–Wave freeze-out parameters and integrated yields in OO.
- **Chapter 8: Comparison between Particle Production in PbPb and OO Collisions** – Compares Blast–Wave freeze-out parameters and particle ratios between PbPb and OO as a function of charged-particle multiplicity. The chapter focuses on the system-size dependence of radial flow, kinetic freeze-out and strangeness and baryon production.
- **Chapter 9: Conclusions** – Summarises the main experimental results and their physics implications, highlighting the combined picture emerging from PbPb and OO collisions at the same energy.
- **Chapter 10: Outlook** – Discusses prospects for future analyses with improved reconstruction, extended p_{T} reach and higher statistics, and outlines open questions and possible extensions of the work.
- **Appendix A: Frequently Asked Questions** – Collects practical clarifications and technical notes that complement the main text.

Chapter 2

Theoretical Framework

2.1 The Standard Model(SM)

Physics fundamentally searches for patterns, one grand design behind the diversity of phenomena in our universe. The SM of particle physics is perhaps the deepest realization of this endeavor: a theory that encodes the fundamental building blocks of the reality in which we live and their interactions, through symmetry (spatial and temporal invariance) and mathematics [20, 21, 22].
The SM is more than a mere inventory of particles; it is a dynamic tapestry formed from the strands of quantum field theory(QFT), bringing together three of the four fundamental forces of nature (the electromagnetic, the weak, and the strong interactions) [23, 24]. Within this scheme (Table 2.1), matter is constructed from quarks and leptons, organized in three families (or generations), while the particles that mediate their interactions (the gauge bosons) allow for interactions and correlations. In 2012, the Higgs boson [25, 26] closed the book on this set of theories, yet much remains unknown.

Particle Type	**Generations**	**Examples**
Quarks	up, down, charm, strange, top, bottom	u, d, c, s, t, b
Leptons	electron, muon, tau	e, μ, τ
Gauge Bosons	photon, W, Z, gluon	$\gamma, W^{\pm}, Z^0, g$
Higgs Boson	-	H

TABLE 2.1: Overview of the fundamental particles in the Standard Model [27]

However, even this beautiful model is not the whole story. The SM cannot, for example, explain gravity, the nature of dark matter, or the preponderance of matter over antimatter. But for the questions being asked in this thesis, the behaviour of nuclear matter at extreme energies, the SM, and, in particular, the theory of Quantum Chromodynamics (QCD), provides a robust and predictive framework [1, 2].

2.2 QCD: The Theory of the Strong Force

The Quantum Chromodynamics (QCD) is the field of SM that describes the **strong interaction**, the fundamental force that is responsible for binding quarks to protons, neutrons, and, ultimately, atomic nuclei, the dominant component of visible matter in the universe.

The QCD, in principle, is described as a non-Abelian gauge theory based on the color symmetry group $SU(3)_C$ [1, 28, 29]. Its force carriers, the **gluons**, contain color charge, allowing them to interact not only with quarks but also with each other.

QCD's self-interacting nature distinguishes it from the Abelian theory of electromagnetism (QED) and gives birth to two defining features: **asymptotic freedom** at short distances and **confinement** at large distances [2, 30].

The dynamics of the theory are governed by the **QCD Lagrangian density**:

$$\mathcal{L}_{\text{QCD}} = \sum_{f=1}^{N_f} \bar{\psi}_f \left(i\gamma^\mu D_\mu - m_f \right) \psi_f - \frac{1}{4} F^a_{\mu\nu} F^{a\,\mu\nu}, \tag{2.1}$$

where ψ_f is the quark field of flavor f and mass m_f, and N_f is the number of active quark flavors.

The **covariant derivative** introduces the coupling between quarks and gluons:

$$D_\mu = \partial_\mu - i g_s T^a A^a_\mu, \tag{2.2}$$

where g_s is the strong coupling constant, A^a_μ are the eight gluon fields, and T^a are the generators of the $\text{SU}(3)_\text{C}$ algebra.

The **gluon field-strength tensor**, which encapsulates the self-interactions among gluons, is defined as

$$F^a_{\mu\nu} = \partial_\mu A^a_\nu - \partial_\nu A^a_\mu + g_s f^{abc} A^b_\mu A^c_\nu, \tag{2.3}$$

where f^{abc} are the structure constants of $\text{SU}(3)$.

The term $g_s f^{abc} A^b_\mu A^c_\nu$ is unique to non-Abelian theories and leads to gluon self-coupling, a property absent in Quantum Electrodynamics (QED). This feature is responsible for the two defining characteristics of QCD: **asymptotic freedom** at short distances and **confinement** at large distances.

Gauge invariance under local $\text{SU}(3)_\text{C}$ transformations ensures the conservation of color charge and determines the form of the quark–gluon and three-gluon interaction vertices. This compact formulation forms the basis for both perturbative calculations at high momentum transfer and non-perturbative lattice computations in the low-energy regime of the strong interaction [31, 32, 33].

2.2.1 Running coupling constants

The strength of the strong interaction in QCD is determined by the coupling constant α_s, which depends on the characteristic momentum transfer or energy scale Q of the process. This scale dependency is caused by the renormalization procedure, which absorbs divergences of perturbation theory into redefined coupling and field parameters [28, 29].

The evolution of α_s with the energy scale μ is governed by the **renormalization group equation (RGE)** [32], expressed in terms of the β-function as:

$$\beta(\alpha_s) = \frac{\partial \alpha_s}{\partial \ln \mu^2}. \tag{2.4}$$

The β-function can be expanded perturbatively as a power series in α_s,

$$\beta(\alpha_s) = -\beta_0\, \alpha_s^2 - \beta_1\, \alpha_s^3 - \beta_2\, \alpha_s^4 - \cdots, \tag{2.5}$$

where the coefficients β_i depend on the gauge group and the number of active quark flavours n_f. For QCD, the leading coefficients are known to four loops in the $\overline{\text{MS}}$(modified minimal subtraction) scheme which is the most widely used renormalization scheme in perturbative QCD. [34, 35]:

$$\beta_0 = \frac{11N_C - 2n_f}{12\pi}, \quad \beta_1 = \frac{17N_C^2 - 5N_C n_f - 3C_F n_f}{24\pi^2}, \tag{2.6}$$

with $N_C = 3$ and $C_F = (N_C^2 - 1)/(2N_C)$.

At one-loop accuracy, Eq. (2.4) can be integrated to give:

$$\alpha_s(Q^2) = \frac{1}{\beta_0 \ln(Q^2/\Lambda_{\text{QCD}}^2)}, \tag{2.7}$$

where Λ_{QCD} is the QCD scale parameter, defined as the energy at which the perturbative expansion ceases to be valid.

In principle, the sign of β_0 determines the qualitative behavior of the coupling. In QED, $\beta_0 > 0$ indicates that the coupling rises with energy; while, in QCD, $\beta_0 > 0$ has a negative sign in Eq. (2.5), leading to a *decrease* of α_s. This feature, termed as **asymptotic freedom**, suggests that quarks interact poorly when probed across short distances or substantial momentum transfers [27, 28, 29].

The opposite limit, $Q \to \Lambda_{\text{QCD}}$, corresponds to $\alpha_s \to \infty$, where perturbation theory fails and confinement takes over. In this non-perturbative regime, analytical methods are unreliable, and lattice QCD gives the most precise estimates of α_s (Fig. 2.1) and associated quantities [36].

2.2.2 The Phase Diagram of QCD

In atomic systems, electrons may be separated from their nuclei by providing enough energy, either by heating the gas or applying strong electromagnetic fields. An analogous process occurs for hadronic matter: by reaching sufficiently high temperatures or energy densities, the composite hadrons *melt* liberating their elementary constituents, quarks and gluons. This transition marks the onset of a new phase of strongly interacting matter, the Quark Gluon PLasma (**QGP**).

Due to the confinement of color charge, quarks and gluons cannot be isolated at ordinary densities and temperatures. In order to deconfine them, the energy scale of the system must be increased dramatically via compression or heating. Lattice QCD calculations imply that when the energy density surpasses a critical value $\varepsilon_c \simeq 1\,\text{GeV}/\text{fm}^3$, hadronic matter transitions to the deconfined phase [37, 38]. The corresponding critical temperature is found to be $T_c = 154 \pm 9$ MeV [39]. A schematic representation of the resulting **QCD phase diagram** is shown in Fig. 2.2. At present, the general features of the diagram can be summarized as follows:

1. **Low temperature, high baryon density:** At low temperatures but high baryochemical potential ($\mu_B \to \infty$), a transition from nuclear matter to deconfined quark matter can occur under extreme compression, reaching densities many times higher than the nuclear saturation density $\rho_0 \approx 0.15\,\text{fm}^{-3}$ [37, 41]. These circumstances are relevant to neutron star cores and possibly in neutron-star mergers, when cold, dense quark matter or color-superconducting phases may exist.

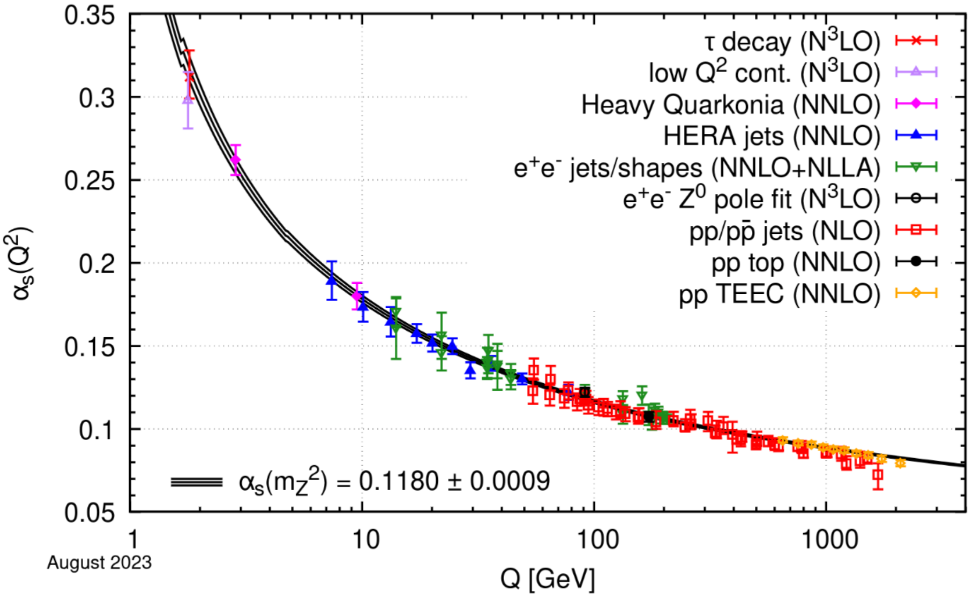

FIGURE 2.1: Measurements of the QCD coupling $\alpha_s(Q^2)$ as a function of the energy scale Q, in various collision systems and via different processes. The orders of QCD perturbation theory are reported in brackets. The numerical value of α_s at the Z pole is also reported [40].

2. **High temperature, low baryon density:** In ultra-relativistic heavy-ion collisions, where $\mu_B \to 0$, deconfinement happens by heating the system above T_c. According to lattice QCD, this transition is a *crossover*, not a real phase transition: thermodynamic observables such as the entropy and energy density change smoothly with temperature [38, 39].

3. **Intermediate region:** At intermediate μ_B and T, theoretical models anticipate a first-order phase transition, which terminates at a **critical point** in the (T, μ_B) plane [42]. Across a first-order boundary, the entropy $S(T)$ and the energy density shows discontinuities, with the transition taking place via latent heat.

The first case (low T, large μ_B) is not accessible to the current collider experiments but may be realized in compact astrophysical objects. The second and third regimes may, however, be explored in the laboratory by altering the beam energy in heavy-ion collisions. The LHC achieves high temperatures with virtually disappearing μ_B, whereas RHIC and upcoming facilities like FAIR and NICA study intermediate states using beam-energy-scan programs. [44, 45].

The highest energy densities so far have been reached at the LHC, where lead–lead collisions at $\sqrt{s_{\rm NN}} = 5.02$ TeV (Run 2) and 5.36 TeV (Run 3) produce conditions similar to those of the early Universe a few microseconds after the Big Bang [46, 47]. In these collisions, the fireball formed is nearly net-baryon–free and exhibits characteristics consistent with the deconfined QGP phase.

2.3 The Quark Gluon Plasma

One of the most significant predictions of lattice QCD, transition from the hadronic phase, when quarks and gluons are confined, to a deconfined phase of highly interacting matter, known as the Quark-Gluon Plasma (QGP) [33]. This plasma is analogous to an electromagnetic plasma, but with color-charged constituents instead of

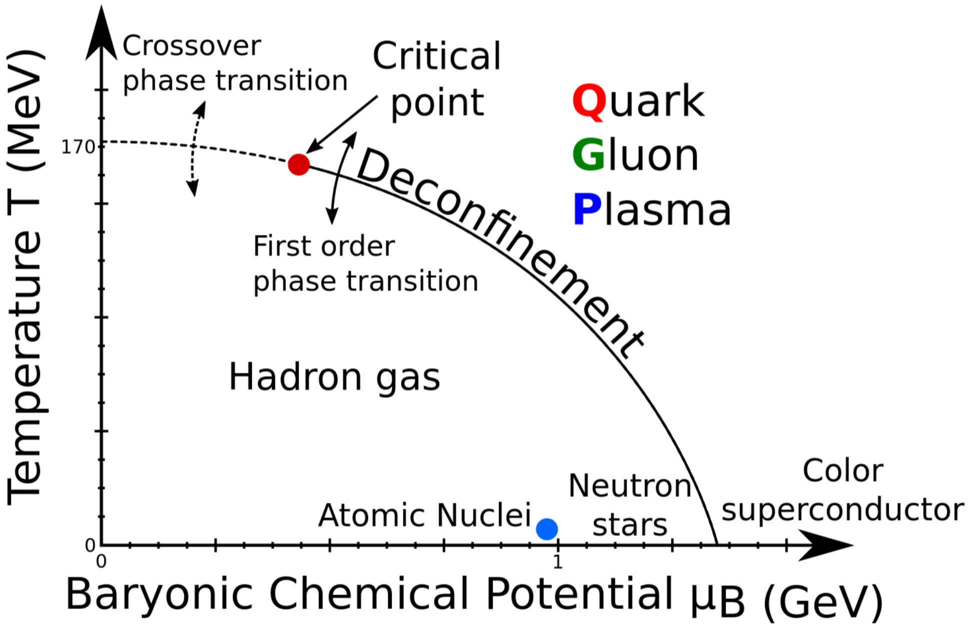

FIGURE 2.2: Schematic representation of the phase diagram of strongly interacting matter, analogous to the classical Clapeyron diagram. The baryochemical potential μ_B represents the net baryon content of the system. [43].

electric charges.

Consistent with the phase diagram discussed earlier, lattice QCD confirms a smooth crossover around

$$T_c = 155 \pm 9 \text{ MeV}. \tag{2.8}$$

Across this temperature region, the pressure, energy density, and entropy density exhibit a smooth yet rapid change, as illustrated in Fig. 2.3. Below T_c, these quantities are well reproduced by the **Hadron Resonance Gas (HRG)** model, in which the system is treated as an ideal gas composed of all known hadrons and resonances [48].

Another key feature predicted by lattice QCD is the restoration of chiral symmetry, which breaks spontaneously during the hadronic phase. The chiral condensate $\langle\bar{\psi}\psi\rangle$ drops with temperature and approaches zero in the deconfined phase, indicating the restoration of chiral symmetry. Lattice QCD is presently confined to locations with low baryochemical potential ($\mu_B \lesssim 300$ MeV) due to the **sign problem**, which causes numerical instability in the Monte Carlo assessment of the QCD path integral. At larger μ_B, multiple approaches are used: Taylor expansions at $\mu_B = 0$, analytical continuation from imaginary chemical potentials, effective QCD-inspired models, and holographic (AdS/CFT-based) approaches [49, 37].

These investigations suggest a rich QCD phase diagram in the (T, μ_B) plane. At small μ_B, the transition is smooth, but at higher μ_B, a line of first-order phase transitions emerges, leading to a **critical point**. The precise position (or even existence) of this crucial point is still an outstanding subject in QCD matter research. The STAR Collaboration's recent observations of conserved variables, including net-proton number, in the RHIC Beam Energy Scan program offer intriguing insights into this section of the phase diagram [50].

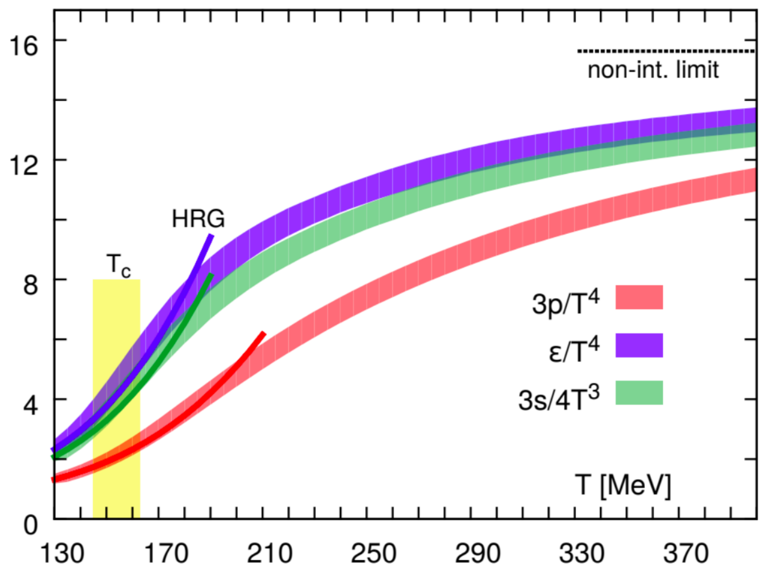

FIGURE 2.3: Temperature dependence of the pressure p, energy density ϵ, and entropy density s, normalized by powers of T, obtained from lattice QCD at zero baryon chemical potential. At low temperatures, the results agree with the Hadron Resonance Gas model, while above T_c the system transitions smoothly to a deconfined plasma [38, 39].

In summary, the QGP is a deconfined, tightly linked state of quarks and gluons regulated by QCD that exists above a threshold temperature of around 1.8×10^{12} K. The work combines theoretical QCD, lattice thermodynamics, and experimental heavy-ion physics to shed light on the early Universe and the characteristics of matter at high energy densities.

2.4 Heavy-ion colllisions: Collision centrality

A fundamental difference between proton-proton (pp) and heavy-ion (A-A) collisions lies in its collision geometry. A proton can be approximated a point-like elementary particle, while a nucleus is an extended structure made up of several nucleons. Thus, when two nuclei collide, only a percentage of their constituent nucleons interact, depending on the impact parameter b, which is the transverse distance between the colliding nuclei's centers at closest approach. A frequently used approach to describe the collision geometry is the Glauber model [51]. It basically assumes that nuclear collisions are an incoherent superposition of nucleon-nucleon collisions. The optical limit assumes that the trajectories of protons and neutrons, considered as independent and indistinguishable elementary particles, remain unaffected by their interaction.

In this method, all calculated observables are determined as a function of the impact parameter (b), which is defined as the projection onto the plane perpendicular to the beam direction of the vector linking the centers of the colliding ions. A schematic view of the collision geometry is shown in Fig. 2.4, where A and B denote the mass numbers of the projectile and target nuclei, respectively. The likelihood of finding a nucleon inside the nucleus A at the transverse coordinates $\mathbf{s}$ is described by the

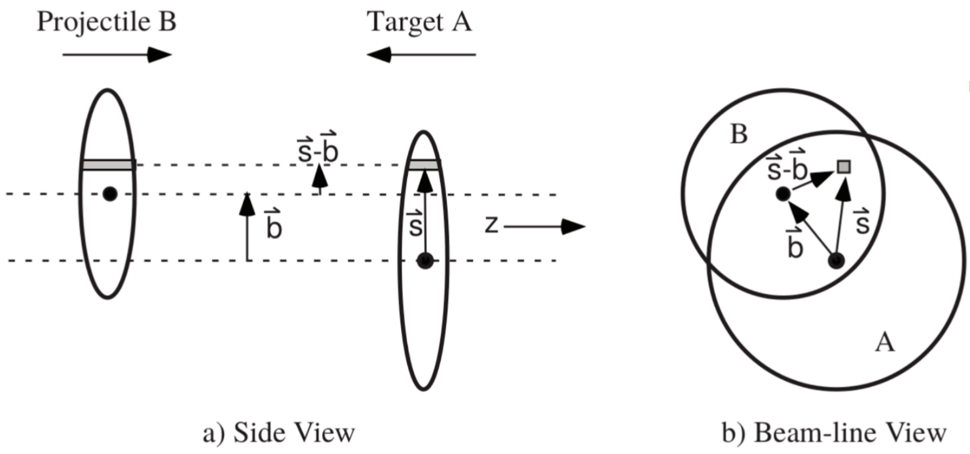

FIGURE 2.4: Schematic representation of the longitudinal and transverse geometry of an ion-ion collision. The impact parameter b defines the separation between the centers of the nuclei in the transverse plane [51].

nuclear thickness function (T_A):

$$T_A(\mathbf{s}) = \int_{-\infty}^{+\infty} \rho_A(\mathbf{s}, z_A)\, dz_A. \tag{2.9}$$

where $\rho_A(\mathbf{s}, z_A)$ is the nuclear density, usually parameterized with a Woods-Saxon distribution normalized to the mass number A [52].

The nuclear overlap function $T_{AB}(\mathbf{b})$ describes the overlap of the two projected thickness functions. Since both T_A and T_B already live in the transverse plane, their convolution is performed over the transverse area element d^2s:

$$T_{AB}(\mathbf{b}) = \int T_A(\mathbf{s})\, T_B(\mathbf{s} - \mathbf{b})\, d^2s. \tag{2.10}$$

Thus, T_A involves an integration over dz_A because it reduces a three-dimensional density to two dimensions, whereas T_{AB} integrates over d^2s because it combines two already projected two-dimensional densities.

For a given impact parameter b, the probability of having exactly n binary nucleon-nucleon interactions is assumed to follow a binomial distribution:

$$P(n, \mathbf{b}) = \frac{N_{\text{trial}}!}{n!\,(N_{\text{trial}} - n)!} \left[T_{AB}(\mathbf{b})\, \sigma_{\text{NN}}^{\text{inel}}\right]^n \left[1 - T_{AB}(\mathbf{b})\, \sigma_{\text{NN}}^{\text{inel}}\right]^{N_{\text{trial}} - n}, \tag{2.11}$$

where $\sigma_{\text{NN}}^{\text{inel}}$ is the inelastic nucleon-nucleon cross section. The quantity $N_{\text{trial}} = A \times B$ denotes the total number of possible nucleon-nucleon pairs between the two nuclei, i.e. the number of nucleons in nucleus A times the number of nucleons in nucleus B.

The differential inelastic A-B cross section $((\sigma_{A+B}^{inel}))$ is then obtained by requiring at least one binary collision:

$$\frac{d^2\sigma_{A+B}^{\text{inel}}}{db^2} = 1 - \left[1 - T_{AB}(\mathbf{b})\, \sigma_{\text{NN}}^{\text{inel}}\right]^{AB}. \tag{2.12}$$

Assuming spherical nuclei, only the magnitude $b = |\mathbf{b}|$ is relevant, and the total inelastic nucleus-nucleus cross section is obtained by integrating Eq. (2.12) over all possible impact parameters:

$$\sigma^{\text{inel}}_{A+B} = 2\pi \int_0^\infty b\, db \left[1 - \left(1 - T_{AB}(\mathbf{b})\, \sigma^{\text{inel}}_{\text{NN}}\right)^{AB}\right]. \tag{2.13}$$

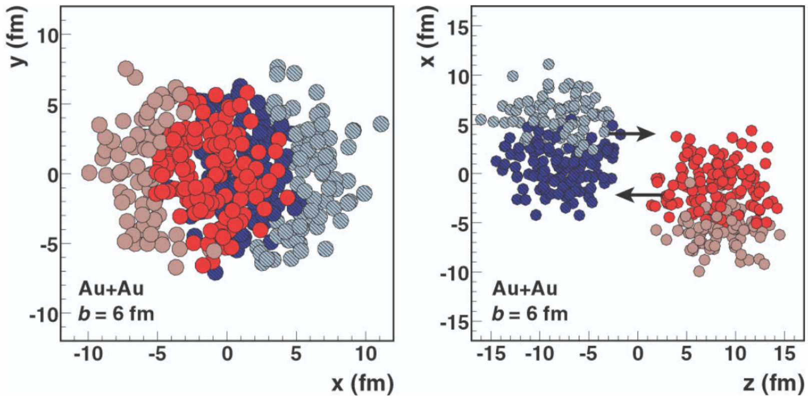

FIGURE 2.5: Example of a Glauber Monte Carlo simulation of an Au-Au collision at $\sqrt{s_{\text{NN}}} = 200$ GeV with impact parameter $b = 6$ fm. (a) View in the transverse plane; (b) view along the beam axis. Dark-colored circles indicate participant nucleons while light-colored ones represent spectators [51].

Experimentally, heavy-ion collisions are categorized according to their **centrality**, the degree of geometrical overlap between the two nuclei. These classes are are defined as percentiles of the total cross section in Eq. (2.13) and determined by correlating final-state observables with the collision geometry. Typical observables include the number of charged particles produced in a specific pseudorapidity range, the total energy deposited in forward detectors, or the number of spectator nucleons detected in zero-degree calorimeters. The measured distributions are then compared to Glauber model predictions to extract the corresponding average values of $\langle N_{\text{part}} \rangle$ and $\langle N_{\text{coll}} \rangle$ for each centrality interval [53, 54]. An instance of a collision simulated with such a model showing the participant and spectator nucleons is reported in Fig. 2.5. This classification allows the study of centrality-dependent observables, such as particle yields, flow coefficients, and nuclear modification factors, which are essential for understanding the collective dynamics of the created medium.

2.4.1 Space Time Evolution of a Heavy-Ion Collision

Figure 2.7 [11, 55] depicts the evolution of the system formed by ultra-relativistic heavy-ion collisions. Lorentz-contracted nuclei at the LHC move at almost the speed of light ($\gamma \approx 2700$ for PbPb) and overlap for just a brief period ($t_{\text{overlap}} \approx 0.005$ fm$/c$). Right after the collision ($t = z = 0$), a dense system of gluons and quarks is produced in a highly non-equilibrium state. After the impact, the created fireball evolves through a sequence of distinct but overlapping stages, as summarized in Fig. 2.7 and outlined below:

1. **Pre-equilibrium phase ($t \lesssim 1$ fm$/c$):** At this early stage, partons from incoming nuclei interact vigorously, resulting in a dense combination of gluons and quarks. Color fields are quickly fragmented into partons by gluon splitting. Using the uncertainty relation $\Delta E\, \Delta t \approx \hbar$, with ΔE corresponding to the mean

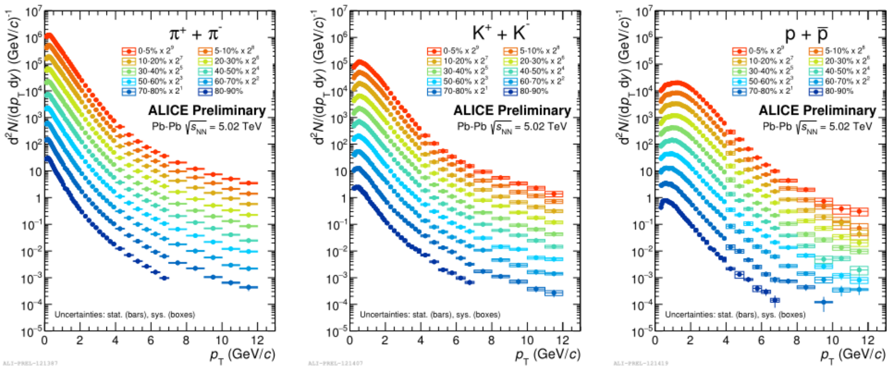

FIGURE 2.6: Caption

transverse mass $\langle m_T \rangle$, one calculates the usual formation time of these secondary quanta as $\tau_{\text{form}} \approx 0.1$ fm/c at LHC energies. During this time, hard scatterings produce partons with high transverse momentum, which can split into jets or high-mass hadrons. Prompt photons emit without additional contact with the medium.

2. **Thermalization ($t \sim 1$ fm/c):** Through frequent parton-parton interactions, the system achieves approximate thermal equilibrium. Inelastic scatterings aid in chemical equilibration by changing parton flavors. At this step, the medium achieves an energy density of $\epsilon_0 \sim 15$ GeV/fm^3 [33], indicating a locally equilibrated QGP.

3. **Hydrodynamic expansion and cooling ($t \sim$ 1-10 fm/c):** Once equilibrated, the QGP behaves almost as a perfect fluid that expands hydrodynamically due to huge pressure gradients between the hot central area and the surrounding vacuum. This expansion converts internal energy into collective flow, thereby cooling the medium as it dilutes in space-ime [11].

4. **Hadronization ($t \sim$ 10-20 fm/c):** As the system cools below the pseudo-critical temperature $T_c \approx 155$ MeV, the deconfined quarks and gluons recombine into hadrons via a continuous crossover transition [39, 38]. The interactions among the newly formed hadrons maintain approximate local equilibrium, marking the onset of the hadronic phase.

5. **Chemical freeze-out:** When the temperature decreases to around $T_{\text{ch}} \simeq$ 155-160 MeV, inelastic collisions stops, resulting in a fixed relative abundance of different hadron species. The system becomes a chemically frozen hadron gas, as predicted by lattice QCD and statistical hadronization models [48].

6. **Kinetic freeze-out:** As the fireball expands further and the hadron's mean free path exceeds their typical separation, elastic scatterings also halt. This occurs at $T_{\text{fo}} \approx 120$ MeV, after which the particles flow freely to the detectors, while retaining their momentum distributions [56].

2.5 Probing the QGP

Ultra-relativistic heavy-ion collisions provide a range of experimental observables that offer insight into the development of the QGP. Since the QGP cannot be directly observed, its presence and properties must be inferred from the particles emerging

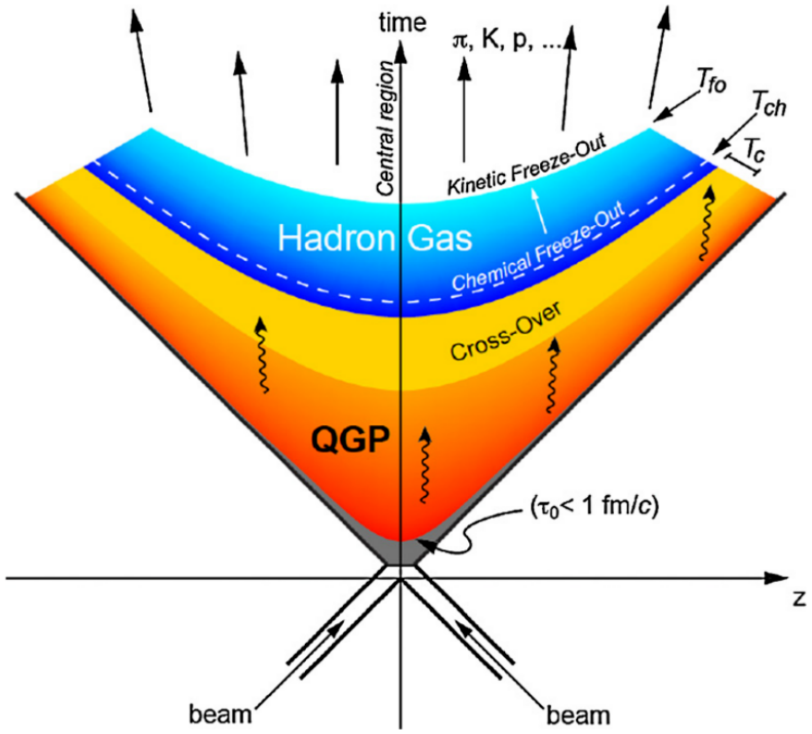

FIGURE 2.7: Space-time diagram illustrating the main stages in the evolution of a heavy-ion collision: initial overlap, pre-equilibrium, QGP formation, expansion, hadronization, and freeze-out [11].

from the collision and the patterns they encode. These observables are classified according to the momentum transfer Q involved in their production, with formation times scaling as $t \sim 1/Q^2$.

Hence, hard processes (large Q^2) have higher sensitivity to the earliest stages of the collision, whereas soft processes (small Q^2) reflect the thermalized medium's collective behavior.

High-momentum hadrons and jets

According to the Glauber model, the production cross section of high-p_T hadrons in nucleus-nucleus collisions scales with the number of binary nucleon-nucleon contacts ($\langle N_{coll} \rangle$). In order to determine whether a medium has been created or not, it is possible to use the so called nuclear modification factor R_{AA}, defined as

$$R_{AA}(p_T) = \frac{1}{\langle N_{coll} \rangle} \frac{dN_{AA}/dp_T}{dN_{pp}/dp_T}. \tag{2.14}$$

Without medium effects, $R_{AA} = 1$ for high-p_T hadrons. Significant departures from unity from central to peripheral collison regimes have been reported in experiments [57, 58]. For low-p_T hadrons, R_{AA} is expected to be lower than unity because soft-particle production scales with the number of participating nucleons rather than with $\langle N_{coll} \rangle$ [51]. This behaviour is visible in Fig. 2.7, where the R_{AA} measured by the ALICE and CMS experiments at the LHC is shown. Focusing on the ALICE results, the expected suppression in the presence of a medium is evident from the red markers: a significant $R_{AA} < 1$ is observed across the whole measured p_T range, confirming that a dense medium is created in PbPb collisions. For comparison, the same figure also reports the results for p-Pb collisions, where no such suppression is observed.

In contrast, in PbPb collisions, a strong suppression ($R_{AA} < 1$) is seen at $p_T > 3$ GeV/c, reaching a minimum near 7 GeV/c. This suppression reflects the parton energy loss in the deconfined medium via elastic scatterings and medium-induced gluon radiation (gluonstrahlung) [59, 60]. In the figure, the ALICE PbPb data are

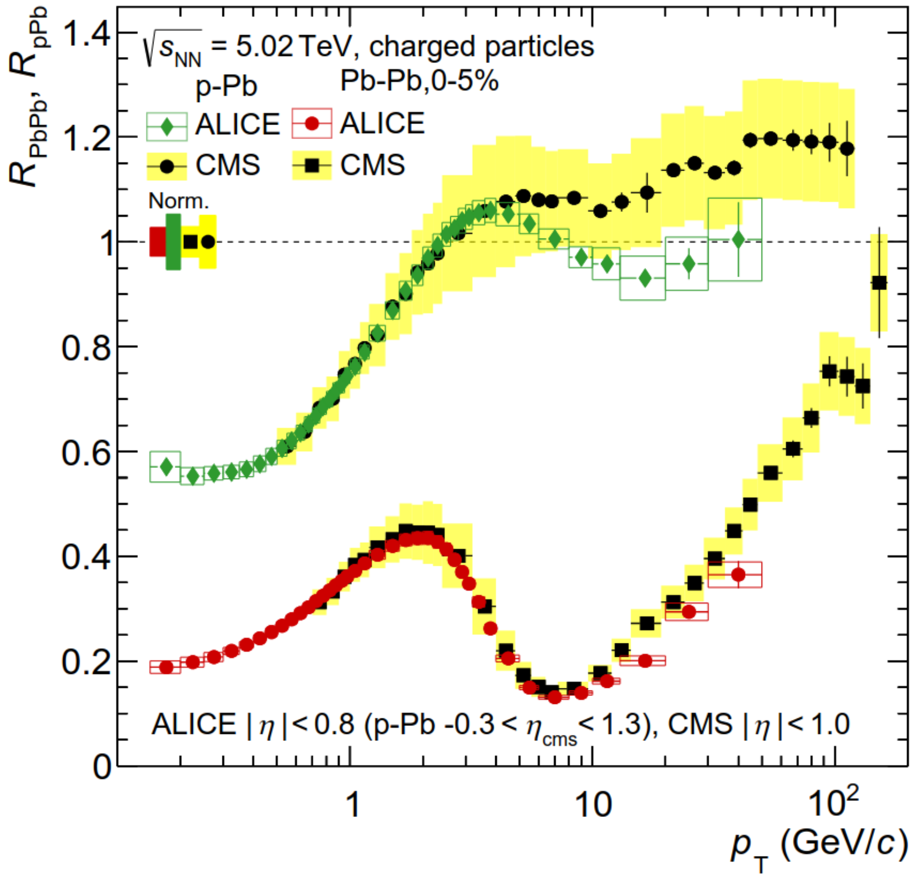

FIGURE 2.8: Nuclear modification factor R_{AA} of charged hadrons in p–Pb and Pb–Pb collisions at $\sqrt{s_{NN}} = 5.02$ TeV measured by the ALICE and CMS collaborations [57, 58].

shown as red circular markers, while the CMS PbPb results appear as yellow squares with shaded systematic uncertainties. The p-Pb reference measurements are represented by green diamonds (ALICE) and black circles (CMS).

In p-Pb collisions without the formation of a decondined medium, a moderate enhancement of the nuclear modification factor ($R_{pPb} > 1$) around $p_T \approx 2$ - 3 GeV/c is observed. The *Cronin effect* [61], caused by repeated parton scatterings inside the nucleus prior to fragmentation, is categorized as a cold nuclear matter effect along with modifications of nuclear parton distribution functions.

Energy-loss effects are also observed in fully reconstructed jets. Jets are collimated sprays of particles originating from the fragmentation and hadronization of high-energy quarks or gluons produced in the early stages of the collision [62]. When a hard scattering produces two partons with large transverse momentum, the resulting pair of back-to-back jets is referred to as a dijet system. In vacuum, dijets are expected to be balanced in transverse momentum; however, in the presence of a QGP, one or both jets may lose energy while traversing the medium, leading to a measurable imbalance [63, 64].

In heavy-ion collisions, the parton traversing through the medium loses energy, expanding and softening the associated jet. This leads to **dijet imbalance**, which is a clear manifestation of jet quenching. Figure 2.9 shows an example of a dijet event observed by CMS in Pb–Pb collisions at $\sqrt{s_{\mathrm{NN}}} = 2.76$ TeV [65], where one jet(the one located at ϕ 0 and$\eta \pi/2$) loses substantial energy in the QGP.

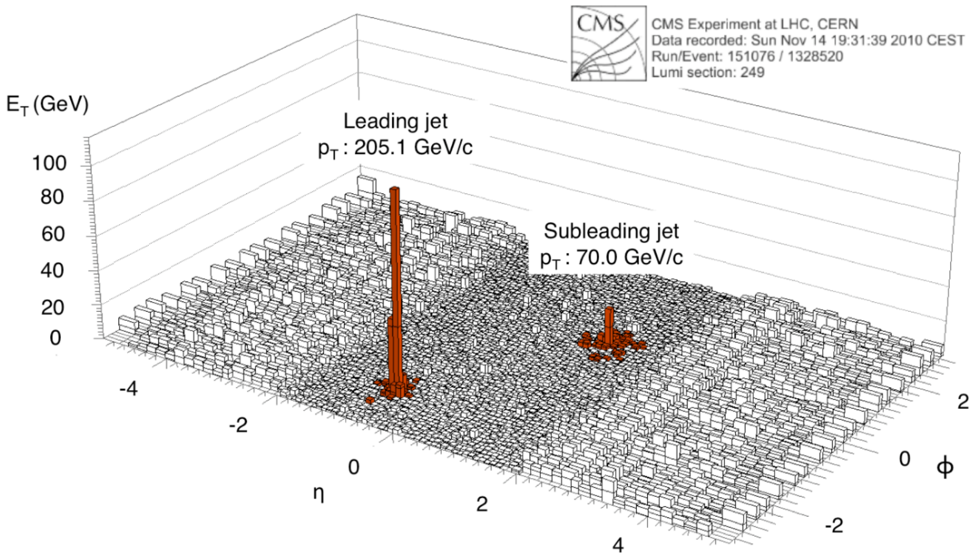

FIGURE 2.9: Example of dijet imbalance in a Pb–Pb collision at $\sqrt{s_{\mathrm{NN}}} = 2.76$ TeV observed by CMS [65]. The asymmetric energy deposition reflects parton energy loss in the QGP.

Heavy-flavour hadrons

Heavy-flavour hadrons with charm (c) or beauty (b) quarks, are produced only in hard scatterings because $m_{c,b} > 1\ \mathrm{GeV}/c^2$. Therefore, thermal processes have no impact on their production. Their propagation through the medium provides a sensitive probe of its transport properties.

The suppression of D and B mesons at low and intermediate p_{T} directly indicates heavy-quark energy loss in the QGP [66]. Heavy quarks interact mostly through gluon exchange, therefore their energy loss and flow patterns limit the medium's coupling strength and density. This effect is clearly visible in Fig. 2.10, where the average R_{AA} of prompt D mesons measured by ALICE exhibits a significant reduction below unity in central PbPb collisions, demonstrating that charm quarks lose energy while propagating through the medium. In contrast, the p-Pb reference results remain consistent with unity, confirming that the observed suppression originates from final-state interactions in the QGP rather than from cold nuclear matter effects.

Quarkonia

Color screening in the QGP is sensitively probed by bound states of heavy quark-antiquark pairs ($Q\bar{Q}$), such as charmonium (J/ψ, ψ') and bottomonium (Υ, Υ', Υ'') [68].

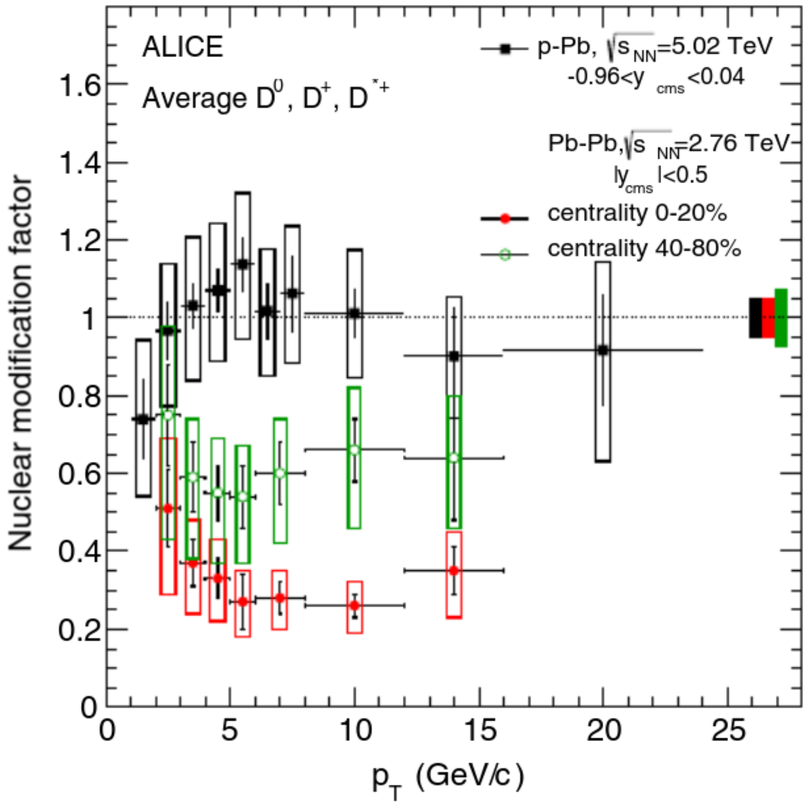

FIGURE 2.10: Average nuclear modification factor R_{AA} of prompt D^0, D^+ and D^{*+} mesons measured by the ALICE Collaboration in PbPb collisions at $\sqrt{s_{NN}} = 5.02$ TeV for the 0-20% (red markers) and 40-80% (green markers) centrality classes. The p-Pb reference measurement at the same energy is shown as black markers, illustrating the absence of suppression in collision systems where no QGP is formed [67].

In a deconfined medium, the attractive potential between Q and $\bar{Q}$ is screened by the color charges of the surrounding partons. This phenomenon is analogous to Debye screening in electromagnetic plasmas, where the presence of free charges reduces the effective range of the Coulomb potential. In such plasmas, the electric potential is exponentially screened over the Debye length λ_D, which decreases with increasing temperature or charge density.

A similar mechanism occurs in the QGP, the color-Debye screening length decreases as the temperature rises, weakening the binding between the heavy quark and antiquark. When the screening length becomes smaller than the size of the quarkonium bound state, the potential can no longer sustain the binding, leading to the dissociation of the state. This results in a suppression of quarkonium yields in nucleus-nucleus collisions relative to pp collisions, providing a direct signal of color screening in a deconfined medium.

At the LHC, bottomonium states are sequentially suppressed, with highly excited states melting at lower temperatures (Fig. 2.11) [69]. Conversely, in the charmonium sector, partial regeneration of J/ψ is observed at LHC energies due to recombination of thermalized $c\bar{c}$ pairs in the medium [70].

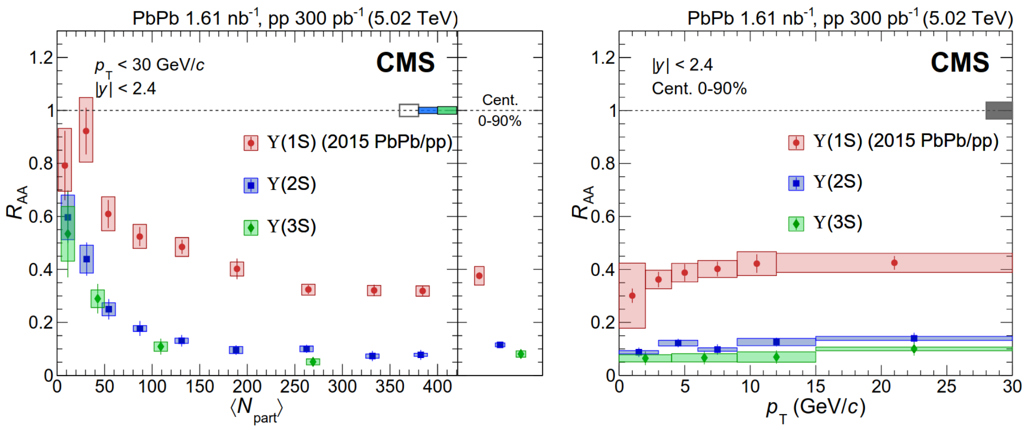

FIGURE 2.11: Sequential suppression of bottomonium states in Pb–Pb collisions at $\sqrt{s_{\rm NN}} = 5.02$ TeV measured by CMS [69]. Left: $R_{\rm AA}$ vs. centrality; right: $R_{\rm AA}$ vs. $p_{\rm T}$.

2.5.1 Soft Probes

The majority of the particles emitted in ultra-relativistic heavy-ion collisions are low-transverse-momentum hadrons, commonly known as *soft probes*. These are mainly produced in the final stages of the system evolution, after the formation and expansion of the deconfined phase. Since they reflect the collective properties of the fireball rather than the initial hard scatterings, soft probes are key observables for understanding the macroscopic dynamics, freeze-out conditions, and equation of state of the QGP.

Hadron multiplicities and spectra

At LHC energies, tens of thousands of particles are emitted per event. The average yields of the various hadron species are set at chemical freeze-out, when inelastic reactions stop. Light hadrons such as $\pi^{\pm}$ and $K^{\pm}$ mesons, along with protons and antiprotons, dominate the final-state composition [71]. More massive baryons and hyperons (e.g. Λ, Ξ, Ω) and light (anti)nuclei are created, albeit with exponentially decreased yields based on their mass.

The hadrochemical composition of the system offers direct information on the temperature and baryochemical potential at chemical freeze-out. These values can be derived from fits of hadron yields using the statistical hadronisation model (SHM), discussed in detail in Chapter **??**. At LHC energies, SHM analyses indicate a chemical freeze-out temperature $T_{\rm ch} \approx 156 \pm 3$ MeV and a baryochemical potential $\mu_B \approx 0$, consistent with lattice QCD predictions [48]. However, the transverse momentum ($p_{\rm T}$) spectra of the identified hadrons contain information about the collective dynamics of the system. In the absence of collective expansion, the spectra would follow an exponential dependence on the transverse mass $m_{\rm T} = \sqrt{p_{\rm T}^2 + m^2}$:

$$\frac{dN}{dp_{\rm T}} \propto \exp(-m_{\rm T}/T_{\rm slope}). \tag{2.15}$$

However, experimental results show a clear violation of this simple scaling: the apparent slope parameter $T_{\rm slope}$ increases with particle mass, particularly for $p_{\rm T} < m$.

This behavior is commonly expressed as:

$$T_{\text{slope}} = T_{\text{fo}} + \frac{1}{2} m \langle v_{\text{T}} \rangle^2, \tag{2.16}$$

where T_{fo} is the kinetic freeze-out temperature and $\langle v_{\text{T}} \rangle$ the average transverse flow velocity. Equation 2.16 shows that the observed spectral shapes result from the convolution of random thermal motion and an ordered collective expansion. The combined effects of thermal and collective motion are often modeled using the **Blast-Wave** (BW) parameterization [13]. The BW model assumes locally thermalized sources boosted radially in the transverse plane. Fits of identified hadron spectra using this approach yield quantitative estimates of T_{fo} and $\langle v_{\text{T}} \rangle$, revealing strong collective flow that rises with collision centrality.

Full relativistic hydrodynamic simulations provide a more thorough picture by combining the QGP equation of state with viscous evolution equations. Such models successfully reproduce the shapes of π, K, and p spectra at low p_{T} within 10-20% accuracy [72, 71]. Figure 2.12 compares experimental data from ALICE to hydrodynamic calculations for semi-central PbPb collisions.

The other soft probes are described in the next chapter.

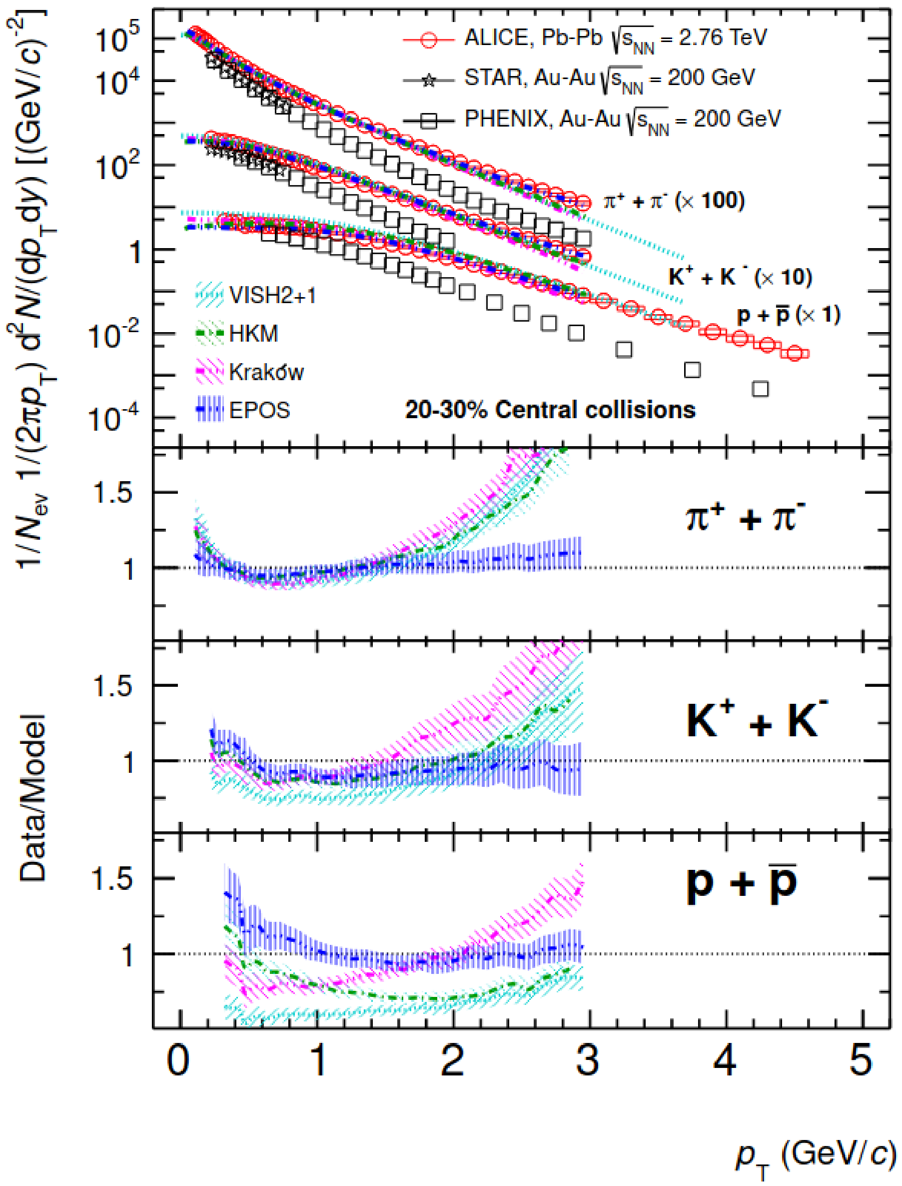

FIGURE 2.12: Transverse-momentum spectra of $\pi^{\pm}$, $K^{\pm}$, and (anti)protons measured by ALICE in PbPb collisions at $\sqrt{s_{\rm NN}}$ = 2.76 TeV, compared to hydrodynamic model predictions [71].

Chapter 3

Light-flavour hadron production

Light-flavour hadrons, composed of up (u), down (d), and strange (s) quarks, represent the bulk of the particles produced in ultra-relativistic collisions. Their production contains important information on the mechanics of hadronization as well as the thermodynamic and dynamical properties of the medium created in heavy-ion collisions [11, 33]. Because $\pi^{\pm}$, $K^{\pm}$, and $p(\bar{p})$ have distinct mass and flavor sectors, they are especially sensitive to the transition from partonic to hadronic degrees of freedom [71].

At the LHC, ALICE measures identified hadrons with great precision over a large p_{T} range and across multiple collision systems [73, 74]. These observables limit the kinetic and chemical freeze-out conditions, the extent of collective expansion, and the mechanisms driving the production of particles from the smallest (pp) to the largest (PbPb) systems.

3.1 Production mechanisms across systems

Quantum Chromodynamics (QCD) governs partonic interactions, which produce particles in high-energy collisions. Although microscopic processes are ubiquitous, their relative relevance varies with system size and event multiplicity [48].

3.1.1 pp collisions

In pp collisions, hadron production is predominantly driven by the fragmentation of partons emerging from hard or semi-hard scatterings [75]. Soft processes dominate the bulk of particle production, while multiple parton interactions (MPI), color reconnection, and the evolution of parton shower regulates the transition from the perturbative to the non-perturbative regimes [76]. Event generators such as PYTHIA and HERWIG explain these mechanisms [77]. In the context of heavy-ion physics, pp collisions serve as the baseline for studying nuclear and medium effects [78].

3.1.2 p-Pb collisions

Proton–lead (p-Pb) collisions are an intermediate step between pp and PbPb collisions, allowing the separation of initial-state nuclear effects, such as modifications of parton distribution functions and multiple scattering from final-state collective phenomena [79, 80]. High-multiplicity p-Pb events exhibit flow-like azimuthal correlations and enhanced strangeness production [81], indicating the onset of collectivity even in small systems.

3.1.3 PbPb collisions

In PbPb collisions at LHC energies, the initial conditions attained immediately after the impact correspond to energy densities substantially beyond the QCD deconfinement threshold, $\varepsilon_c \approx 1$ GeV/fm^3, as anticipated by lattice calculations [39, 38]. Bjorken energy-density estimations based on observed transverse energy densities provide $\varepsilon_0 \gtrsim 10$ - 15 GeV/fm^3 at $\tau_0 \simeq 1$ fm/c, indicating the system enters a deconfined regime.

At such energy densities, partons rapidly interact and equilibrate locally, resulting in a virtually inviscid fluid exhibiting a strong collective expansion and low shear viscosity to entropy density ratio, $\eta/s \lesssim 0.2$ [11, 33].

As the medium expands hydrodynamically, pressure gradients turn the initial spatial anisotropies into momentum anisotropies, which are then later observed empirically as flow harmonics. The interplay between the expansion rate and the equation of state dictates the trajectory of cooling towards the pseudo-critical temperature, $T_c \simeq 155$ MeV, where hadronization occurs. Below this temperature, the system transforms into a chemically frozen hadronic gas whose composition remains constant, while elastic scatterings continue to influence the final momentum spectra until kinetic freeze-out [48, 71, 82].

The final spectrum of π, K, and p reflect the cumulative influence of this evolution. The slope of the low-p_{T} spectra encodes the temperature and transverse flow velocity at freeze-out, while the relative yields carry the imprint of the previous chemical stage. As a result, identified-hadron observables in Pb–Pb collisions limits the QCD equation of state, the medium's transport coefficients, and the hadronization dynamics of the expanding fireball all at the same time.

3.2 Thermal models of particle production

The bulk of the particles produced in the final state of a heavy-ion collision belong to the class of *soft probes*. The production reflects the collective and thermalized nature of the medium at freeze-out. As already discussed in the previous chapter, these particles carry information about the bulk properties of the system and its evolution from a deconfined partonic phase to a hadronic gas. To quantitatively describe their production and composition, a statistical (thermal) approach can be adopted.

Originally proposed by Fermi [83] and later developed by Hagedorn [84], the statistical description of the production of hadrons provide a natural framework in order to deal with the complex, non-perturbative regime of QCD where numerous particles are created simultaneously. This approach poists that, after hadronization and prior to the kinetic freeze-out, the system enters a state of thermal and chemical equilibrium, thereby allowing the use of equilibrium thermodynamics to characterize the hadron yields. One of the most noteworthy achievements of the statistical models is their ability to recreate, with exceptional accuracy, the measured particle abundances at chemical freeze-out when inelastic collisions cease and the relative hadron yields stabilize [48].

The formulation of the statistical hadronisation model (SHM) is described here, along with its thermodynamic underpinnings and application to heavy-ion and small collision systems. These approaches allow for the extraction of the system's chemical freeze-out temperature, baryochemical potential, and volume, establishing a direct link between experimental hadron yield data and the QCD phase diagram.

3.2.1 Formalism and partition function

The thermodynamic properties of the system in equilibrium are encoded in the partition function Z, from which all macroscopic observables can be derived. In the grand-canonical ensemble, the mean multiplicity $\langle N \rangle$, energy $\langle E \rangle$, and entropy $\langle S \rangle$ of a system with temperature T and chemical potential μ_B are given by:

$$\langle N \rangle = \frac{1}{\beta} \frac{\partial \ln Z}{\partial \mu_B}, \quad \langle E \rangle = -\frac{\partial \ln Z}{\partial \beta} + \mu_B \langle N \rangle, \quad \langle S \rangle = k_B \frac{\partial (T \ln Z)}{\partial T}, \tag{3.1}$$

where $\beta = 1/(k_B T)$ and k_B is Boltzmann's constant. The pressure P is obtained from the partition function as:

$$P = \frac{1}{\beta} \frac{\partial \ln Z}{\partial V}. \tag{3.2}$$

For relativistic heavy-ion collisions, the system volume is large compared to the de Broglie wavelength of the particles, justifying the grand-canonical treatment. In this ensemble, both energy and particle number can fluctuate within a small subvolume ΔV, while the quantum numbers (baryon number B, strangeness S, and electric charge Q) are conserved on average over the full system.

The grand-canonical partition function for a hadron species s with degeneracy g_s, mass m_s, and chemical potential μ_s is written as [85]:

$$\ln Z_s(T, V, \mu_s) = \frac{V g_s}{2\pi^2 \hbar^3} \int_0^\infty p^2 \, dp \, \ln\Big(1 + \theta_s \lambda_s e^{-\beta E}\Big), \tag{3.3}$$

where $\lambda_s = e^{\beta \mu_s}$ is the fugacity, $\theta_s = +1$ for fermions and -1 for bosons, and $E = \sqrt{p^2 + m_s^2}$.

By differentiating Eq. (2.5), one obtains the average multiplicity:

$$\langle N_s \rangle = \frac{V g_s}{2\pi^2 \hbar^3} \int_0^\infty \frac{p^2 \, dp}{\lambda_s^{-1} e^{\beta E} + \theta_s}. \tag{3.4}$$

Expanding the logarithmic term in a power series yields an analytical form of the partition function:

$$\ln Z_s(T, V, \mu_s) = \frac{V g_s}{\beta 2\pi^2 \hbar^3} \sum_{k=1}^{\infty} \frac{(\theta_s \lambda_s)^k}{k^2} m_s^2 K_2(k \beta m_s), \tag{3.5}$$

where K_2 denotes the modified Bessel function of the second kind.

The total chemical potential of species i depends on its conserved quantum numbers as:

$$\mu_i = B_i \mu_B + S_i \mu_S + Q_i \mu_Q, \tag{3.6}$$

where μ_B, μ_S, and μ_Q represent the baryon, strangeness, and electric charge chemical potentials, respectively.

3.2.2 Ensemble choice and system-size dependence

The grand-canonical formulation is ideally suited for describing large systems such as PbPb central collisions, where the system volume guarantees that quantum-number conservation exists on average. However, in smaller systems (e.g. pp or p-Pb collisions), the relevant correlation volumes become comparable to the particle mean free path. In these cases, it is crucial to impose exact local conservation of some specific quantum numbers, notably strangeness, leading to the employment of a *canonical ensemble* [86, 87]. Canonical suppression effects become substantial in low-multiplicity events, which naturally explains the observed decrease in the strange-hadron yields in small systems.

In order to explain incomplete chemical equilibration of strange quarks, a strangeness saturation factor γ_s is commonly used. This parameter adjusts the fugacity as $\lambda_s \to \gamma_s \lambda_s$, hence adjusting the relative creation of strange hadrons. In small systems, $\gamma_s < 1$ implies partial equilibration, but in central heavy-ion collisions, $\gamma_s \to 1$ represents full strangeness saturation.

3.2.3 Model fits and extracted parameters

By fitting measured yields of identified hadrons (π, K, p, Λ, Ξ, Ω, etc.) using the Statistical Hadronisation Model (SHM), one may extract the chemical freeze-out temperature T_{ch}, baryochemical potential μ_B, and system volume V. The fit guarantees the conservation of net quantum numbers while minimizing the deviation between model predictions and experimental results.

A global fit to ALICE measurements in central PbPb collisions at $\sqrt{s_{\mathrm{NN}}} = 2.76$ TeV yields $T_{\mathrm{ch}} = 156.5 \pm 1.5$ MeV, $\mu_B = 0.7 \pm 3.8$ MeV, and $V = 5280 \pm 410$ fm^3, with a good overall agreement ($\chi^2/\mathrm{NDF} = 1.6$) across nine orders of magnitude in particle yields [48, 88]. Notably, the chemical freeze-out temperature is consistent with the pseudo-critical temperature for the QCD phase transition predicted by lattice QCD ($T_c = 154 \pm 9$ MeV [39]), indicating that hadronisation occurs roughly concurrently with chemical decoupling. The derived baryochemical potential is close to zero within uncertainties, implying that matter and antimatter are created in about equal amounts at midrapidity in central PbPb collisions at the LHC. However, this conclusion is subject to a significant degree of uncertainty since the SHM fits do not fully account for associated systematic errors between particles and antiparticles, and the entire covariance matrix of the experimental data is not publicly available.

A more robust strategy, especially at low collision energies, is to fit particle to antiparticle yield ratios, which cancel out many of the related effects. The development of the freeze-out parameters with impact energy is summarized in Fig. 3.1. The diagram shows the chemical freeze-out temperature T_{ch} and baryochemical potential μ_B extracted from hadron yield measurements over a wide range of $\sqrt{s_{\mathrm{NN}}}$, from AGS and SPS to RHIC and LHC energies. As the energy increases, T_{ch} rises and saturates around 155-160 MeV, while μ_B gradually drops to zero. This trend represents the progressive transition to a virtually baryon-symmetric state, in which pair creation takes precedence over baryon transport. The resulting freeze-out curve delineates a region in the (T, μ_B) plane that coincides with the phase boundary predicted by lattice QCD, indicating that chemical freeze-out occurs close to the QCD crossover transition. An further and complementary way to probe the baryon number transport is to study the dependence of μ_B on collision centrality at fixed $\sqrt{s_{\mathrm{NN}}}$. At lower beam energies, when baryon halting becomes prominent, central collisions exhibit greater μ_B values due to increased baryon transit from beam rapidity to midrapidity. This trend has been systematically studied by the STAR Collaboration in the RHIC Beam Energy Scan (BES) I [89], where SHM parameters were extracted from antiparticle-to-particle yield ratios for different centrality classes and energies. The results, shown in Fig. 3.2, reveal that μ_B increases with both decreasing $\sqrt{s_{\rm NN}}$ and increasing average number of participating nucleons $\langle N_{\rm part}\rangle$, confirming that baryon number stopping plays a more prominent role in the most central collisions at lower energies.

Recent analyses at the LHC have extended this approach to $\sqrt{s_{\rm NN}} = 5.36$ TeV, investigating possible centrality-dependent modifications of μ_B within the high-energy regime where baryon stopping is expected to be minimal. Such measurements provide valuable cross-checks of the baryon–antibaryon symmetry assumption and are discussed in detail in this thesis.

3.2.4 Production of light-flavour hadrons across colliding systems

The statistical approach described in the preceding section may be directly confronted with experimental data from various collision systems. The comparison of model predictions and observations of hadron yields, ratios, and correlations provides a rigorous evaluation of the statistical hadronisation picture and its general application beyond massive heavy-ion systems.

Strangeness enhancement and canonical effects

While considering particle production with strangeness content, a suppression w.r.t other light quarks such as u and d is usually expected. This is owing to the conservation of quantum numbers (no strangeness being present in the initial state) and also due to the large constituent mass of the s quark ($m_s = 1.4 \cdot m_u$). This can be explained by the strong interactions conserving the strangeness number explicitly, thereby for the entire system $\Sigma S = 0$. Now this consideration has a very little effect if the source has a large volume since the conservation of strangeness has to be respected in average for the whole system. However, the canonical ensemble that is needed in order to describe the smaller systems such as pp or e^+e^-, indicates the production of strange hadrons in pairs for local strangeness conservation, results in a large energetic threshold that the overall system needs to overcome (canonical suppression). Consequently, such processes are unlikely to happen in volumes with small sources. Instead the grand-canonical formulation assumes the average strangeness quantum number conservation, an instance that can be easily reproduced in heavy-ion collisions. Therefore, as expected, the strangeness suppression is indeed observed in smaller collision sysytems such as pp, $p\bar{p}$ and e^+e^- (Fig 3.3)

In heavy ion collisions, owing to the large energy densities, s quarks can be produced thermally. In the deconfined phase, the pressence of large gluon density can lead to an increased production of $s\bar{s}$ pairs via the gluon fusion processes. Additionally, the chiral symmetry restoration in proximity to the deconfined transition temperature lowers the mass of the constituents below ≈ 150 MeV, thereby decreasing the energetic threshold for its production [91]. The combined effect of these two phenomenon, significantly reduce the timescale for strangeness saturation and chemical equilibrium [90]. Therefore, compared to smaller systems, strangeness enhancement was proposed as a signature of QGP formation [92]. This enhanced strange-quark production was posited as a hallmark of deconfinement, resulting from increasing $gg \rightarrow s\bar{s}$ rates in a partonic medium for a very long time. However, it has recently been demonstrated that the observed behavior of (multi)strange hadron yields with multiplicity can be quantitatively recreated within the conventional formulation of SHM, without the need for explicit deconfinement. In this approach,the exact local conservation of strangeness in small systems results in the suppression of the production rates, which progressively vanishes as the system volume increases [93].

Figure 3.4 shows the most recent ALICE measurements of strange-to-non-strange hadron yield ratios in pp, p-Pb, and PbPb collisions at different centre-of-mass energies. The ratios show a continuous evolution with charged-particle multiplicity, increasing with multiplicity until they saturate for center PbPb collisions, when the grand-canonical limit is attained. The enhancement becomes more pronounced with increasing strangeness content, from kaons to multi-strange baryons [90] such as Ξ and Ω. The results are compared with PYTHIA 8 (Monash tune) [94], EPOS-LHC [95], and DIPSY model calculations [96], as well as with canonical SHM predictions obtained with THERMAL-FIST [97]. The smooth evolution with multiplicity and the saturation toward central PbPb values demonstrate the transition from canonical to grand-canonical behaviour.

The data are compared with model calculations made with PYTHIA 8 (Monash tune), EPOS-LHC, and DIPSY, including rope hadronization, as well as canonical SHM calculations using THERMAL-FIST. While conventional PYTHIA underestimates yields except at the lowest multiplicities, models with a collective or color-rope component (EPOS-LHC, DIPSY) mimic the growing trend. A quantitative agreement is reached with the classical SHM, in which the suppression of strange-particle creation at low multiplicity occurs naturally due to precise strangeness conservation. In the THERMAL-FIST implementation, this suppression can be parameterised through a multiplicity-dependent correlation volume V_c, or equivalently, a strangeness saturation factor γ_s, which evolves from $\gamma_s \approx 0.7$ in low-multiplicity pp events to $\gamma_s \approx 1$ in central PbPb collisions.

3.3 Collective Flow

The bulk evolution of the medium formed by heavy-ion collisions exhibits a strong collective behavior, with large pressure gradients developed in the early stages driving an expansion analogous to that of a nearly perfect fluid. This collective motion, generally referred to as *flow*, transforms the initial geometric anisotropies of the collision zone into quantifiable anisotropies in the final-state momentum distributions of emitted hadrons [72, 98]. The observed collective patterns gives clear evidence for the creation of a strongly interacting QGP that behaves as a relativistic fluid with extremely low shear viscosity to entropy density ratio, $\eta/s \lesssim 0.2$ [99, 11].

A few moments after impact ($t \lesssim 1$ fm$/c$), the high energy density causes local thermalization of partons, resulting in the formation of the deconfined QGP. The pressure gradients formed by this hot and dense state initiate a hydrodynamic expansion in all spatial directions. As the medium cools, the partonic degrees of freedom transforms into hadrons around the pseudo-critical temperature $T_c \approx 155$ MeV [38, 39], and the system then continues to expand as a hadronic gas until all elastic interactions halt at kinetic freeze-out.

This collective expansion is reflected in the spectral shapes and angular distributions of the emitted particles. At midrapidity, the radial component of the flow elevates heavier hadrons to higher p_{T}, producing the characteristic mass ordering observed in the p_{T} spectra [71, 82]. Meanwhile, the anisotropic component of the expansion translates the initial geometric asymmetries of the nuclear overlap into anisotropies in azimuthal momentum space, measured by the flow harmonics v_n [100, 101]. The simultaneous description of these events within relativistic hydrodynamics establishes the QGP as a strongly coupled, nearly perfect fluid [98, 33].

Measurements at RHIC and the LHC show that the magnitude of collective flow is substantially dependent on the system size, centrality, and final-state multiplicity. In central PbPb collisions, collective motion dominates the dynamics of the production of particles up to p_{T} of several GeV/c, while flow-like characteristics have been observed in small systems such as p-Pb and high-multiplicity pp collisions [81, 80, 102]. These findings indicate that collective behaviour may emerge in any sufficiently dense QCD system, independent of its initial geometric scale.

The following subsections describe two complementary aspects of the collective expansion: the isotropic (radial) component, modelled using the Boltzmann–Gibbs Blast-Wave (BGBW) parametrisation, and the anisotropic component, quantified by the flow coefficients v_n extracted from the azimuthal distributions of produced particles.

3.3.1 The Boltzmann-Gibbs Blast-Wave (BGBW) model

A widely employed phenomenological framework used for describing the combined effects of thermal motion and collective expansion during kinetic freeze-out is the *Boltzmann-Gibbs Blast-Wave* (BGBW) model [103]. It denotes a simplified limit of hydrodynamic freeze-out in which particles are emitted instantaneously from a cylindrically symmetric, radially expanding surface with constant proper time. Starting from the Cooper-Frye formula and assuming Boltzmann statistics and boost invariance at midrapidity, the transverse mass spectrum can be expressed as:

$$\frac{dN}{dy\, m_{\mathrm{T}}\, dm_{\mathrm{T}}} \propto g\, m_{\mathrm{T}} \int_0^R r_{\mathrm{T}}\, dr_{\mathrm{T}}\, K_1\left(\frac{m_{\mathrm{T}} \cosh \rho(r_{\mathrm{T}})}{T_{\mathrm{kin}}}\right) I_0\left(\frac{p_{\mathrm{T}} \sinh \rho(r_{\mathrm{T}})}{T_{\mathrm{kin}}}\right), \tag{3.7}$$

where I_0 and K_1 are modified Bessel functions, R is the transverse radius of the source, and T_{kin} denotes the *kinetic freeze-out temperature*, the temperature at which elastic interactions cease and particles decouple from the medium. The transverse flow rapidity $\rho(r_{\mathrm{T}}) = \tanh^{-1}[\beta(r_{\mathrm{T}})]$ encodes the radial expansion velocity profile,

$$\beta(r_{\mathrm{T}}) = \beta_s \left(\frac{r_{\mathrm{T}}}{R}\right)^n, \tag{3.8}$$

where β_s is the maximum (surface) velocity and n defines the shape of the velocity profile. For this parametrisation, the mean transverse velocity is given by:

$$\langle \beta_{\mathrm{T}} \rangle = \frac{2}{2+n}\, \beta_s \tag{3.9}$$

The BGBW model allows simultaneous fitting of the p_{T} spectra of identified hadrons such as π, K, and p, assuming that they come from a common thermalized source described by $(T_{\mathrm{kin}}, \langle \beta_{\mathrm{T}} \rangle, n)$. Alternatively, individual fits to a single species can be used to extrapolate spectra into unmeasured p_{T} regimes for yield integration.

The BGBW analysis of PbPb collisions at LHC energies reveals a clear dependence of the extracted parameters on the event centrality and system size. With increasing centrality (or multiplicity), the average transverse velocity $\langle \beta_{\mathrm{T}} \rangle$ grows steadily, indicating stronger collective expansion in denser systems, while the kinetic freeze-out temperature T_{kin} decreases, suggesting a longer evolution before decoupling. For peripheral collisions, the smaller degree of collectivity leads to larger T_{kin} and smaller $\langle\beta_T\rangle$, consistent with an earlier freeze-out of a smaller, less equilibrated system.

The comparison of results across energies and systems shows that $\langle\beta_T\rangle$ increases from RHIC to LHC energies but tends to saturate at $\langle\beta_T\rangle \approx 0.65$-$0.7$ for central PbPb collisions. This behaviour indicates that the additional energy available at higher $\sqrt{s_{NN}}$ primarily leads to higher particle multiplicities rather than to significantly faster expansion of the fireball [11]. In smaller systems such as pp and p-Pb, the blast-wave fits yield T_{kin} and $\langle\beta_T\rangle$ values that follow the same multiplicity-dependent trend, implying that collective-like effects emerge whenever the final-state density becomes sufficiently large [81].

Although the BGBW model does not explicitly incorporate viscosity or full hydrodynamic evolution, its parameters provide an intuitive overview of the interplay between temperature and collective flow at the final stage of the collision. Particularly, the kinetic freeze-out temperature T_{kin} is consistently found to be lower than the chemical freeze-out temperature T_{ch} obtained from statistical-hadronisation fits, supporting a picture in which the system continues to expand and cool after chemical equilibrium has been established, until elastic interactions finally cease [48].

3.3.2 Anisotropic flow

The fireball's expansion is not isotropic at azimuthal angle φ. Non-central collisions cause elliptical deformation of the overlap region between colliding nuclei, leading to spatial and momentum anisotropies due to hydrodynamic pressure gradients. This collective anisotropy is characterized by the Fourier coefficients v_n in the azimuthal particle distribution:

$$\frac{dN}{d(\varphi - \Psi)} = \frac{N}{2\pi}\left(1 + 2\sum_{n=1}^{\infty} v_n \cos[n(\varphi - \Psi)]\right), \tag{3.10}$$

where Ψ denotes the reaction-plane angle. The second harmonic coefficient v_2 (elliptic flow) reflects the almond-shaped overlap geometry of semi-central collisions, while higher-order coefficients (v_3, v_4, ...) arise from event-by-event fluctuations in the initial density profile.

Anisotropic flow is an important observable for restricting the transport parameters of the QGP. The size and centrality of v_2 rely on the shear viscosity-entropy density ratio (η/s) and the thermalization timeframe [99, 72]. Experimental data from both RHIC and the LHC are well described by hydrodynamic models assuming an early-thermalized, nearly perfect fluid with $\eta/s \approx 0.1$–0.2 [98, 101]. This behavior establishes the QGP as the most perfect fluid known in nature.

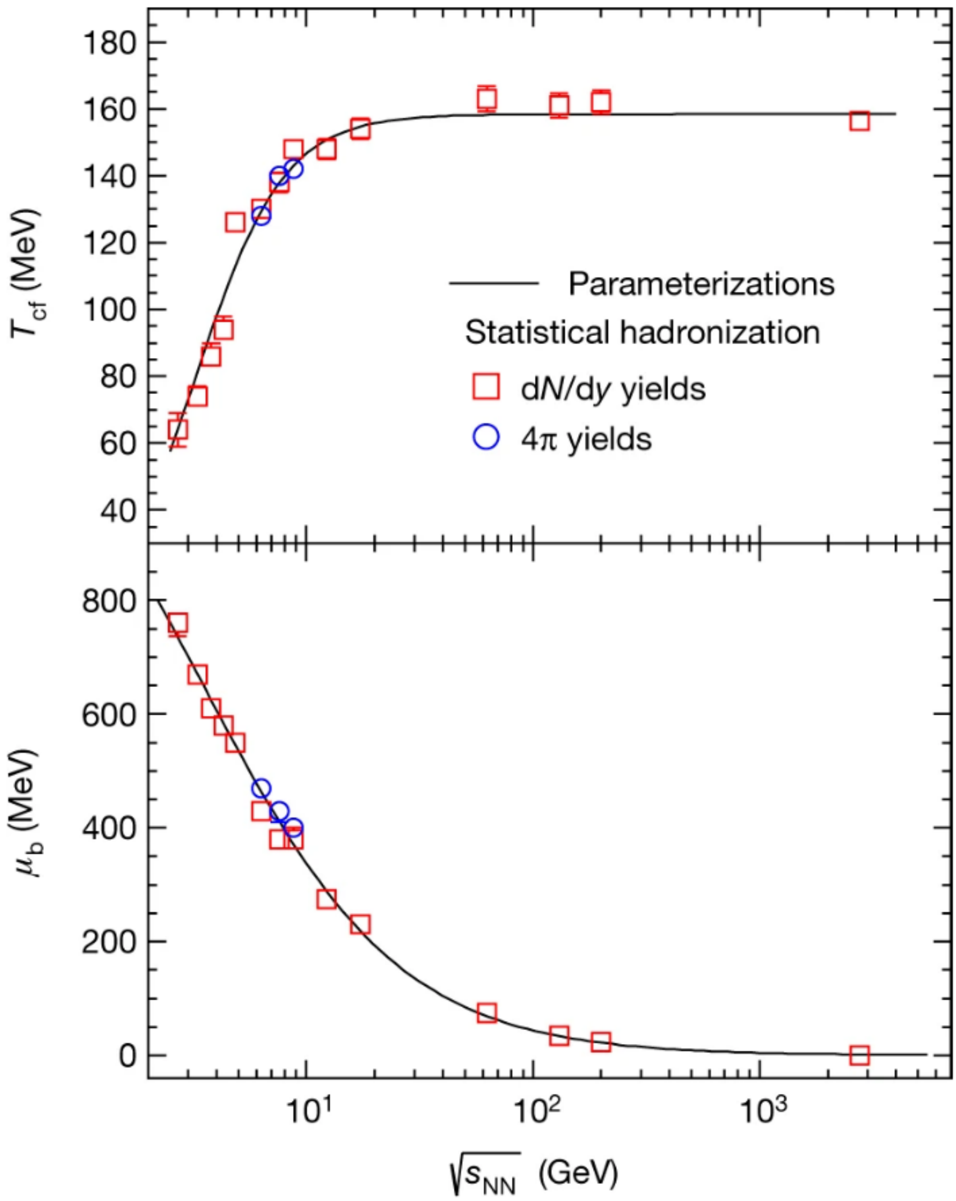

FIGURE 3.1: Chemical freeze-out temperature T_{ch} and baryochemical potential μ_B extracted from hadron yield measurements at the AGS, SPS, RHIC, and LHC, as a function of the centre-of-mass energy $\sqrt{s_{NN}}$. The solid and dashed lines represent phenomenological parameterisations of the freeze-out curve [48].

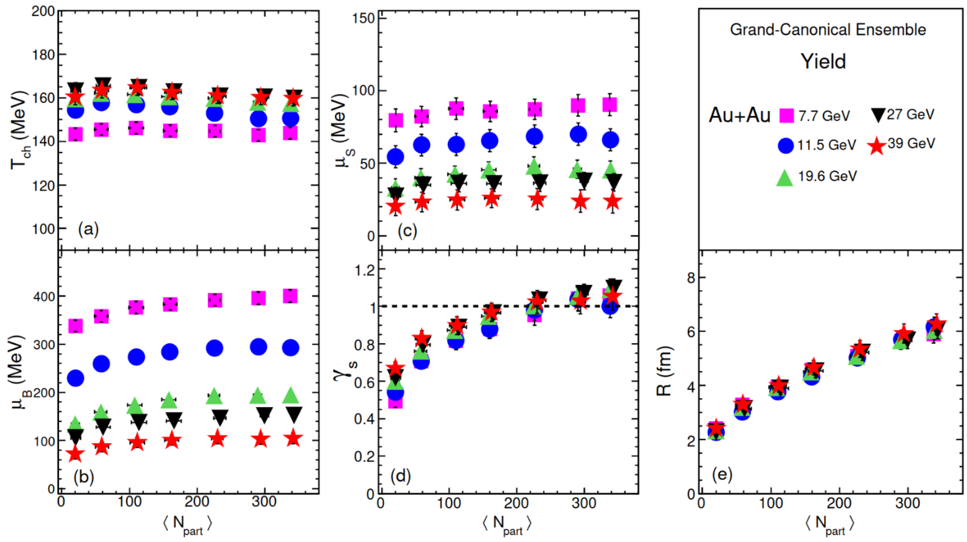

FIGURE 3.2: Centrality dependence of the baryochemical potential μ_B obtained by the STAR Collaboration at various beam energies in the RHIC Beam Energy Scan I [89]. The increase of μ_B with $\langle N_{\text{part}} \rangle$ at low $\sqrt{s_{\text{NN}}}$ indicates stronger baryon stopping in central collisions.

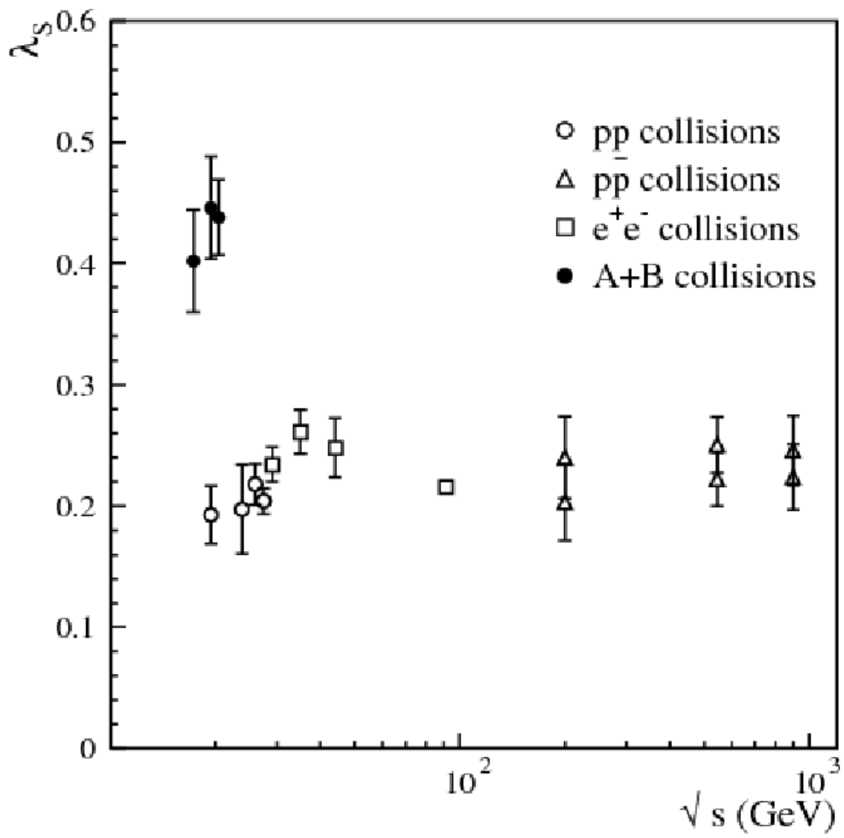

FIGURE 3.3: Strangeness suppression factor taht is measured via scaling of the net strange content to the non-strange one for different collision systems: $\lambda_s = 2\langle s\bar{s}\rangle / \langle u\bar{u} + d\bar{d}\rangle$ [90].

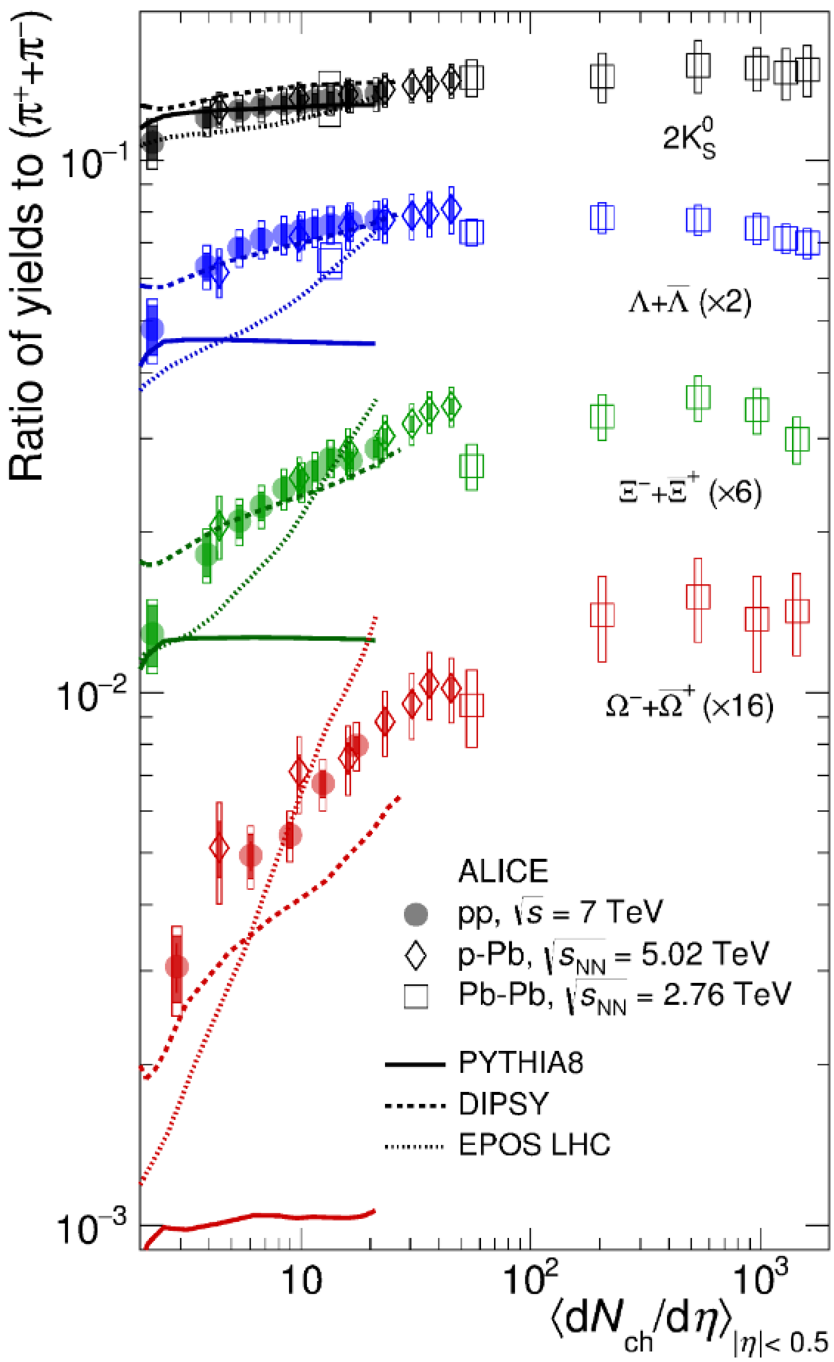

FIGURE 3.4: Yield ratios of (multi)strange hadrons to charged pions measured by the ALICE Collaboration in pp, p-Pb, and PbPb collisions at the LHC [90].

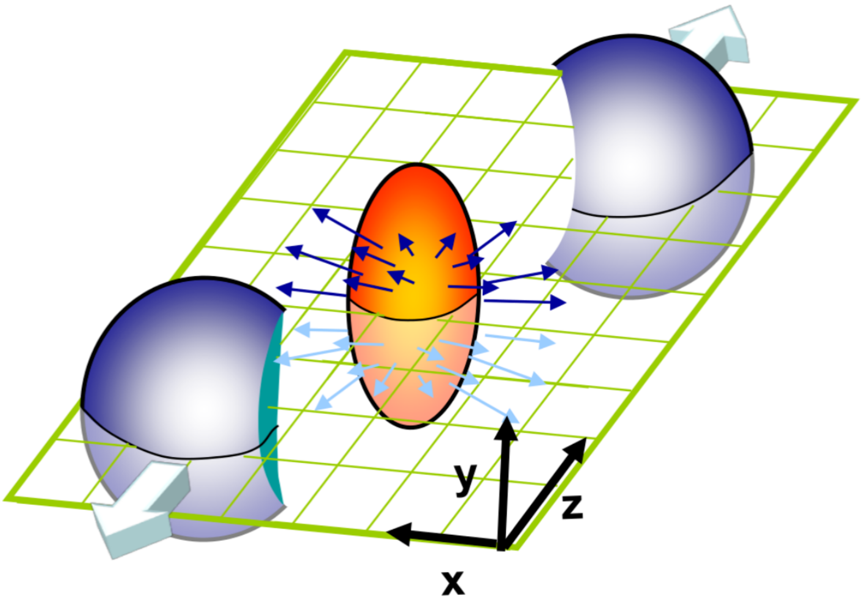

FIGURE 3.5: Schematic representation of the anisotropic overlap region in a semi-central heavy-ion collision. The pressure gradients are larger along the short axis of the overlap region, leading to elliptic flow (v_2).

Chapter 4

The ALICE Experiment

4.1 Overview and Motivation

This chapter includes a brief overview of CERN's history, along with some insights on the LHC. In addition, a detailed explanation of the ALICE experiment along with its construction and functionality of the detectors are provided.

4.2 CERN

The European Organization for Nuclear Research, abbreviated as CERN (from the French *Conseil Européen pour la Recherche Nucléaire*), is a multinational laboratory based near Geneva, Switzerland. It currently consists of 23 member states and employs approximately 3200 staff members, while hosting nearly 14,000 researchers worldwide, including physicists, engineers, technicians, and students [104]. CERN was founded in 1954 and has since made landmark contributions to both fundamental physics and technology. For example, the invention of the multi-wire proportional chamber (MWPC) by Georges Charpak at CERN revolutionized particle detection, earning the 1992 Nobel Prize in Physics [105]. CERN has also designed and operated a wide range of accelerators, from early linear accelerators such as Linac 2 (commissioned in 1978) to synchrotrons like the Proton Synchrotron (PS) and the Super Proton Synchrotron (SPS). The most powerful of these is the Large Hadron Collider (LHC), the world's highest-energy particle accelerator, which is described in detail in the following section [106].

4.3 The Large Hadron Collider (LHC)

The Large Hadron Collider (LHC) is the world's largest and most powerful particle accelerator. It is located in a 26.7 km circular tunnel situated about 100 m underground near Geneva, straddling the Franco-Swiss border [106]. The LHC is designed to accelerate and collide both protons and heavy ions at unprecedented energies. Proton-proton (pp) collisions have reached center-of-mass energies up to $\sqrt{s} = 14$ TeV, while LHC employs 1232 superconducting dipole magnets, each generating a magnetic field of 8.36 T. Prior to injection into the main ring, particles are pre-accelerated in a chain of linear and circular accelerators known as the *injector complex*. For protons, the sequence consists of Linac 2 (replaced by Linac 4 in 2020), the Proton Synchrotron Booster (PSB), the Proton Synchrotron (PS), and finally the Super Proton Synchrotron (SPS) [107]. For heavy ions, beams are first accelerated in Linac 3 and subsequently stored and cooled in the Low Energy Ion Ring (LEIR) before being transferred to the PS and SPS.

Typical bunch intensities are of order 10^{11} protons or 9×10^7 lead ions per bunch. The LHC has two separate vacuum beam pipes, enabling beams to circulate clockwise and counterclockwise. They cross at four interaction points where the major experiments are located: ALICE, ATLAS, CMS, and LHCb. At design luminosities, up to 6×10^8 collisions per second can occur at these points, providing an enormous dataset for exploring fundamental physics [106].

While all four experiments record LHC collisions, they focus on distinct physics goals: ATLAS and CMS on general-purpose high-energy physics, LHCb on flavor physics and CP violation, and ALICE as the dedicated heavy-ion experiment designed to explore the QGP.

The ATLAS and CMS detectors are general-purpose experiments designed to explore a wide range of physics both within and beyond the Standard Model. They are particularly renowned for their leading role in the discovery of the Higgs boson in 2012, a milestone achievement that confirmed the mechanism of electroweak symmetry breaking [108, 109].

By contrast, the LHCb experiment was purpose-built to investigate heavy-flavor physics, with a focus on precision measurements of CP violation and rare decays of hadrons containing b and c quarks. Among its major achievements is the discovery of exotic hadronic states, including pentaquarks, which provided key insights into the dynamics of the strong interaction [110]. Finally, the A Large Ion Collider Ex-

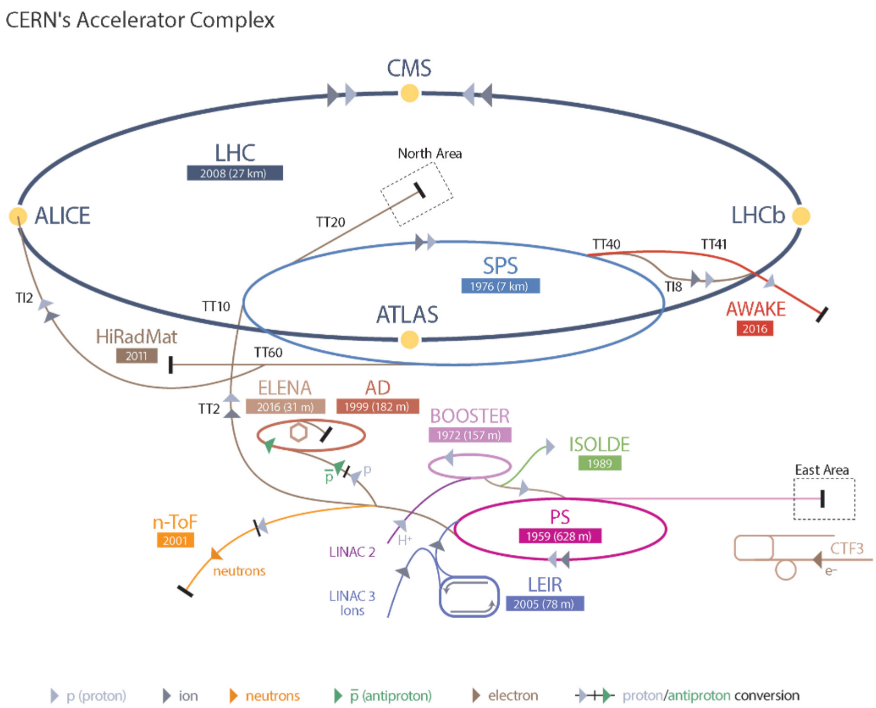

FIGURE 4.1: Schematic view of the CERN Large Hadron Collider (LHC) accelerator complex, showing the chain of pre-accelerators and the main ring where proton and heavy-ion beams collide at up to $\sqrt{s_{\rm NN}} = 5.36$ TeV.

periment (ALICE) experiment is the only LHC detector dedicated specifically to the study of heavy-ion physics. Its primary goal is to investigate strongly interacting matter under extreme conditions of temperature and density, with a focus on the formation and properties of the QGP [111].

This chapter describes the ALICE detector and its subsystems in depth, with a focus on the tracking and PID detectors, which are critical for identifying π, K, and p at midrapidity.

This thesis analyzes data acquired during LHC Run 3. The ALICE configuration for Run 3 will be discussed. Section 4.4.1 summarizes the key changes done during Long Shutdown 2 (2019-2021), which greatly boosted ALICE performance for Run 3 and beyond.

4.4 ALICE setup

ALICE is one of four key experiments at the CERN LHC that is especially designed to examine ultra-relativistic heavy-ion collisions. The major objective of ALICE is to examine the characteristics of strongly interacting matter at high energy densities and temperatures, where quarks and gluons are predicted to form a deconfined phase known as the QGP. [111].

ALICE is distinguished by its capacity to function in the setting of central PbPb collisions, which result in unparalleled particle multiplicities at the LHC. The detector was intended to handle charged-particle concentrations of up to 8000 particles per unit of speed in the most central collisions, while retaining outstanding tracking and particle-identification (PID) performance [112]. ALICE delivers strong PID throughout a large transverse-momentum range, from $p_{\mathrm{T}} \sim 0.15\ \mathrm{GeV}/c$ (where bulk physics dominates) to around 20 GeV/c, spanning the perturbative region where hard probes are significant [112, 113]. The general ALICE setup in RUN 3 is detailed

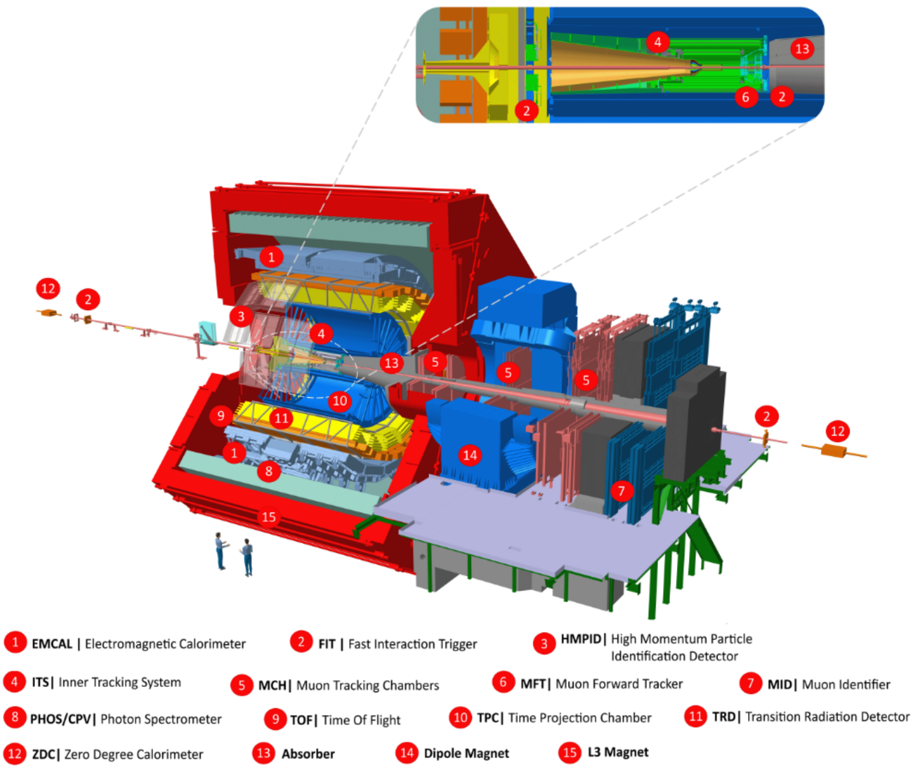

FIGURE 4.2: ALICE detector systems after the LS2 upgrade [114].

in Fig. 4.2. The equipment itself is huge, measuring around 26 meters in length, 16 meters in diameter, and weighing close to 10,000 tons. Its pseudorapidity acceptability is separated into two major regions:

- The Central Barrel, which surrounds the interaction point, is contained inside the enormous solenoidal magnet that generates a 0.5 T magnetic field. This section houses the essential tracking and PID detectors (including the Inner Tracking System, Time Projection Chamber, and Time-Of-Flight detector). The magnetic field allows for exact momentum reconstruction and charge discrimination by bending the paths of charged particles.

- The Muon Spectrometer, encompassing the forward rapidity area ($-4 < \eta < -2.5$), is dedicated to monitoring heavy-flavor probes such as quarkonia via muonic decay channels. It has no direct function in the current π, K, p study.

Following Run 2 (2015-2018), ALICE received a considerable update during Long Shutdown 2 (2019-2021), in preparation for Run 3 (2022-present).

4.4.1 ALICE Upgrade during LS2

During the first two LHC operations, the ALICE experiment produced outstanding physics results spanning a wide range of observables, including the characterisation of the QGP and the discovery of collective phenomena in tiny systems. However, several subsystems and readout infrastructures were not adjusted to properly use the enhanced luminosity predicted for Runs 3 and 4. To extend its reach to rare probes and low-p_{T} measurements, during the LHC Long Shutdown 2 (2019-2021), ALICE underwent a comprehensive upgrade l [115, 116].

The primary goal of this upgrade were to considerably improve vertexing precision, increase readout capability to accommodate larger event frequencies, and enable continuous data gathering. The upgraded ALICE detector now functions as a high-rate experiment, capable of recording interaction rates of up to 50 kHz in Pb–Pb and 200 kHz in pp collisions. This marks an increase of more than two orders of magnitude compared to the Run 2 configuration and enables the collection of large, unbiased datasets essential for precision studies of rare processes such as low-p_{T} heavy-flavour production, thermal dilepton emission, and light (anti)nuclei formation. In Pb–Pb collisions, the vastly increased integrated luminosity allows detailed differential measurements of QGP properties, including collective flow, jet quenching, and heavy-flavour transport, with unprecedented statistical precision. It also opens the possibility to study event-by-event fluctuations, correlations, and the production of rare and short-lived hadronic states, thereby deepening the understanding of the microscopic structure and evolution of the strongly interacting medium created in ultra-relativistic heavy-ion collisions [115, 117]. [117].

The most significant upgrade concerned the **Inner Tracking System (ITS)**, which was completely replaced by the new **ITS2** [118]. Composed of seven layers of monolithic active pixel sensors (MAPS) based on the ALPIDE technology, the ITS2 provides a factor 3 improvement in transverse and factor 6 in longitudinal impact-parameter resolution compared to the previous system. The reduction of the beam-pipe diameter from 60 mm to 36 mm and the ultra-low material budget (0.35 % X/X_0 per layer) ensure excellent tracking and vertexing even for particles with very low transverse momentum.

The **Time Projection Chamber (TPC)** underwent a major transformation with the replacement of its multi-wire proportional chambers by quadruple Gas Electron Multiplier (GEM) foils [119]. This upgrade enables continuous readout operation without gating, while mitigating space-charge distortions at high interaction rates.

Other central-barrel detectors were also modernized to cope with the increased data throughput. The readout electronics of the **Transition Radiation Detector (TRD)**,

Time-of-Flight (TOF), **Electromagnetic Calorimeter (EMCal)**, **PHOS**, and **Zero-Degree Calorimeters (ZDC)** were upgraded for high-rate operation. The **High Momentum Particle Identification Detector (HMPID)** received new front-end electronics and additional absorbers to extend its use in studies of (anti)nuclei cross sections. A completely new **Muon Forward Tracker (MFT)** was installed upstream of the hadron absorber in the muon spectrometer, improving the secondary-vertex resolution for muons from open heavy-flavour decays and quarkonia [115].

The detectors previously responsible for timing, triggering, and luminosity determination (T0, V0, and AD) were replaced by the **Fast Interaction Trigger (FIT)** system [120]. FIT provides minimum-bias triggering, centrality and event-plane determination, and accurate interaction-time measurement with sub-50 ps resolution.

Finally, a completely new online–offline computing model, the **O^2** framework, was developed to handle the continuous readout mode [115]. The O^2 system merges online data compression, reconstruction, and calibration with offline analysis in a unified environment, enabling real-time event processing and long-term data preservation.

Together, these upgrades transform ALICE into a precision, high-throughput experiment optimized for Run 3 and beyond. The improved vertexing, PID performance, and continuous readout open new opportunities for investigating the QGP through rare probes, correlations, and detailed studies of hadronization dynamics.

4.4.2 ALICE Coordinate System and Detector Overview

ALICE's coordinate system is specified as a right-handed orthogonal Cartesian system, with its origin at the nominal interaction point of the colliding beams [111].

The x-axis is perpendicular to the beam direction and points to the center of the LHC ring. The y-axis runs perpendicular to both the x-axis and the beam line, pointing vertically up. The z-axis is parallel to the beam direction and orientated counterclockwise. This convention ensures a consistent description of particle trajectories within the detector and allows for comparison across subsystems.

A transformation from Cartesian coordinates (x, y, z) to spherical coordinates (r, θ, ϕ) is provided by:

$$x = r \sin\theta \cos\phi, \quad y = r \sin\theta \sin\phi, \quad z = r \cos\theta. \tag{4.1}$$

4.5 Experimental Setup Overview

During Run 3 of the LHC (beginning of 2022), the **ALICE** detector has been operating as a high-rate, continuously read out experiment, optimized for the study of ultra-relativistic heavy-ion collisions and high-multiplicity pp and p-Pb events. The detector offers excellent charged particle tracking and PID over a broad transverse momentum range, with full azimuthal coverage and pseudorapidity acceptance of $|\eta| < 0.9$ in the central barrel [111, 112, 114].

Each subsystem is briefly described below, emphasizing the configuration relevant to Run 3 operations.

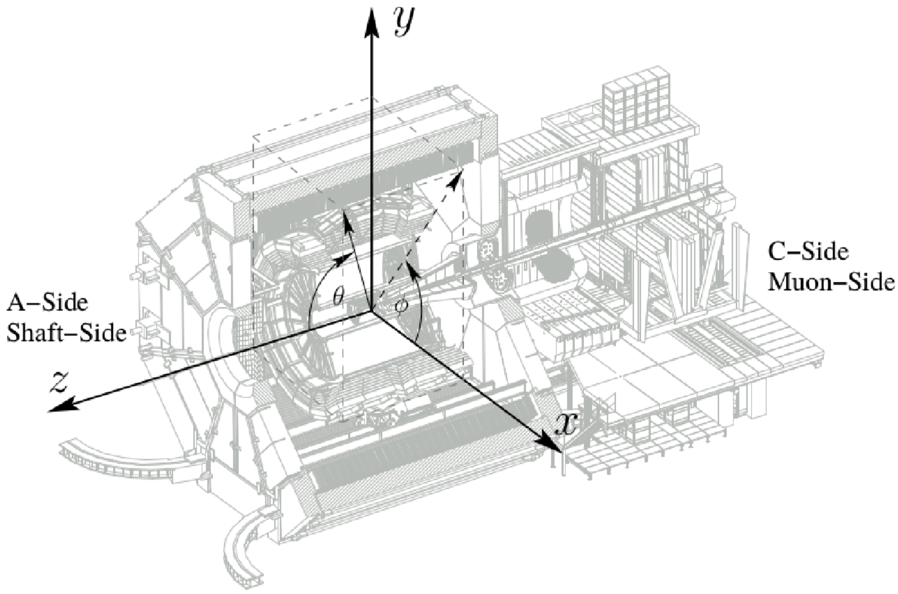

FIGURE 4.3: The coordinate system convention of the ALICE detector [112].

4.5.1 Inner Tracking System (ITS2)

The **ITS2** is the innermost detector enclosing the beam pipe. It was completely replaced during LS2 in order to improve vertexing precision and low p_T tracking capabilities [121].

The ITS2 comprises of seven concentric layers of Monolithic Active Pixel Sensors (MAPS) based on the ALPIDE technology, covering the radial range from 22 mm to 430 mm. Each sensor offers a spatial resolution of approximately 5 μm and a material budget as low as 0.35% X_0 per layer, resulting in minimal multiple scattering. This configuration achieves a factor of $\sim$3 improvement in transverse impact-parameter resolution compared to Run 2. The ITS2 is crucial for primary-vertex reconstruction, secondary-vertex identification, and improving the momentum resolution of low-p_T tracks.

4.5.2 Time Projection Chamber (TPC)

The **Time Projection Chamber (TPC)** serves as the main tracking and PID detector in the central barrel [122]. It is a cylindrical drift chamber 5 m long and 5.6 m in diameter, filled with a Ne-CO_2-N_2 gas mixture. Charged particles traversing the gas leave ionization trails, which drift under a uniform electric field ($E = 400$ V/cm) toward the readout planes at both endcaps. The TPC provides up to 159 space points per track, enabling precise three-dimensional reconstruction and dE/dx-based particle identification.

A major LS2 upgrade replaced the multi-wire proportional chambers with quadruple Gas Electron Multiplier (GEM) stacks, allowing *continuous readout* at interaction rates up to 50 kHz in Pb–Pb collisions without ion backflow [123].

The upgraded TPC offers a dE/dx resolution of 5-6%, ensuring efficient $\pi/K/p$ separation up to $p_T \approx 1$ GeV/c, and statistical separation at higher momenta via the relativistic rise region.

4.5.3 Transition Radiation Detector (TRD)

The **TRD** surrounds the TPC and helps electron identification above $p_T \sim 1$ GeV/c. It detects transition radiation photons emitted when ultra-relativistic particles pass through layers of radiator material, and measures their ionization energy loss in drift chambers. The TRD also contributes to track reconstruction and fast online triggering [124].

4.5.4 Time-Of-Flight (TOF) Detector

The **Time-Of-Flight (TOF)** detector is crucial for particle identification in the intermediate p_T range (0.3-5 GeV/c) [125]. It is positioned at a radius of about 3.7 m and covers $|\eta| < 0.9$ with full azimuthal acceptance. The TOF is composed of Multigap Resistive Plate Chambers (MRPCs) with an intrinsic time resolution of ~ 50 ps in Run 3. Combining TOF timing (t_{TOF}) with the track length and momentum (p) measured in the TPC enables computation of the particle velocity β and mass:

$$m^2 = \frac{p^2}{c^2}\left(\frac{1}{\beta^2} - 1\right).$$

The joint use of TPC dE/dx and TOF timing provides clean separation between pions, kaons, and protons across a wide p_T range. Together, these two detectors form the backbone of ALICE's hadron identification capabilities.

4.5.5 Electromagnetic Calorimeters (EMCal and PHOS)

The **EMCal** and **PHOS** calorimeters measure the energy of photons and neutral mesons, contributing to jet and high-p_T studies.

The EMCal covers $|\eta| < 0.7$ across a large azimuthal region ($\Delta\varphi \approx 107°$) and has a reasonable energy resolution ($\sigma_E/E \approx 4.8\%/\sqrt{E} \oplus 1.7\%$) [126].

The **PHOS**, built from $PbWO_4$ crystals, provides higher energy resolution ($\sigma_E/E \approx 1.8\%/\sqrt{E} \oplus 1.1\%$) in a smaller acceptance, optimized for photon spectroscopy and direct-photon measurements [127].

4.5.6 Muon Spectrometer

At forward rapidities ($-4 < \eta < -2.5$), the **Muon Spectrometer** detects muons from quarkonium and open heavy flavour decays. It incorporates a hadron absorber, a dipole magnet with 3 T · m bending power, five tracking stations, and two trigger stations. This subsystem permits studies into quarkonium suppression, recombination, and heavy-quark energy loss in the QGP [128, 114] .

4.5.7 Fast Interaction Trigger (FIT) System

The **FIT** replaces the previous T0, V0, and AD detectors and acts as the main interaction trigger, centrality estimator, and luminosity monitor [114]. It comprises of two detector arrays (FT0 and FV0) based on Cherenkov and scintillator technology, located on either side of the interaction point. The FIT offers timing with a precision better than 50 ps and is utilized to estimate the collision time (t_0), reject beam–gas background, and perform online event selection.

4.5.8 Zero-Degree Calorimeters (ZDCs)

The **ZDCs**, placed ±112.5 m from the interaction point along the LHC beam line, estimate the energy of spectator nucleons emitted in the vicinity of the beam direction. They are used for estimating the event plane and determining the centrality in Pb–Pb collisions [129, 114] .

4.6 Computing and Analysis Framework

ALICE's Run 3 data-taking capabilities, notably in PbPb collisions at interaction rates up to 50 kHz, require a new strategy to data processing, storage, and analysis.

Raw data rates exceed many terabytes per second, making traditional computing systems that rely entirely on central facilities unworkable.

ALICE uses a hybrid model that blends the innovative Online-Offline (O^2) architecture with the resources of the Worldwide LHC Computing Grid (WLCG) [130, 112].

Distributed Computing and WLCG

The WLCG provides a global, distributed computing infrastructure that integrates storage and processing capabilities from hundreds of computing centers across the world.

ALICE relies on the grid to perform operations like as large-scale Monte Carlo event production, detector-response simulations, and data reprocessing.

The WLCG's distributed nature promotes resilience, scalability, and effective load balancing across several geographical sites [130]. Grid jobs often include:

- Reconstruction and compression of raw detector data.
- Large-scale Monte Carlo production and detector simulations using GEANT [131].
- Storage and dissemination of Analysis Object Data (AOD) files to users globally.

The Online-Offline (O^2) ALICE system

Alongwith the upgraded to the detectors, the ALICE computing infrastructure was completely redesigned during LS2 to handle continuous readout and efficient processing of the large data volumes expected in LHC Run 3 and beyond [115, 117]. The new **Online-Offline (O^2) system** integrates real-time data acquisition, calibration, and reconstruction in a single computing environment, bridging the conventional boundary between online and offline processing.

The O^2 model primarily focuses on the *early data reduction and compression* during the data taking. Instead of retaining the entire raw detector output, the O^2 system performs *synchronous reconstruction* in real time, applying the first-pass calibration and compressing the raw data to minimize the volume by almost an order of magnitude. Subsequently, the *asynchronous reconstruction* is executed using the final calibration constants, producing physics-quality data (Analysis Object Data, AOD) which is analysis-ready. This two-stage model ensures that only the scientifically useful and calibrated data are retained, considerably optimizing the use of storage and computing resources.

The O^2 software framework constitutes of three main components:

- **Transport Layer:** facilitates inter-process communication between the nodes and the computing devices, thereby managing message exchange efficiently within the distributed system.
- **Data Model:** specifies the structure and serialization of exchanged messages. It supports several data formats, such as, APACHE ARROW for fast in-memory data interchange and ROOT-serializable objects for long-term storage [132, 133].
- **Data Processing Layer (DPL):** serves as a high-level orchestration engine, that abstracts the underlying complexity. It automatically creates the workflow topology, handles multiplexing and pipelining, and is used for almost all data-processing tasks in ALICE, including simulation, reconstruction, and analysis.

In the O^2 continuous readout mode, the smallest processing unit is a *time frame*, which represents a 2.85 ms snapshot of data. Each time frame may be processed individually at all stages, starting from data taking, synchronous and asynchronous reconstruction, to user analysis, allowing for high parallelism and scalability. The reconstructed outputs are saved as AOD files in ROOT format, which provides an optimal balance between data compression and accessibility.

The analytical data model of Run 3 is based on a collection of flat tables that are arranged in a relational database-like structure, with all entities connected through indexed keys. This approach allows rapid query operations and efficient table joining, making the O^2 framework quite modular and flexible for end-user analytics. Each analysis task, implemented in `C++`, is defined as a DPL data processor with explicit input and output parameters. Tasks can be integrated into *workflows*, which process data sequentially, guaranteeing proper pipelining and dependency management.

Through this integrated architecture, the O^2 system allows ALICE to function as a fully online experiment, capable of continuous high-rate data processing while retaining offline-quality reconstruction. This paradigm shift is a key computing evolution in high-energy physics, enabling ALICE to exploit its full physics potential in Runs 3 and 4 [115, 117].

Analysis Frameworks: AliPhysics and Beyond

While the backbone of reconstruction has transferred to O^2, user-level physics analyses remain strongly reliant on the well-established **AliPhysics** framework.

AliPhysics, built on ROOT [134], provides a robust set of analytic tools, including data filtering, event and track selection, particle identification, and observable extraction.

In Run 3, AliPhysics has been complemented with the **O^2 Analysis Framework**, a new, task-oriented framework built to harness parallelism and large-scale processes.

The two frameworks are compatible, with O^2 delivering excellent performance and AliPhysics enabling continuity and flexibility for user-level investigations.

Monte Carlo and Detector Simulations

Monte Carlo simulations are critical for correcting detector effects, calculating efficiency, and assessing systematic uncertainty.

PYTHIA and HIJING event generators model particle creation, whereas GEANT 3 and GEANT 4 simulate particle passage through detector material, including secondary interactions and energy loss [131, 135, 136].

The simulated events are recreated using the same chain as the real data, providing a consistent foundation for data-MC comparisons.

4.7 Detector summary and Relevance to This Thesis

The ALICE detector was designed to be the most flexible heavy-ion experiment at the LHC, allowing researchers to investigate the features of strongly interacting matter at high energy densities. Its full suite of subsystems, which includes the central barrel, forward detectors, and muon spectrometer, delivers unprecedented granularity and precision among modern collider experiments.

The central barrel detectors (ITS, TPC, TRD, TOF, EMCal, DCal, PHOS, and HMPID) provide superior tracking and particle identification capabilities across a wide momentum range. They can reconstruct and identify hadrons, electrons, and photons with amazing precision, even in the high-multiplicity environment of central PbPb collisions. The forward detectors (V0, ZDC, and others) are critical for global event characterisation, including collision centrality, event-plane identification, and background rejection. Finally, the muon spectrometer, together with the Muon Forward Tracker in Run 3, broadens ALICE's reach to quarkonium and heavy-flavor phenomena at high speeds.

By merging the results of these subsystems, ALICE offers an unparalleled chance to conduct a comprehensive, high-precision investigation of detected hadron spectra. This is critical for addressing the key aims of this thesis: exploring freeze-out dynamics, collective behavior, and hadronization processes in PbPb collisions at $\sqrt{s_{\mathrm{NN}}} = 5.36$ TeV.

To summarize, ALICE's detector architecture not only allows for high-precision reconstruction of global and differential observables, but also distinguishes the experiment as the preeminent resource for researching the QGP using identifiable hadron spectra. The next chapter will discuss the datasets, analytical methodologies, and reconstruction procedures used to achieve these physics objectives.

4.8 Data Reconstruction

The accuracy of data reconstruction is crucial for accurately studying hadron spectra in PbPb collisions. With the start of LHC Run 3, ALICE started a new phase of continuous readout and online reconstruction, enabled by the O^2 computing framework [137]. The LHC is expected to have high interaction rates of up to 50 kHz for PbPb and 500 kHz for pp collisions, necessitating this paradigm change.

The move necessitated the development of new concepts like the *Time Frame* (TF) and major improvements in tracking, calibration, and PID processes. The purpose of this section is to summarize the major reconstruction methodologies pertinent to this thesis. We focus on three major aspects:

- event creation and online reduction of the data stream,
- track reconstruction in continuous readout mode, and
- PID techniques based on TPC and TOF information, which serve as the foundation for the π, K, and p analysis.

4.8.1 Event Building

In Run 3, ALICE functions without a hardware trigger. Detector signals are continually captured and arranged into **Time Frames** (TFs), which are the smallest units of information for online and offline processing. A TF is a customizable time frame of order 10 microseconds, substantially bigger than the maximum TPC electron drift duration ($\sim$ 100 microseconds). This option avoids splitting tracks from a single collision across many TFs, lowering inefficiencies to less than 1% [138].

Data from detectors is gathered via **First Level Processors** (FLPs), a farm of $\sim$200 compute nodes that execute local processing, including cluster detection and tracklet reconstruction. The partially processed TFs are delivered to Event Processing Nodes (EPNs) for global reconstruction tasks such as track creation, vertex determination, and collision association. During this step, overlapping interactions within the same TF are separated, and complete events are assembled.

The first raw data stream is around 4 TB/s. After processing at the FLPs, the rate is lowered to $\sim$150 GB/s for pp and $\sim$700 GB/s for PbPb. After event reconstruction on EPNs, the ultimate data flow to permanent storage is $\sim$30 GB/s for pp and $\sim$140 GB/s for PbPb ([137]). Given the amount, not all raw data can be permanently preserved. Instead, the goal is to recreate the whole dataset online and store compact analysis-ready objects, known as **AO2D files**, which are used as input for physics studies.

The use of continuous reading and live reconstruction has significant ramifications for our study. This method measures π, K, and p spectra with excellent statistical accuracy and precise track-to-vertex association, even in center PbPb collisions.

4.8.2 Tracking

This thesis relies on accurate track reconstruction to create identifiable hadron spectra (π, K, p) from clean track samples with well-defined kinematics and origins.

Track reconstruction in ALICE begins with the conversion of detector signals into

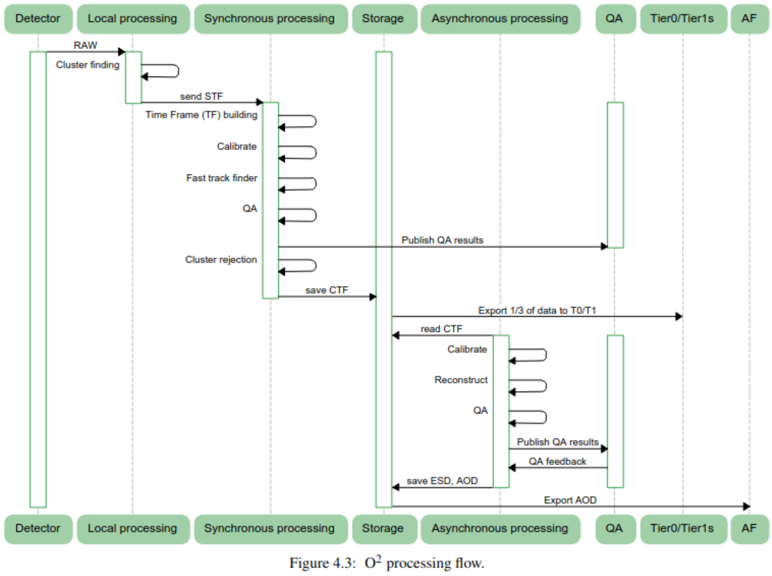

FIGURE 4.4: Schematic overview of the ALICE O^2 reconstruction chain in Run 3, illustrating the continuous readout, event building, and online reduction strategy [139].

clusters. In the TPC, charged particles ionize the drift gas, and the resulting electrons drift to the readout chambers, where they are recorded as charge clusters. In the ITS, silicon sensors register localized hits. These raw signals are processed into clusters that represent the particle trajectory at each detector layer [112].

The first step of the reconstruction chain is the formation of **tracklets**, short track segments built locally within individual detectors. By combining tracklets from the ITS with clusters in the TPC, tracks are propagated through the detector volume and optimized using a Kalman filter approach [140].

Several categories of reconstructed tracks are defined in ALICE:

- **ITS-only tracks:** Constructed exclusively from ITS clusters, these tracks are crucial for reconstructing very low-p_{T} particles ($p_{\mathrm{T}} \lesssim 200$ MeV/c) that do not reach the TPC. They are also used in secondary vertex finding (photon conversions, weak decays).

- **TPC-only tracks:** Built solely from TPC clusters, these tracks lack precise vertex information. They are mainly used for quality assurance, cosmic-ray studies, and specific reconstruction tasks.

- **Global tracks:** The primary tracks used in physics analyses, obtained by combining ITS and TPC information. Global tracks provide excellent precision in both momentum measurement and vertexing. They also form the basis for particle identification (PID) when matched with TOF and TRD signals.

- **Afterburned tracks:** Constructed by matching unused ITS clusters to TPC tracks. This category is particularly important for displaced tracks originating from long-lived particles such as $K^0_S \to \pi^+\pi^-$, $\Lambda \to p\pi^-$, or cascade decays ($\Xi \to \Lambda\pi$).

In Run 3, the **continuous readout mode** introduces additional complexity. Each reconstructed track may overlap in time with multiple collisions within the same *Time*

Frame (TF). To address this, a dedicated **track-to-collision re-association algorithm** is deployed. This algorithm compares the time stamp of each track with the reconstructed collision times in the TF and reassigns the track to the most compatible primary vertex, within strict timing tolerances [139, 141]. This ensures the correct association of tracks with collisions, thereby minimizing background contamination and avoiding signal duplication.

The final reconstructed tracks are stored in the **AO2D data format**, which represents the standard input to all physics analyses. Each track record contains not only the kinematic variables (momentum, rapidity, azimuthal angle), but also PID observables (TPC dE/dx, TOF timing, TRD likelihoods) and the covariance matrices. These tracks thus provide the essential building blocks for all Run 3 analyses, including the identified hadron spectra (π, K, p) that form the core of this thesis.

TPC Energy Loss Measurement

The TPC provides PID through measurements of the specific energy loss (dE/dx) of charged particles traversing the detector gas volume. As particles ionize the medium, the released electrons are drifted and collected on the readout pads. The mean energy loss per unit length is well described by the Bethe-Bloch formula:

$$\left\langle -\frac{dE}{dx} \right\rangle = Kz^2 \frac{Z}{A} \frac{1}{\beta^2} \left[\frac{1}{2} \ln \left(\frac{2m_e c^2 \beta^2 \gamma^2 W_{\max}}{I^2} \right) - \beta^2 - \frac{\delta(\beta\gamma)}{2} \right], \tag{4.2}$$

where β and γ are the relativistic kinematic variables, z is the charge of the incident particle, Z and A are the atomic number and mass number of the medium, I is the mean excitation potential, and $W_{\max}$ the maximum energy transfer in a single collision.

Because of the Landau tail of energy loss distributions, ALICE employs a truncated-mean method: the highest ionization clusters are excluded, and the mean of the remaining clusters is used to estimate dE/dx. This enhances the Gaussianity of the response and provides a resolution of around 5% for long tracks at midrapidity [112].

TOF Velocity Measurement

The TOF detector tracks the flight time of charged particles from the contact location to the TOF module. The velocity β is calculated using the track length (L) and momentum (p):

$$\beta = \frac{L}{c\, t_{\mathrm{TOF}}}, \qquad m = \frac{p}{\gamma\beta c}. \tag{4.3}$$

The TOF system can differentiate pions, kaons, and protons up to $p_{\mathrm{T}} \sim 5$ GeV/c, with a resolution of around 50-60 ps in Run 2 and $\sim$30 ps in Run 3 [142].

Combined PID Strategy

The Combined PID Strategy

At low momenta, the TPC dE/dx bands are well separated, allowing for precise particle identification.

TOF separates intermediate momenta when the dE/dx curves for π, K, and p overlap. At higher momenta ($p_T \gtrsim 5$ GeV/c), when both TPC and TOF lose discrimination power, ALICE utilizes additional detectors: the HMPID (Cherenkov radiation), EMCal (shower shape for electrons and photons), and TRD (electron identification).

For analysis, the observed signals are compared to theoretical predictions. The normalized variable $n\sigma$ is defined as:

$$n\sigma_i = \frac{\text{Signal}_{\text{measured}} - \text{Signal}_{i,\text{expected}}}{\sigma_i}, \tag{4.4}$$

where i represents the particle species.

This variable is roughly Gaussian distributed and can be used to select species using $|n\sigma|$ cuts or probability density functions (Bayesian PID).

Illustration

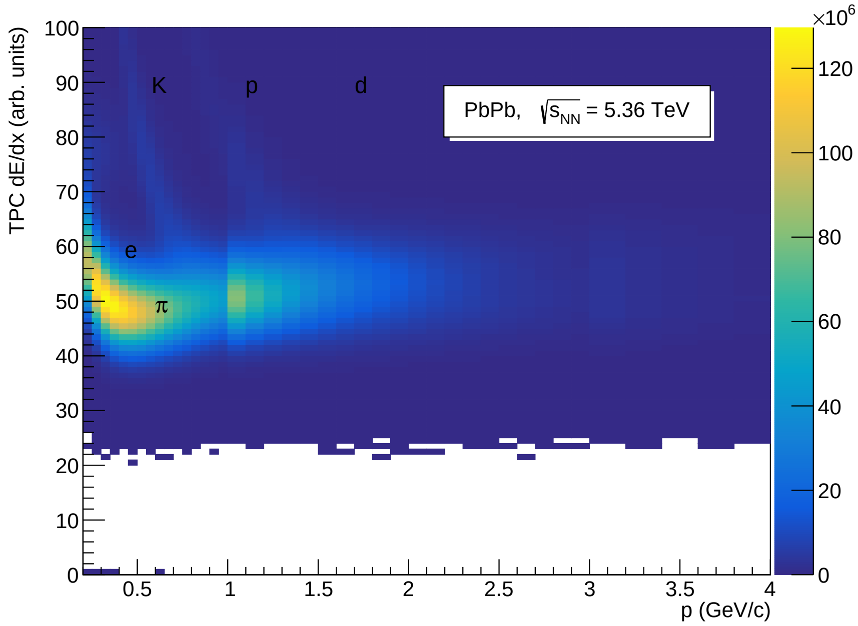

FIGURE 4.5: TPC dE/dx as a function of momentum for charged tracks in Run 3 PbPb collisions. Distinct particle species are visible and compared to the Bethe-Bloch expectation [112].

Relevance to This Thesis

The accurate separation of π, K, and p across the full p_T range is the essential experimental foundation of this work. The methods described above underpin the extraction of the identified hadron spectra that form the central physics analysis of this thesis. By combining dE/dx from the TPC with TOF information and applying optimized selection criteria, high-purity samples of π, K, and p are reconstructed, enabling the precise measurement of spectra in PbPb collisions at $\sqrt{s_{NN}} = 5.36$ TeV.

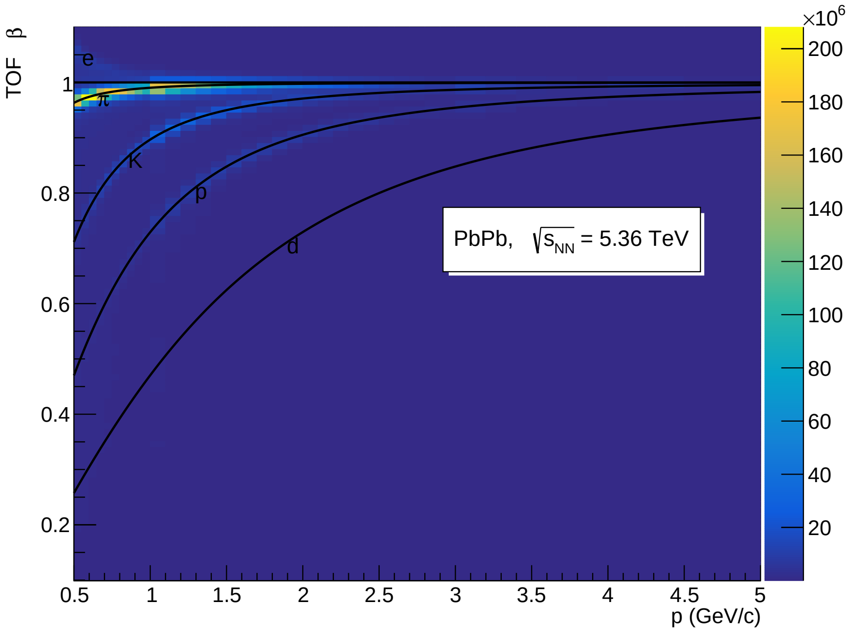

FIGURE 4.6: TOF velocity measurement β as a function of momentum, showing clear separation between π, K, and p up to several GeV/c [142].

Relevance to This Thesis

The study in this thesis heavily depends on the Run-3 computing paradigm.

The hadron spectra for π, K, and p are retrieved from AO2D datasets generated by the O^2 framework.

The reconstruction and PID techniques mentioned above, when paired with large-scale MC productions on the grid, lay the groundwork for accurate measurements. Furthermore, the creation of specific macros and analytic procedures inside AliPhysics enabled this study to manage the complexity of PbPb collisions at $\sqrt{s_{NN}} = 5.36$ TeV while assuring repeatability and scalability.

Chapter 5

Data Samples & Analysis Strategy

5.1 Introduction

The study of recognized hadrons in ultra-relativistic heavy-ion collisions offers one of the most direct insights into the features of the highly interacting matter produced in such situations. Heavy-ion physics relies heavily on measuring π, K, and p, which account for the majority of particle creation and leave traces of the medium's history. Their yields and momentum distributions provide information on the freeze-out circumstances, collective flow, and potential fingerprints of deconfinement and chiral symmetry restoration in the QGP phase.

The ALICE experiment at the LHC can measure identified hadrons across a broad transverse momentum (p_{T}) range using complementary sub-detectors: the TPC for ionization energy loss ($\mathrm{d}E/\mathrm{d}x$) measurements and the TOF detector for velocity determination. The combination of these systems allows for high-purity particle identification from low to intermediate p_{T}, where the majority of hadron creation occurs.

Furthermore, the centrality dependence of hadronic spectra sheds light on the impact of system size and collision geometry. Central collisions, which have a substantial overlap between nuclei, result in larger energy densities and stronger collective phenomena, whereas peripheral collisions have lower medium effects. Comparing particle production across centrality classes allows us to restrict models of hadronization, hydrodynamic expansion, and partonic energy loss.

The current study uses Run 3 PbPb data at $\sqrt{s_{\mathrm{NN}}} = 5.36$ TeV, which provides exceptional statistics and enhanced detector calibrations compared to earlier LHC runs. This allows for a more exact assessment of particle yields and spectra, offering both continuity with previous data and the prospect of discovering new patterns in heavy-ion collision phenomenology. But before, we present a basic overview of how such events are provided, triggered, and recorded by ALICE, before refining down to the specific datasets and simulations utilized in this thesis.

5.1.1 Heavy-ion collisions at the LHC

From Beams to Collisons

The LHC accelerates stripped $^{208}\mathrm{Pb}^{82+}$ nuclei to 2.68 TeV per nucleon, resulting in $\sqrt{s_{\mathrm{NN}}} = 5.36$ TeV. When bunches intersect at the ALICE interaction site, many nucleon-nucleon interactions take place simultaneously.

Collision geometry and centrality

The geometry of a heavy-ion collision is regulated by the *impact parameter* b, which is defined as the transverse distance between the centers of the colliding nuclei at closest approach. Small values of b correlate to center, virtually head-on collisions, whereas large values correspond to periphery, grazing interactions.

Heavy-ion studies use the Glauber model to relate this geometric image to empirically observable values. In a Monte Carlo implementation, each nucleus is characterized by a Woods-Saxon density profile, from which nucleon locations are randomly selected. Nucleons are deemed to be inelastic if their transverse spacing is smaller than a threshold set by the inelastic nucleon-nucleon cross section at the given energy. This approach generates statistical distributions for:

- N_{part} represents the number of nucleons with at least one inelastic interaction.
- N_{coll} represents the number of binary collisions, considering each nucleon-nucleon interaction separately.
- the nuclear overlap function,

$$T_{AA}(b) = \frac{N_{\text{coll}}(b)}{\sigma_{\text{NN}}}, \tag{5.1}$$

  which governs the scaling of hard processes from pp to AA collisions.

Experiments are used to determine *centrality classes*, as the effect parameter b cannot be directly seen. These are given as percentiles of the total hadronic cross section, based on an experimental observable that is monotonically associated with multiplicity, such as forward-detector amplitude or charged-particle density. For example, 0-5% centrality corresponds to the 5% most central (lowest-b) collisions, whereas 70-80% centrality indicates peripheral events with minimal overlap.

A Glauber model fit determines the relationship between the experimental observable and geometric quantities b, N_{part}, and T_{AA}.

Luminosity & event rate

The instantaneous luminosity L is the most important parameter for determining a collider's performance. It measures the flow of incoming particles per unit area and time, as well as the collision rate when multiplied by the appropriate interaction cross section. Generally, it is represented as:

$$L = \frac{N_b^2 f_{\text{rev}} n_b}{4\pi\sigma_x\sigma_y}, \tag{5.2}$$

where N_b is the number of ions per bunch, n_b is the number of colliding bunch pairs, f_{rev} is the revolution frequency of the LHC beams, and σ_x, σ_y are the transverse beam sizes at the interaction point.

In heavy-ion operation, the bunch population N_b is less than in proton running (10^8 ions per bunch vs. 10^{11} protons). However, the inelastic PbPb cross section is exceptionally large: $\sigma_{\text{PbPb}} \approx 7.8$ b, compared to ~ 75 mb for pp collisions at the same energy. As a result, even low luminosities in PbPb produce significant interaction rates.

The event rate is

$$R = L\,\sigma_{\mathrm{PbPb}}\,. \tag{5.3}$$

Under normal Run 3 circumstances, this translates to tens of kHz of hadronic interactions in ALICE.

High rates improve statistical precision, but complicate operation in the continuous reading mode used in Run 3. This technique streams detector data into large time frames (tens of μs), allowing several collisions to occur inside the same frame. When this happens, reconstruction must untangle overlapping interactions, which is known as pileup.

Pileup has two effects on measurements: (i) many principal vertices complicate track association, and (ii) overlapping detector signals broaden timing distributions, reducing PID performance (particularly in TOF). Thus, while increasing luminosity enhances accessible data, it also increases the likelihood of pileup, which can skew observables.

In addition to the instantaneous luminosity, investigations mention the "integrated luminosity" of a dataset.

$$\mathcal{L}_{\mathrm{int}} = \int L(t)\,dt, \tag{5.4}$$

which represents the total accumulated beam exposure over the course of a run.

The usual measure of dataset size in pp physics is integrated luminosity, which is calculated by dividing event yields by $\mathcal{L}_{\mathrm{int}}$. In heavy-ion collisions, however, the situation is different. The inelastic PbPb cross section is exceptionally big ($\sigma_{\mathrm{PbPb}} \sim$ 7.8 b). Most observables of importance are provided *per event* within centrality classes rather than in absolute cross-section units.

Integrated luminosity still plays a significant role:

- It quantifies the overall size of a dataset and allows comparisons across running periods (e.g., Run 2 vs. Run 3).
- It constrains analyses of rare probes (jets, heavy flavor, quarkonia) whose production cross sections are small compared to the total inelastic rate.
- It validates the consistency between the delivered luminosity and the recorded number of triggered events, once trigger efficiencies are accounted for.

During PbPb operation at the LHC, typical integrated luminosities per period are of order a few $\mu\mathrm{b}^{-1}$, equating to billions of minimum-bias interactions recorded.

The O^2 framework

The way ALICE stores and handles its data underwent a significant technological change with Run 3. A unified O^2 framework (Online–Offline computing system) has taken the place of the conventional division between "online" (trigger and DAQ) and "offline" (reconstruction on stored raw data).

The O2 framework incorporates a number of innovative components:

- **Real-time data compression:** If uncompressed, the TPC's continuous raw data stream would be more than terabytes per second. Using cluster finding, zero suppression, and optimized entropy coding, O^2 reduces the volume in real-time by more than an order of magnitude.
- **GPU-accelerated tracking:** It is very possible to parallelize the reconstruction of charged-particle trajectories in the TPC. By taking advantage of contemporary GPU farms, O^2 is able to conduct online tracking at the full interaction rate (up to 50 kHz for Pb–Pb) and provide reconstructed tracks almost instantly.
- **Online calibration:** Numerous detector parameters change over time, including alignment, time-of-flight offsets, and TPC drift velocity. O^2 constantly gets new calibration constants while data is being collected and uses them almost instantly, which cuts down on the time between data collection and physics-quality reconstruction.
- **Unified software stack:** O^2 eliminates the divergence that previously existed between fast online monitoring and slower offline reconstruction by combining the online and offline stages and ensuring that the same algorithms and calibrations are applied consistently.

The pipeline's output is the AO2D format, which is already generated at the data collection location and is small but ready for analysis.

ALICE's ability to handle Run3's massive collision rates while maintaining the accuracy required for soft-physics observables like identified hadron spectra is due to this rethinking of data flow.

Triggering in ALICE

At the LHC, particle bunches cross every 25 ns, resulting in a collision frequency of 40 MHz. For PbPb running, not every crossing leads in an interaction, but the sheer amount of raw crossings exceeds the ALICE data acquisition (DAQ) system's capacity. Without a trigger mechanism, it would be difficult to separate key physics events from the flow of data.

The Function of Triggers A trigger is a real-time selection layer that determines which events are read and recorded for later analysis. Trigger design in heavy-ion running is dictated by two requirements: (i) maximising efficiency for real hadronic collisions and (ii) suppressing backgrounds such as empty crossings, beam-gas interactions, and ultra-peripheral electromagnetic events.

Minimum-bias triggers Unlike pp physics, where dedicated triggers frequently choose uncommon high-p_T events, heavy-ion studies depend on a large minimum-bias sample. This seeks to incorporate almost all inelastic hadronic PbPb collisions, providing an impartial reference across centralities.

ALICE's principal minimum-bias trigger is the `sel8` condition, which needs activity in one of the two forward T0 detectors:

- T0A, covering forward pseudorapidity in the $+z$ direction,
- T0C, covering backward pseudorapidity in the $-z$ direction.

A signal in either array is adequate to detect a collision. Because virtually all hadronic PbPb events create forward-going charged particles, this condition is highly efficient.

Background rejection and efficiency The `sel8` trigger is supported by additional online and offline tests, such as correlations between forward and backward detectors and consistency with the reconstructed vertex. While these improvements are implemented after readout, the `sel8` condition offers an important first-level assurance that the recorded event corresponds to a true PbPb interaction.

Why `sel8` matters? By design, `sel8` delivers:

- high efficiency (>95%) for hadronic PbPb interactions,
- uniform acceptance across centrality classes,
- minimal bias for soft-physics observables.

For these reasons, `sel8` is the typical baseline trigger for recognized particle observations in ALICE.

Continuous readout and time frames

During Runs 1 and 2, ALICE used a typical triggered readout, which meant that detector signals were only recorded when a hardware trigger (such as minimum-bias, central, or rare-event triggers) activated. This strategy limited the collection rate to a few kilohertz due to the readout speed of ALICE's main tracking detector, the TPC.

However, the physics aims of Run 3 need capturing nearly all PbPb interactions supplied by the LHC at rates up to 50 kHz in order to obtain adequate data for uncommon probes such as heavy flavor, jets, and quarkonia. To address this difficulty, ALICE used a completely new paradigm: continuous readout.

Principle of continuous readout In continuous mode, the TPC and other subdetectors no longer rely on a hardware trigger to determine whether to read out. Instead, they continually send their signals into a global data buffer. The data is divided into huge chunks called time frames, each lasting tens of microseconds. Because numerous LHC bunch crossings occur over this time interval, each time frame contains signals from many collisions.

Event reconstruction is done offline by identifying main vertices inside each time frame and assigning tracks to them. This "software-triggered" solution eliminates typical hardware trigger constraints and guarantees that no contact is lost during the input step.

Advantages: Continuous reading has many significant benefits:

- **High efficiency:** almost all interactions within the LHC fill are recorded, increasing physics reach.
- **No dead time**: Unlike triggered readout, the system does not lose events while the detector clears between triggers.
- **Flexibility**: event categorization and selection are moved to the software level, allowing more advanced algorithms to be used with complete detector information.

Challenges The advantages come with new challenges that must be addressed in reconstruction and analysis:

- **Pileup within time frames:** when many collisions occur in the same frame, reconstruction must separate overlapping events. This necessitates exact vertexing and careful matching of tracks to the right vertex.
- **Edge distortions:** tracks that begin or terminate near the start or end of a time frame may require partial reconstruction because the frame boundary truncates their signals. If not handled properly, such tracks might skew momentum spectra or PID distributions.
- The continuous stream generates high raw data rates, requiring real-time compression and calibration within the O^2 computing system.
- **Calibration complexity:** Continuous operation necessitates accurate synchronization of detectors and time stamps, allowing signals from disparate subsystems to be matched to the same collision.

Summary Continuous reading is a significant technological improvement in Run 3, allowing ALICE to fully leverage the high interaction rates of PbPb running. It substitutes hardware-based event selection with flexible software-based reconstruction, but it necessitates effective control of pileup and time-frame edge effects. These concerns have a direct influence on the quality and purity of samples used in physics studies.

Event reconstruction and passes

ALICE data are initially stored as raw detector signals, which must be converted into useable physics objects like as tracks, vertices, and PID observables. The O^2 computing architecture performs this transition through its reconstruction chain.

This chain generates the `AO2D` format, which is a compact but analysis-ready dataset that includes:

- reconstructed primary and secondary vertices,
- charged-particle tracks with kinematic parameters,
- PID signals from the TPC, TOF, ITS, and other subsystems,
- event-level quantities such as centrality estimators and trigger decisions.

The `AO2D` input format, which balances compactness and thoroughness, is the standard for Run3 analysis.

Reconstruction passes The same raw data are often reprocessed multiple times in order to incorporate improved calibrations and refined algorithms. These iterations are known as *reconstruction passes*.

- Early passes (e.g. pass1, pass2) are produced quickly after data taking to enable quality assurance and rapid-turnaround analyses, but they rely on preliminary calibration constants.
- Intermediate passes (e.g. pass3, pass4) include improved detector alignment and calibration updates based on more statistics.

- Final passes (e.g. pass5 for Run 3) are generated once calibrations and reconstruction algorithms are mature, and provide reference-quality samples for precision analyses.

Each pass produces a new AO2D, superseding earlier versions.

Calibration and alignment improvements The main motivation for repeated passes is the availability of improved detector calibrations, including:

- TPC drift velocity and space-charge corrections, crucial for accurate momentum determination at high occupancy,
- ITS and TPC alignment constants, refined with additional statistics,
- TOF channel-by-channel time offsets, improving timing resolution and thus PID performance,
- FT0 and ZDC timing calibrations, sharpening event-time determination and enhancing pileup rejection.

These refinements ensure that reconstructed quantities are as accurate and precise as possible.

Data formats In addition to AO2D, ALICE also produces *Derived AO2Ds* (DAODs), which contain only the reduced set of information required for a specific analysis, further reducing data size. While raw data and intermediate calibration streams are preserved, they are rarely accessed directly for physics analyses.

Summary Reconstruction passes guarantee that the best available detector knowledge is propagated into the final analysis samples. The AO2D serves as the bridge between ALICE's complex detector systems and physics analyses, and later passes such as pass5 are essential for minimizing systematic uncertainties in published results.

Implications

Luminosity, centrality estimate, triggers, continuous readout, reconstruction passes, and anchoring MC all contribute to the data-taking envelope for this thesis. These selections determine pileup rejection, define the measurement's phase space, and serve as the foundation for all efficiency and secondary-particle adjustments.

5.2 Data Samples

The current study uses PbPb collision data from the LHC Run 3 campaign with a nucleon-nucleon center-of-mass energy of $\sqrt{s_{\mathrm{NN}}} = 5.36$ TeV. The dataset is from the `LHC23zzh` period and was reconstructed in the `AO2D.root` format with the `pass4` reconstruction chain. It includes the most recent calibration constants and alignment information. This guarantees high-fidelity tracking, vertexing, and particle identification, which serves as a firm platform for precise measurements.

Compared to Run 2, Run 3 data benefit from higher luminosity and major detector enhancements. The ALICE TPC has received a readout update, allowing for continuous data collecting. Improved calibration processes increase the reliability of energy loss (dE/dx) measurements. Similarly, the TOF detector has been enhanced for greater occupancy situations, expanding its particle identification capabilities into the difficult domain of central PbPb collisions.

Two aspects drive the dataset selection process. First, Run 3's statistical reach enables differential examinations of recognized particle spectra over a large centrality range, including peripheral collisions with low multiplicities. Second, the increased systematic control provided by revised reconstruction techniques minimizes uncertainty in efficiency adjustments, allowing for more robust comparisons to theoretical models and prior ALICE papers.

A general-purpose MC production has been used to assess secondary particle contamination, acceptance corrections, and efficiencies. To guarantee uniform detector conditions and reconstruction techniques, this MC is anchored to the same reconstruction pass (apass5) of the 2023 PbPb data. The MC simulations are based on realistic physics event generators that have been adjusted to replicate particle production in Pb–Pb collisions at the LHC. GEANT4 is then used to simulate the entire detector.

This study compares published results from ALICE Run 2 at $\sqrt{s_{NN}} = 5.02$ TeV [143] for consistency and benchmarking purposes. Such cross-run consistency tests are critical for distinguishing physics-driven trends from detector- or analysis-related aberrations, assuring the trustworthiness of any reported changes in particle production.

5.3 Event Selection

A strong event selection method is required to ensure that only true heavy-ion interactions contribute to the analysis. The main vertex location was limited within ± 10 cm along the beam axis relative to the nominal contact point, minimizing acceptance distortions and ensuring uniform detector coverage.

Several quality filters were used to reduce background and badly reconstructed events. The `sel8` trigger required activity in either T0A or T0C, guaranteeing little bias in the selection of hadronic interactions. The `removeNoSameBunchPileup` algorithm rejected pileup events, particularly those resulting from numerous bunch crossings. Furthermore, time-frame boundary events were omitted to eliminate edge effects that might distort track reconstruction. A consistency criterion between the reconstructed main vertex and the FT0 time significantly decreased contamination from spurious vertices.

Centrality, which reflects the collision geometry, was calculated using the FT0C amplitude distribution. The complete range of 0-100% was initially studied, but due to the non-uniformity of extremely peripheral encounters, the study was restricted to 0-70%. This decision combines statistical reach and dependability, keeping systematic uncertainties from centrality determination under control.

5.4 Track Selection

Once high-quality events had been identified, further limitations were placed on individual tracks to ensure robust reconstruction and prevent contamination from background sources. The study was limited to charged particles within the central pseudorapidity area ($|\eta| \leq 0.8$) and rapidity ($|y| \leq 0.5$), which covered the region of uniform detector acceptance. Transverse momentum was limited to the range $0.1 \leq p_{\mathrm{T}} \leq 10$ GeV/c, where tracking and identification efficiencies are effectively controlled.

To provide accurate tracking in the TPC, at least 70 crossed pad rows were required, with a ratio of crossed rows to findable clusters greater than 0.8. This ensured that tracks were adequately sampled, reducing the influence of reconstruction artifacts. The quality of trajectory fits was regulated by requiring χ^2/cluster < 4 in TPC and < 36 in ITS.

To eliminate secondary tracks caused by weak decays, material interactions, or mis-reconstruction, strict distance-of-closest-approach (DCA) criteria were used: $|\mathrm{DCA}_z| \leq$ 2.0 cm along the beam axis and $|\mathrm{DCA}_{xy}| \leq 0.05$ cm in the transverse plane. To establish consistency amongst detector subsystems, ITS and TPC refits were implemented, along with the golden χ^2 criteria.

These parameters improve the quality of the chosen track sample, guaranteeing that the following yield extraction matches the genuine primary particle generation in PbPb collisions.

5.5 Particle Identification (PID)

The detection of charged hadrons is based on the complementing capabilities of the tracking and timing detectors. At low transverse momentum ($p_{\mathrm{T}} \leq 1.2$ GeV/c), particles are identified largely by their particular energy loss ($\mathrm{d}E/\mathrm{d}x$) measured in the TPC. At higher momenta, when the Bethe-Bloch curves for various particle species converge, the TOF system provides extra separation power by measuring the velocity of each track with picosecond precision.

The approach uses the n_σ variable, which measures the divergence of a measured signal from the predicted response for a certain particle species. Regarding the TPC:

$$n_{\sigma,i}^{\mathrm{TPC}} = \frac{\mathrm{d}E/\mathrm{d}x - \langle \mathrm{d}E/\mathrm{d}x \rangle_i}{\sigma_{\mathrm{d}E/\mathrm{d}x}}, \tag{5.5}$$

and for the TOF:

$$n_{\sigma,i}^{\mathrm{TOF}} = \frac{\Delta t - \Delta t_i}{\sigma_{\mathrm{TOF}}}, \tag{5.6}$$

where $i = \pi, K, p$. Here, the numerator represents the difference between the measured detector signal and the expected mean for species i, while the denominator normalizes by the detector resolution.

Typically, particle yields are obtained by fitting n_σ distributions in discrete p_{T} intervals. To accommodate for detector resolution issues, TPC-based analysis uses Gaussian functions with exponential tails, as well as linear/exponential background components. The TOF fits follow a similar idea, but expand the range to $p_{\mathrm{T}} \approx 4.5\,\mathrm{GeV}/c$.

Combining the two approaches provides continuous coverage of identified spectrum ranging from 0.1 to 4.5 GeV/c. The overlap zone between TPC and TOF is particularly essential, acting as a consistency check and anchor for systematic uncertainty estimations.

5.6 Yield Extraction Methods

To calculate raw particle yields, the n_σ distributions are studied in narrow p_{T} bins. Each distribution is defined as a superposition of signal and background components, with characteristics specific to the detector response.

The TPC signal is dominated by a Gaussian distribution that indicates detector resolution, with an exponential tail added to account for asymmetric oscillations in energy loss measurements. The background, which is made up of incorrect tracks and residual contributions from other particle species, is described using a combination of linear and exponential factors. The *total fit* function will then read:

$$f(x) = \begin{cases} A \cdot \exp\left[-\frac{(x-\mu)^2}{2\sigma^2}\right], & x \leq \mu + \delta, \\ A \cdot \exp\left[-\frac{\delta^2}{2\sigma^2}\right] \cdot \exp\left(-\alpha(x-\mu-\delta)\right), & x > \mu + \delta \end{cases} + B + Cx + De^{-\beta x}, \tag{5.7}$$

where A, μ, and σ control the Gaussian core, while the exponential tail is governed by parameters δ and α. The final terms represent the background.

The TOF approach is basically similar: Gaussian functions (potentially with asymmetric extensions) are fitted to the time distributions, along with an extra linear background. This approach enables yield extraction of up to $p_{\mathrm{T}} \approx 4.5\,\mathrm{GeV}/c$.

In both situations, raw particle counts are acquired by integrating the fitted signal component over the appropriate n_σ window. The spectra are then normalized based on the number of examined events and scaled by bin width. Comparisons of positive and negative charges help to understand possible detector asymmetries, while the overlap region between TPC and TOF guarantees that the two approaches work consistently.

5.7 Corrections and Systematic Uncertainties

Raw particle yields derived from TPC and TOF fits cannot be directly compared to theoretical predictions or prior observations. Several detection and analytic issues must be addressed before physical spectra may be produced. These remedies address inefficiencies in reconstruction, contamination from non-primary particles, and distortions in centrality-dependent settings.

5.7.1 Efficiency corrections

The likelihood of reconstructing and identifying a specific particle is determined by the tracking system's and PID detectors' responses. Efficiency for each species is assessed by simulating PbPb events and propagating resultant tracks via a comprehensive detector response model. The adjustment factor is applied as:

$$N^{\text{corr}} = \frac{N^{\text{raw}}}{\epsilon_{\text{trk}} \cdot \epsilon_{\text{PID}}}, \tag{5.8}$$

where ϵ_{trk} is the track reconstruction efficiency and ϵ_{PID} is the species-dependent PID efficiency. In the combined TPC-TOF case, an additional *matching efficiency* is included, reflecting the probability that a track reconstructed in the TPC is successfully associated with a TOF hit.

5.7.2 Secondary particle subtraction

Not all reconstructed tracks are derived from initial hadrons generated at the contact location. Secondary contributions include weak decays (e.g., $\Lambda \to p\pi^-$) and interactions with detector material. Simulations are used to quantify these effects, determining the percentage of primary particles based on p_{T} and centrality. The raw spectra are scaled by this factor.

$$N^{\text{primary}} = N^{\text{raw}} \cdot f_{\text{primary}}\,. \tag{5.9}$$

For kaons, the correction is negligible, while for protons and antiprotons it is substantial, particularly at low p_{T}.

5.7.3 Systematic uncertainties

Several sources add to the overall systematic error budget:

- **Tracking:** Variations in track-quality cuts (DCA, χ^2) affect efficiency estimations.
- **PID calibration:** Uncertainties in detector response functions impact fitting yields.
- **Fit stability:** Changing functional forms (Gaussian vs. Gaussian + exponential) checks signal extraction's robustness.

These uncertainties are assessed by repeating the study under different settings and examining the distribution of findings. The final corrected spectra are therefore given with both statistical and systematic error bars, providing a clear picture of measurement dependability.

5.8 Combined Corrected Spectra

After efficiency and secondary-particle corrections, the TPC and TOF findings were integrated to provide continuous spectra for pions, kaons, and protons spanning the transverse momentum range $0.1 \leq p_{\text{T}} \leq 4.5$ GeV/c. This combination is carried out in the overlapping region of applicability, where the consistency of the two detectors offers a useful cross-check of systematic uncertainties.

The adjusted spectra show the predicted centrality dependence: yields are largest in center collisions and gradually fall toward periphery events, indicating a smaller number of involved nucleons. For pions, the agreement between TPC and TOF corrected spectra is typically good throughout all centrality classes, with only slight differences in the overlap region. Kaons show bigger differences, particularly at low p_T, when TPC-based findings tend to outperform TOF-based ones. Protons exhibit the greatest detector-dependent differences: TPC corrections frequently exceed published Run 2 findings, whilst TOF tends to under-correct in center events. Peripheral collisions exhibit increased consistency.

Despite the mismatches, the overall trends remain strong. The adjusted spectra have the predicted ordering of particle abundances ($\pi > K > p$) and replicate the distinctive morphologies seen in earlier LHC runs. Comparisons with published Run 2 data at $\sqrt{s_{NN}} = 5.02$ TeV indicate continuity, but higher statistics in Run 3 allow for finer binning in both p_T and centrality.

These spectra serve as the foundation for physics interpretations offered in subsequent chapters, such as studies of hadronization, radial flow, and baryon-to-meson amplification.

5.9 Analysis Strategy Summary

The analytical technique used in this study aims to produce accurate measurements of identifiable hadron spectra in PbPb collisions at $\sqrt{s_{NN}} = 5.36$ TeV. Starting with carefully selected events and high-quality tracks, particle identification is achieved utilizing TPC and TOF data. Raw yields are retrieved by fitting to detector response distributions in discrete transverse momentum intervals, with consistency checks between the two detectors to ensure robustness.

Corrections for reconstruction efficiency, PID performance, and secondary contamination are implemented in a systematic manner, yielding completely corrected spectra for pions, kaons, and protons across a wide centrality and momentum range. The overlap between TPC and TOF adds crucial redundancy, allowing systematic uncertainties to be identified and managed.

The obtained spectra provide the critical experimental foundation for the physics interpretations presented in following chapters. They allow for quantitative comparisons to theoretical models, the extraction of particle ratios (p/π, K/π), and the characterisation of collective flow and hadronization mechanisms. As a result, the approach described here assures that the observations are both statistically exact and systematically dependable, which strengthens their importance in investigating the emergent features of the QGP.

Chapter 6

PbPb Analysis & Results

6.1 Yield Extraction

In order to measure the identified hadron spectra in ALICE, the capacity to distinguish between different particle species is required.

In this work, the PID is carried out using data from two of ALICE's most important detctors, the TPC and the TOF.

Via measuring the specific energy loss (dE/dx) of the charged particles in its gas volume, the TPC is capable of offering an exceptional separation at **low transverse momenta** ($p_{\mathrm{T}} \lesssim 0.7$ GeV/c). The Bethe-Bloch curves for $\pi^{\pm}$, $K^{\pm}$ and $p(\bar{p})$ are quite ell-separated at these momenta, thereby enabling accurate yield extraction with a little overlap.

The separation power of the TPC drops steadily as the Bethe-Bloch curves converges at **higher** p_{T}. By estimating the particle velocities with a time resolution of ~ 80 ps, the TOF detector plays a very crucial role in this area, thereby expanding the PID capability into the intermediate momentum range up to several GeV/c.

The yields of π, K, and p can be reliably extracted over the entire momentum range relevant for this analysis by combining the two detectors to achieve continuous PID coverage across a wide p_{T} interval, mainly TPC for low p_T, while TOF for high p_T.

Therefore, successful yield extraction requires careful analysis of the TPC signal at low momenta and the TOF signal at higher momenta, with overlapping areas acting as critical consistency checks between the two methods.

The next subsections describe how to use these complimentary detectors to retrieve raw yields.

6.1.1 Yield Extraction with TPC Signal

The TPC, ALICE's main tracking and particle identification detector, accurately monitors the specific energy loss (dE/dx) of charged particles passing through its drift gas volume.[144].

The measured dE/dx for each reconstructed track is usually expressed in terms of the variable after being compared to the Bethe-Bloch expectation for a specific particle species.

$$n_{\sigma,\mathrm{TPC}} = \frac{1}{\sigma_{dE/dx}} \left((dE/dx)_{\mathrm{meas}} - (dE/dx)_{\mathrm{exp}} \right), \tag{6.1}$$

where $\sigma_{dE/dx}$ denotes the detector resolution. For the ALICE TPC, the dE/dx resolution for minimum–ionizing particles is typically $\sigma_{dE/dx} \approx 5-6\%$ in central PbPb collisions and can reach $\approx 4-5\%$ in pp or low-occupancy environments [145, 146]. This number indicates how many standard deviations a given track deviates from the expected Bethe-Bloch value for a certain particle hypothesis.

Binning Strategy

The $n_{\sigma,\mathrm{TPC}}$ distributions are built in small transverse momentum (p_{T}) intervals in order to extract raw particle yields. For direct comparison, the binning adheres to the standard used in Run 2 analyses:

- π: `[0.2, 0.25, 0.3, 0.35, 0.4, 0.45, 0.5, 0.55, 0.6]` GeV/c
- K: `[0.25, 0.3, 0.35, 0.4, 0.45, 0.5, 0.55, 0.6]` GeV/c
- p: `[0.3, 0.35, 0.4, 0.45, 0.5, 0.55, 0.6, 0.65, 0.7, 0.75, 0.8]` GeV/c

This binning ensures sufficient statistical accuracy and consistency with prior PbPb results.

Fitting Methodology

The extraction of raw particle yields from the TPC signal relies on the precise modeling of the $n_{\sigma,\mathrm{TPC}}$ distributions in narrow transverse-momentum (p_{T}) intervals. These distributions represent the normalized deviation of each measured track's specific energy loss $(dE/dx)_{\mathrm{meas}}$ from the expected Bethe-Bloch value $(dE/dx)_{\mathrm{exp}}$ for a given particle hypothesis, expressed in units of the detector resolution $\sigma_{dE/dx}$. A distinct peak close to $n_{\sigma,\mathrm{TPC}} = 0$ corresponds to particles of the species under consideration, while the shoulders and non-Gaussian tails have their origins from overlapping species, Landau ionization fluctuations, and residual calibration effects. To quantitatively extract the raw yields, a composite analytical model is fitted to the $n_{\sigma,\mathrm{TPC}}$ distributions. The model simultaneously accounts for both the *signal component* associated with the target hadron species and the *smooth background* arising from neighboring particle species and detector effects. The total fit function is defined as:

$$f(x) = \begin{cases} [0]\ \exp\left(-\frac{(x-[1])^2}{2[2]^2}\right), & x \le [1]+[3], \\ [0]\ \exp\left(-\frac{([1]+[3]-[1])^2}{2[2]^2}\right) \exp\left(-[3]\frac{x-[1]-[3]}{[2]^2}\right), & x > [1]+[3], \end{cases} + [4] + [5]\,x + [6]\,e^{-[7]x}. \tag{6.2}$$

This piecewise function reproduces both the symmetric Gaussian core and the asymmetric high-side tail of the observed $n_{\sigma,\mathrm{TPC}}$ peaks. For $x \le [1]+[3]$, the function reduces to a Gaussian function centered at [1], which represents the mean of the distribution, with a width [2] that corresponds to its standard deviation. This Gaussian part describes the ideal detector response in the absence of non-Gaussian tails. For $x > [1]+[3]$, an exponential tail is introduced to model the asymmetric energy-loss fluctuations characteristic of the TPC's ionization process. The parameters [0], [1], [2], and [3] thus control the amplitude, mean, width, and tail slope of the signal, respectively. The additive terms [4], [5]x, and [6]$e^{-[7]x}$ describe the residual background, combining constant, linear, and exponential components to accommodate the smooth underlying distribution.

Signal Function. The signal component, $S(x)$, is explicitly given by the first part of Eq. (6.2):

$$S(x) = \begin{cases} [0]\ \exp\Big(-\dfrac{(x-[1])^2}{2[2]^2}\Big), & x \leq [1]+[3], \\ [0]\ \exp\Big(-\dfrac{([1]+[3]-[1])^2}{2[2]^2}\Big)\ \exp\Big(-[3]\dfrac{x-[1]-[3]}{[2]^2}\Big), & x > [1]+[3]. \end{cases} \tag{6.3}$$

The true shape of the TPC response is captured by this hybrid Gaussian–exponential form: the exponential extension on the upper side accommodates for non-Gaussian tailing caused by asymmetric ionization and resolution issues, while the Gaussian core reflects the majority of well-measured tracks. In high-statistics fits over all p_{T} bins, this physically based parametrization provides sub-percent accuracy on the mean and width.

Background Function. The contributions from misidentified particles and detector fluctuations are modeled by the background component, $B(x)$. It is parameterized as:

$$B(x) = [4] + [5]\,x + [6]\ \exp(-[7]x). \tag{6.4}$$

The exponential term permits a greater fall-off for large positive n_σ, indicating the start of contamination from higher-ionizing species, while the constant and linear terms replicate the smooth baseline. Stable fits are guaranteed by this adaptable backdrop without affecting the signal yield.

Fit Strategy and Validation. In small p_{T} and centrality intervals, each fit is carried out separately. To guarantee continuity and convergence, initial parameter seeds are spread amongst adjacent bins. To cover the whole signal while reducing areas dominated by unrelated components, fit ranges are optimized for each particle type. Range limitations, background forms, and initialization values are changed to perform robustness checks. Excellent modeling fidelity is demonstrated in every instance when the fits replicate the data with $\chi^2/\mathrm{NDF} \simeq 1$.

Representative Fit Results. Typical examples of the $n_{\sigma,\mathrm{TPC}}$ fits for π^+, K^+, and p candidates in different p_{T} intervals are shown in Figs. 6.1 - 6.3. In each panel, the data points are overlaid with the total fit (blue line), the background component (red dashed line), and the isolated signal contribution (green shaded area). The fits clearly demonstrate the separation power of the TPC and the stability of the model across species and p_{T}.

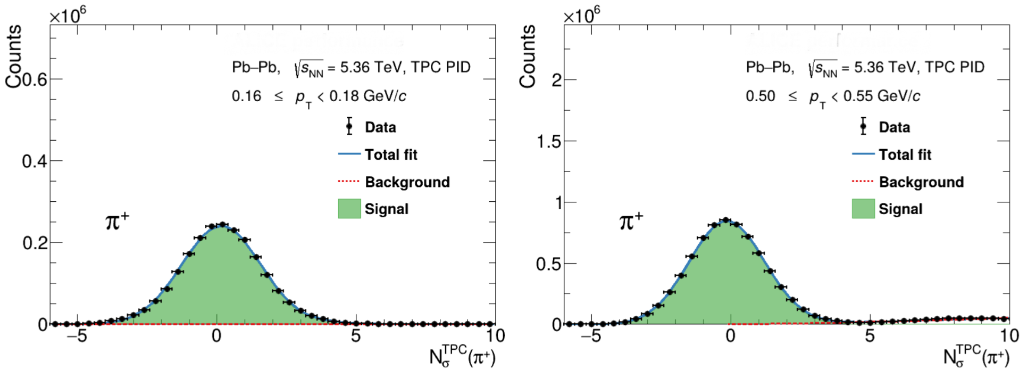

FIGURE 6.1: Representative $n_{\sigma,\mathrm{TPC}}$ distributions for π^+ candidates in Pb-Pb collisions at $\sqrt{s_{\mathrm{NN}}} = 5.36$ TeV for two p_{T} intervals. The data are shown with statistical uncertainties, the total fit (blue), background (red dashed), and extracted signal (green filled).

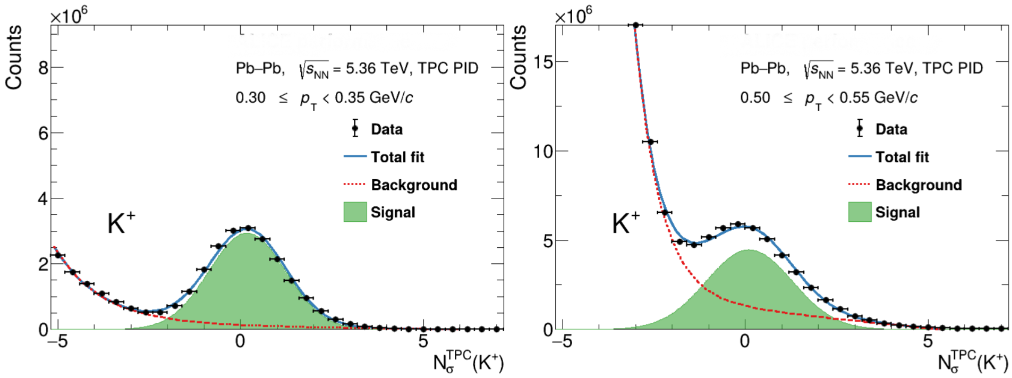

FIGURE 6.2: Example fits to the $n_{\sigma,\mathrm{TPC}}$ distributions for K^+ candidates in Pb-Pb collisions at $\sqrt{s_{\mathrm{NN}}} = 5.36$ TeV, illustrating the model's performance across two p_{T} intervals. The total fit, background, and signal components are indicated as in Fig. 6.1.

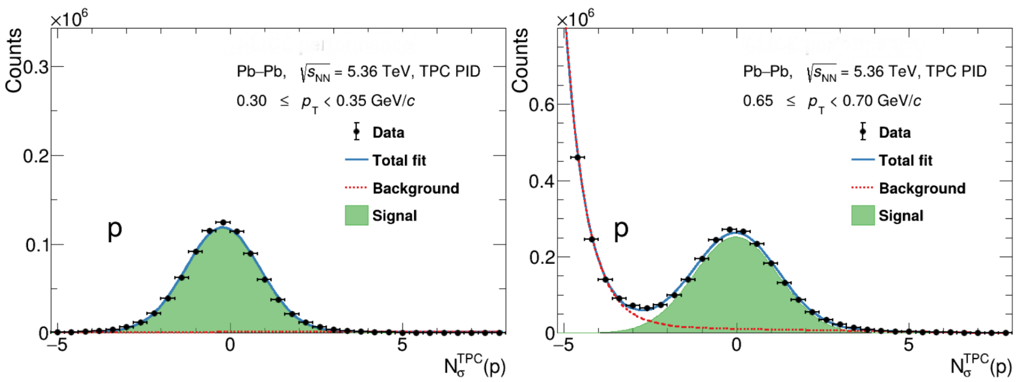

FIGURE 6.3: Representative $n_{\sigma,\mathrm{TPC}}$ distributions for protons in two p_{T} intervals. The fits exhibit the clear signal separation and the robustness of the combined signal-plus-background model even at higher ionization levels.

The selected TPC fit function correctly reproduces the signal shape and background trends over the whole phase space, as confirmed by the high-quality agreement between the data and model. These extracted raw yields serve as the basis for further corrections (efficiency, acceptance, and contamination) and ultimately for the construction of the final identified hadron spectra in PbPb collisions at $\sqrt{s_{\mathrm{NN}}} = 5.36$ TeV.

Raw-yield extraction and normalization (TPC): Once the $n_{\sigma,\mathrm{TPC}}$ fit converges in a given p_{T} bin, the *signal-only* component $S(x)$ (the first, piecewise term in Eq. (6.2)) is frozen and integrated over the fit range to obtain the raw counts. The per-event, per-p_{T}-width raw yield is then

$$N_{\mathrm{raw}}^{\mathrm{TPC}}(p_{\mathrm{T}}) = \frac{1}{N_{\mathrm{ev}}}\,\frac{1}{\Delta p_{\mathrm{T}}}\,\frac{1}{\Delta x}\int_{x_{\min}}^{x_{\max}} S(x)\,dx, \tag{6.5}$$

where N_{ev} is the number of selected events in the centrality class (FT0C), Δp_{T} is the width of the transverse-momentum bin, and Δx denotes the n_σ bin width. The integration limits $x_{\min}$ and $x_{\max}$ define the signal region in $n_{\sigma,\mathrm{TPC}}$ around the peak of the particle species under study. They are chosen symmetrically around the fitted Gaussian mean, typically

$$x_{\min} = [1] - n_\sigma\,[2], \qquad x_{\max} = [1] + n_\sigma\,[2],$$

where [1] and [2] are respectively the mean and standard deviation of the Gaussian core of the fit, and n_σ is the size of the extraction window (usually between 2 and 3). Statistical uncertainties are propagated from the fit; while for the baseline piecewise Gaussian+tail a Poisson approximation on the integrated counts is used as cross-check.

The three panels in Fig. 6.4 show the centrality dependence of the *raw* TPC pion spectra, i.e. the distributions before any acceptance or efficiency corrections and without the removal of secondary tracks. To reveal a large dynamic range, the vertical axis is logarithmic. As mentioned in the legend, the centrality classes are multiplied by powers of two to prevent overlap; these scale factors are simply used for visualization and do not affect the ratios displayed in the lower panels. In order to emphasize the remaining form variations across centralities, the bottom ratio panels use 30–40% as a reference.

The overall trend is a monotonic decrease of the raw yield with increasing peripherality which is expected on physics grounds. More central collisions involve a larger number of participant nucleons (N_{part}), thus producing a higher multiplicity of charged-particles and creating a larger and longer-lived medium. Consequently, the per-event yields are higher in central events and fall towards peripheral ones. The ratios are relatively flat versus p_{T}, indicating that spectral *shape* is broadly similar between centralities over the TPC range, with modest hardening/softening effects consistent with the change in radial flow intensity and the relative weight of soft versus hard processes. Because all spectra are normalized per event and per Δp_{T}, the observed centrality dependence is not a normalization artifact but reflects genuine production differences. Systematic-uncertainty bands are not shown here; they are evaluated separately from fit-model and track selection variations (see 6.3).

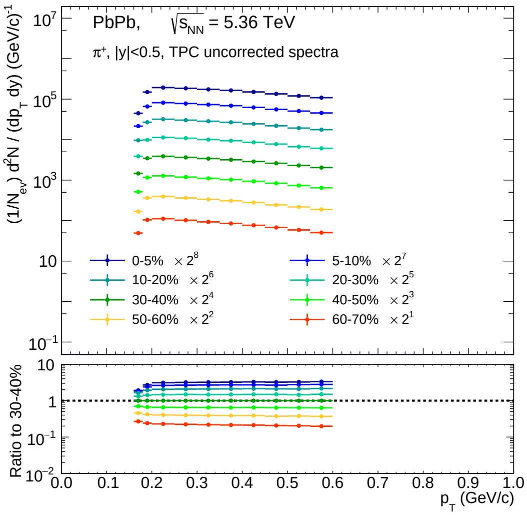

(A) π^+ raw yields vs. p_T in centrality classes (top, log scale), with curves multiplied by powers of two as indicated; bottom: ratio to 30-40%.

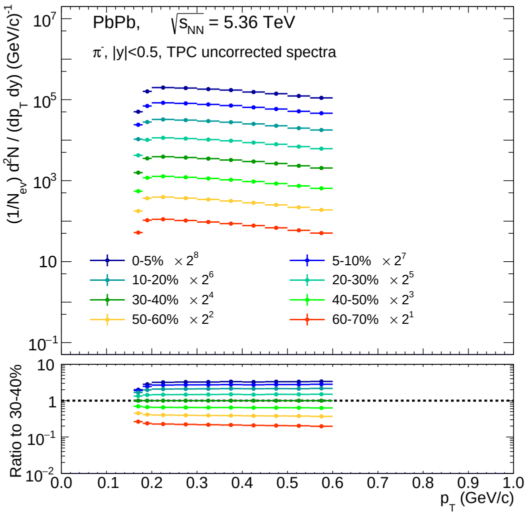

(B) π^- counterpart, same conventions as panel a.

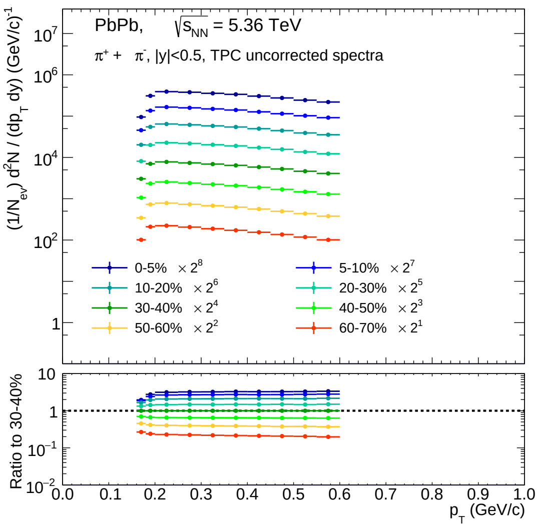

(C) $\pi^+ + \pi^-$ combined raw yields. Top: log scale; bottom: ratio to 30-40%. Multiplicative offsets are applied only for presentation; ratios are unaffected.

FIGURE 6.4: TPC raw-yield systematics for pions in Pb-Pb at $\sqrt{s_{NN}} =$ 5.36 TeV. Each top panel shows a single charge (π^+, π^-); the bottom panel shows the charge-summed spectrum. Error bars indicate statistical uncertainties. See text for the discussion.

Analogously to the pion case, the $n_{\sigma,\mathrm{TPC}}$ fits for kaons are performed in narrow p_T intervals across centrality classes. The extracted raw yields for K^+, K^-, and their combined sum are shown in Fig. 6.5.

The spectra exhibit the expected steeply falling trend with p_T and a clear centrality dependence: yields are higher in central collisions due to the larger number of participant nucleons (N_{part}) and the enhanced strangeness production in the denser medium. The ratios to the 30-40% bin (lower panels) remain flat, indicating that the kaon spectral shape changes little with centrality within the TPC p_T range. This reflects the approximate scaling of soft strangeness production with the overall charged-particle multiplicity, a well-established feature in PbPb collisions.

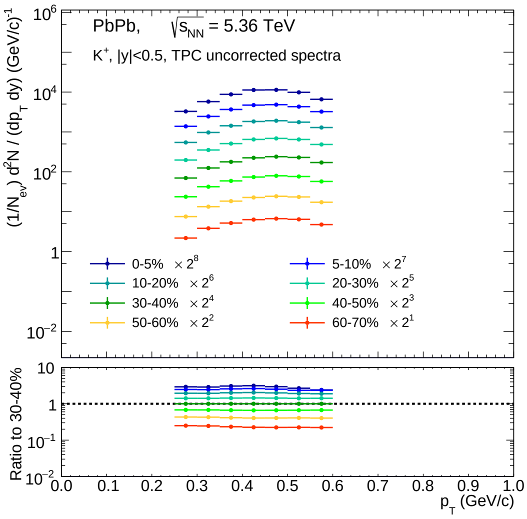

(A) K^+ raw yields vs. p_T in various centrality classes.

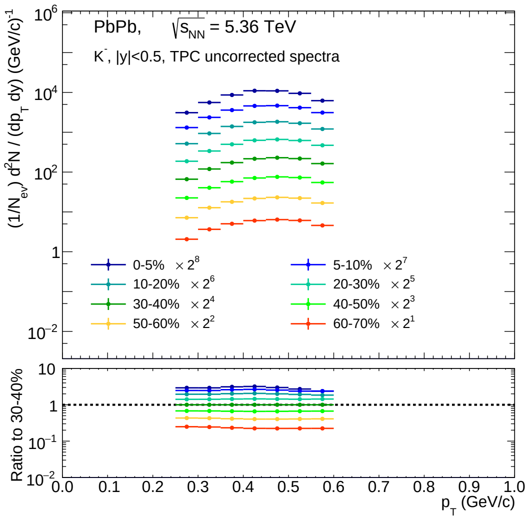

(B) K^- raw yields vs. p_T, same conventions.

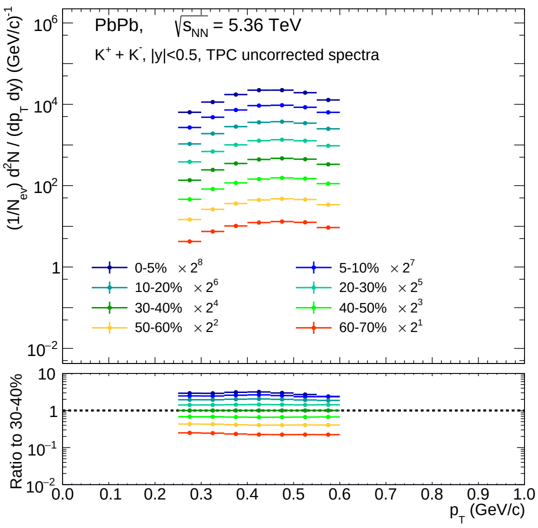

(C) Combined $K^+ + K^-$ raw yields (top: log scale; bottom: ratio to 30 - 40%).

FIGURE 6.5: TPC raw kaon spectra in PbPb at $\sqrt{s_\mathrm{NN}} = 5.36$ TeV. Each upper panel shows one charge state; the lower panel shows the charge sum. The overall yield decreases with increasing centrality percentile, reflecting the centrality dependence of strangeness production.

The proton and antiproton raw yields extracted from the $n_{\sigma,\mathrm{TPC}}$ fits are presented in Fig. 6.6.

As for pions and kaons, the overall normalization decreases toward peripheral collisions due to the smaller number of participating nucleons and the reduced fireball volume. However, an additional feature appears: at low p_T, the p yield is slightly higher than the $\bar{p}$ yield. This asymmetry originates from secondary protons produced by weak decays (e.g. $\Lambda \to p\pi^-$) and from hadronic interactions with the detector material, which preferentially generate additional protons. At higher p_T, the contamination fraction decreases, and the p and $\bar{p}$ spectra converge, as expected for primary baryon production in a nearly baryon-symmetric system at midrapidity.

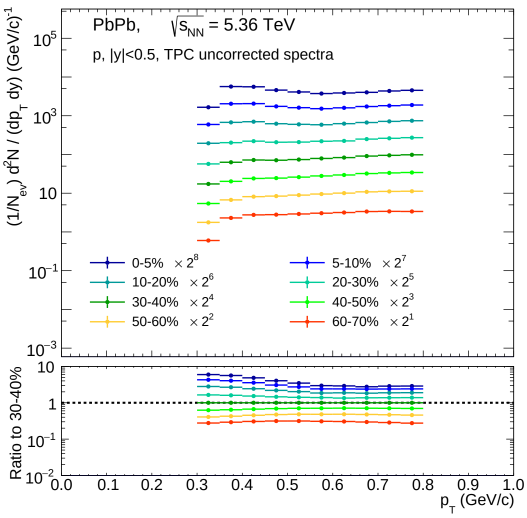

(A) Proton raw yields vs. p_{T} in various centrality classes.

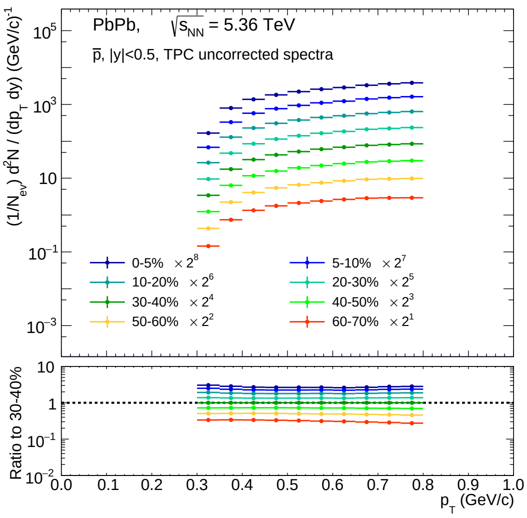

(B) Antiproton raw yields vs. p_{T}, same conventions.

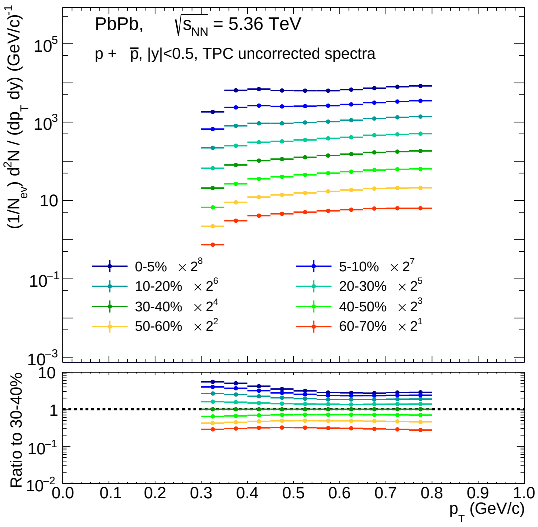

(C) Combined $p + \bar{p}$ raw yields (top: log scale; bottom: ratio to 30–40%).

FIGURE 6.6: TPC raw proton and antiproton spectra in PbPb at $\sqrt{s_{\mathrm{NN}}} = 5.36$ TeV. The small proton excess at low p_{T} reflects secondary contamination from weak decays and material interactions.

Particle-to-antiparticle raw-yield ratios

The TPC-based particle-to-antiparticle ratios are shown in Fig. 6.7 for $\pi^{\pm}$, $K^{\pm}$, and $p(\bar{p})$.

As expected for PbPb collisions at LHC energies, where the baryochemical potential at midrapidity is effectively zero, the particle-to-antiparticle ratios for both pions and kaons remain very close to unity across the full p_{T} range. This confirms the approximate charge symmetry of the system and indicates that no large charge-dependent reconstruction biases are present in the TPC-based spectra.

A closer inspection of the ratios, however, reveals small but systematic deviations from unity. For pions, the ratio π^{+}/π^{-} tends to fall slightly below unity at the lowest measured momenta ($p_{\mathrm{T}} \lesssim 0.25$ GeV/c), driven primarily by the well-known difference in hadronic interaction cross sections of positive and negative pions with detector material. At higher p_{T} the ratio returns to unity and remains flat within a few percent.

For kaons, the ratio shows the opposite trend: a mild enhancement of K^{+}/K^{-} is visible at low and intermediate p_{T}, typically at the level of 2-5% depending on centrality. This behaviour is consistent with the slightly larger absorption probability and secondary interaction rate of K^{-} in detector material, as well as the different decay topologies of the two charges that affect the TPC track-quality selection. Above $p_{\mathrm{T}} \approx 0.6$ GeV/c, the kaon ratio stabilises and the charge asymmetry becomes negligible compared with systematic uncertainties.

Overall, the observed charge asymmetries for both pions and kaons are small, well understood from known detector and interaction effects, and remain far below the percent-level precision required to impact the corrected spectra or the physics conclusions of this work.

For protons, a modest excess of particle over antiparticle yield is observed at low p_{T}, consistent with the enhanced contribution of secondary protons from weak decays and hadronic interactions. The ratio approaches unity at higher p_{T}, where such secondaries are negligible, confirming that the primary baryon production is symmetric. Overall, the TPC results agree with the TOF ratios (see sec. 6.1.2) in the overlapping momentum region, demonstrating the robustness and internal consistency of the PID and yield extraction procedures.

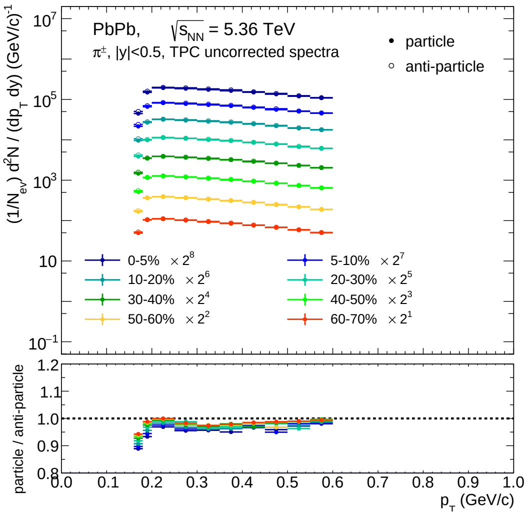

(A) Uncorrected $\pi^{\pm}$ spectra and particle/antiparticle ratios from the TPC analysis.

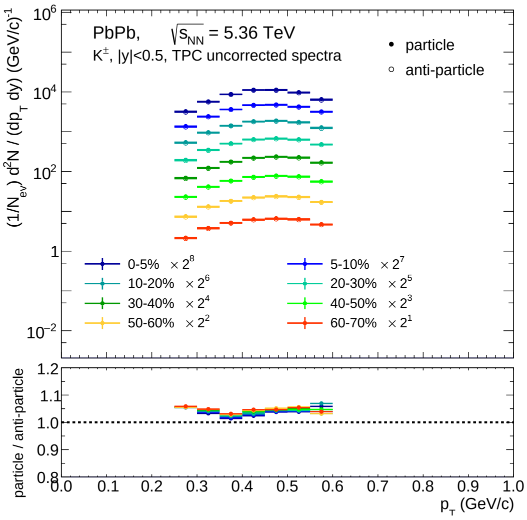

(B) Uncorrected $K^{\pm}$ spectra and particle/antiparticle ratios from the TPC analysis.

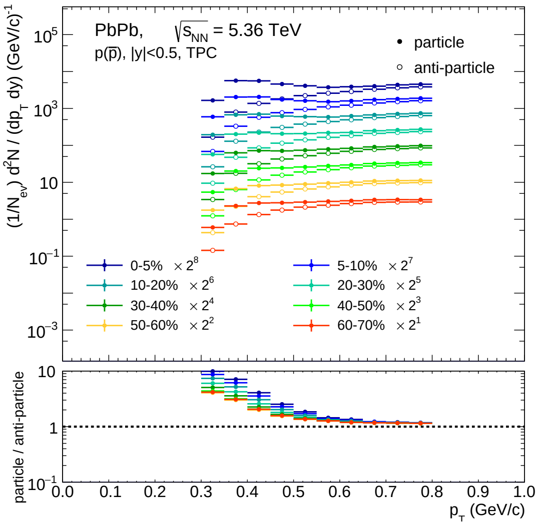

(C) Proton and antiproton spectra and particle/antiparticle ratios from the TPC analysis.

FIGURE 6.7: TPC particle-to-antiparticle raw-yield ratios in PbPb collisions at $\sqrt{s_{\mathrm{NN}}} = 5.36$ TeV. The pion and kaon ratios are unity within uncertainties; the slight proton excess at low p_{T} reflects secondary contributions.

6.1.2 Yield Extraction with TOF Signal

The Time-of-Flight (TOF) detector provides PID via precise timing of the reconstructed tracks, thereby enabling the separation of π, K, and p over a large momentum range at midrapidity. Of each track, the measured flight time is then compared to the expectation under a pre-existing mass hypothesis; the deviation, being expressed in units of the TOF resolution, and is defined as:

$$n_{\sigma,\mathrm{TOF}} \equiv \frac{t_{\mathrm{meas}} - t_{\mathrm{exp}}(m)}{\sigma_t}, \tag{6.6}$$

where t_{meas} is the measured time, $t_{\text{exp}}(m)$ is the expected time for the hypothesis $m \in \{\pi, K, p\}$, and σ_t is the total time resolution (intrinsic TOF, start-time, and tracking contributions). The distribution of $n_{\sigma,\text{TOF}}$ around zero encodes the signal for the chosen species, while non-Gaussian tails and out-of-species tracks constitute the background.

Binning Strategy

The $n_{\sigma,\text{TOF}}$ distributions are built in small p_{T} intervals in order to extract raw particle yields. For direct comparison, the binning adheres to the standard used in Run 2 analyses:

- $\pi^{\pm}$: `[0.5, 0.55, 0.6, 0.65, 0.7, 0.75, 0.8, 0.85, 0.9, 0.95, 1.0, 1.1, 1.2, 1.3, 1.4, 1.5, 1.6, 1.7, 1.8, 1.9, 2.0, 2.2, 2.4, 2.6, 2.8, 3.0, 3.2, 3.4, 3.6]` GeV/c
- $K\pm$: `[0.5, 0.55, 0.6, 0.65, 0.7, 0.75, 0.8, 0.85, 0.9, 0.95, 1.0, 1.1, 1.2, 1.3, 1.4, 1.5, 1.6, 1.7, 1.8, 1.9, 2.0, 2.2, 2.4, 2.6, 2.8, 3.0, 3.2, 3.4]` GeV/c
- $p(\bar{p})$: `[0.65, 0.7, 0.75, 0.8, 0.85, 0.9, 0.95, 1.0, 1.1, 1.2, 1.3, 1.4, 1.5, 1.6, 1.7, 1.8, 1.9, 2.0, 2.2, 2.4, 2.6, 2.8, 3.0, 3.2, 3.4, 3.6, 3.8]` GeV/c

Consistency with previous PbPb results and adequate statistical precision are guaranteed by this binning.

Baseline model at low-intermediate p_{T}

When the target species is well separated, the total fit function is a Gaussian core with a right-hand exponential tail (`Signal4`) plus a linear+exponential background (`Bkg4`); this is the `tot4` model:

$$\begin{aligned} f_{\text{tot4}}(x) = & \underbrace{\Theta([1]+[3]-x)\,[0]\,\exp\left(-\frac{(x-[1])^2}{2[2]^2}\right)}_{\text{Signal } S_4(x)} \\ & + \underbrace{\Theta(x-[1]-[3])\,[0]\,\exp\left(-\frac{[3]^2}{2}\right)\,\exp\left(-\frac{[3]\,(x-[1]-[3])}{[2]^2}\right)}_{\text{Signal tail}} \\ & + \underbrace{[4]+[5]\,x+[6]\,e^{-[7]x}}_{\text{Background } B_4(x)}\,. \end{aligned} \tag{6.7}$$

where [0] is the signal amplitude, $[1] \equiv \mu$ the peak position, $[2] \equiv \sigma$ the core width, and [3] the exponential-tail parameter; [4], [5] are the constant/linear background terms, and [6], [7] the amplitude/slope of the decaying exponential background component.

This piecewise expression models both the signal and the residual background in a single analytical form. The Heaviside step functions Θ are used to define the transition point between the Gaussian core and the exponential tail.

Signal term $S_4(x)$. The signal component represents the genuine TOF response of a specific particle species (for example, a pion, kaon, or proton). The first term (line 1 in Eq. 6.7) is a Gaussian distribution centered at the mean position [1], with a width parameter [2] corresponding to the detector resolution. The prefactor [0] scales the amplitude of the peak.

At values of x greater than $[1] + [3]$, the Gaussian smoothly transitions into an exponential decay (line 2 of Eq. 6.7). The exponential term, controlled by the slope parameter [3], models the asymmetric right-hand tail that arises from non-Gaussian detector effects, time-of-flight resolution fluctuations, and imperfect track matching. The multiplicative factor $\exp(-[3]^2/2)$ ensures continuity at the transition point between the Gaussian core and the exponential tail.

Background term $B_4(x)$. The background describes the smooth underlying contribution from misidentified tracks and random combinatorial effects. It consists of three additive terms:

- a constant offset [4],
- a linear term $[5]\,x$ that allows for mild slope variations across the n_σ range,
- and an exponential term $[6]\,e^{-[7]x}$ which captures possible asymmetric tails from residual background fluctuations.

This flexible background form, $B_4(x)$, enables a stable description of the non-peaking parts of the n_σ distribution without biasing the signal region.

Motivation for the functional form: The TOF detector measures the difference between the measured and expected time-of-flight for a given mass hypothesis, normalized to the detector resolution. Due to the finite timing resolution and the non-Gaussian nature of timing fluctuations, the n_σ distributions are not perfectly symmetric. The combination of a Gaussian core and an exponential tail therefore provides a realistic empirical description of the signal shape. The background component ensures a smooth baseline fit across the entire n_σ range.

Continuity and smoothness: The definition of Eq. 6.7 guarantees that both $S_4(x)$ and its first derivative are continuous at $x = [1] + [3]$, ensuring physical smoothness across the transition region. This property is crucial for stable minimization and consistent yield extraction.

Parameter interpretation:

- [0]: overall normalization of the signal;
- [1]: mean position of the signal peak;
- [2]: Gaussian width (resolution);
- [3]: exponential tail parameter (controls asymmetry);
- [4], [5], [6], [7]: coefficients of the background function.

High p_{T} contamination models

At higher p_{T}, the $n_{\sigma,\mathrm{TOF}}$ distributions of different hadron species begin to overlap due to the reduced separation power of the TOF detector. The time-of-flight difference between pions, kaons, and protons decreases approximately as $1/p_{\mathrm{T}}$, causing their respective peaks to merge gradually into one another. In this regime, a simple single-species fit is no longer sufficient, as the tails of neighbouring species contribute to the same region of the n_σ spectrum.

To account for this inter-species contamination, the baseline fit model described in Eq. (6.7) is extended by introducing additional Gaussian components that represent the contaminating species. These additional terms are standard, normalized Gaussian functions ($\mathcal{G}$) defined as:

$$\mathcal{G}(x;\mu,\sigma) = \frac{1}{\sqrt{2\pi}\sigma} \exp\left[-\frac{(x-\mu)^2}{2\sigma^2}\right],$$

where μ and σ correspond to the expected peak position and width of the contaminant species, respectively. Each contaminant component has its own amplitude parameter (A_i) which scales its contribution relative to the signal and background. The contaminant Gaussians are added to the total fit function while the main signal shape (`Signal4`) remains unchanged.

Pions at high p_{T} ($p_{\mathrm{T}} \gtrsim 2.6$ GeV/c)(`tot4K`): At high p_{T}, the kaon peak gradually enters the positive $n_{\sigma,\pi}$ region. Therefore, for pions, the fit function is modified to include a kaon Gaussian on the right-hand side of the signal:

$$f_{\mathrm{tot4K}}(x) = S_4^{(\pi)}(x) + B_4(x) + A_K\,\mathcal{G}(x\,;\,\mu_K,\sigma_K)\,. \tag{6.8}$$

Here, $S_4^{(\pi)}(x)$ and $B_4(x)$ denote the signal and background functions defined previously. The kaon contaminant is represented by a normalized Gaussian centered at $\mu_K > 0$ (typically initialized around $\mu_K \approx 3$) with a width $\sigma_K \approx 1$. This additional component captures the right-side shoulder produced by kaons that are misidentified as pions in this momentum range. The amplitude A_K quantifies the contamination fraction.

Kaons at high p_{T} ($p_{\mathrm{T}} \gtrsim 2.2$ GeV/c)(`tot4PIinK`): For kaons, the contamination arises primarily from the left-hand side, where the pion peak overlaps. The corresponding model adds a pion Gaussian to the left of the kaon signal:

$$f_{\mathrm{tot4}\,\pi\in K}(x) = S_4^{(K)}(x) + \underbrace{(b_0 + b_1 x)}_{\text{linear background}} + A_\pi\,\mathcal{G}(x\,;\,\mu_\pi,\sigma_\pi)\,, \tag{6.9}$$

where the exponential background term is omitted to avoid unphysical upturns in the fit. The pion contaminant parameters are typically initialized with $\mu_\pi < 0$ and constrained to $\sigma_\pi \in [0.6, 1.2]$ to maintain physical consistency. The addition of the pion Gaussian ensures a proper modeling of the left-hand tail of the kaon peak, which otherwise would bias the extracted yield.

Protons at very high p_T(tot4PIK_inP): At the highest transverse momenta, the TOF separation between all three species, pions, kaons, and protons, becomes minimal. For proton identification, both pions and kaons contribute significant contamination on the left-hand side of the $n_{\sigma,p}$ distribution. Therefore, the proton fit function is extended with two Gaussian contaminant components:

$$f_{\text{tot4}\,(\pi,K)\in p}(x) = S_4^{(p)}(x) + (b_0 + b_1 x) + A_\pi\,\mathcal{G}(x\,;\,\mu_\pi,\sigma_\pi) + A_K\,\mathcal{G}(x\,;\,\mu_K,\sigma_K)\,. \quad (6.10)$$

Only a linear background term is used here, as including an exponential component would risk absorbing part of the kaon and pion shoulders. This two-Gaussian extension ensures that the fit remains stable even when the individual peaks are highly blended.

Seeding, Constraints, and Fit Stability

Parameter initialization and constraints play a critical role in ensuring the robustness of the fits across all p_T and centrality intervals. Seed values are propagated bin-by-bin to maintain smooth parameter evolution with p_T, minimizing discontinuities in the extracted yields. The main signal peak is always initialized near $\mu \approx 0$, consistent with the particle hypothesis. Contaminant Gaussians are initialized at physically motivated positions corresponding to the expected mean n_σ values of other species: for example, $\mu_\pi \in [-8.5, -4]$ and $\mu_K \in [-5, -2]$ in proton fits. The widths are constrained to $\sigma \in [0.8, 1.8]$ to prevent over-broadening.

At high p_T, where the n_σ distributions flatten, the exponential term in the background is disabled, leaving only the linear form $(b_0 + b_1 x)$. This prevents the background function from mimicking the tails of overlapping peaks and ensures that the contaminant components absorb all species-specific contributions.

Overall, this modular fitting strategy allows for a consistent, physically motivated description of the $n_{\sigma,\text{TOF}}$ distributions across the full momentum range, from well-separated peaks at low p_T to heavily overlapping structures at high p_T. The introduction of explicit contaminant Gaussians provides accurate yield extraction and prevents bias in the final spectra, particularly in the region where the TOF detector's particle identification power begins to diminish.

Signal and Background Separation; S/B Evaluation

Once the fit procedure described above converges for a given p_T and centrality bin, the fitted components are fixed (*frozen*) and used to visualize the relative contributions of the signal, background, and contaminant species. This visual decomposition provides a direct validation of the model quality and facilitates the assessment of systematic uncertainties related to background subtraction.

The final visualization includes three distinct components:

$$\begin{aligned} \text{Signal:} &\quad S(x) \ \ \text{(green filled region)},\\ \text{Background:} &\quad B(x) \ \ \text{(red dashed line)},\\ \text{Contaminants:} &\quad \mathcal{G}_{\pi,K}(x) \ \ \text{(thin colored curves)}. \end{aligned}$$

The signal function $S(x)$ corresponds to the primary species under study (as defined by $S_4(x)$ or its extended forms in Eqs. (6.8)–(6.10)), while $B(x)$ represents the empirical background component. When applicable, additional Gaussian terms

$\mathcal{G}_{\pi,K}(x)$ describe secondary contaminant species. Each component is plotted with consistent color coding for clarity across the analysis.

Signal-to-Background Ratio: To quantify the purity of the fitted signal and assess fit quality, a diagnostic signal-to-background ratio (S/B) is computed for each bin. The S/B ratio is defined as the ratio of the integral of the signal component to that of the background component, both calculated within a $\pm 2\sigma$ window centered around the fitted signal mean μ:

$$\frac{S}{B} = \frac{\int_{\mu-2\sigma}^{\mu+2\sigma} S(x)\,dx}{\int_{\mu-2\sigma}^{\mu+2\sigma} B(x)\,dx}. \tag{6.11}$$

Here, μ and σ are the mean and width parameters obtained from the fit to the signal peak.

The choice of a $\pm 2\sigma$ window, rather than the canonical $\pm 3\sigma$, is motivated by the specific characteristics of the $n_{\sigma,\mathrm{TPC}}$ distributions. While a $\pm 3\sigma$ range would capture a slightly larger fraction of the true signal, it would also include regions where the non-Gaussian tails and residual background become significant. In contrast, the $\pm 2\sigma$ interval contains more than 95% of the Gaussian core of the distribution and remains largely free from distortions introduced by the asymmetric tail component of the fit function. Using this narrower but cleaner window ensures that the computed S/B ratio faithfully reflects the purity of the central signal peak rather than being diluted by tail contributions that are not representative of the true detector response.

This localized definition of S/B reflects the effective purity of the identified signal region and serves as an indicator of the stability of the yield extraction.

This annotation provides a quick visual benchmark for the signal significance in each p_{T} interval and helps identify regions where background contamination becomes dominant. Typical S/B ratios are high at low and intermediate transverse momenta, where the TOF detector maintains good species separation, and gradually decrease at higher p_{T} where the n_σ distributions begin to overlap. Nonetheless, even in these challenging regions, the extended models described in Sec. 6.1.2 ensure that the extracted yields remain reliable and consistent across species.

Model Choice per Species and p_{T}. The specific model used in each p_{T} interval depends on the degree of particle separation in the TOF detector:

- **Pions ($\pi^\pm$):** use `tot4` at low and intermediate p_{T}; switch to `tot4K` (Eq. 6.8) at high p_{T} to include kaon contamination on the right-hand side.
- **Kaons ($K^\pm$):** use `tot4` at low p_{T}; switch to `tot4PIinK` (Eq. 6.9) for $p_{\mathrm{T}} \gtrsim 2.2\,\mathrm{GeV}/c$, using only a linear background.
- **Protons ($p, \bar{p}$):** use `tot4` up to intermediate p_{T}; at very high p_{T}, where the TOF separation between pions, kaons, and protons becomes minimal, adopt the extended `tot4PIK_inP` model (Eq. 6.10). This model includes two additional Gaussian contaminant components representing the overlapping pion and kaon contributions on the left-hand side of the $n_{\sigma,p}$ distribution, along

with a purely linear background term to prevent absorption of these shoulders. The contaminant parameters are initialized using the auxiliary `leftPIK` pre-fit (Eq. 6.10) to stabilize the global fit at the highest momenta.

This adaptive model selection strategy mirrors the analysis macro logic: it preserves stability where species are well separated and introduces explicit contaminant templates only where necessary at higher p_T.

Raw-yield extraction and normalization (TOF): Once the $n_{\sigma,\mathrm{TOF}}$ fit converges in a given p_T and centrality bin, the *signal-only* component $S(x)$ of the total fit function is frozen and integrated over the full fit range to obtain the raw counts. This procedure isolates the yield of the target particle species while excluding the background and contaminant Gaussian contributions. The per-event, per-p_T-width raw yield is defined as:

$$N_{\mathrm{raw}}^{\mathrm{TOF}}(p_T) = \frac{1}{N_{ev}} \frac{1}{\Delta p_T} \frac{1}{\Delta x} \int_{x_{\min}}^{x_{\max}} S(x)\,dx, \tag{6.12}$$

where N_{ev} denotes the number of analyzed events in the centrality class (FT0C), Δp_T is the bin width, and Δx is the n_σ bin width. The integration limits are chosen to include both the Gaussian core and the exponential tail, ensuring complete signal capture.

Uncertainties are propagated from the covariance matrix of the fit, accounting for correlations between amplitude, mean, and width parameters. As a validation, the signal yield is also obtained via direct numerical integration of the background-subtracted histogram, with consistent results within statistical precision.

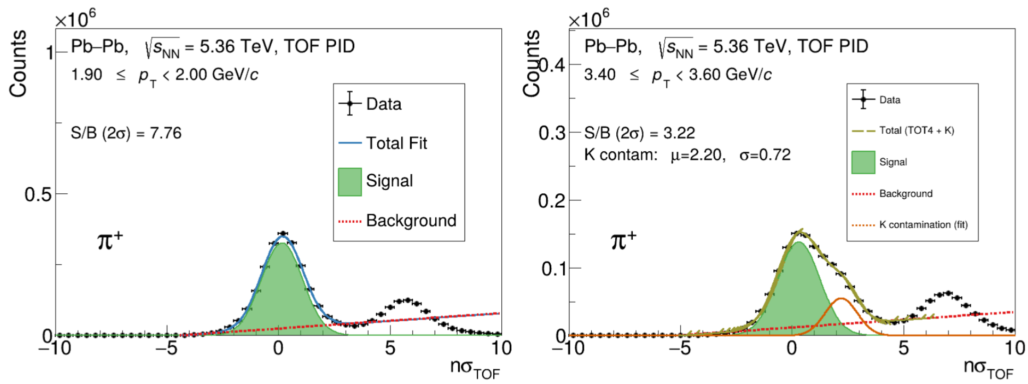

FIGURE 6.8: Representative $n_{\sigma,\mathrm{TOF}}$ distributions for π^+ candidates in Pb-Pb collisions at $\sqrt{s_{\mathrm{NN}}} = 5.36$ TeV, showing low- (left) and high-p_T (right) intervals. The total fit (blue line), background (red dashed), and signal (green filled) components are displayed. At higher p_T, kaon contamination on the right-hand side is modeled with an additional Gaussian term.

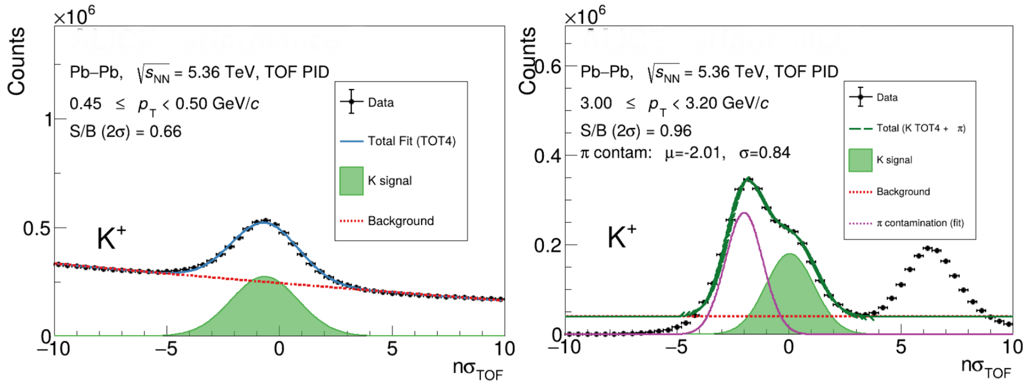

FIGURE 6.9: Example fits to the $n_{\sigma,\mathrm{TOF}}$ distributions for K^+ candidates at low (left) and high (right) p_T intervals. The total fit (solid blue) includes a Gaussian core with an exponential tail, and at high p_T an additional pion contaminant Gaussian on the left-hand side, following Eq. (6.9).

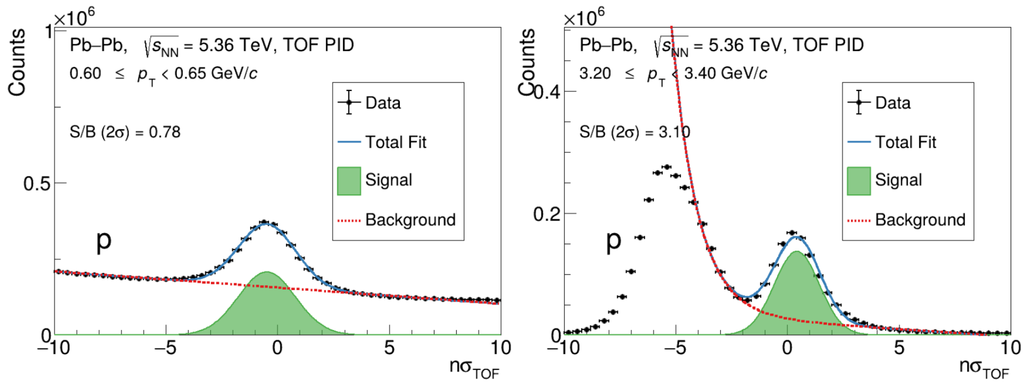

FIGURE 6.10: Representative $n_{\sigma,\mathrm{TOF}}$ fits for protons in two p_T intervals. At high p_T, the fit includes pion and kaon contamination components according to Eq. (6.10). The green region indicates the extracted proton signal.

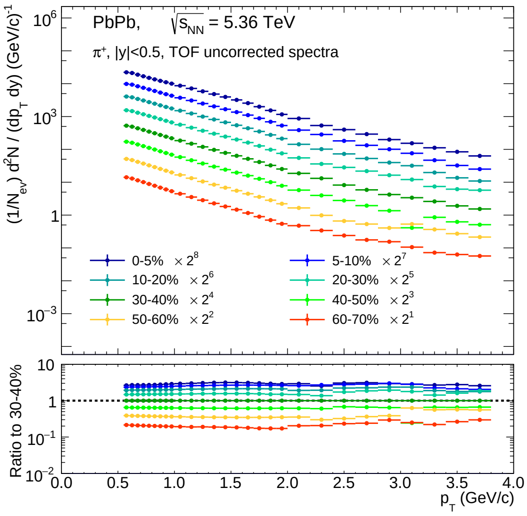

(A) π^+ raw yields vs. p_T in centrality classes (top, log scale), with curves multiplied by powers of two as indicated; bottom: ratio to 30-40%.

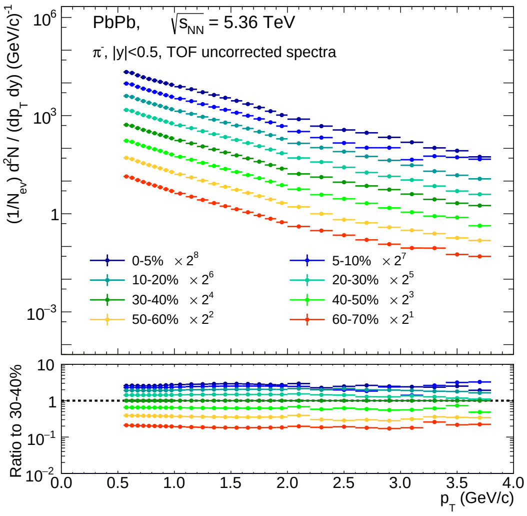

(B) π^- counterpart, same conventions as panel a.

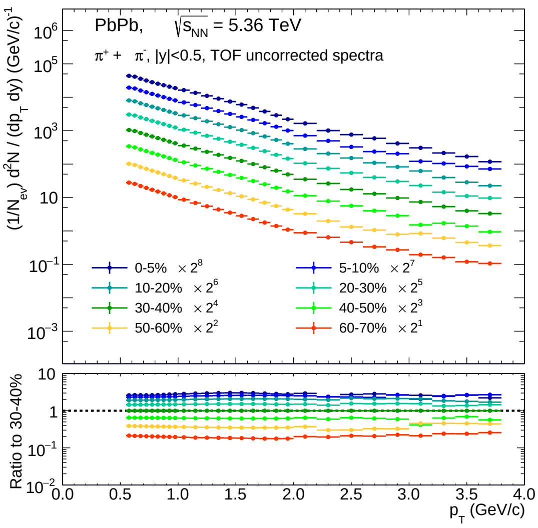

(C) $\pi^+ + \pi^-$ combined raw yields. Top: log scale; bottom: ratio to 30-40%. Multiplicative offsets are applied only for presentation; ratios are unaffected.

FIGURE 6.11: TOF raw-yield for pions in Pb-Pb at $\sqrt{s_{\mathrm{NN}}} = 5.36$ TeV. Each top panel shows a single charge (π^+, π^-); the bottom panel shows the charge-summed spectrum. Error bars indicate statistical uncertainties. See text for discussion.

The three panels summarize the centrality dependence of the *raw* (i.e. the distributions before any acceptance or efficiency corrections and without the removal of secondary tracks) TOF spectra for pions. The vertical axis is logarithmic to expose a wide dynamic range. To avoid overlap, the centrality classes are multiplied by powers of two as indicated in the legend; these scale factors are for visualization only and do not enter the ratios shown in the lower panels. The bottom ratio panels take 30-40% as a reference to highlight the residual shape differences between centralities.

The trends shown in Fig. 6.11 demonstrate the consistency of the TOF-based yield extraction across centrality intervals. The spectra follow a smooth power-like decrease with p_T, and the ratios indicate similar spectral shapes across centralities.

The overall decrease of yields with increasing centrality percentile is driven by the smaller number of participant nucleons and reduced system size in peripheral collisions, consistent with expectations from bulk particle production dynamics in heavy-ion collisions. The kaon raw yields extracted from the $n_{\sigma,\mathrm{TOF}}$ fits are shown in Fig. 6.12. The results closely mirror the pion behavior, exhibiting a power-law–like decrease with p_{T} and a strong dependence on collision centrality. The yield magnitude decreases toward peripheral events, consistent with the suppression of strangeness production in smaller systems. The ratios to the 30-40% reference bin demonstrate that the spectral shapes are largely invariant across centralities within the TOF acceptance range.

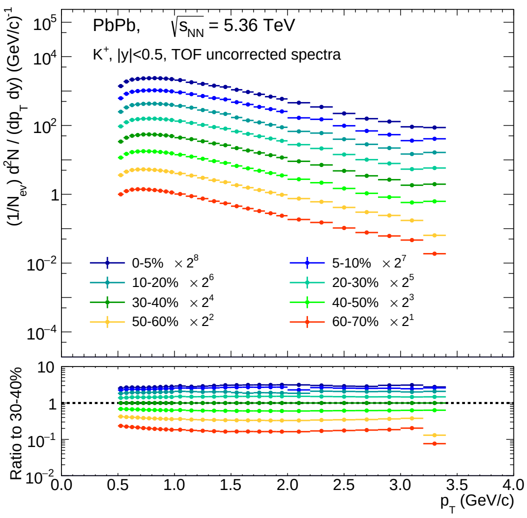

(A) K^+ raw yields vs. p_{T} in various centrality classes.

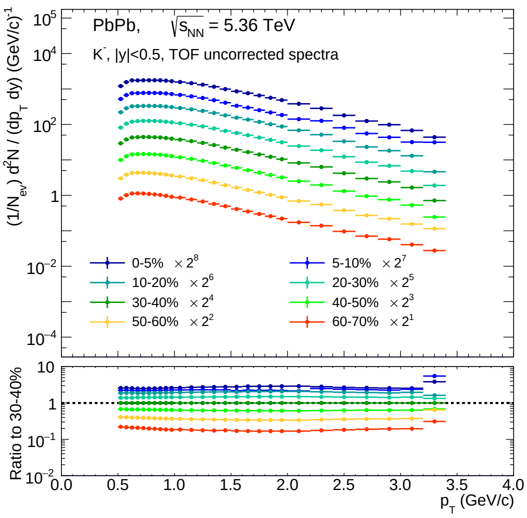

(B) K^- raw yields vs. p_{T}, same conventions.

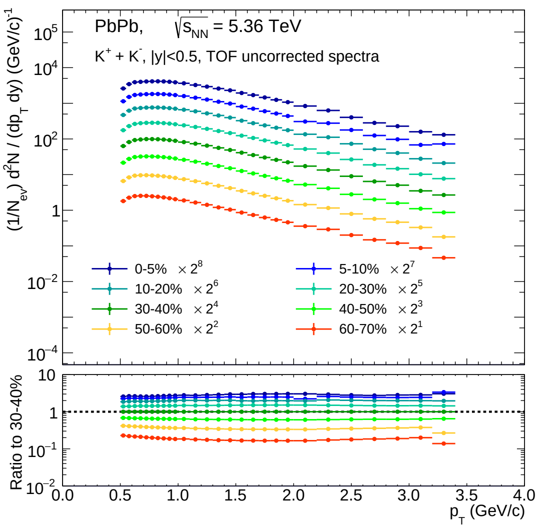

(C) Combined $K^+ + K^-$ raw yields (top: log scale; bottom: ratio to 30–40%).

FIGURE 6.12: TOF raw kaon spectra in PbPb collisions at $\sqrt{s_{\mathrm{NN}}} = 5.36$ TeV. The overall centrality dependence follows that observed for pions, consistent with bulk strangeness scaling with charged-particle multiplicity.

Figure 6.13 presents the TOF-based raw yields for protons and antiprotons. The overall yield hierarchy across centralities matches that seen for pions and kaons, while the proton yields remain slightly higher than the anti-protons at low p_T, in line with the TPC observations. This excess arises primarily from secondary protons originating from weak hyperon decays and interactions with detector material, which contribute more to the p spectrum than to the $\bar{p}$ one. As p_T increases, the contamination becomes negligible, and the two spectra converge.

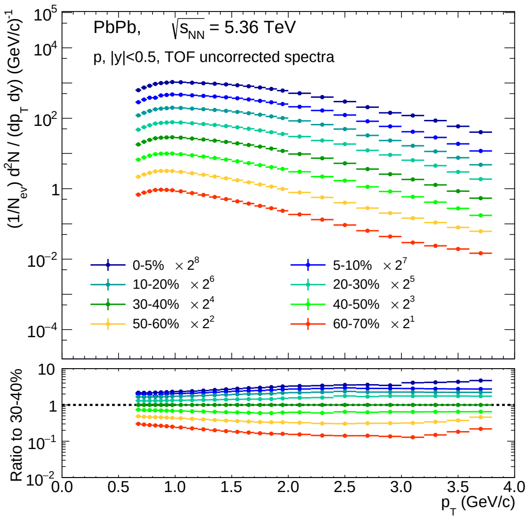

(A) Proton raw yields vs. p_T in various centrality classes.

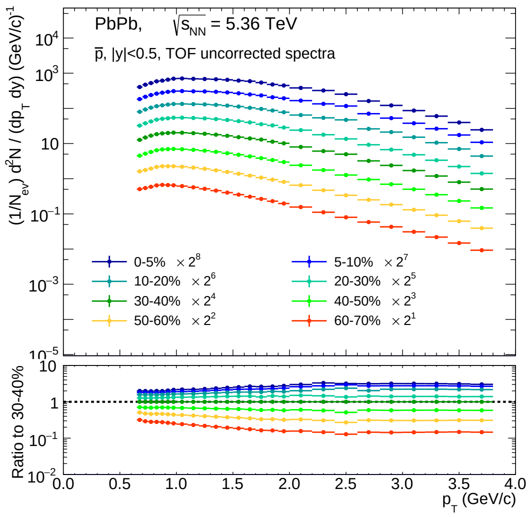

(B) Antiproton raw yields vs. p_T, same conventions.

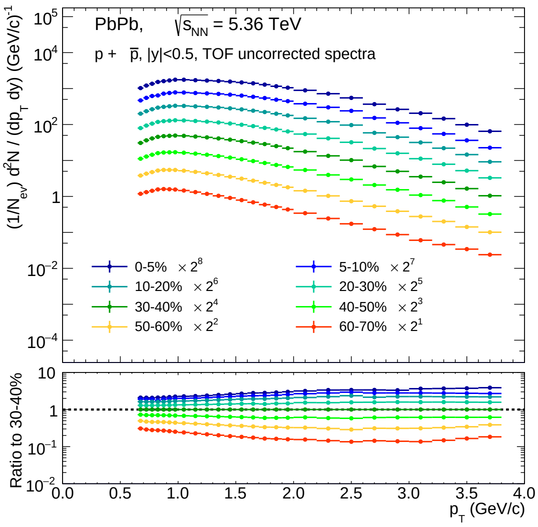

(C) Combined $p + \bar{p}$ raw yields (top: log scale; bottom: ratio to 30-40%).

FIGURE 6.13: TOF raw proton and antiproton spectra in PbPb at $\sqrt{s_{NN}} = 5.36$ TeV. The small proton excess at low p_T reflects secondary and material contributions.

Particle-to-antiparticle raw-yield ratios (TOF)

The TOF-based analysis extends the ratio study to higher p_T, where the detector provides enhanced particle separation. The ratio is defined analogously as:

$$R_{TOF}(p_T) = \frac{N_{raw}^{TOF}(\text{particle})}{N_{raw}^{TOF}(\text{antiparticle})}. \tag{6.13}$$

Figures 6.14 show the uncorrected TOF spectra and corresponding particle-to-antiparticle ratios for $\pi^{\pm}$, $K^{\pm}$, and $p(\bar{p})$ across all centrality classes. For both pions and kaons, the ratios are overall flat and consistent with unity within uncertainties, indicating that particle and antiparticle production remains nearly symmetric throughout the measured p_{T} range.

A small increment in the particle yield relative to its antiparticle is visible in some centrality classes, particularly at intermediate p_{T}. This effect is minor and compatible with residual charge asymmetries originating from limited acceptance differences, small variations in track reconstruction efficiency, or minor baryon-number transport to midrapidity.

At higher p_{T}, slight fluctuations in the ratios are observed, which are attributed to limited statistics and reduced fit stability in the $n_{\sigma,\mathrm{TOF}}$ tails. These fluctuations are within statistical expectations and do not represent a physical asymmetry.

For protons, the ratio shows a slightly larger deviation from unity at low and intermediate p_{T}, where the proton yield exceeds that of antiprotons. This is an expected feature arising from the contribution of secondary protons produced by weak decays (e.g. $\Lambda \rightarrow p\pi^{-}$) and interactions with detector material, which preferentially enhance the positive baryon yield. As p_{T} increases, the fraction of these secondary protons decreases rapidly, and the $p/\bar{p}$ ratio approaches unity, consistent with a baryon-symmetric medium.

Overall, the TOF ratios confirm that the production of particles and antiparticles remains balanced at midrapidity in Pb-Pb collisions at $\sqrt{s_{\mathrm{NN}}} = 5.36$ TeV. The small residual deviations at low p_{T} are consistent with known detector and physics effects.

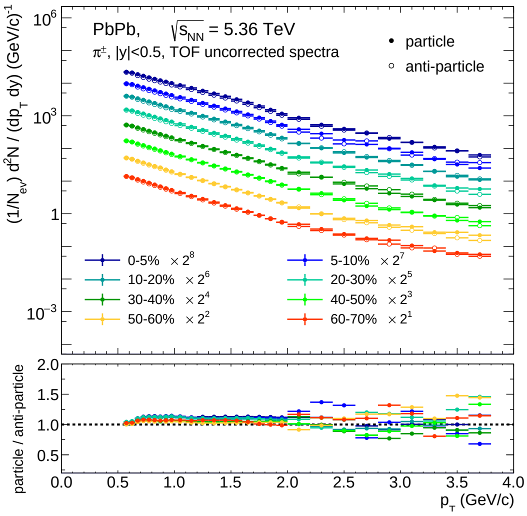

(A) Uncorrected $\pi^{\pm}$ spectra and particle/antiparticle ratios from the TOF analysis.

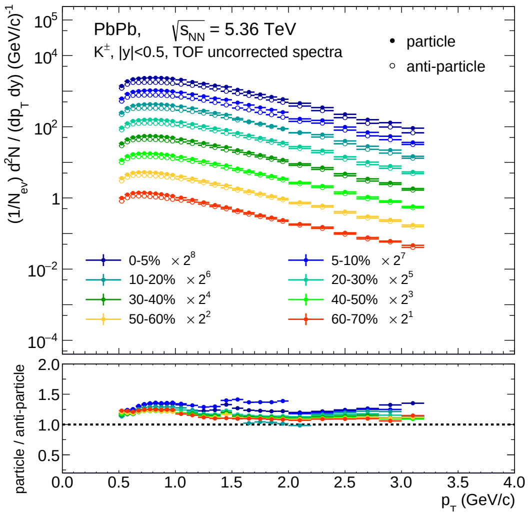

(B) Uncorrected $K^{\pm}$ spectra and particle/antiparticle ratios from the TOF analysis.

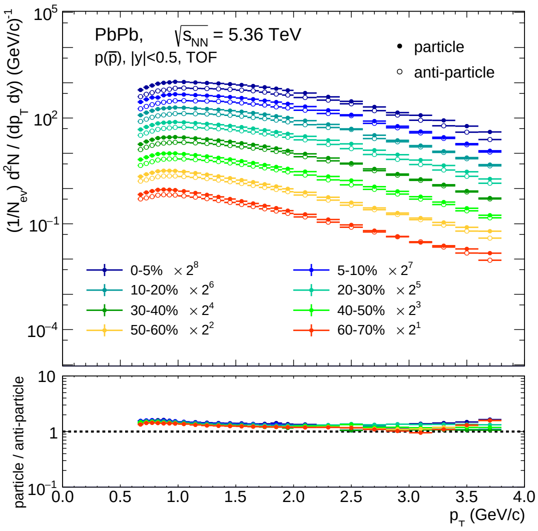

(C) Proton and antiproton spectra and particle/antiparticle ratios from TOF.

FIGURE 6.14: TOF particle-anti particle raw-yield in Pb-Pb at $\sqrt{s_{NN}}$ = 5.36 TeV. Error bars indicate statistical uncertainties. See text for discussion.

6.2 From raw to corrected spectra

The results presented thus far correspond to the *raw* per-event yields extracted from detailed fits to the n_{σ} distributions in finely binned transverse momentum intervals. These yields represent the number of tracks identified as a given species within the fiducial detector acceptance and after explicit rejection of background and inter-species contamination through the analytical fit procedure.

However, by construction, such raw yields still carry the imprint of the detector's response: they are affected by finite geometrical acceptance, reconstruction and tracking inefficiencies, imperfect PID response, and the presence of residual secondary particles originating from weak decays or material interactions. Consequently, these raw yields cannot yet be interpreted as direct observables of the underlying physics processes.

To obtain quantitatively meaningful spectra that can be compared across centrality classes, with theoretical models, and with results from other experiments, the measured yields must be corrected for the full chain of instrumental effects. This transformation converts detector-level quantities into *particle-level* observables, representing the true kinematic distributions of primary particles produced in the collision.

The following subsections details this correction procedure, which constitutes one of the most critical stages of the analysis. It involves evaluating the detector acceptance, tracking and PID efficiencies, and TOF matching probability using detailed Monte Carlo simulations and data-driven techniques, as well as correcting for the contribution of secondary tracks. The resulting acceptance and efficiency corrected spectra form the foundation for the subsequent physics interpretation and for the extraction of integrated particle yields, mean transverse momenta, and particle ratios in PbPb collisions at $\sqrt{s_{\mathrm{NN}}} = 5.36$ TeV.

6.2.1 Acceptance and efficiency corrections

All efficiency corrections are derived using a full Monte Carlo (MC) simulation of the ALICE detector, which includes a detailed description of detector geometry, material budget, and response functions. Simulated Pb-Pb events at $\sqrt{s_{\mathrm{NN}}} = 5.36$ TeV are generated with PYTHIA and propagated through the ALICE apparatus using the GEANT4 transport code.

Reconstructed tracks are processed with the same reconstruction chain, calibration parameters, and selection criteria used for real data, ensuring identical analysis conditions. This allows a direct, bin-by-bin determination of efficiencies as a function of transverse momentum, rapidity, particle species, and collision centrality.

Tracking efficiency in the TPC

The **tracking efficiency** quantifies the probability that a primary charged particle produced within the detector acceptance is successfully reconstructed and passes the standard track quality criteria described in Sec. 6.3. It is computed from Monte Carlo simulations as the ratio:

$$\varepsilon_{\mathrm{tracking}}(p_{\mathrm{T}}) = \frac{N_{\mathrm{reco}}^{\mathrm{MC}}(\text{primary, MC PID}, |y| < 0.5, |\eta| < 0.8)}{N_{\mathrm{gen}}^{\mathrm{MC}}(\text{primary, MC PID}, |y| < 0.5)}. \tag{6.14}$$

Here:

- $N_{\mathrm{gen}}^{\mathrm{MC}}$ is the number of generated primary particles of a given species (based on MC truth);
- $N_{\mathrm{reco}}^{\mathrm{MC}}$ is the subset of those that are reconstructed and pass all analysis cuts;
- the numerator and denominator both require the same kinematic and acceptance selections ($|y| < 0.5$, $|\eta| < 0.8$), and the true MC particle identity is enforced.

Only primary particles are considered, as the contribution of secondaries is treated separately via the data-driven correction discussed in Sec. 6.3. The same reconstruction and selection criteria (minimum number of TPC clusters, DCA cuts, χ^2 per cluster, etc.) are applied to reconstructed MC tracks as to data, guaranteeing consistency between efficiency corrections and the raw-yield extraction.

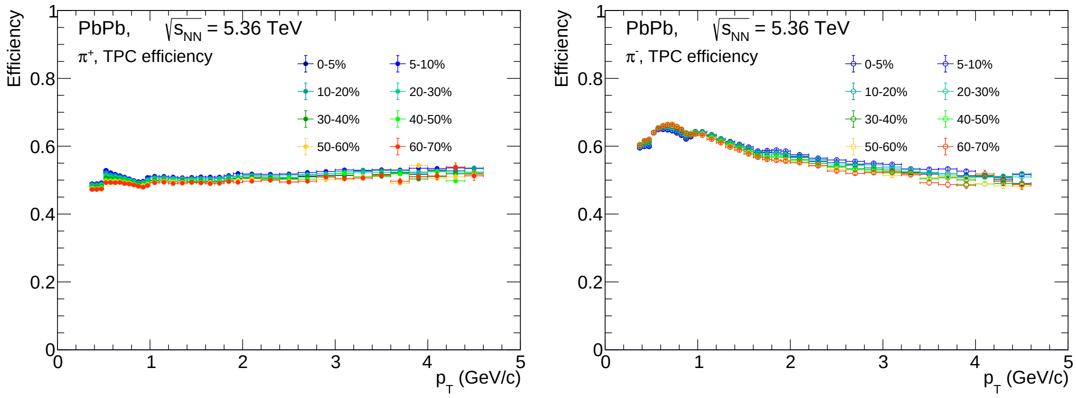

(A) TPC tracking efficiency for π^+ as a function of p_T across centrality intervals.

(B) Same as (a) but for π^-.

FIGURE 6.15: TPC tracking efficiencies for π^+ and π^- in Pb-Pb collisions at $\sqrt{s_{NN}} = 5.36$ TeV, obtained from full Monte Carlo simulations.

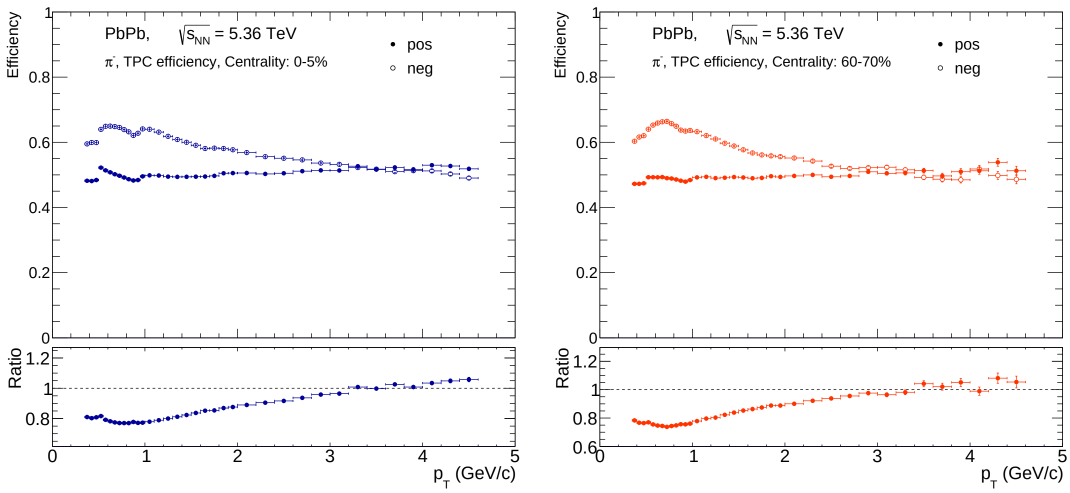

(A) Comparison of π^+ and π^- tracking efficiencies in the most central (0-5%) Pb-Pb collisions.

(B) Same comparison for the most peripheral (60-70%) collisions.

FIGURE 6.16: Charge-symmetric comparison of TPC tracking efficiencies for pions in central (0-5%) and peripheral (60-70%) Pb-Pb collisions.

The tracking efficiency of the TPC for π^+ and π^- as a function of p_T and centrality is shown in Fig. 6.15, while Fig. 6.16 presents a direct comparison between positive and negative pions for the most central (0-5%) and the most peripheral (60-70%) Pb-Pb collisions at $\sqrt{s_{NN}} = 5.36$ TeV.

For both π^+ and π^-, the efficiency increases rapidly at low p_T ($p_T < 0.5$ GeV/c), where the combined effects of curvature, multiple scattering, and energy loss limit the number of TPC clusters used for reconstruction. Beyond $p_T \approx 0.6$ GeV/c, the efficiency reaches a broad plateau around 50-60%, consistent across all centralities. The small decrease at very high p_{T} (> 3.5 GeV/c) is primarily due to the increasing fraction of tracks crossing the TPC at shallow angles, which slightly reduces cluster collection efficiency.

A mild centrality dependence is observed: in the most central (0-5%) collisions, where the track density and space-charge distortions are largest, the overall efficiency is reduced by $\sim$5% compared to peripheral collisions. This is an expected behavior since higher multiplicities in central Pb-Pb events increase the probability of overlapping clusters and track merging in the TPC, particularly for low-momentum pions. In contrast, peripheral collisions exhibit slightly higher and more uniform efficiencies across the entire p_{T} range, reflecting the lower occupancy and reduced diffusion distortions.

The charge-separated comparison in Fig. 6.16 reveals a clear difference between the reconstruction efficiencies of π^+ and π^-, particularly at low p_{T}. In the most central 0-5% collisions (Fig. 6.16a), the efficiency for positive pions is lower by up to 10-20% compared to that for negative pions in the region $p_{\mathrm{T}} < 3$ GeV/c. While some level of charge asymmetry is expected due to the combined effects of the TPC electric and magnetic fields, which bend positive and negative tracks in opposite directions, the magnitude observed here exceeds the typical few-percent level expected purely from geometrical and field-configuration effects and further investiagtion into this is required.

At higher p_{T} (> 3 GeV/c), where curvature effects become negligible and tracks traverse the detector in more similar trajectories, the π^+ and π^- efficiencies converge within a few percent, indicating that the charge-dependent effect is confined primarily to the low-momentum regime. In peripheral events (Fig. 6.16b), the asymmetry is significantly reduced, and the efficiency ratio approaches unity across all momenta, consistent with lower space-charge distortions and reduced track density.

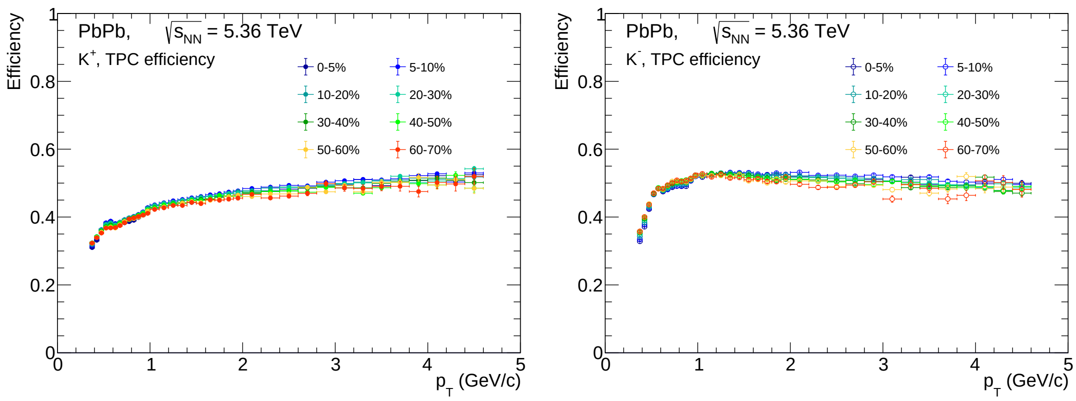

(A) TPC tracking efficiency for K^+ as a function of p_{T} across centrality intervals.

(B) Same as (a) but for K^-.

FIGURE 6.17: TPC tracking efficiencies for K^+ and K^- in Pb-Pb collisions at $\sqrt{s_{\mathrm{NN}}} = 5.36$ TeV, obtained from full Monte Carlo simulations.

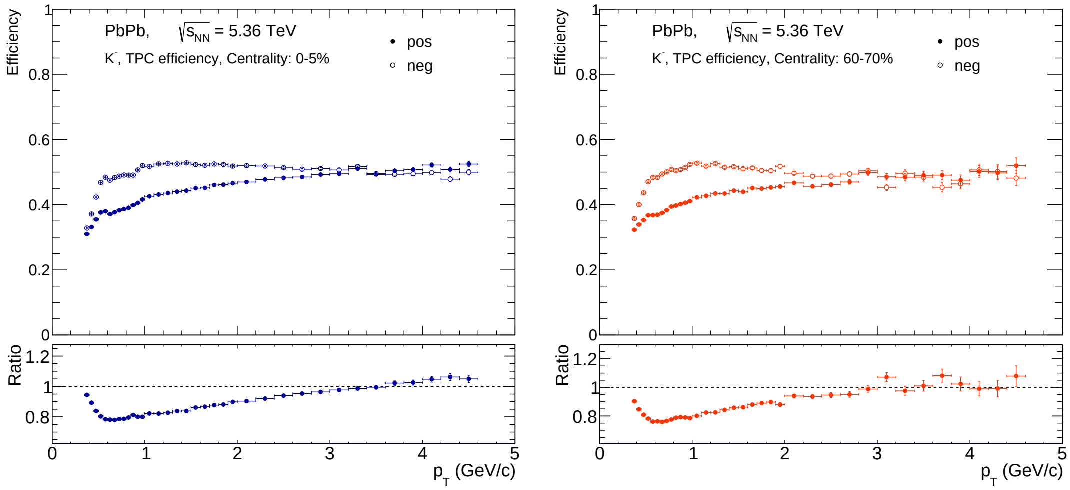

(A) Comparison of K^+ and K^- tracking efficiencies in the most central (0-5%) Pb-Pb collisions.

(B) Same comparison for the most peripheral (60-70%) collisions.

FIGURE 6.18: Charge-symmetric comparison of TPC tracking efficiencies for kaons in central (0-5%) and peripheral (60-70%) Pb-Pb collisions.

The TPC tracking efficiencies for $K^{\pm}$, shown in Figs. 6.17a-6.17b, exhibit a gradual rise with p_T and a plateau around $\epsilon_{TPC} \simeq$ 0.45-0.55 at intermediate and high momenta. The efficiency loss below $p_T \sim 0.5$ GeV/c arises from strong curvature, increased energy loss, and track merging in high-multiplicity environments. The plateau reflects the intrinsic geometrical acceptance and track-quality selections. Efficiency variations across centralities are within a few percent, with slightly lower values in the most central collisions due to space-charge effects and higher occupancy.

A clear charge asymmetry is observed between K^+ and K^-, particularly at low p_T, where K^+ efficiencies are up to 15-23% lower than those for K^- (Figs. 6.18a and 6.18b). While small differences are expected from the combined influence of the TPC electric and magnetic fields, which bend positive and negative tracks into slightly different detector regions, the large asymmetry needs further investigation.

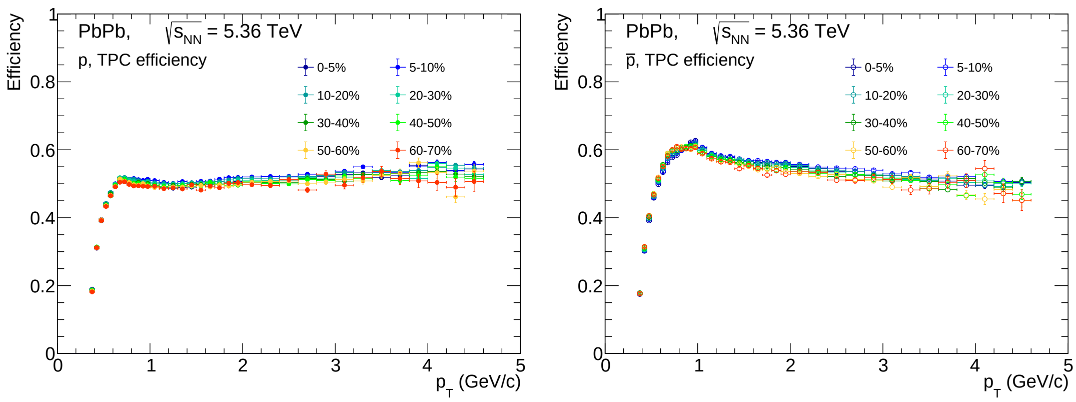

(A) TPC tracking efficiency for p as a function of p_T across centrality intervals.

(B) Same as (a) but for $\bar{p}$.

FIGURE 6.19: TPC tracking efficiencies for p and $\bar{p}$ in Pb-Pb collisions at $\sqrt{s_{NN}} = 5.36$ TeV, obtained from full Monte Carlo simulations.

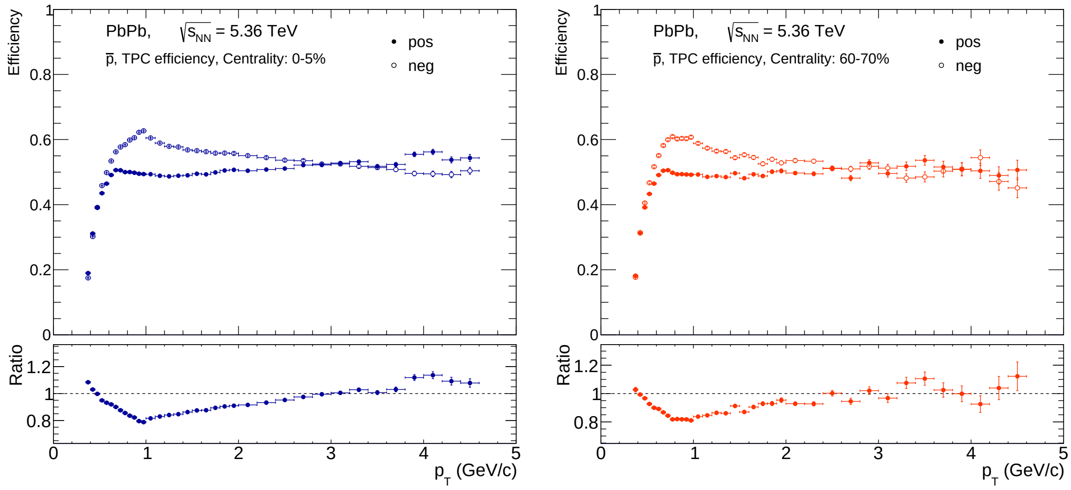

(A) Comparison of p and $\bar{p}$ tracking efficiencies in the most central (0-5%) Pb-Pb collisions.

(B) Same comparison for the most peripheral (60-70%) collisions.

FIGURE 6.20: Charge-symmetric comparison of TPC tracking efficiencies for protons in central (0-5%) and peripheral (60-70%) Pb-Pb collisions.

For both p-species(6.19a and 6.19b), the overall efficiency rises steeply at low transverse momentum ($p_T < 0.6$ GeV$/c$), reflecting the limited acceptance and the increased curvature and multiple scattering of low-rigidity tracks in the magnetic field. Above $p_T \approx 1.0$ GeV$/c$, the efficiency reaches a broad plateau of $\epsilon_{TPC} \approx 0.50$-$0.55$, where it remains nearly constant up to the highest measured momenta. This plateau corresponds to the intrinsic geometrical acceptance and to the efficiency of pattern recognition and track quality selection (requiring a minimum number of crossed pad rows and constraints on the χ^2 per cluster). The centrality dependence is modest, with the most central events (0-5%) showing slightly lower efficiency compared to peripheral collisions (60-70%), due to increased cluster overlap and the influence of space-charge distortions under high track density.

A more detailed comparison of positive and negative charges is provided in Figs. 6.20a and 6.20b. These ratios reveal a distinct charge-asymmetric behavior: the reconstruction efficiency for antiprotons ($\bar{p}$) is systematically lower than that for protons, particularly at low p_T, where the difference reaches up to 10–15%. The asymmetry gradually diminishes with increasing momentum, approaching unity above $p_T \approx 2.5$-3.0 GeV$/c$. This trend is physically well understood and arises from a combination of effects.

In principle, at low momentum, antiprotons undergo a larger rate of inelastic and annihilation processes when traversing the beampipe, ITS, and TPC gas volume. These processes lead to irrecoverable track losses, resulting in a systematically reduced reconstruction probability for $\bar{p}$. In contrast, protons experience mainly elastic or low-energy hadronic interactions, which do not prevent reconstruction in most cases. Additionally, the opposite curvature of positive and negative tracks in the combined electric and magnetic fields of the TPC causes them to probe slightly different regions of the detector. Local variations in drift velocity and field inhomogeneities can therefore introduce small charge-dependent reconstruction biases, particularly under high space-charge conditions in central events. However, the opposite trend is observed in Fig. 6.20, which something purely geometric effects wouldn't predict.

This suggests that additional reconstruction-related or simulation-induced asymmetries persists.

At high p_T, the rigidity of the tracks minimizes both curvature-related differences and material interaction probabilities, leading to nearly identical efficiencies for protons and antiprotons. The residual differences at the few-percent level are within statistical and systematic uncertainties of the Monte Carlo simulation and are propagated as a small charge-dependent systematic uncertainty on the efficiency correction.

Matching efficiency in the TOF

The **TOF efficiency** quantifies the probability that a primary charged particle produced within the detector acceptance is reconstructed, matched to a hit in the Time-Of-Flight (TOF) detector, and passes the corresponding selection criteria used in the analysis.

Unlike the TPC tracking efficiency, which reflects the standalone performance of the tracking system, the TOF efficiency incorporates the combined effects of particle reconstruction, detector acceptance, and the geometrical and timing response of the TOF array. It is determined from Monte Carlo simulations as the ratio:

$$\varepsilon_{\text{TOF}}(p_T) = \frac{N_{\text{TOF}}^{\text{MC}}(\text{primary, MC PID}, |y| < 0.5, |\eta| < 0.8)}{N_{\text{gen}}^{\text{MC}}(\text{primary, MC PID}, |y| < 0.5)}, \tag{6.15}$$

where:

- $N_{\text{gen}}^{\text{MC}}$ is the number of primary particles of the considered species generated within the kinematic acceptance;
- $N_{\text{TOF}}^{\text{MC}}$ is the subset of those that are reconstructed and produce a valid hit in the TOF detector;
- both numerator and denominator are evaluated with the same kinematic and acceptance cuts ($|y| < 0.5$, $|\eta| < 0.8$), and the true MC particle identity is enforced.

This efficiency therefore reflects the overall probability that a particle traverses the full detector, reaches the TOF wall, and is successfully associated with a TOF hit. Only primary particles are considered, since the secondary contamination is removed via the data-driven procedure discussed in Sec. 6.3.

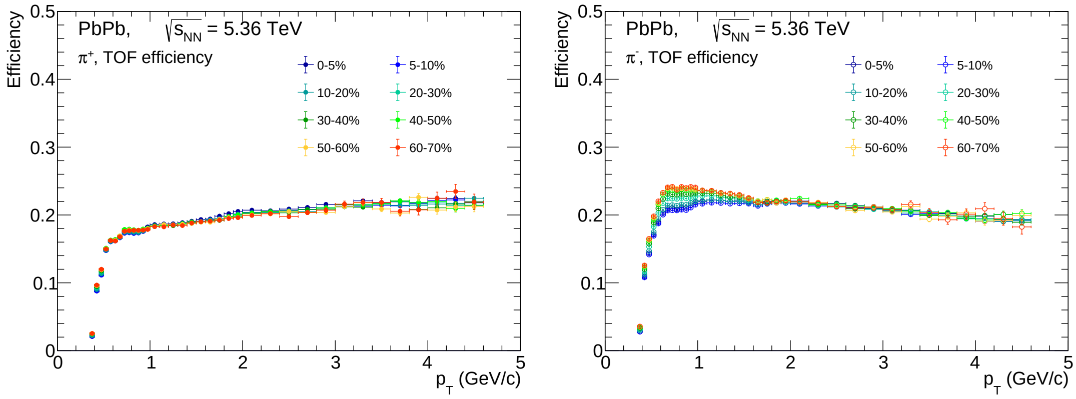

(A) TOF efficiency for π^+ as a function of p_T across centrality intervals.

(B) Same as (a) but for π^-.

FIGURE 6.21: TOF efficiencies for π^+ and π^- in Pb-Pb collisions at $\sqrt{s_{NN}} = 5.36$ TeV, obtained from full Monte Carlo simulations.

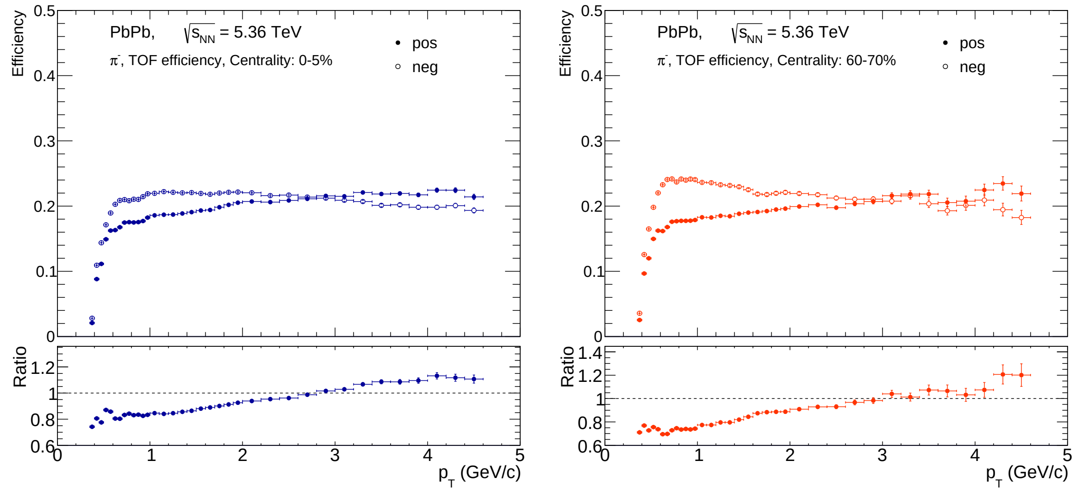

(A) Comparison of π^+ and π^- TOF efficiencies in the most central (0-5%) collisions.

(B) Same comparison for the most peripheral (60-70%) collisions.

FIGURE 6.22: Charge-symmetric comparison of TOF efficiencies for pions in central (0-5%) and peripheral (60-70%) Pb-Pb collisions.

The TOF efficiencies for $\pi^{\pm}$, $K^{\pm}$, and $p(\bar{p})$ obtained from Monte Carlo simulations are presented in Figs. 6.21-6.25, together with the charge-comparison ratios for the most central (0-5%) and the most peripheral (60-70%) Pb-Pb collisions at $\sqrt{s_{NN}} = 5.36$ TeV.

For all particle species, the efficiency exhibits a characteristic steep rise at low transverse momentum, followed by a broad plateau that extends up to the highest measured p_T. The initial increase corresponds to the momentum threshold required for the particles to reach the TOF detector, located at a radial distance of approximately 3.7 m. At very low p_T, particles are strongly curved by the magnetic field or, in the case of kaons, decay in flight before reaching the TOF wall, resulting in a reduced efficiency.

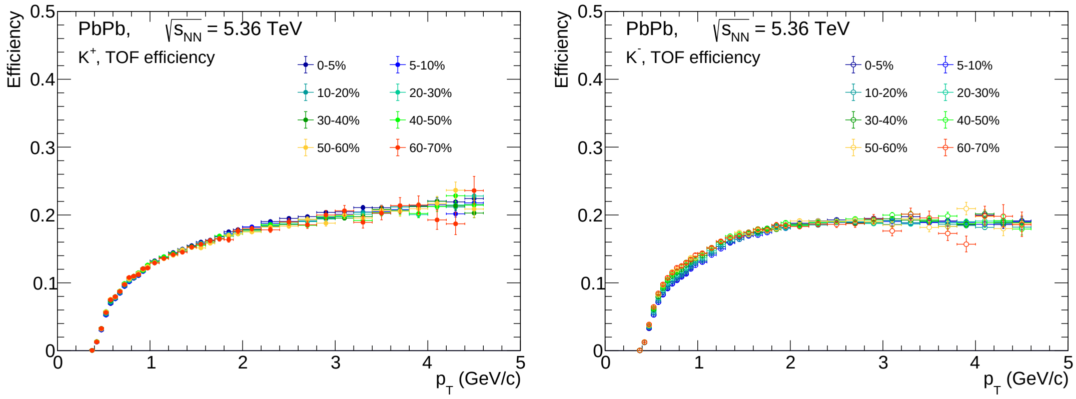

(A) TOF efficiency for K^+ across centrality intervals.

(B) Same as (a) but for K^-.

FIGURE 6.23: TOF efficiencies for K^+ and K^- in Pb-Pb collisions at $\sqrt{s_{\text{NN}}} = 5.36$ TeV.

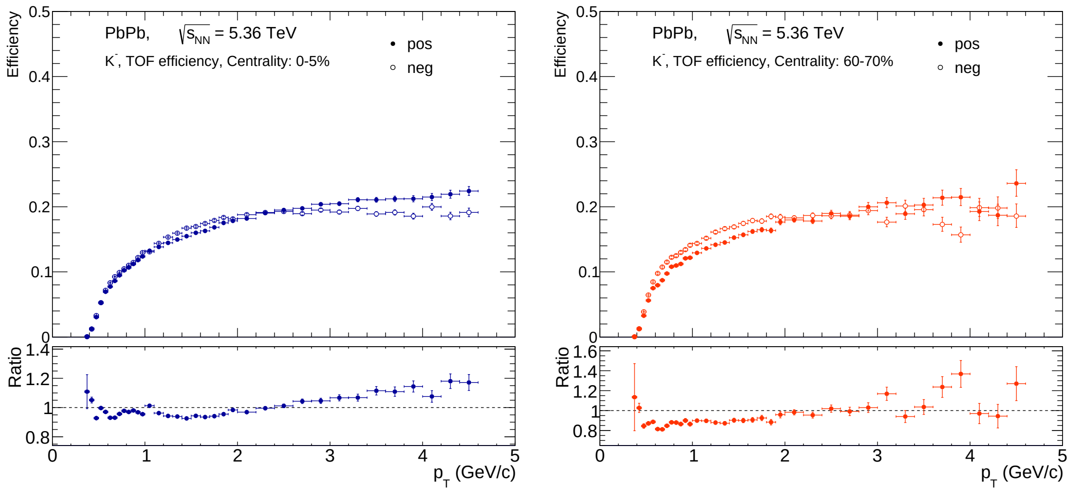

(A) Comparison of K^+ and K^- TOF efficiencies in the most central (0-5%) collisions.

(B) Same comparison for the most peripheral (60-70%) collisions.

FIGURE 6.24: Charge-symmetric comparison of TOF efficiencies for kaons in central (0-5%) and peripheral (60-70%) Pb-Pb collisions.

For kaons (Fig. 6.23), the efficiency follows a similar pattern to that of pions, reaching a stable plateau above $p_{\text{T}} \approx 1$ GeV/c. At lower momenta, the efficiency drops steeply because many kaons decay in flight ($K^{\pm} \to \mu^{\pm}\nu_{\mu}$), preventing them from reaching the TOF wall. The efficiency plateaus at $\epsilon_{\text{TOF}} \simeq 0.3$ depending on centrality. The small charge asymmetry observed at low p_{T} arises from the combined influence of the magnetic field and decay kinematics but remains within the assigned systematic uncertainty.

For protons and antiprotons (Figs. 6.25, 6.26a, and 6.26b), the TOF efficiency reaches slightly higher plateau values of $\epsilon_{\text{TOF}} \approx 0.4$, reflecting the larger rigidity and reduced multiple scattering of baryons. A clear charge asymmetry is visible at low p_{T}, where the antiproton efficiency is lower than that of protons by 10-15%. This difference originates from the higher annihilation and inelastic interaction cross-sections of $\bar{p}$ in the detector material, leading to an increased probability of absorption before reaching the TOF. At higher transverse momenta, the asymmetry gradually disappears, and both efficiencies converge within uncertainties.

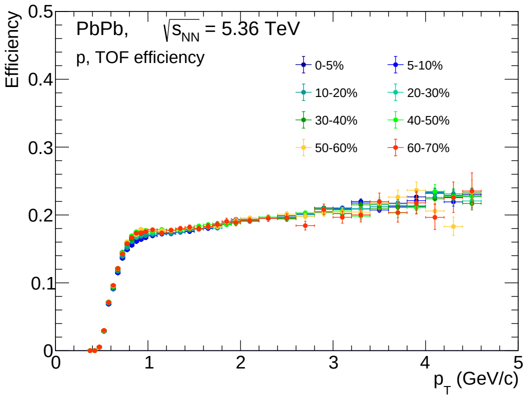

(A) TOF efficiency for p across centrality intervals.

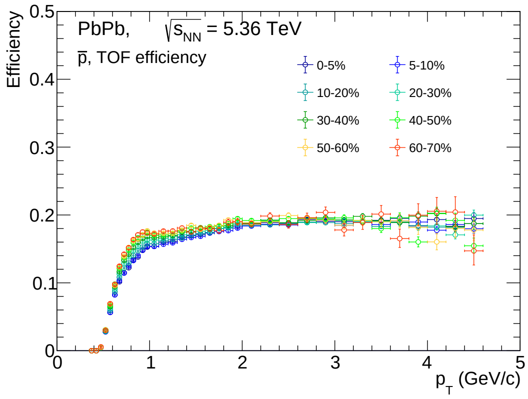

(B) Same as (a) but for $\bar{p}$.

FIGURE 6.25: TOF efficiencies for p and $\bar{p}$ in Pb-Pb collisions at $\sqrt{s_{\mathrm{NN}}} = 5.36$ TeV.

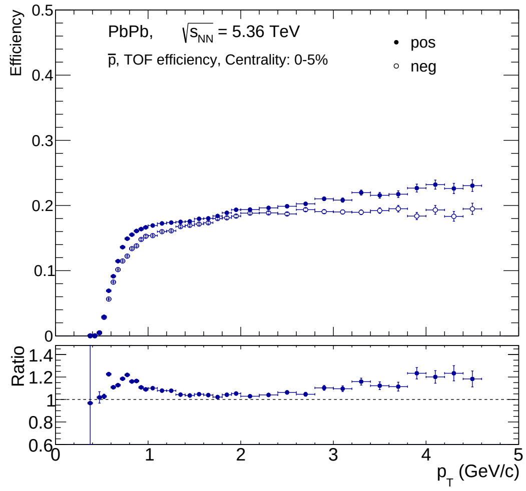

(A) Comparison of p and $\bar{p}$ TOF efficiencies in the most central (0-5%) collisions.

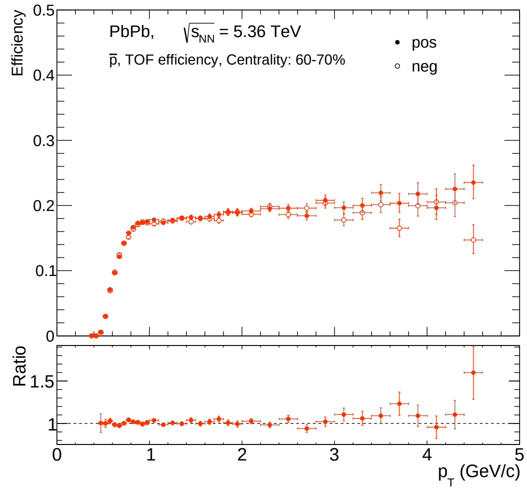

(B) Same comparison for the most peripheral (60-70%) collisions.

FIGURE 6.26: Charge-symmetric comparison of TOF efficiencies for protons in central (0-5%) and peripheral (60-70%) Pb-Pb collisions.

6.2.2 Efficiency smoothing and parametrization

The raw efficiency points obtained from the MC simulations exhibit bin-to-bin fluctuations, particularly at higher p_{T}, where statistical precision decreases due to the rapidly falling particle yields. Although these variations are purely statistical in origin, they can introduce artificial structure into the corrected spectra when directly applied in the yield normalization. To mitigate this effect and to ensure a stable, physically smooth efficiency correction, analytical fits are employed to parametrize the p_{T}-dependence of the reconstruction and matching efficiencies.

For each particle species and charge, the efficiency distributions are fitted with empirical functions that accurately reproduce the rise at low momentum and the plateau behavior at intermediate and high p_{T}. Two functional forms were tested: an error-function–based sigmoid,

$$\epsilon(p_{\mathrm{T}}) = p_0 + p_1 \frac{1}{2}\left[1 + \mathrm{erf}\left(\frac{p_{\mathrm{T}} - p_2}{p_3}\right)\right],$$

and a generalized logistic form with an optional linear tail,

$$\epsilon(p_{\mathrm{T}}) = a + \frac{b}{1 + \exp[-(p_{\mathrm{T}} - c)/d]} + e\, p_{\mathrm{T}}.$$

Both describe the efficiency evolution adequately, with differences in the tail region above 1.5 GeV/c captured by the additional linear term in the latter. The best function is selected based on the minimum root-mean-square error (RMSE) and χ^2/ndf values evaluated in the high-p_{T} interval, ensuring that the asymptotic region remains well constrained.

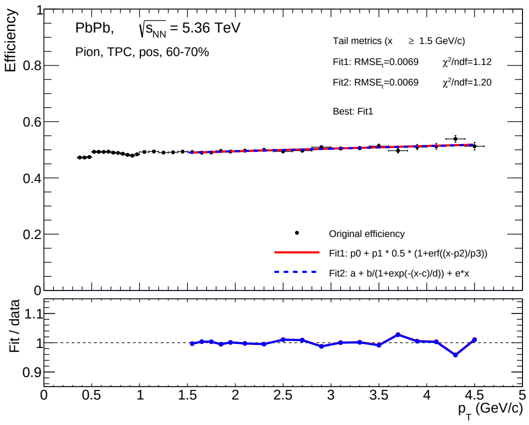

(A) π^+ efficiency in the TPC for 60-70% centrality

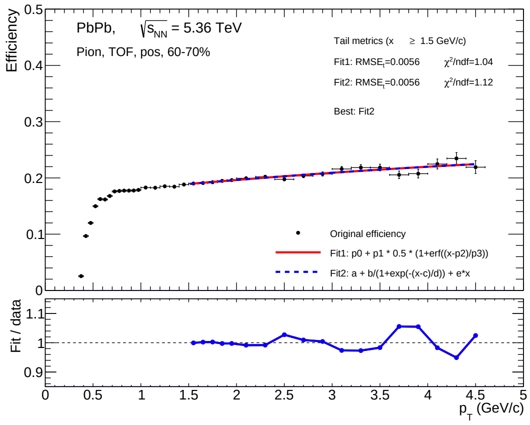

(B) π^+ efficiency in the TOF for 60-70% centrality

FIGURE 6.27: Fitted efficiency curves for pions in Pb-Pb collisions at $\sqrt{s_{\mathrm{NN}}} = 5.36$ TeV. The markers represent the Monte Carlo efficiency points, while the solid (red) and dashed (blue) lines show the two analytical parametrizations described in the text. The lower panels display the fit-to-data ratios.

Figures 6.27a-6.29b summarize representative examples of the fit-based smoothing procedure applied to the TPC and TOF efficiencies for pions, kaons, and (anti) protons in the 60-70% centrality class. For each particle species and charge, the upper panels show the efficiency points obtained from Monte Carlo simulations, together with the two analytical parametrizations (Fit 1 and Fit 2), while the lower panels display the fit/data ratios.

Both functions, the error-function sigmoid (Fit 1) and the generalized logistic form with a small linear tail (Fit 2), capture the underlying efficiency trends across the full p_{T} range, with typical deviations below 3%. The fitted curves provide a physically motivated, continuous description of the detector performance and effectively suppress the residual statistical fluctuations visible in the raw efficiency points at high p_{T}.

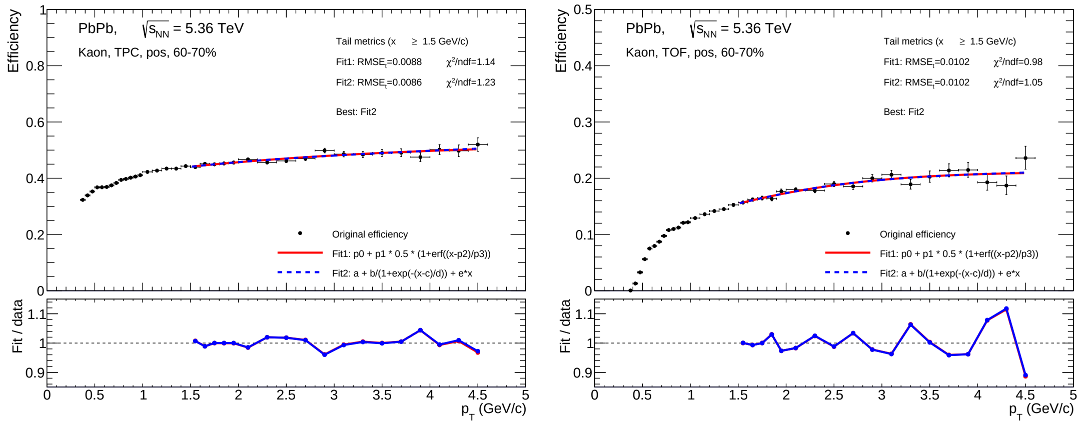

(A) K^+ efficiency in the TPC for 60-70% centrality (B) K^+ efficiency in the TOF for 60-70% centrality

FIGURE 6.28: Fitted efficiency curves for kaons in Pb-Pb collisions at $\sqrt{s_{\rm NN}} = 5.36$ TeV. The markers represent the Monte Carlo efficiency points, while the solid (red) and dashed (blue) lines show the two analytical parametrizations described in the text. The lower panels display the fit-to-data ratios.

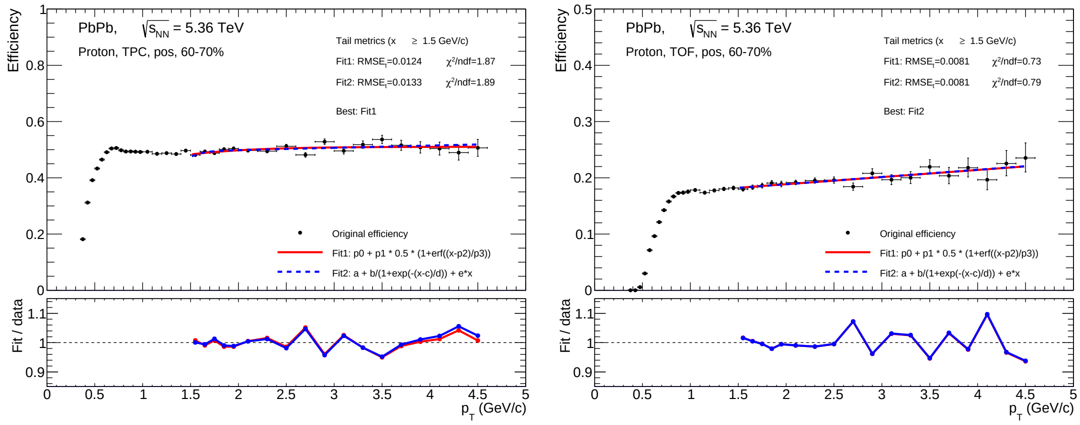

(A) p efficiency in the TPC for 60-70% centrality (B) p efficiency in the TOF for 60-70% centrality

FIGURE 6.29: Fitted efficiency curves for protons in Pb-Pb collisions at $\sqrt{s_{\rm NN}} = 5.36$ TeV. The markers represent the Monte Carlo efficiency points, while the solid (red) and dashed (blue) lines show the two analytical parametrizations described in the text. The lower panels display the fit-to-data ratios.

For **pions**, shown in Figs. 6.27a and 6.27b, both TPC and TOF efficiencies display a remarkably flat dependence beyond $p_{\rm T} \approx 1.5$ GeV/c. The fit residuals confirm a consistent description to within 2%, with Fit 1 slightly outperforming the general logistic form for the TPC case, owing to its flexible tail term. For the TOF efficiency, which exhibits stronger statistical oscillations at high $p_{\rm T}$, the general logistic function (Fit 2) yields a more stable asymptotic behaviour and the lowest χ^2/ndf, thereby providing the best overall representation.

In the case of **kaons** (Figs. 6.28a and 6.28b), the efficiencies follow a characteristic turn-on shape below $p_{\rm T} \approx 0.6$ GeV/c and reach a plateau of $\epsilon_{\rm TPC} \approx 0.55$ and $\epsilon_{\rm TOF} \approx 0.20$. The TPC efficiencies are very smooth across the full range and are well described by the logistic function (Fit 2), which accommodates the slow saturation at high $p_{\rm T}$. The TOF efficiencies, in contrast, show moderate bin-to-bin scatter due to limited statistics, and the two models perform nearly indistinguishably, with Fit 2 providing the slightly better RMSE value. The fit/data ratios remain consistent with unity, validating the reliability of the parametric description even in the sparsely populated high-p_T region.

The **proton** efficiencies (Figs. 6.29a and 6.29b) exhibit the typical baryon pattern, characterized by a broader plateau and a gentle positive slope at intermediate p_T. The TPC efficiency shows negligible centrality dependence in this regime, and the sigmoid function (Fit 1) accurately reproduces the measured points with residuals below 5%. For the TOF efficiency, which is intrinsically lower and affected by larger statistical fluctuations, the logistic form (Fit 2) provides a slightly improved stability in the extrapolation domain above 3 GeV/c. In all cases, the RMSE and χ^2/ndf values reported in the figures demonstrate that the fits are well within the statistical precision of the simulation.

Across all particle species, the choice between the two functional forms has no impact on the corrected yields beyond the assigned systematic uncertainty. The fitted efficiencies are used as smooth, continuous inputs to the final correction procedure, ensuring numerical stability when interpolating between adjacent p_T bins or combining TPC and TOF responses. In addition, the analytical parametrizations facilitate the evaluation of correlated systematic variations by allowing controlled shifts of the fit parameters within their covariance matrix.

In summary, the applied fits yield physically consistent and statistically robust efficiency parametrizations for all hadron species. The resulting smooth functions eliminate unphysical bin-level noise from MC fluctuations, enable seamless integration with particle identification corrections, and ensure that the derived spectra reflect genuine detector performance rather than statistical artefacts.

6.2.3 Feed-down and fraction of primary particles

In addition to the acceptance and tracking efficiencies, the correction of raw yields requires the estimation of the fraction of primary particles in each transverse momentum interval. This step removes contributions from secondary particles originating from two dominant sources: weak decays of long-lived particles such as $\Lambda \rightarrow p\pi^-$ and $K^0_S \rightarrow \pi^+\pi^-$, and hadronic interactions of particles with the detector material, resulting in secondary production or, in the case of antibaryons, annihilation processes. These backgrounds distort the measured transverse momentum spectra and, if not properly corrected, can bias the extracted particle yields and ratios.

The separation of primary and non-primary tracks is achieved by exploiting the distribution of the distance of closest approach to the reconstructed primary vertex in the transverse plane, DCA_{xy}. Primaries are characterized by a narrow peak centered around zero, reflecting the detector's intrinsic spatial resolution, whereas secondaries populate the broad non-Gaussian tails of the distribution. The characteristic shape and width of each component are obtained from full Monte Carlo (MC) simulations, where the origin of each reconstructed particle is unambiguously known.

The data distributions are then decomposed using the `Fraction Fitter` framework, which performs a binned maximum-likelihood fit of the measured DCA_{xy} spectrum with a linear combination of the three MC-derived templates:

$$N_{\text{data}}(DCA_{xy}) = f_{\text{prim}}\, T_{\text{prim}}(DCA_{xy}) + f_{\text{sec}}\, T_{\text{sec}}(DCA_{xy}) + f_{\text{mat}}\, T_{\text{mat}}(DCA_{xy}),$$

subject to the normalization constraint $f_{\text{prim}} + f_{\text{sec}} + f_{\text{mat}} = 1$. Here, $T_i(DCA_{xy})$ denotes the normalized shape of component i in MC, and f_i the corresponding fitted fraction in data. An illustrative example for positive pions is shown in Fig. 6.30a, where the measured DCA_{xy} distribution (black points) is compared to the MC templates for primary (blue), secondary (red), and material (green) contributions. The resulting total fit, shown in Fig. 6.30b, reproduces the data across several orders of magnitude, confirming that the simulation accurately captures both the detector resolution and the material budget.

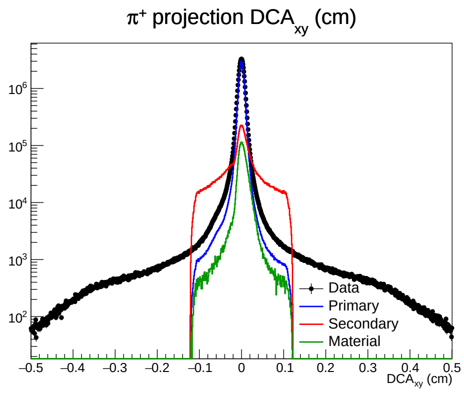

(A) Template inputs. Measured DCA_{xy} distribution (black) together with MC templates for primaries (blue), secondaries from weak decays (red), and material interactions (green).

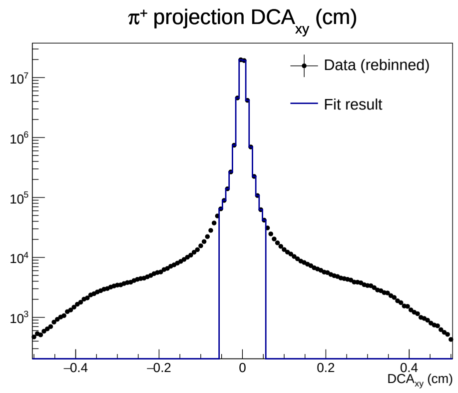

(B) Fit result. Fraction Fitter decomposition of the rebinned data, showing the total model (blue) over several orders of magnitude.

FIGURE 6.30: Illustration of the primary/secondary separation using the DCA_{xy} method (example: π^+ at low p_{T}). (a) Inputs to the Fraction Fitter: data and MC-derived templates. (b) Result of the binned maximum-likelihood fit. The fitted primary fraction $f_{\text{prim}}(p_{\text{T}})$ obtained per bin is later used to correct the raw yields.

The fitted coefficient $f_{\text{prim}}(p_{\text{T}})$ is subsequently used to correct the raw spectra by scaling the per-bin yields:

$$N_{\text{corr}}(p_{\text{T}}) = N_{\text{raw}}(p_{\text{T}})\, f_{\text{prim}}(p_{\text{T}}),$$

thereby retaining only the fraction of tracks originating from the primary vertex. The primary particle fraction, extracted via the template fits to the DCA_{xy} distributions, exhibits a mild dependence on collision centrality and particle species, reflecting the varying background conditions and detector occupancy across event classes. Figures 6.31a-6.31d summarize the primary fractions for positive and negative pions and protons, obtained independently for the TPC and TOF analyses.

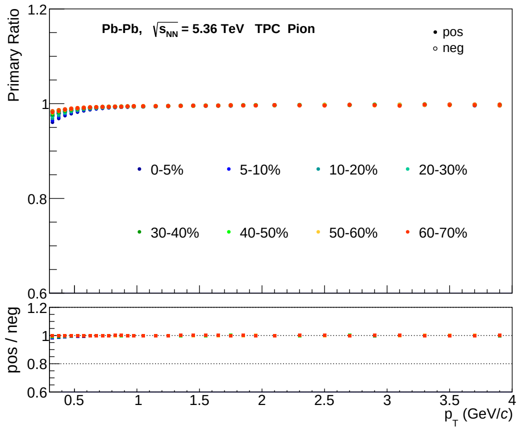

(A) π: TPC primary ratio ($f^+_{\text{prim}}/f^-_{\text{prim}}$) vs p_T, colored by centrality. The bottom panel shows pos/neg.

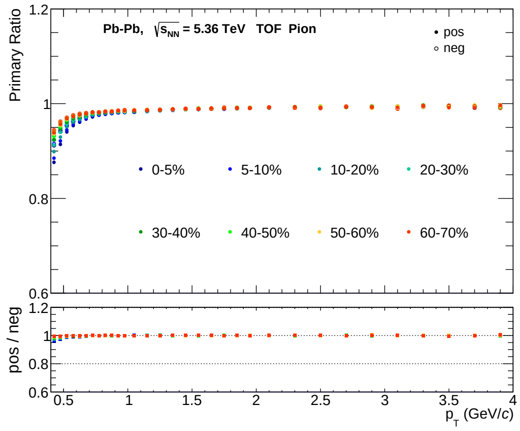

(B) π: TOF primary ratio, same conventions as (a).

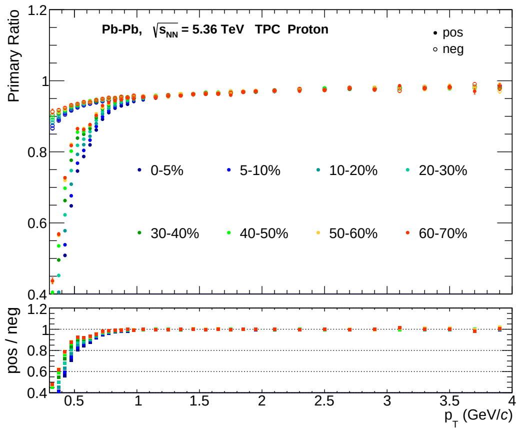

(C) p: TPC primary ratio ($f^+_{\text{prim}}/f^-_{\text{prim}}$) vs p_T, colored by centrality.

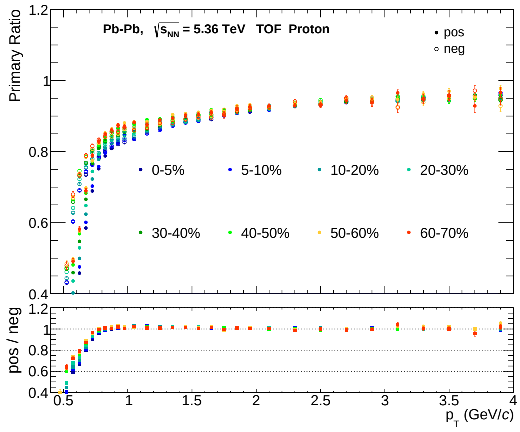

(D) p: TOF primary ratio, same conventions as (c).

FIGURE 6.31: Charge-asymmetric primary fractions for pions and protons, shown for TPC (left column) and TOF (right column). Points indicate the per-p_T primary fraction ratio for positive over negative charges, with different centralities in distinct colors.

At a general level, the fraction of primaries is highest in peripheral collisions, where the overall track density and secondary-particle production are reduced. Toward central events, the increased particle multiplicity and larger material traversal probability lead to a small decrease in f_{prim}, particularly at low transverse momentum. This trend is most pronounced for baryons, which are more susceptible to secondary contamination from weak hyperon decays and, in the case of antiprotons, to annihilation in the detector material. For mesons (pions and kaons), the effect remains at the level of a few percent and is largely independent of centrality, reflecting the excellent vertexing and tracking performance of the TPC even in the highest multiplicity environments.

The lower panels of Figs. 6.31a-6.31d show the ratio of primary fractions between positive and negative particles, $f^+_{\text{prim}}/f^-_{\text{prim}}$, as a function of p_T and centrality. For pions, this ratio remains unity within statistical precision over the full kinematic range and across all centralities, confirming the charge-symmetric response of the tracking system and the negligible impact of secondary and material interactions. This behaviour is consistent with expectations, since the pion contamination from weak decays (e.g. $K_S^0 \to \pi^+\pi^-$) is symmetric in charge and efficiently removed by the DCA_{xy} selection.

In contrast, the proton and antiproton ratios exhibit a modest but systematic departure from unity, most visible below $p_\mathrm{T} \lesssim 1$ GeV/c. This asymmetry originates from two combined effects:

- a larger feed-down contribution to the proton sample from Λ decays, which increases the apparent primary fraction for p relative to $\bar{p}$
- the higher inelastic interaction and annihilation cross-section of antiprotons in the detector material, which leads to a slight suppression of their reconstructed yield.

Both effects are more pronounced in central events, where the material path length and secondary particle density are largest, but diminish rapidly with increasing p_T. Beyond $p_\mathrm{T} \approx 2$ GeV/c, the positive and negative baryon fractions converge, indicating that both species experience similar reconstruction efficiencies and negligible secondary contamination at higher momenta.

For kaons, no significant secondary contribution is observed, as their weak-decay channels involve short-lived resonances (e.g. $\phi \to K^+K^-$) that decay essentially at the primary vertex. Consequently, the primary ratio $f_\mathrm{prim}^{K^+}/f_\mathrm{prim}^{K^-}$ is unity by construction, and no correction or centrality dependence is introduced for this species.

Overall, the smooth and charge-symmetric behavior of the primary fractions across centralities confirms the robustness of the DCA_{xy}-based decomposition and the validity of the template fitting procedure. The residual deviations observed for baryons at low p_T are well understood in terms of hadronic interaction cross-sections and are treated as a systematic uncertainty in the final spectra.

6.2.4 Spectra correction

The raw particle yields obtained in the previous sections represent an intermediate experimental quantity. Although, they encode the species-separated particle counts extracted from the PID probability distributions, they still carry the imprint of detector limitations. In particular, reconstruction inefficiencies, geometric acceptance, TOF matching losses, and contamination from weak-decay secondaries all bias the raw spectra toward smaller values and distort their centrality evolution. To enable a quantitative comparison with theoretical models, other experiments, and global systematics, the raw spectra must therefore be extracted into the true per-event yields of *primary* particles at midrapidity.

This is achieved through a two-step correction procedure applied to each p_T bin individually. First, the spectra are divided by the reconstruction efficiency, $\varepsilon_\mathrm{tot}(p_\mathrm{T})$, which incorporates all detection- and selection-related losses. Secondly, they are corrected for the primary-particle purity, $f_\mathrm{primary}(p_\mathrm{T})$, obtained from the data-driven DCA analysis described in Sec. 6.2.3. The fully corrected yield is thus:

$$\frac{1}{N_\mathrm{ev}}\frac{\mathrm{d}^2N}{\mathrm{d}p_\mathrm{T}\mathrm{d}y} = \frac{N_\mathrm{raw}(p_\mathrm{T})}{\varepsilon_\mathrm{tot}(p_\mathrm{T}) \times f_\mathrm{primary}(p_\mathrm{T})}. \tag{6.16}$$

All corrections are computed separately for each particle species, charge state, centrality interval, and detector (TPC-based PID or TOF-based PID), ensuring full consistency across the entire analysis. The corrected spectra retain the detailed structure of the raw yields but are rescaled to represent physically meaningful primary-particle production rates.

The next part of this section presents the corrected spectra separately for the TPC-based and TOF-based PID approaches, highlighting their complementary kinematic coverage and demonstrating the consistency of the correction procedure across the two detectors.

Corrected yields using TPC-based PID

For particles identified using the TPC n_σ method, the dominant correction is the TPC reconstruction efficiency. In addition, the primary fractions for pions, kaons, and protons are obtained from DCA-template fits applied directly to TPC-selected tracks and therefore already incorporate detector- and centrality-dependent secondary production, and background from material interactions.

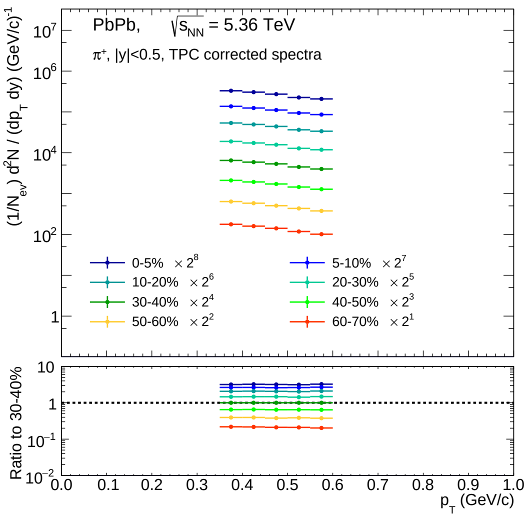

(A) π^+ efficiency- and purity-corrected yield as a function of p_T for all centrality intervals.

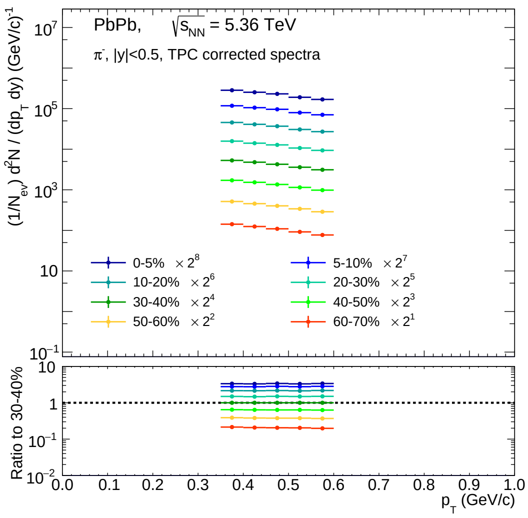

(B) π^- corrected spectra, same centrality classes as in (a).

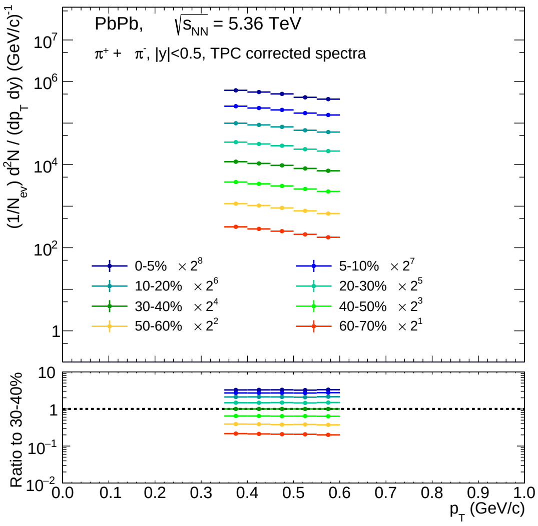

(C) Combined $(\pi^+ + \pi^-)$ corrected yield. Top panel: logarithmic scale; bottom: ratio to the 30-40% class.

FIGURE 6.32: TPC-based, efficiency- and primary-fraction-corrected pion yields in Pb-Pb collisions at $\sqrt{s_{NN}} = 5.36$ TeV.

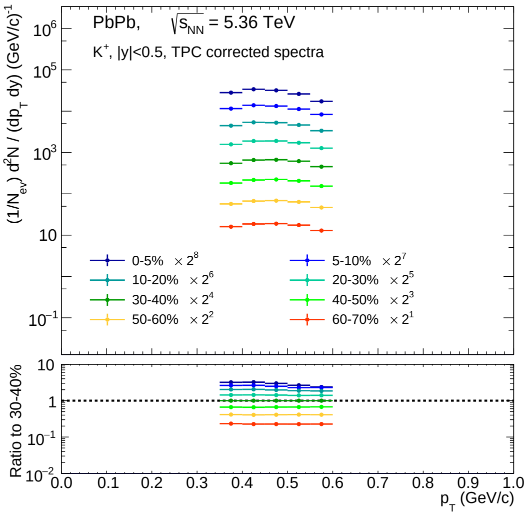

(A) K^+ efficiency- and purity-corrected yield as a function of p_{T} for all centrality intervals.

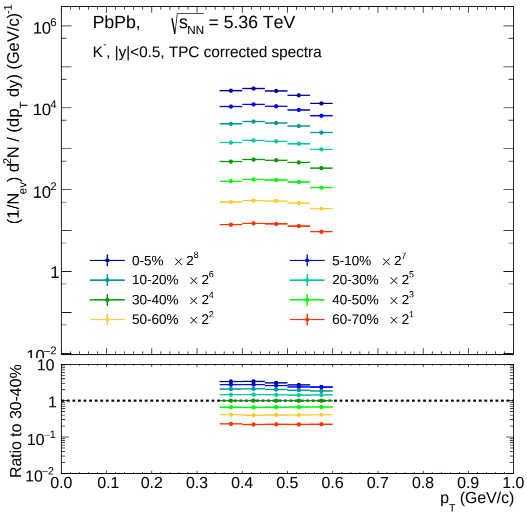

(B) K^- corrected spectra, same centrality classes as in (a).

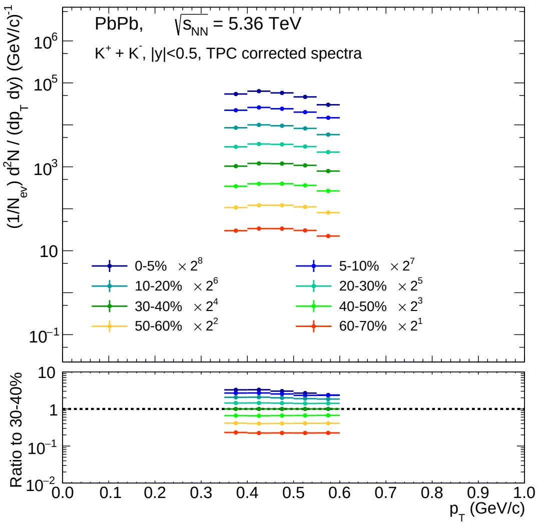

(C) Combined $(K^+ + K^-)$ corrected yield. Top panel: logarithmic scale; bottom: ratio to the 30-40% class.

FIGURE 6.33: TPC-based, efficiency- and primary-fraction-corrected pion yields in Pb-Pb collisions at $\sqrt{s_{\mathrm{NN}}} = 5.36$ TeV.

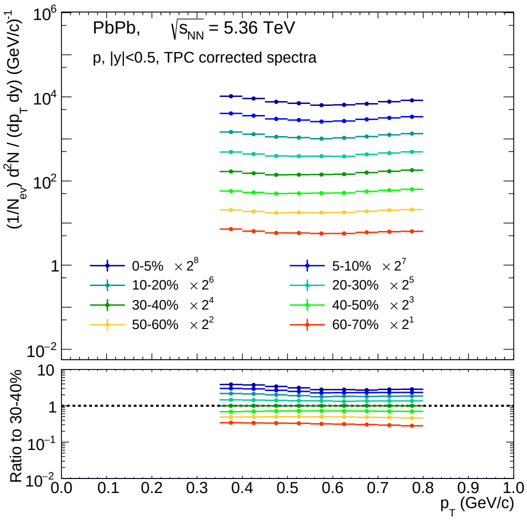

(A) p efficiency- and purity-corrected yield as a function of p_T for all centrality intervals.

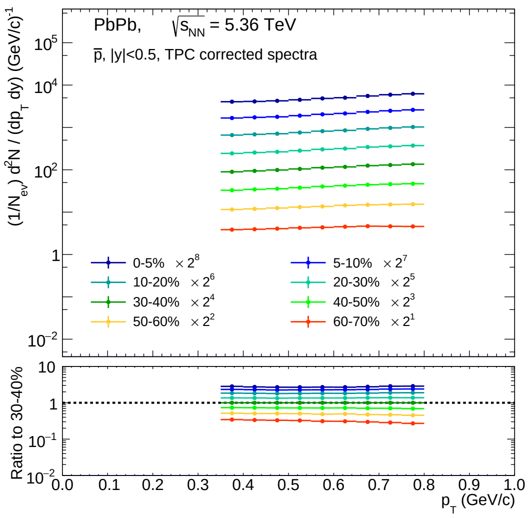

(B) $\bar{p}$ corrected spectra, same centrality classes as in (a).

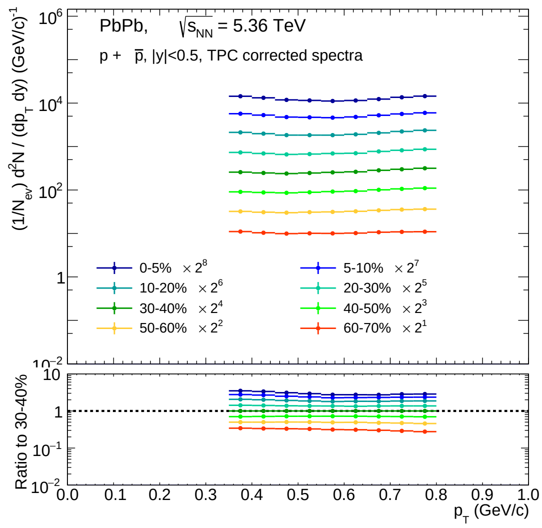

(C) Combined $(p + \bar{p})$ corrected yield. Top panel: logarithmic scale; bottom: ratio to the 30-40% class.

FIGURE 6.34: TPC-based, efficiency- and primary-fraction-corrected proton yields in Pb-Pb collisions at $\sqrt{s_{NN}} = 5.36$ TeV.

The corrected TPC spectra (Figs. 6.32, 6.34) closely follow the shapes of the raw distributions(Figs. 6.16, 6.18, 6.20), exhibiting the expected mass ordering at low p_T and a pronounced centrality dependence. Because TPC efficiencies reach plateaus of 50-60% at intermediate momenta, the overall correction is moderate and dominated by small species- and charge-dependent variations. In particular, the large efficiency asymmetries observed at low p_T for opposite charges are substantially suppressed after purity corrections are applied, leading to π^+ and π^- spectra that agree within uncertainties over the whole range. Similar behavior is found for kaons and protons, confirming that the efficiency and primary-fraction corrections properly compensate detector-level charge asymmetries.

Corrected yields using TOF-based PID

The corrected spectra obtained with TOF PID use the same formalism as in Eq. 6.16, but with the total efficiency now dominated by the TOF-matching efficiency rather than by TPC tracking alone. As shown in Sec. **??**, the TOF efficiency exhibits its own characteristic dependence on momentum and very slightly on centrality, with a pronounced low-p_{T} turn-on followed by a stable plateau around 18-22%. Charge-dependent differences in matching probability persist for all species, though at a reduced level compared to the TPC, and are fully corrected by applying the efficiency separately to positive and negative charges.

The corrected TOF spectra extend the accessible p_{T} range to significantly higher momenta than the TPC-based results, owing to the superior time-of-flight separation at large $\beta\gamma$. At low momentum, the TOF-corrected yields smoothly connect to the corresponding TPC-corrected spectra, ensuring continuity across both PID methods. At intermediate and high momenta, where the TOF dominates the PID capability, the spectra display a clean and stable behavior with minimal detector-induced distortions.

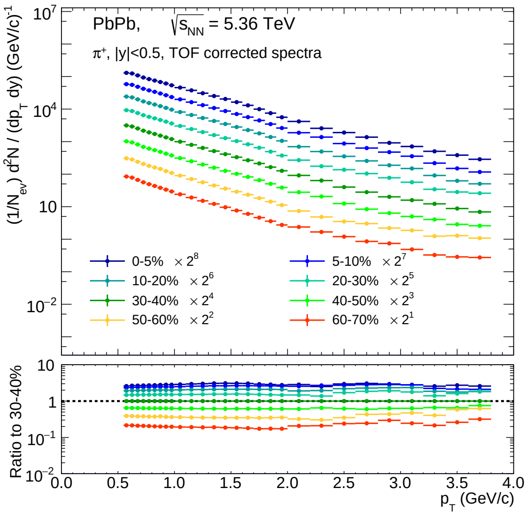

(A) π^+ efficiency- and purity-corrected yield as a function of p_{T} for all centrality intervals.

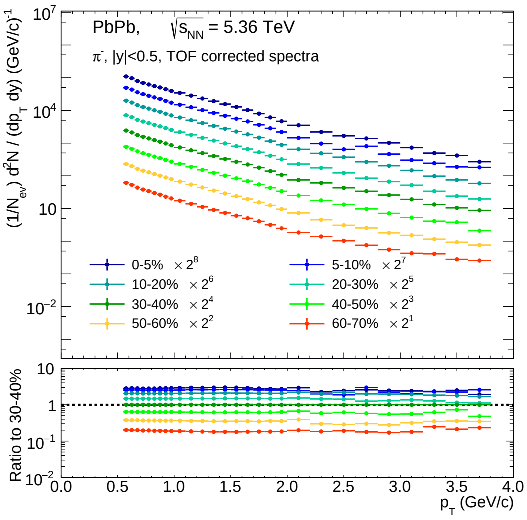

(B) π^- corrected spectra, same centrality classes as in (a).

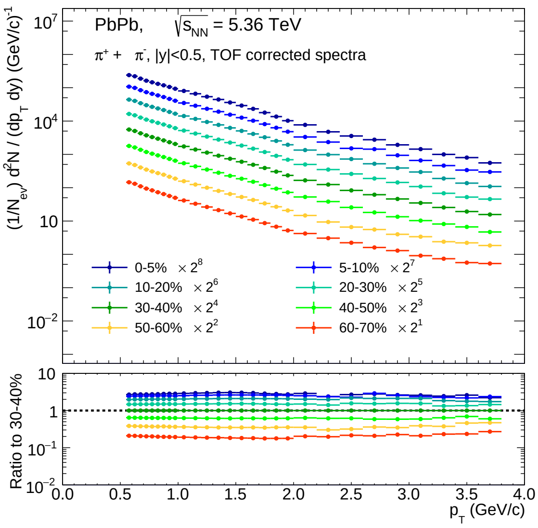

(C) Combined $(\pi^+ + \pi^-)$ corrected yield. Top panel: logarithmic scale; bottom: ratio to the 30-40% class.

FIGURE 6.35: TOF-based, efficiency- and primary-fraction-corrected pion yields in Pb-Pb collisions at $\sqrt{s_{\mathrm{NN}}} = 5.36$ TeV.

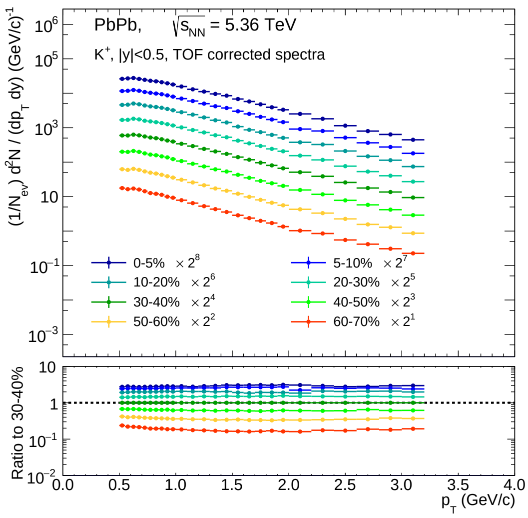

(A) K^+ efficiency- and purity-corrected yield as a function of p_T for all centrality intervals.

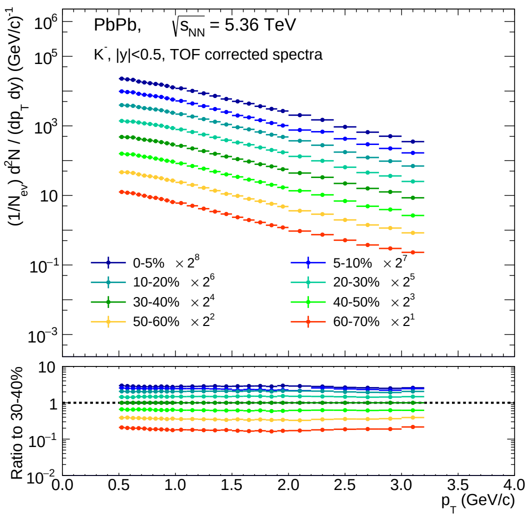

(B) K^- corrected spectra, same centrality classes as in (a).

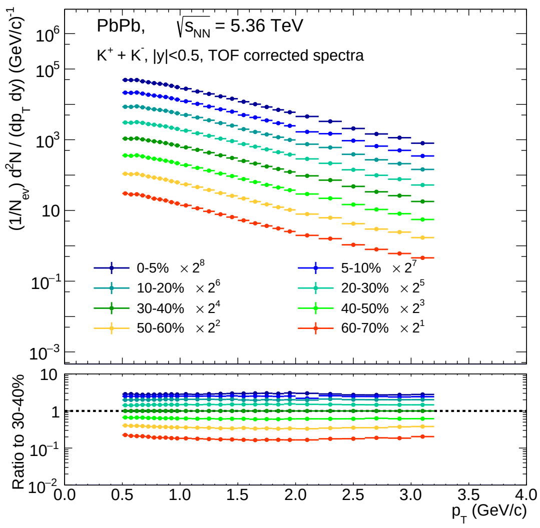

(C) Combined $(K^+ + K^-)$ corrected yield. Top panel: logarithmic scale; bottom: ratio to the 30-40% class.

FIGURE 6.36: TOF-based, efficiency- and primary-fraction-corrected pion yields in Pb-Pb collisions at $\sqrt{s_{NN}} = 5.36$ TeV.

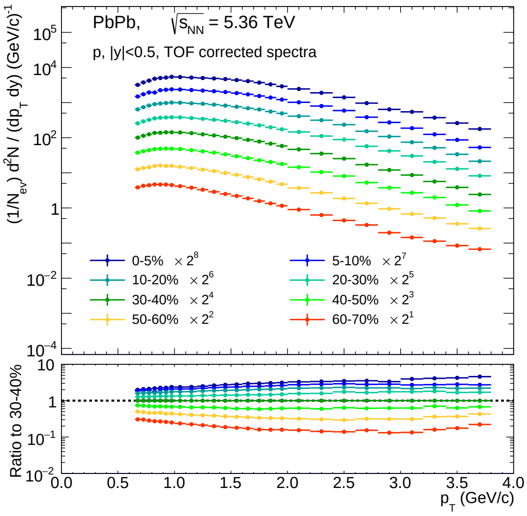

(A) p efficiency- and purity-corrected yield as a function of p_T for all centrality intervals.

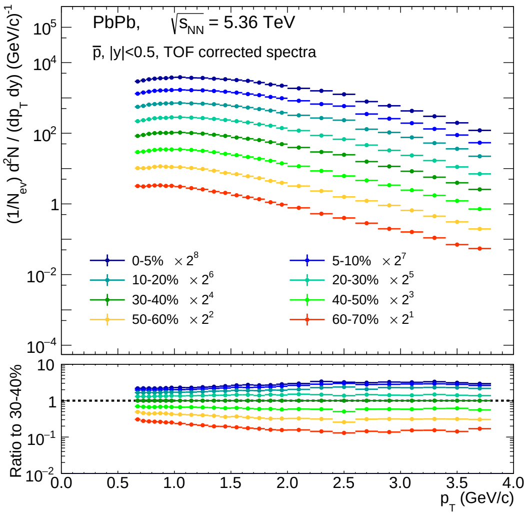

(B) $\bar{p}$ corrected spectra, same centrality classes as in (a).

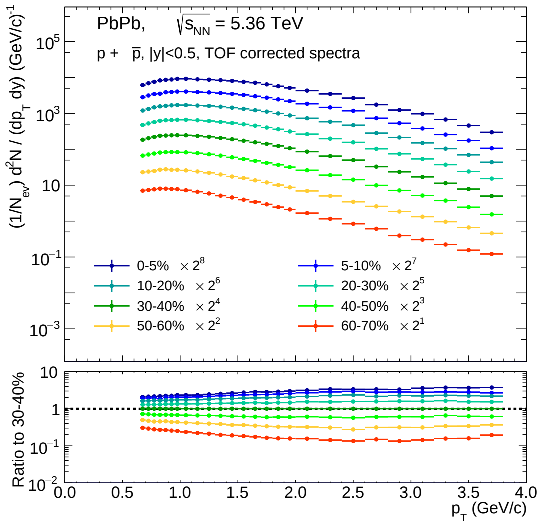

(C) Combined $(p + \bar{p})$ corrected yield. Top panel: logarithmic scale; bottom: ratio to the 30-40% class.

FIGURE 6.37: TOF-based, efficiency- and primary-fraction-corrected proton yields in Pb-Pb collisions at $\sqrt{s_{NN}} = 5.36$ TeV.

Small localized irregularities in the corrected spectra are observed which are purely statistical in origin, stemming from the finite Monte Carlo samples used for efficiency estimation and from uncertainties in the DCA-derived primary fractions.

6.3 Systematic-uncertainty evaluation

A reliable determination of identified particle spectra requires not only a precise extraction of raw yields and accurate efficiency corrections, but also a robust estimate of the associated systematic uncertainties.

Systematic effects quantify the sensitivity of the final corrected spectra to analysis choices that are not uniquely defined but fall within reasonable variations of the reconstruction, fitting, and selection procedures. The guiding principle is simple: we vary, one at a time, the ingredients that could plausibly bias the result and we repeat the full chain (raw-yield extraction → efficiency correction → primary-fraction correction). The resulting spread of the corrected yields is interpreted as a systematic uncertainty.

Two complementary classes of variations are considered:

1. **PID-model dependence**: sensitivity to the analytic description of the TPC/TOF response used to extract raw yields;

2. **Track-selection dependence**: stability of the reconstructed sample under changes of the TPC track-quality criteria (cluster requirements and DCA cuts).

For every particle species, charge, centrality class, and p_{T} bin we obtain an alternative corrected yield for each variation. The relative deviation with respect to the nominal result defines the corresponding systematic contribution. We treat the two categories as uncorrelated and add them in quadrature to obtain the **total systematic uncertainty**. The methodology and physics motivation for each source are described in detail below.

6.3.1 PID-related systematic uncertainty

Raw yields are determined from binned likelihood fits to the TPC n_σ (or TOF time residual) distributions in narrow p_{T} intervals. To assess the model dependence, we repeat the fits with alternative functional forms that explicitly probe signal asymmetries, contaminant peaks, and the flexibility of the smooth background. The PID-induced variation in a given bin is defined as

$$\delta_{\mathrm{PID}}(p_{\mathrm{T}}) = \max_k \left| \frac{Y_k(p_{\mathrm{T}}) - Y_{\mathrm{nom}}(p_{\mathrm{T}})}{Y_{\mathrm{nom}}(p_{\mathrm{T}})} \right|, \tag{6.17}$$

where Y_{nom} is the nominal yield and Y_k is the yield obtained with the k-th alternative.

TPC variations

In addition to the baseline model (Sec. 6.1.1), we employ the following extended forms:

Combined model (fitted):

$$f^{\mathrm{TPC}}_{\mathrm{comb}}(x) = A_1 \exp\left[-\frac{(x-\mu_1)^2}{2\sigma_1^2}\right] + A_2 \exp\left[-\frac{(x-\mu_2)^2}{2\sigma_2^2}\right] + A_3 \exp\left(\frac{x-x_0}{\lambda}\right)\Theta(x-\mu_2) + A_4 \exp\left[-\frac{(x-\mu_3)^2}{2\sigma_3^2}\right]\left[1+\mathrm{erf}\left(k\frac{x-\mu_3}{\sigma_3}\right)\right]. \tag{6.18}$$

Background (for drawing only):

$$f^{\mathrm{TPC}}_{\mathrm{bkg}}(x) = A_1 \exp\left[-\frac{(x-\mu_1)^2}{2\sigma_1^2}\right] + A_2 \exp\left[-\frac{(x-\mu_2)^2}{2\sigma_2^2}\right] + A_3 \exp\left(\frac{x-x_0}{\lambda}\right)\Theta(x-\mu_2). \tag{6.19}$$

Signal (for integration only):

$$f^{\mathrm{TPC}}_{\mathrm{sig}}(x) = A_1 \exp\left[-\frac{(x-\mu_1)^2}{2\sigma_1^2}\right]\left[1+\mathrm{erf}\left(k\frac{x-\mu_1}{\sigma_1}\right)\right]. \tag{6.20}$$

Only `Combined` model is fitted; `Signal` and `Background` models are overlaid for visualization and for signal integration after the full fit is frozen. The extra Gaussian plus an error-function tail allows for residual asymmetry in the core, while the exponential term accommodates smooth, charge-dependent backgrounds.

TOF variations

Signal:

$$f_{\rm sig}^{\rm TOF}(x) = S_0 \exp\left[-\frac{(x-\mu_s)^2}{2\sigma_s^2}\right]. \tag{6.21}$$

Background:

$$f_{\rm bkg}^{\rm TOF}(x) = B_0 \exp\left[-\frac{(x-\mu_0)}{\tau}\right] + B_1 \exp\left[-\frac{(x-\mu_1)^2}{2\sigma_1^2}\right] + B_2 \exp\left[-\frac{(x-\mu_2)^2}{2\sigma_2^2}\right]. \tag{6.22}$$

Combined (fitted):

$$f_{\rm comb}^{\rm TOF}(x) = B_0 \exp\left[-\frac{(x-\mu_0)}{\tau}\right] + B_1 \exp\left[-\frac{(x-\mu_1)^2}{2\sigma_1^2}\right] + B_2 \exp\left[-\frac{(x-\mu_2)^2}{2\sigma_2^2}\right] + B_3 \exp\left[-\frac{(x-\mu_3)^2}{2\sigma_3^2}\right]. \tag{6.23}$$

Again, only `Combined` model is fitted. The additional Gaussians capture nearby species whose residual overlap can bias the signal normalization when the separation is marginal. For both detectors, non-convergent or unphysical fits are rejected using cuts on χ^2/NDF, parameter errors, and boundary proximity.

6.3.2 Track-selection (cut-variation) systematic uncertainty

The second pillar of the systematic study is the stability of the result under variations of the reconstruction-quality criteria. The nominal selections are:

- minimum crossed TPC rows: $N_{\rm rows}^{\rm crossed} \geq 70$;
- ratio of crossed to findable clusters: $N_{\rm rows}^{\rm crossed}/N_{\rm Cls}^{\rm findable} > 0.80$;
- TPC χ^2 per cluster < 4;
- DCA cuts: $|{\rm DCA}_{xy}| < 0.05$ cm, $|{\rm DCA}_z| < 2.0$ cm;
- the shared-cluster fraction is implicitly controlled through the above quality requirements.

To map out a realistic envelope, each cut is scanned to a *loose* and a *tight* value:

Variable	Nominal	Loose	Tight
$N_{\rm rows}^{\rm crossed}$	≥ 70	≥ 60	≥ 120
$N_{\rm rows}^{\rm crossed}/N_{\rm Cls}^{\rm findable}$	> 0.80	> 0.75	> 1.2
TPC χ^2/cl.	< 4	< 8	< 2
ITS χ^2/cl.	< 36	< 40	< 20

In addition to varying each cut individually, we perform two coherent tests to capture correlations:

- **all-loose:** all variables set to their loose values;
- **all-tight:** all variables set to their tight values.

The cut-induced uncertainty in each bin is then defined as

$$\delta_{\text{cut}}(p_{\text{T}}) = \max\left\{\max_j \left|\frac{Y_j(p_{\text{T}}) - Y_{\text{nom}}(p_{\text{T}})}{Y_{\text{nom}}(p_{\text{T}})}\right|, \left|\frac{Y_{\text{all-loose}} - Y_{\text{nom}}}{Y_{\text{nom}}}\right|, \left|\frac{Y_{\text{all-tight}} - Y_{\text{nom}}}{Y_{\text{nom}}}\right|\right\}. \tag{6.24}$$

As expected, the sensitivity peaks at low p_{T}, where curvature, multiple scattering, and occupancy-driven cluster overlaps are largest.

6.3.3 Combination and correlation model

Because PID-model choices and track-quality selections probe disjoint aspects of the analysis (signal modeling vs. sample definition), we treat them as uncorrelated and combine them in quadrature:

$$\delta_{\text{tot}}(p_{\text{T}}) = \sqrt{\delta^2_{\text{PID}}(p_{\text{T}}) + \delta^2_{\text{cut}}(p_{\text{T}})}. \tag{6.25}$$

When propagating uncertainties to physics comparisons or spectral fits, we retain bin-to-bin correlations within each category following standard practice: global changes of the PID model are taken as largely correlated across p_{T} in a given centrality, whereas the all-loose/all-tight variations introduce strong correlations over p_{T} by construction.

Before quantifying the systematic uncertainties associated with PID modeling and track-quality selections, it is instructive to examine directly how the *raw* yields respond to these variations.

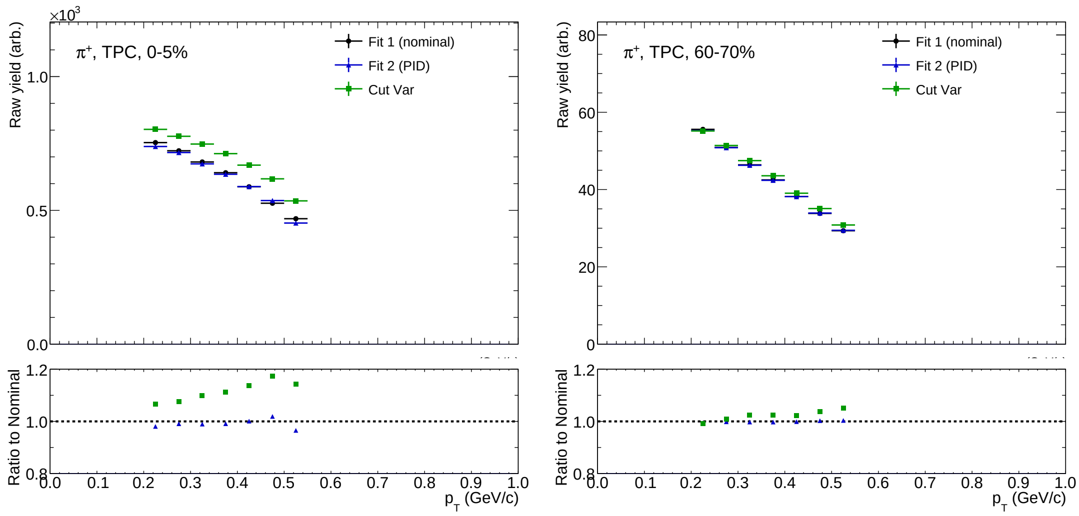

(A) π^+ yield comparison in 0-5% centrality. (B) π^+ raw-yield comparison in 60-70% centrality.

FIGURE 6.38: Comparison of yield extraction under PID and track-cut variations for π^+ in the most central (0-5%) and most peripheral (60-70%) Pb-Pb collisions. The bottom ratio panels (not shown here) quantify the deviation from the nominal fit.

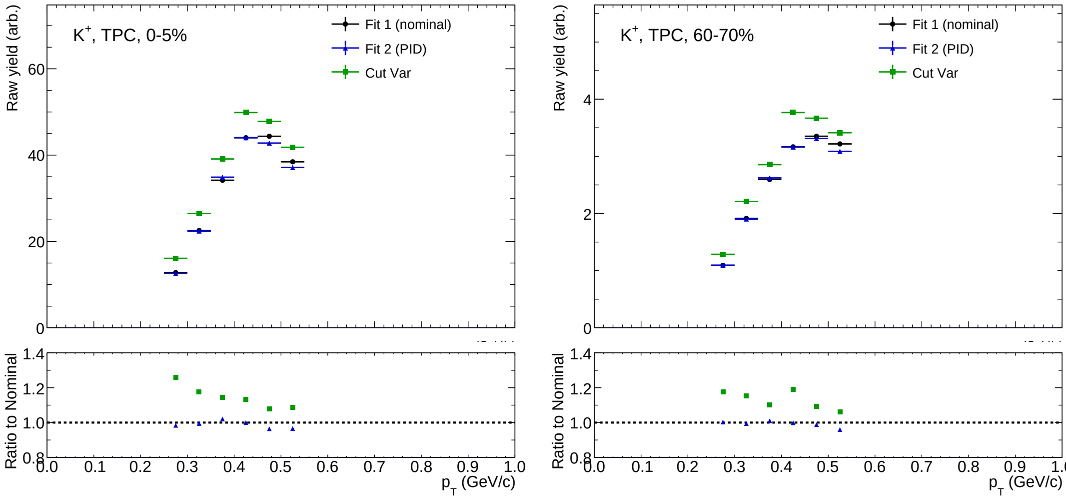

(A) K^+ raw-yield comparison in 0-5% centrality. (B) K^+ raw-yield comparison in 60-70% centrality.

FIGURE 6.39: Yield comparison for K^+ in 0-5% and 60-70% centrality, obtained with nominal PID models, alternative PID parametrizations, and varied track-quality selections.

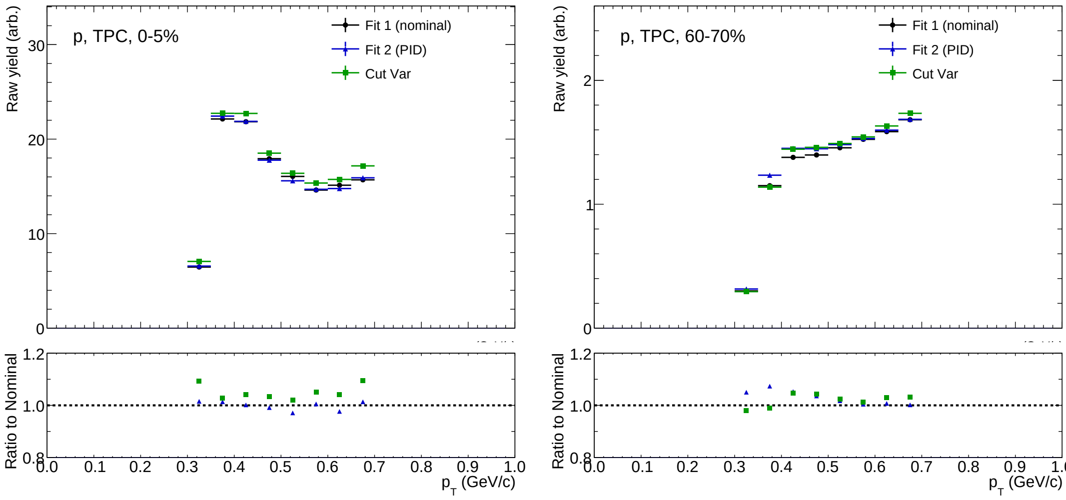

(A) p yield comparison in 0–5% centrality. (B) p yield comparison in 60–70% centrality.

FIGURE 6.40: Proton yield stability under PID-model and track-cut variations for 0-5% and 60-70% centrality. Lower panels (ratios) highlight the charge- and momentum-dependent behaviour.

Figure 6.38-6.40 shows examples for π^+, K^+, p and $\bar{p}$ in the 0-5% and 60-70% centrality class (TPC), comparing:

- the **nominal fit** (Fit 1), using the baseline PID function introduced in Sec. 6.1.1;
- an **alternative PID model** (Fit 2), corresponding to one of the extended signal+background parameterizations discussed in Sec. 6.3.1;
- a **representative cut-variation**, where one of the TPC track selections is chosen from the ones described in the previous section (Sec. 6.3.2). In this case the **all-tight** part was chosen as it displayed the most deviation from the nominal one.

The top panel displays the yields as a function of p_T for the three configurations, while the bottom panel shows the ratio with respect to the nominal fit. Across the full momentum range, the agreement between the nominal and alternative models remains at the few-percent level, with no systematic drift as a function of p_T.

After establishing the stability of the raw-yield extraction in the TPC, we now perform an equivalent evaluation for the TOF detector.

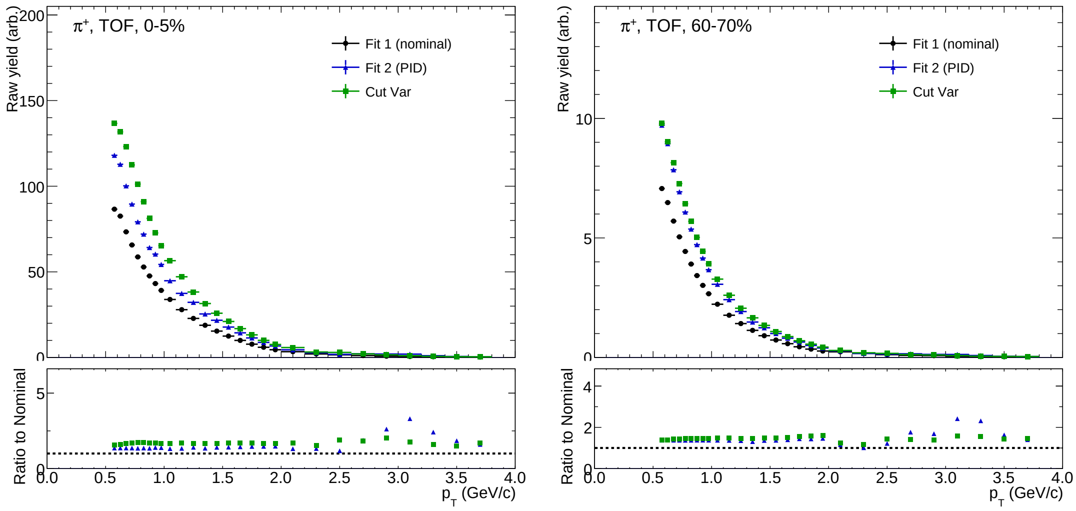

(A) π^+ yield comparison in 0-5% centrality (TOF).

(B) π^+ yield comparison in 60-70% centrality (TOF).

FIGURE 6.41: Comparison of TOF π^+ raw-yield extraction for central (0-5%) and peripheral (60-70%) Pb-Pb collisions. The variations correspond to the nominal fit, alternative PID parametrizations, and the track-cut variations used for TOF-based PID.

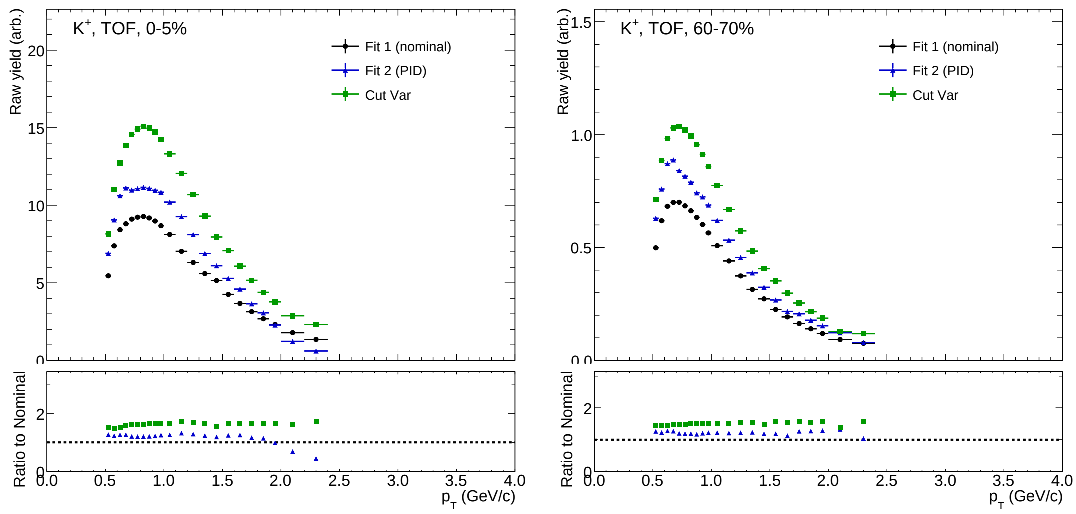

(A) K^+ yield comparison in 0-5% centrality (TOF).

(B) K^+ yield comparison in 60-70% centrality (TOF).

FIGURE 6.42: Yield comparison for kaons in the TOF detector for two centrality intervals.

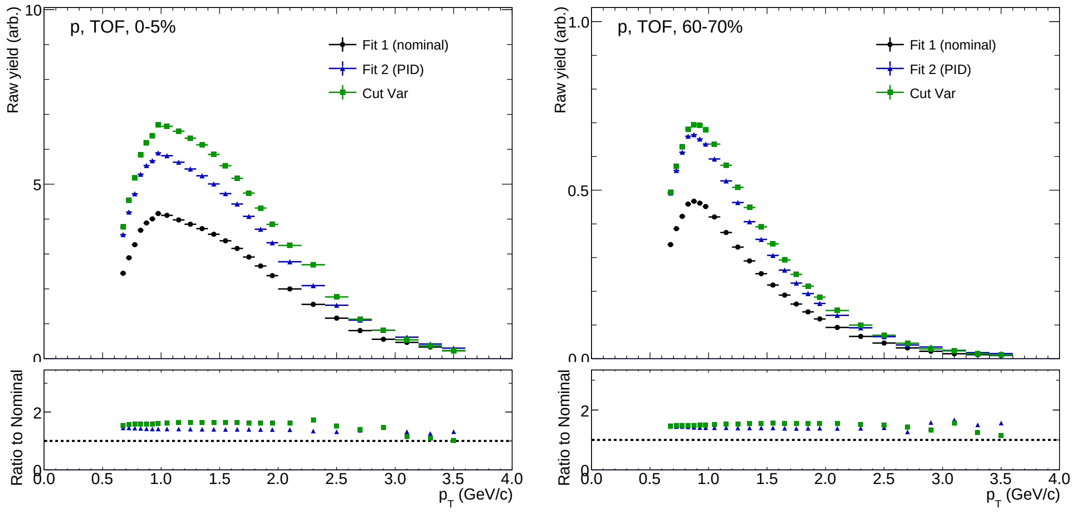

(A) p yield comparison in 0-5% centrality (TOF). (B) p yield comparison in 60-70% centrality (TOF).

FIGURE 6.43: Proton yield stability under TOF PID-model and track-cut variations.

Having established the stability of the yield extraction for all particle species in both the TPC and TOF detectors, the next step is to quantify how these variations propagate into the final measurement. In this section, we present the relative systematic uncertainties as a function of transverse momentum for pions, kaons, and protons.

The following figures (Fig.6.44a - 6.46b) illustrate the breakdown of these contributions for pions, kaons, and protons in the representative 0–5% and 60-70% centrality classes for the TPC (analogous figures for the TOF are shown subsequently). The behaviour of the TPC systematic uncertainties reflects the specific PID environment in the low-momentum region, where particles are identified through the relativistic rise of $\mathrm{d}E/\mathrm{d}x$ and the separation power between hadron species depends sensitively on the detector resolution and on track-quality selections.

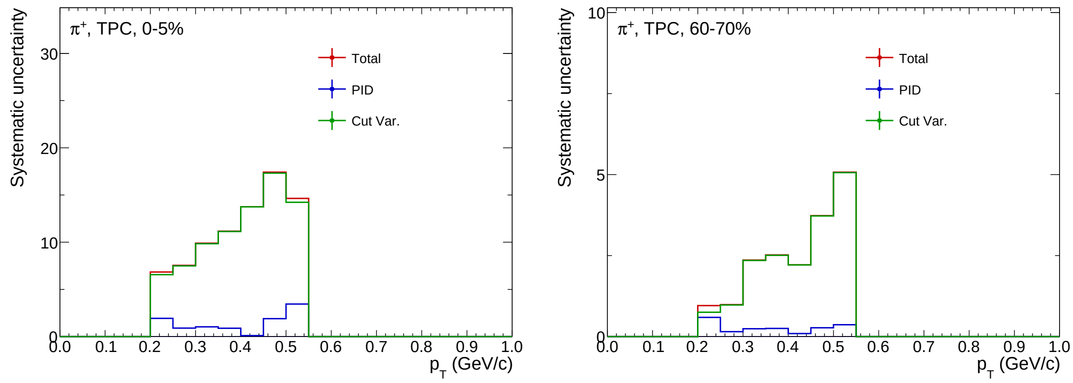

(A) π^+ TPC yield comparison, 0-5%. (B) π^+ TPC yield comparison, 60-70%.

FIGURE 6.44: Yield stability checks for π^+ in the TPC for two representative centrality classes. Black: nominal fit; blue: alternative PID model; green: track-cut variation.

For pions, the total TPC systematic uncertainty is dominated almost entirely by the track-selection variation. The very small $\mathrm{d}E/\mathrm{d}x$ separation between pions and electrons in the momentum range used for the TPC analysis implies that even modest changes to the track-quality requirements impact the shape of the residual background in the PID fit.

Loosening the crossed-rows and χ^2 requirements enhances the fraction of tracks with suboptimal cluster patterns, and consequently broadens the tails of the n_σ^{TPC} distribution. This effect is strongest at low p_{T}, where pion curvature is large and cluster loss due to local distortions is more likely.

PID-model variations contribute at the percent level only, since the pion peak is narrow and nearly Gaussian, and the background modelling is well constrained by the neighbouring charge-combined distributions.

In peripheral events (Fig.6.44b), all components decrease in magnitude, as the track density is lower and space-charge distortions are reduced, leading to more stable fits and smaller sensitivities to cluster-quality variations.

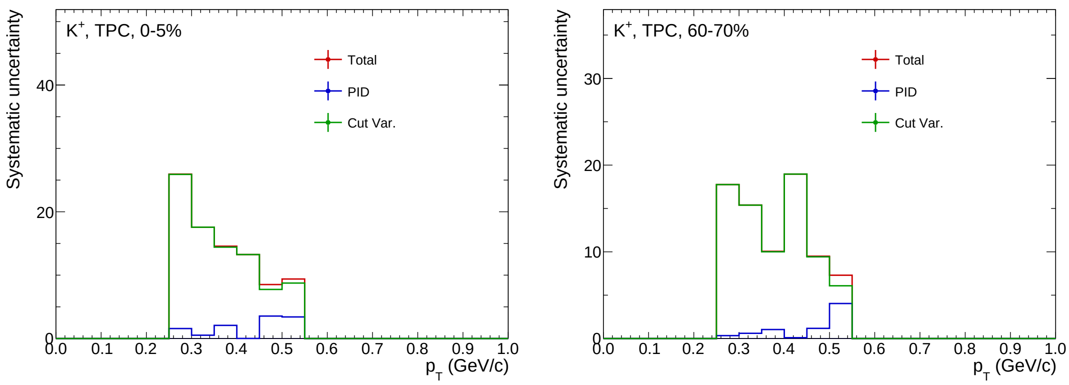

(A) K^+ TPC yield comparison, 0–5%.

(B) K^+ TPC yield comparison, 60-70%.

FIGURE 6.45: Yield comparisons for K^+ in the TPC for central (0-5%) and peripheral (60-70%) Pb-Pb collisions.

For kaons (Fig.6.45a - 6.45b), the TPC uncertainties are noticeably larger than for pions, and this behaviour originates from two physical and detector-related effects. First, kaons occupy the momentum region where the $\mathrm{d}E/\mathrm{d}x$ separation from both pions and protons is modest, making the extraction of kaon raw yields particularly sensitive to the detailed treatment of background components in the fit.

Secondly, kaons constitute a significantly smaller fraction of the charged-hadron population, meaning that any deviation in the modelling of the neighbouring peaks directly influences the extracted signal. Consequently, variations of track-quality cuts have a notably amplified effect: looser χ^2 or cluster-fraction selections increase the amount of misidentified pions and protons leaking into the kaon PID window.

The PID-model uncertainty is non-negligible but typically subdominant, since the kaon peak remains reasonably Gaussian but its relative amplitude is small. Peripheral collisions (Fig. 6.45b) again display reduced sensitivity because the background composition is more stable in lower-multiplicity environments.

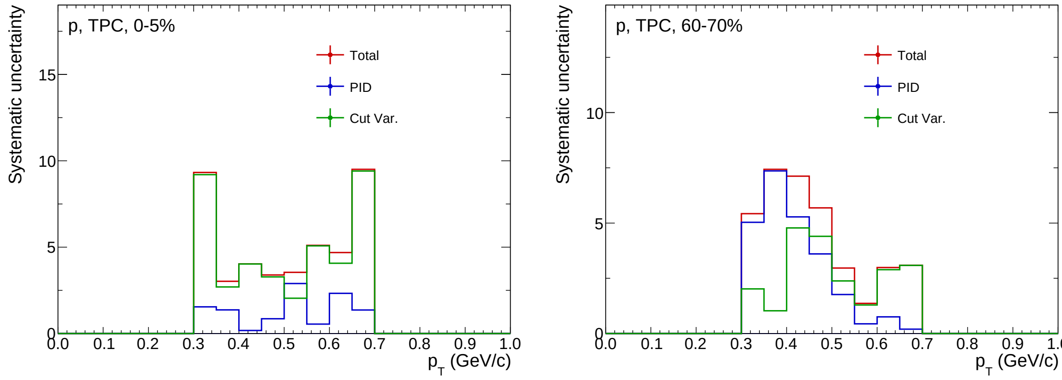

(A) p TPC yield comparison, 0-5%.

(B) p TPC yield comparison, 60-70%.

FIGURE 6.46: Yield stability checks for protons in the TPC for 0-5% and 60-70% centrality intervals. Protons show slightly larger sensitivity to track-cut variations at low p_{T}, consistent with their larger interaction cross section.

For protons (Fig.6.49a - 6.46b), the TPC uncertainties are governed by a delicate interplay of background modelling and track-quality dependence.

At the relatively low momenta accessible to the TPC-only PID method, protons are well separated from kaons in $\mathrm{d}E/\mathrm{d}x$, but the proximity to the charge-symmetric pion tail makes the background parametrisation crucial. PID-model variations are therefore more prominent for protons than for pions, visible as a structured trend in the systematic uncertainty particularly in the 0-5% centrality class.

Track-selection variations also contribute substantially: proton tracks at low p_{T} are more curved and more susceptible to shared clusters and local inefficiencies, leading to pronounced changes when varying the crossed-row or χ^2/cluster criteria. Towards peripheral events, both types of variations shrink in magnitude, as the background becomes smoother and the track-quality distribution stabilises. Overall, the proton TPC uncertainties remain moderate and well-behaved, with a clear physical rationale linked to the interplay of curvature effects, background composition, and cluster-quality stability.

The systematic uncertainties associated with the TOF analysis exhibit a characteristic structure that reflects both the detector response and the kinematics of particle separation. For π^+ (Fig.6.47), the TOF systematic uncertainty displays three distinct momentum regions. Immediately above the TOF turn-on threshold ($p_{\mathrm{T}} \approx 0.6$ GeV/c), the matching and track-quality variations dominate the total uncertainty. In central 0-5% collisions (Fig.6.47a), the high local hit density in the TOF pads increases the probability of shared or misassigned hits, making the yield particularly sensitive to variations of the matching window and TPC-track quality. This leads to systematic deviations of $\sim$ (0.5-0.8)%, whereas in peripheral 60-70% events (Fig.6.47b) the much lower occupancy produces noticeably smaller uncertainties.

In the intermediate region ($0.8 < p_{\mathrm{T}} < 2.5$ GeV/c), the TOF provides excellent π/K separation, and both PID-model and cut-variation uncertainties remain very small, forming a broad and nearly flat plateau. The stability here reflects the fact that the pion signal is clean and well-constrained by the timing resolution.

At higher momenta ($p_{\mathrm{T}} > 2.5$ GeV/c), the π/K time-of-flight difference becomes comparable to the intrinsic TOF resolution, and the extracted pion yield becomes increasingly sensitive to the functional form used in the PID fit. Consequently, the PID component rises and becomes the leading source of uncertainty. This behaviour is evident in both the 0-5% and 60-70% classes, although the magnitudes differ slightly due to the varying background composition and statistical precision of the fits.

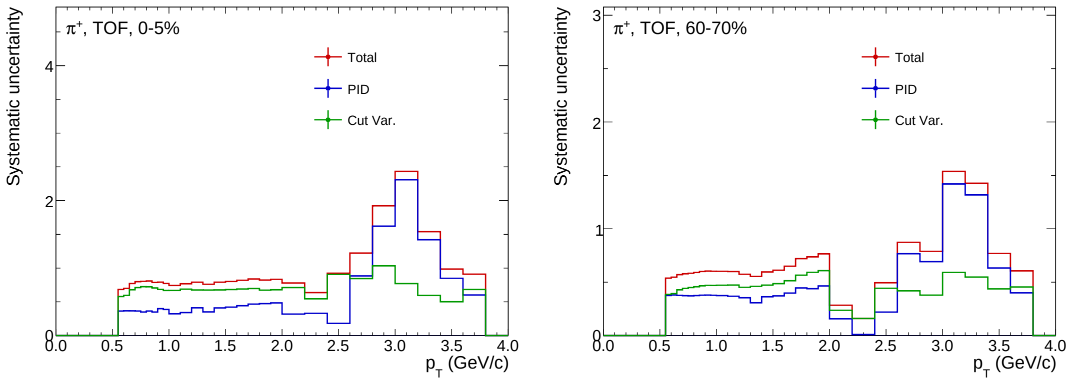

(A) π^+ TOF yield comparison, 0-5%. (B) π^+ TOF yield comparison, 60-70%.

FIGURE 6.47: Yield stability checks for π^+ in the TOF for two representative centrality classes. Black: nominal fit; blue: alternative PID model; green: track-cut variation.

For $K^\pm$ (Fig.6.45), the TOF systematic uncertainties follow a similar qualitative pattern to pions but exhibit stronger momentum dependence due to the more challenging separation from both pions and protons. In the low-p_T region just above the TOF acceptance threshold, the cut-variation uncertainty is the dominant contribution. This effect is amplified relative to pions because kaons are less abundant and the TOF matching residuals depend more sensitively on the exact reconstruction and matching cuts, especially in central collisions.

In the intermediate momentum range ($1 < p_T < 2.0$ GeV/c), the total uncertainties remain modest, although typically somewhat larger than for pions. This reflects the reduced K/π separation compared to π PID, which increases the sensitivity to small changes in the assumed background shape or Gaussian widths. The cut-variation and PID contributions are comparable in this range, each contributing at the level of $\sim$ (0.5-0.7)%.

At higher p_T values the kaon uncertainty rises more rapidly than for pions. Above about $p_T \sim 2.2$ GeV/c, the K/p and K/π bands begin to merge in the TOF timing spectrum, and the yield extraction becomes increasingly dependent on the precise parameterisation of the background and the contaminant contributions. As a result, the PID component dominates the total systematic uncertainty in this region. Central events show a slightly larger rise than peripheral events, consistent with higher combinatorial background and lower signal purity.

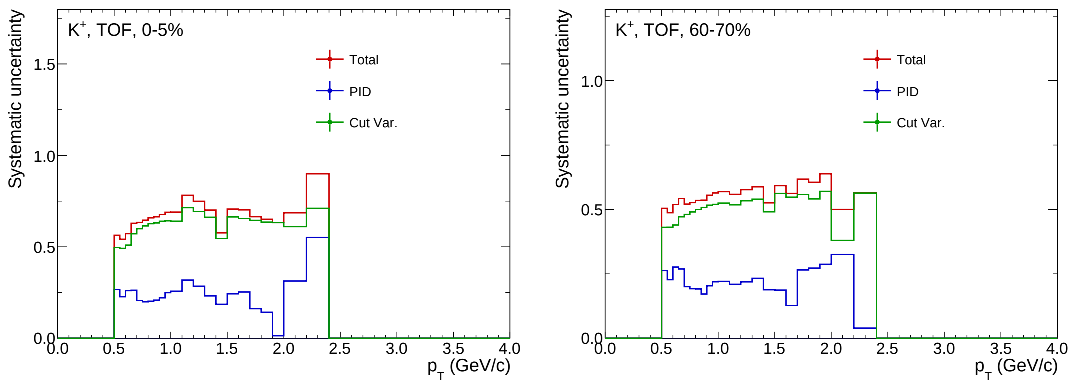

(A) K^+ TOF yield comparison, 0-5%.

(B) K^+ TOF yield comparison, 60-70%.

FIGURE 6.48: Yield comparisons for K^+ in the TOF for central (0-5%) and peripheral (60-70%) Pb-Pb collisions.

For protons(Fig. 6.49), the TOF systematic uncertainties reflect the unique challenge that protons remain non-relativistic up to higher momenta compared to pions and kaons. As with the lighter hadrons, the low-p_T region is dominated by cut-variation uncertainties, particularly in central collisions, where the TPC–TOF matching performance is degraded by high multiplicity. The larger mass of the proton also enhances multiple scattering at low momenta, increasing the sensitivity to DCA and cluster-quality variations.

In the intermediate region ($1 < p_T < 2.5$ GeV/c), the TOF still provides strong p/K separation, and the uncertainties stabilise into a broad plateau. The cut-variation and PID-model dependence are both moderate and roughly comparable, producing total uncertainties of order 0.6–0.8% in central collisions and slightly lower in peripheral ones.

At higher momenta, the proton systematic uncertainty increases due to the gradual convergence of the K/p time-of-flight distributions. Around $p_T \approx 3.0$ GeV/c, the PID-model dependence becomes the leading contribution, with the total uncertainty peaking accordingly. Once again, central collisions show a somewhat stronger rise than peripheral ones, reflecting the more complex background environment and the larger fractional contribution of misidentified kaons in dense events.

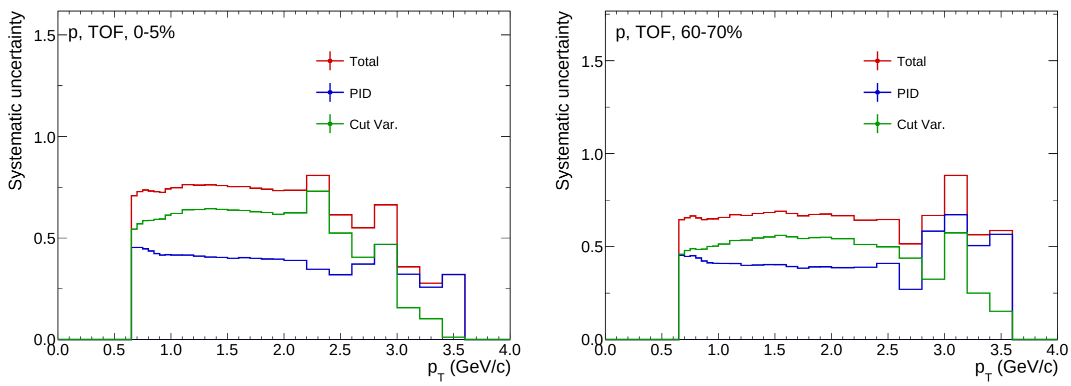

(A) p TOF yield comparison, 0-5%.

(B) p TOF yield comparison, 60-70%.

FIGURE 6.49: Yield stability checks for protons in the TOF for 0-5% and 60-70% centrality intervals.

Overall, the TOF systematic uncertainties for pions, kaons, and protons demonstrate clear and physically well-motivated momentum and centrality dependence: cut-variation uncertainties dominate in the low-p_T region, while PID-related uncertainties dominate once the TOF separation power begins to degrade at higher momenta.

6.4 Corrected spectra and associated systematic uncertainties

The final stage of the analysis consists of constructing the fully corrected transverse–momentum spectra for pions, kaons, and protons in each centrality interval. These spectra incorporate all corrections discussed previously, raw-yield extraction (Secs. 6.1.1–6.1.2), tracking efficiency (Secs. 6.2.1–6.2.1), and the primary-particle fraction (Sec. 6.2.3), as well as the systematic uncertainties quantified in Sec. 6.3. The corrected yield is obtained via:

$$\frac{1}{N_{ev}}\frac{\mathrm{d}^2N}{\mathrm{d}p_T\mathrm{d}y} = \frac{Y_{raw}(p_T)f_{prim}(p_T)}{\varepsilon_{reco}(p_T)\ \Delta p_T\,\Delta y}. \tag{6.26}$$

Both statistical uncertainties (from the fit and efficiency) and systematic uncertainties (PID model, track-selection variations, and primary-fraction variations) are propagated to the final spectra.

6.4.1 TPC and TOF corrected spectra

Following the structure used previously for the raw spectra, the corrected yields are presented separately for TPC and TOF PID regions. In each case, the top panel shows the corrected spectra for all centrality classes on a logarithmic vertical axis, while the bottom panel displays the ratio of each centrality interval to the corresponding published PbPb results at $\sqrt{s_{NN}} = 5.02$ TeV [147].

The corrected transverse-momentum spectra obtained with the TPC for $\pi^{\pm}$, $K^{\pm}$, and $p(\bar{p})$, together with their corresponding systematic uncertainties and the ratios to the published Pb-Pb results at $\sqrt{s_{NN}} = 5.02$ TeV, are illustrated below (Fig.6.50a - 6.52c). They provide a stringent validation of the reconstruction and correction strategy employed in this work.

For pions (Fig.6.50a - 6.52c), the corrected spectra exhibit the expected centrality ordering, with yields increasing and slopes hardening toward central collisions. The associated systematic uncertainties are small, dominated at low p_T by secondary-removal variations and at higher p_T by PID stability. The ratios with respect to the published reference lie systematically above unity by a nearly constant offset of a few to ten percent. The deviation is largely p_T independent, and the combined $\pi^+ + \pi^-$ ratios reflect the same behaviour. A mild ordering with centrality is visible: peripheral classes tend to lie slightly higher than central classes, indicating a centrality-dependent but still predominantly global normalisation difference. The flatness of the ratios in p_T strongly suggests that the observed offset is not caused by a momentum-dependent efficiency mismatch but rather by a global scale effect. Given that pion systematics in this region are small and largely p_T, independent, the offset appears to be a correlated scale difference consistent with normalisation-level uncertainties.

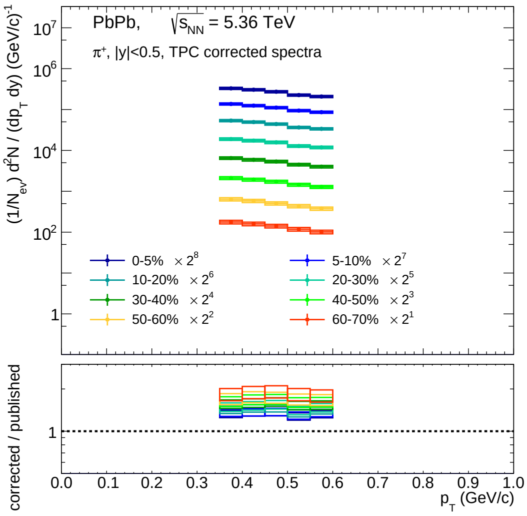

(A) π^+ efficiency- and purity-corrected yield as a function of p_T for all centrality intervals.

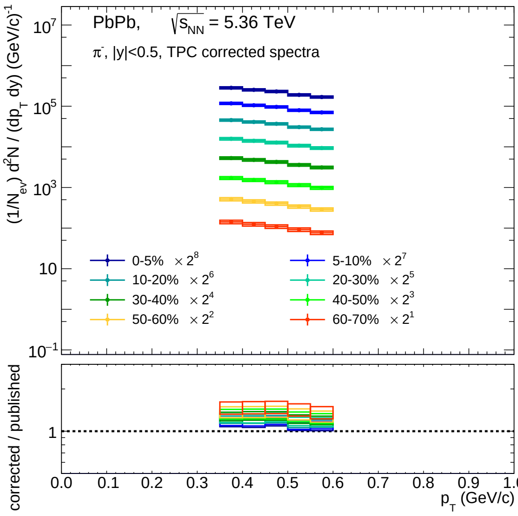

(B) π^- corrected spectra, same centrality classes as in (a).

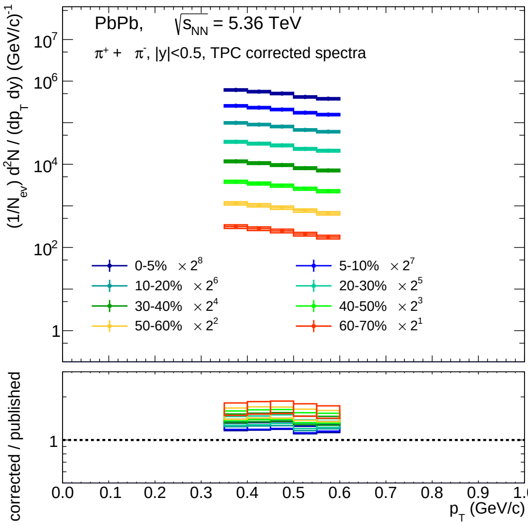

(C) Combined $(\pi^+ + \pi^-)$ corrected yield. Top panel: logarithmic scale; bottom: ratio to the 30-40% class.

FIGURE 6.50: TPC-based, efficiency- and primary-fraction-corrected pion yields in Pb-Pb collisions at $\sqrt{s_{NN}} = 5.36$ TeV.

Kaons, being heavier and more susceptible to decay in flight, display slightly larger and more structured systematic uncertainties, particularly in the low-to-intermediate p_T region where variations in track quality and PID constraints play a larger role. It also displays the characteristic low p_T rise and broad shoulder around intermediate momenta. In contrast to the pions, the ratio panels exhibit a pronounced momentum dependence: a broad enhancement appears in $0.4 \lesssim p_T \lesssim 0.6$ GeV$/c$, where the ratios rise up to 20-40% above unity depending on the centrality class. The effect is present for both charges but is slightly larger for K^+, and again more peripheral classes sit higher than central ones. Such a pattern is typical of PID-model and matching efficiency systematics in the region where kaon to pion separation in the TPC is weakest and where the published reference partially relies on TOF information. Importantly, the ratios tend back toward unity at higher p_T, indicating that the difference is not due to a global normalisation offset but to a species-specific, momentum-localised efficiency or PID modelling effect. The centrality ordering suggests an additional contribution from occupancy-dependent PID or matching corrections, which are naturally more pronounced in peripheral events where statistical uncertainties are smaller and the kaon to pion separation is most delicate.

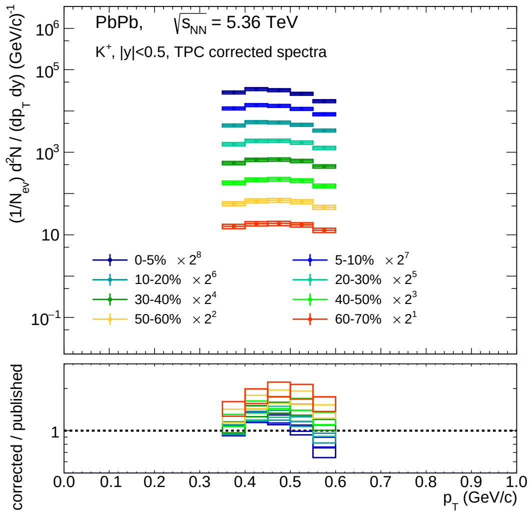

(A) K^+ efficiency- and purity-corrected yield as a function of p_T for all centrality intervals.

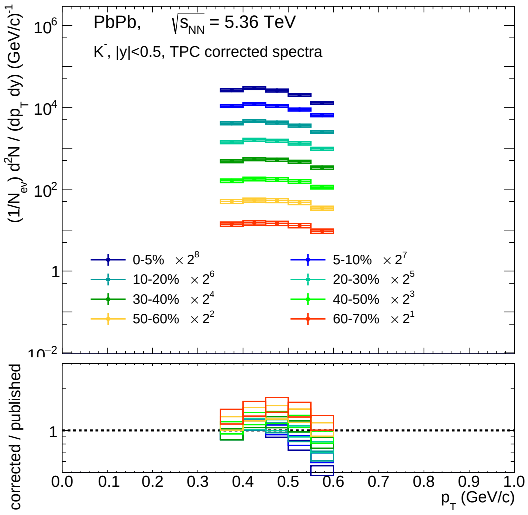

(B) K^- corrected spectra, same centrality classes as in (a).

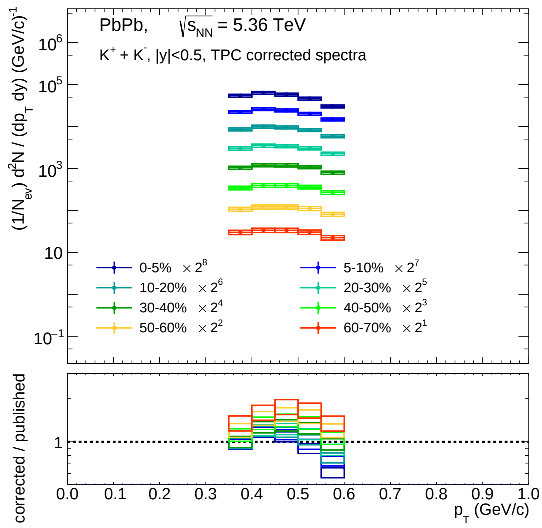

(C) Combined $(K^+ + K^-)$ corrected yield. Top panel: logarithmic scale; bottom: ratio to the RUN2 results

FIGURE 6.51: TPC-based, efficiency- and primary-fraction-corrected pion yields in Pb-Pb collisions at $\sqrt{s_{NN}} = 5.36$ TeV.

The proton (Fig.6.52a - 6.52b) sector exhibits the most distinctive deviations from the published reference. For p, the ratios show a shallow U-shaped structure. For $\bar{p}$, the ratio increases steadily with p_T, reaching ~ 1.3 - 1.6 for the most peripheral classes. The combined $p + \bar{p}$ ratio exhibits a moderated mixture of these trends.

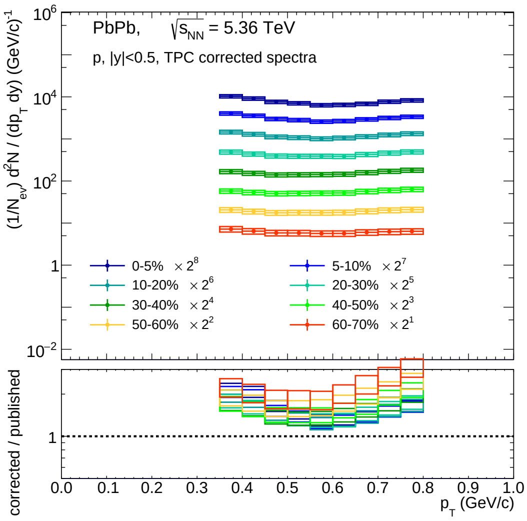

(A) p efficiency- and purity-corrected yield as a function of p_{T} for all centrality intervals.

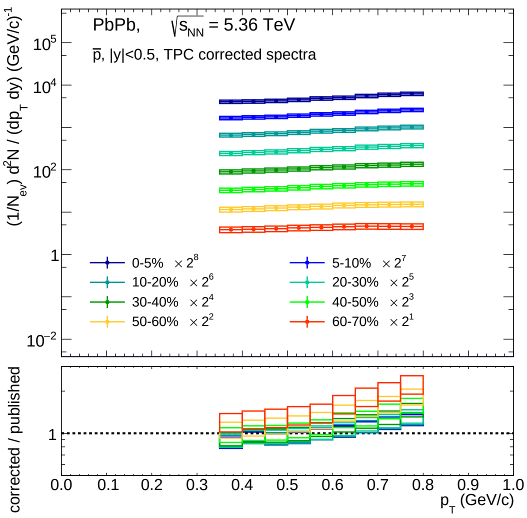

(B) $\bar{p}$ corrected spectra, same centrality classes as in (a).

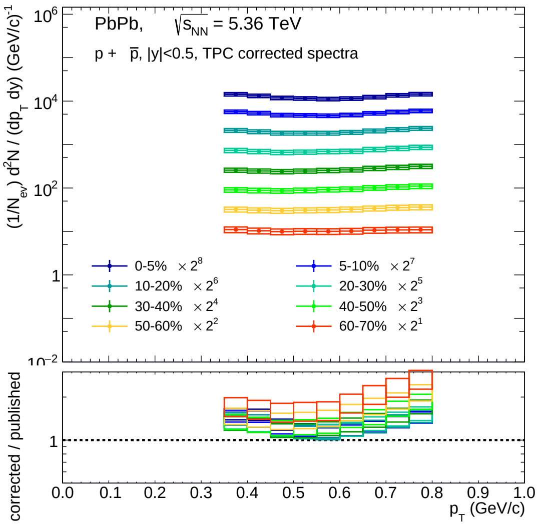

(C) Combined $(p + \bar{p})$ corrected yield. Top panel: logarithmic scale; bottom: ratio to the 30-40% class.

FIGURE 6.52: TPC-based, efficiency- and primary-fraction-corrected proton yields in Pb-Pb collisions at $\sqrt{s_{\mathrm{NN}}} = 5.36$ TeV.

This behaviour is consistent with known sensitivities of proton analyses:

- the modelling of the primary fraction, particularly the feed-down from Λ and Σ decays, which affects protons most strongly at intermediate p_{T}
- the modelling of hadronic interactions and annihilation in detector material, which affects $\bar{p}$ more strongly and in a distinctly momentum-dependent manner

Small differences relative to the published reference in the DCA-template construction, the feed-down constraints, or the hadronic interaction model in the simulation can therefore generate exactly the observed p_{T} dependence. The peripheral classes again show the largest deviations, suggesting that differences in template stability or material-interaction corrections become most visible where statistics are highest and systematic bands smallest. Importantly, the magnitude and form of the deviations remain within the combined statistical and systematic uncertainties assigned in this analysis.

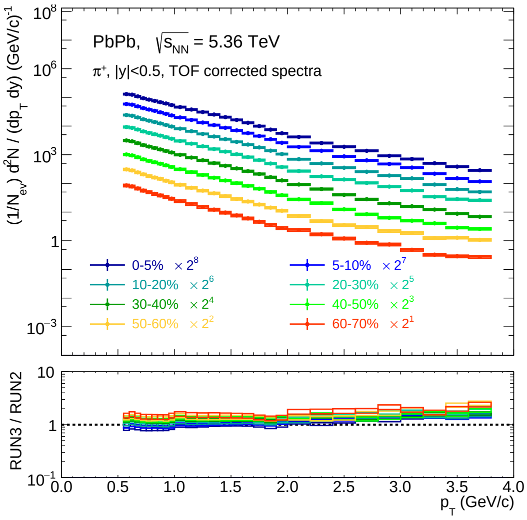

(A) π^+ efficiency- and purity-corrected yield as a function of p_{T} for all centrality intervals.

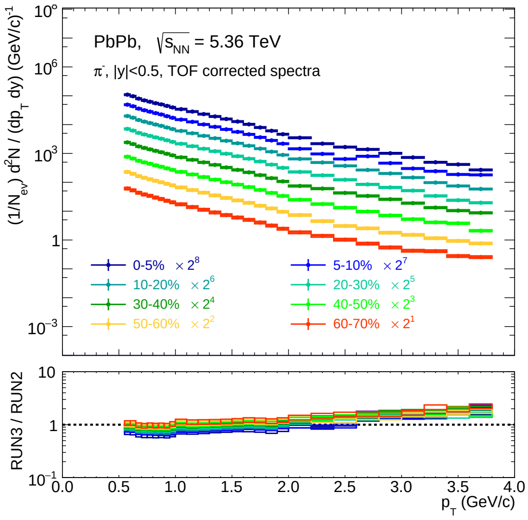

(B) π^- corrected spectra, same centrality classes as in (a).

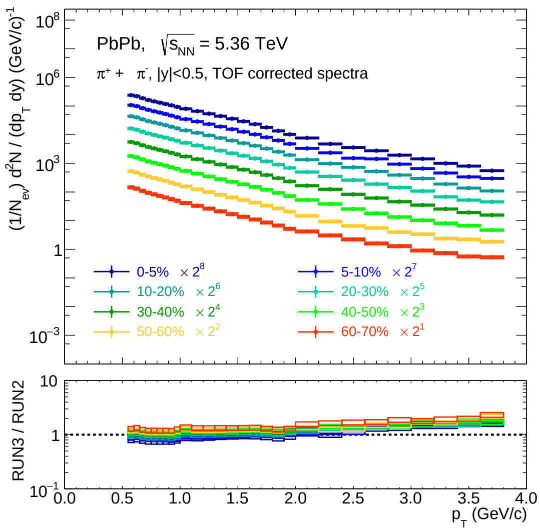

(C) Combined $(\pi^+ + \pi^-)$ corrected yield. Top panel: logarithmic scale; bottom: ratio to the RUN2 results.

FIGURE 6.53: TOF based, efficiency- and primary-fraction corrected pion yields in Pb-Pb collisions at $\sqrt{s_{\mathrm{NN}}} = 5.36$ TeV.

The TOF pion spectra (Fig. 6.53a - 6.53c) extend to significantly larger momenta than in the TPC analysis, and the ratios to the published reference are remarkably stable over the entire p_{T} range. For both charges, the ratios fluctuate narrowly about unity, typically within a few percent for $0.6 < p_{\mathrm{T}} < 3$ GeV/c. The combined spectrum shows the same behaviour. The absence of a strong p_{T} dependence suggests that the TOF matching efficiency, PID selection, and event normalisation are well aligned with those of the published analysis. Small positive deviations at the largest momenta ($p_{\mathrm{T}} \gtrsim 3$ GeV/c), most visible in peripheral collisions, are consistent with modest differences in track-quality or matching-efficiency corrections, where statistics are limited and the TOF turn-off begins to play a role. Importantly, unlike in the TPC-only case, the TOF comparison does not display a global charge-independent offset, further reinforcing that the residual TPC offset originates from low-momentum acceptance differences rather than a flaw in the overall event normalisation.

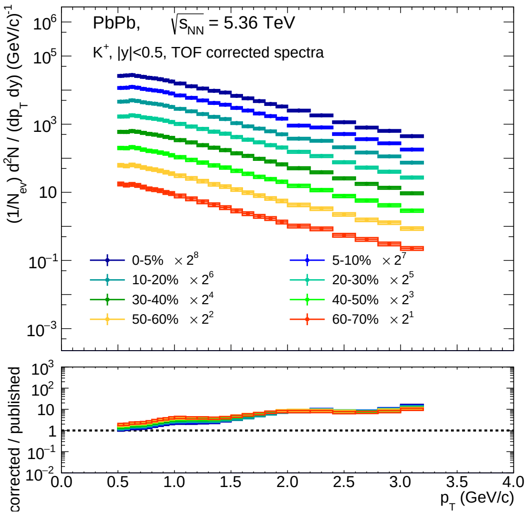

(A) K^+ efficiency- and purity-corrected yield as a function of p_T for all centrality intervals.

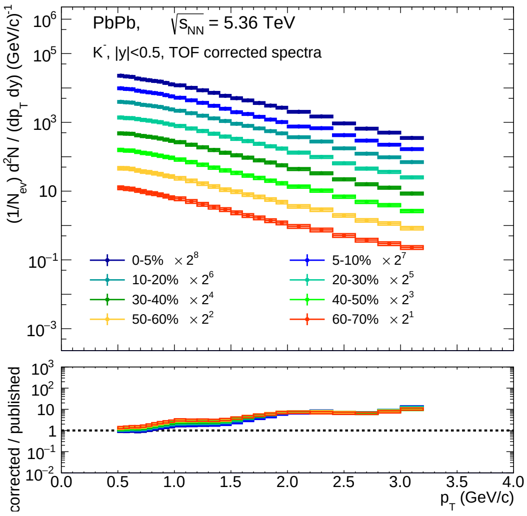

(B) K^- corrected spectra, same centrality classes as in (a).

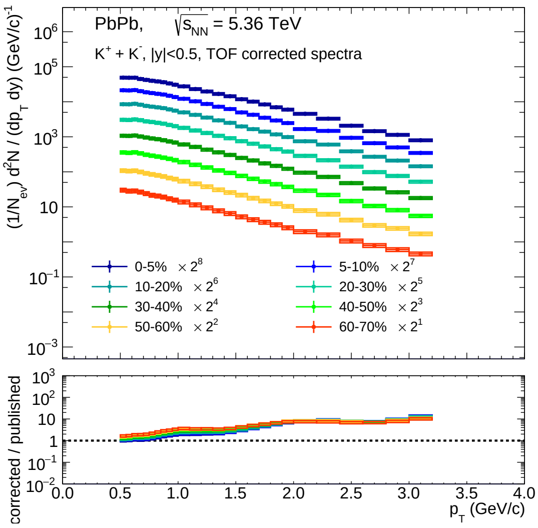

(C) Combined $(K^+ + K^-)$ corrected yield. Top panel: logarithmic scale; bottom: ratio to published

FIGURE 6.54: TOF based, efficiency- and primary-fraction corrected pion yields in Pb-Pb collisions at $\sqrt{s_{NN}} = 5.36$ TeV.

The TOF kaon spectra (Fig.6.54a - 6.54c) also agree well with the published results across all centralities. At low p_T near the matching turn-on ($0.4 < p_T < 0.6$ GeV/c) the ratios display a mild upward trend, reaching $\sim$ 10-20% above unity. This feature is common to all centrality classes and is symmetric between charges within uncertainties. It is consistent with the sensitivity of kaon PID to the TOF matching efficiency and with the well-known transition region where kaon and pion TOF separation begins to degrade. A gentle monotonic rise toward $p_T \gtrsim 2.5$ GeV/c is observed in all centralities; this behaviour suggests small differences in the efficiency parameterisation at high momenta, where the TOF timing resolution and track extrapolation uncertainties grow slowly with p_T.

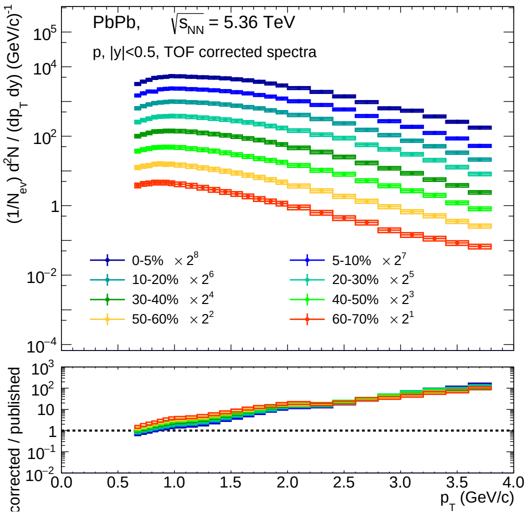

(A) p efficiency- and purity-corrected yield as a function of p_T for all centrality intervals.

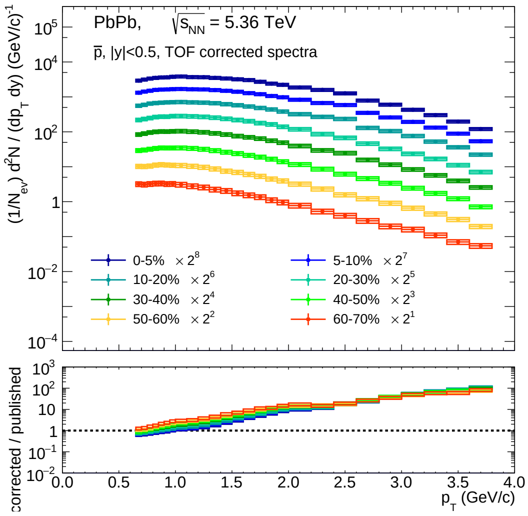

(B) $\bar{p}$ corrected spectra, same centrality classes as in (a).

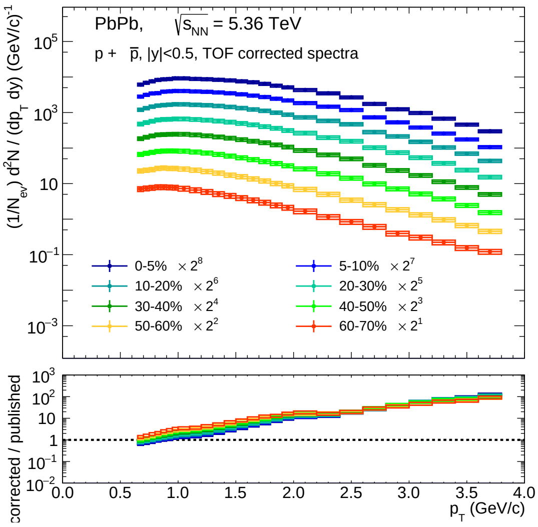

(C) Combined $(p + \bar{p})$ corrected yield. Top panel: logarithmic scale; bottom: ratio to the RUN2 results

FIGURE 6.55: TOF based, efficiency- and primary-fraction corrected proton yields in Pb-Pb collisions at $\sqrt{s_{NN}} = 5.36$ TeV.

The TOF proton sector shows the largest deviations from unity, reflecting its stronger sensitivity to material interactions, secondary contamination, and feed-down corrections. At low momenta ($p_T \lesssim 0.8$ GeV/c) the ratios remain consistent with unity within uncertainties, but a pronounced, monotonic upward drift appears for both p and $\bar{p}$ at higher p_T. At $p_T \approx 2.5$ - 3.5 GeV/c the ratios exceed unity by factors of 2-3, increasing slightly from central to peripheral collisions. The shape is similar for protons and antiprotons, indicating that the dominant contribution is not annihilation in the detector material, but rather a systematic difference in the high-momentum efficiency modeling between our reconstruction chain and that used in the reference. Although the discrepancies are significant at high momentum, their smooth evolution suggests a coherent correlated effect rather than a bin-by-bin instability, and they can therefore be treated as a potential efficiency-model systematic to be investigated further.

6.5 Particle-to-pion ratios

Ratios of hadron yields, in particular K/π and p/π, play a central role in the characterization of the chemical and collective properties of the system created in heavy–ion collisions. Since pions dominate the charged-particle production at low transverse momentum, normalizing kaon and proton yields to pions removes most global scale uncertainties associated with luminosity, event selection, vertex efficiency, and tracking corrections. Furthermore, such ratios suppress residual systematics that are common across species, and therefore offer a more sensitive probe of physics differences between collision energies, centralities, or detector configurations.

From a physics perspective, the K/π ratio reflects the relative abundance of strangeness to light quarks and is connected to the chemical freeze-out temperature and phase-space saturation factors in statistical–hadronisation models. The p/π ratio is sensitive to baryon–meson dynamics, radial-flow effects, and the baryon chemical potential. The p/π enhancement at intermediate p_{T} observed at RHIC and LHC energies is often interpreted in the context of recombination mechanisms or strong collective expansion. Given these physics sensitivities, it is essential to verify that the Run 3 analysis reproduces the well-established patterns seen in Run 2 Pb-Pb collisions at $\sqrt{s_{\mathrm{NN}}} = 5.02$ TeV.

In addition to these physics motivations, ratios provide a stringent internal cross-check of the analysis, any species-dependent bias in PID, efficiency, primary-fraction corrections, or feed-down modelling typically appears more clearly in K/π or p/π than in the individual spectra. To quantify such effects, all ratios presented here are accompanied by a ratio to the published Run 2 measurements, denoted as "Run 3 / Run 2". These comparisons provide a direct diagnostic of the consistency between the new reconstruction and PID framework and the established LHC baseline.

6.5.1 TPC results

Figures 6.56 and 6.57 show the TPC-only $(K^{+}+K^{-})/(\pi^{+}+\pi^{-})$ and $(p+\bar{p})/(\pi^{+}+\pi^{-})$ ratios, respectively, for a broad set of centrality intervals. The overall p_{T} shapes follow the expected behaviour: K/π rises from low p_{T} to a broad maximum around 0.4-0.6 GeV/c, while p/π exhibits the characteristic monotonic increase, consistent with the onset of collective radial flow in more central events.

- K/π **(TPC):** The Run 3 / Run 2 ratio remains close to unity in all centralities, with typical deviations of 10-20%. A mild centrality dependence is visible, where more peripheral classes tend to sit slightly above unity. This behavior mirrors the modest upward shifts seen earlier in the standalone kaon spectra and can be traced to shape differences in the TPC PID modeling in the 0.4-0.6 GeV/c region, where the dE/dx separation between pions and kaons is weakest. The agreement remains well within the combined systematic envelope.

- p/π **(TPC):** The Run 3 / Run 2 ratios are systematically above unity, with a more pronounced centrality ordering (peripheral $>$ central). The deviation increases from $\sim 20\%$ at low p_{T} up to factors of 2-3 in the most peripheral classes at the highest momenta accessible with the TPC. This mirrors the behavior observed in the proton and antiproton spectra individually and is consistent with differences in the primary-fraction correction (hyperon feed-down) and in the modeling of proton energy loss in detector material. The effect is charge-symmetric in the combined ratio, indicating that annihilation modeling of antiprotons is subdominant in this p_T range.

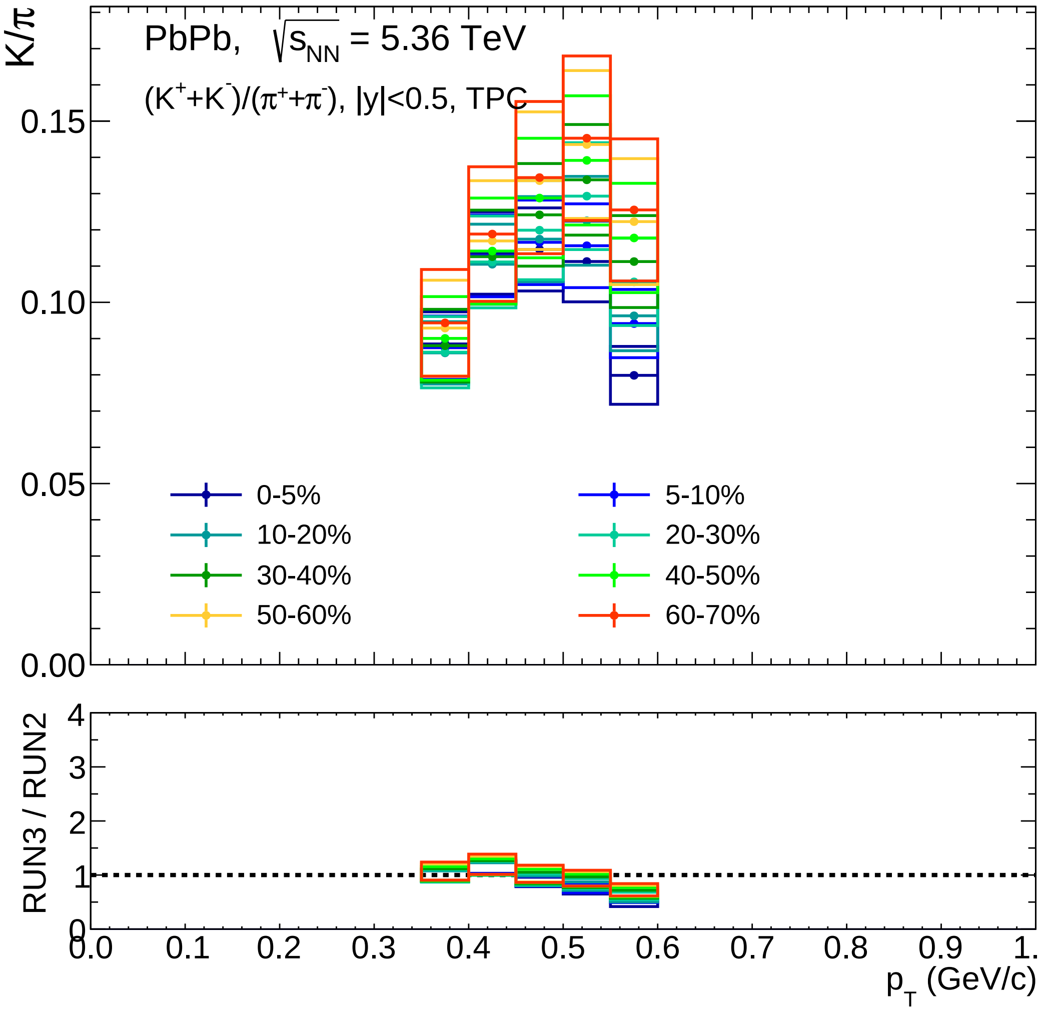

FIGURE 6.56: Transverse momentum dependence of the combined kaon-to-pion ratio $(K^+ + K^-)/(\pi^+ + \pi^-)$ measured with TPC PID for several centrality classes in Pb-Pb collisions at $\sqrt{s_{NN}} = 5.36$ TeV. The bottom panel shows the ratio of the Run 3 measurement to the published Run 2 reference.

Overall, the TPC ratios confirm the conclusions reached in the spectrum comparisons: the pion baseline is stable, kaons show small systematic shifts localized in the PID-transition region, and protons carry the largest species-specific bias associated with feed-down and material interactions. Importantly, the K/π shape is robust, while the p/π deviation suggests that the Run 3 proton corrections require further targeted cross-checks.

6.5.2 TOF results

The TOF based ratios, shown in Figs. 6.58 and 6.59, extend the reach of the measurement up to $p_T \approx 4$ GeV/c, where the TPC PID alone is no longer sufficient. The TOF results exhibit several noteworthy features.

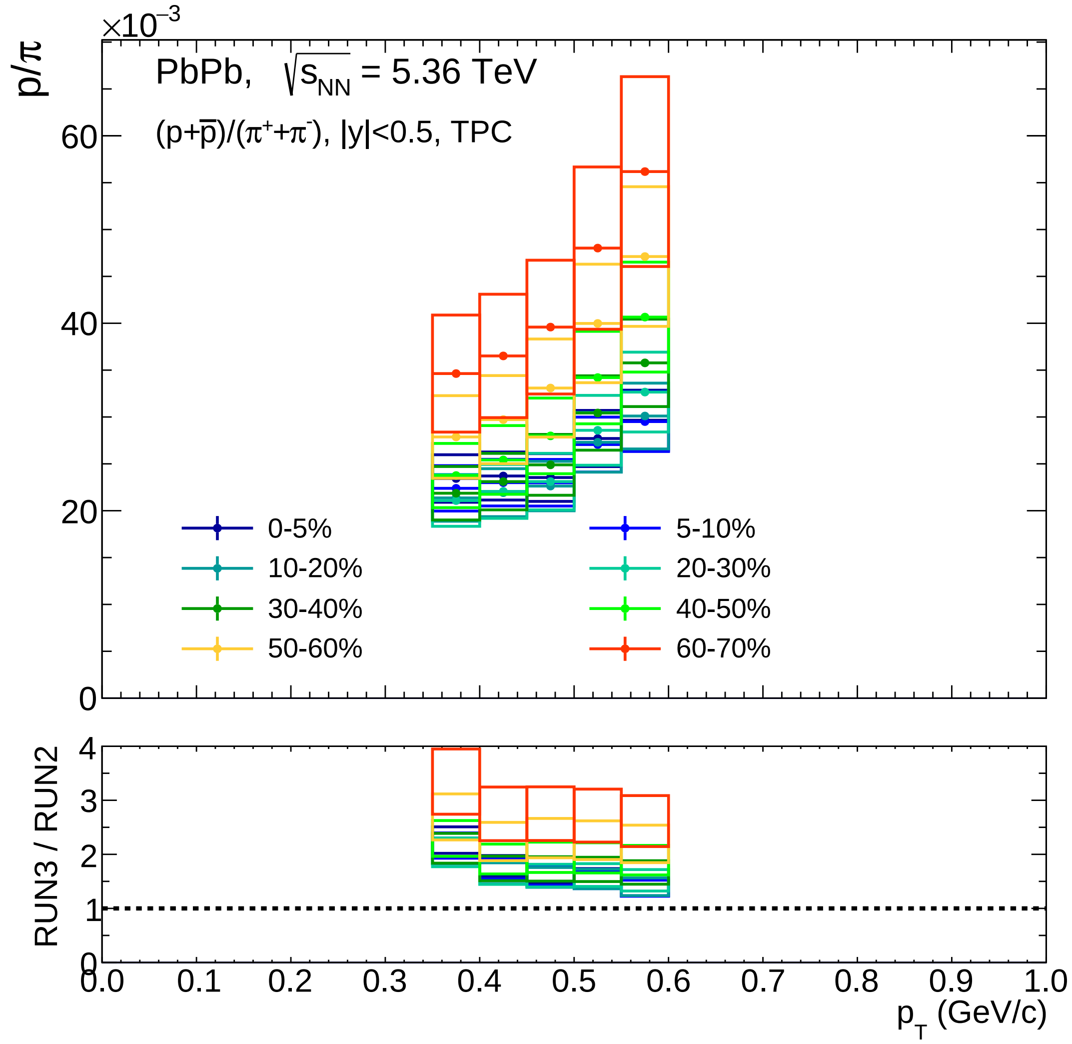

FIGURE 6.57: Transverse-momentum dependence of the combined proton-to-ion ratio $(p+\bar{p})/(\pi^{+}+\pi^{-})$ measured with TPC PID for several centrality intervals. The lower panel displays the Run 3 over Run 2 ratio, used to assess consistency with previously published Pb-Pb results.

- K/π **(TOF):** The Run 3 values agree remarkably well with the Run 2 reference across the full p_T span. Beyond 1 GeV/c, the ratio fluctuates tightly around unity with deviations rarely exceeding 10-15%. A small centrality dependence is present but remains significantly weaker than in the TPC-only case. This stability reflects the high purity of kaon identification in the TOF at intermediate and high momenta and confirms that the TOF matching efficiencies are well controlled.

- p/π **(TOF):** In contrast to kaons, the proton ratios show a clear upward deviation from unity. In the low-p_T region ($0.5 \lesssim p_T \lesssim 1.0$ GeV/c), the ratios clearly exceed unity, most noticeably for the peripheral 60-70% class where values approach a factor of two to three. This enhancement coincides with the momentum range in which proton identification in the TOF detector evolves from partial to full separation, and where the tracking and matching efficiencies are most sensitive to occupancy effects. In addition, small differences in the primary-fraction correction, for example those related to hyperon feed-down or interactions with detector material, naturally have a more pronounced impact in this regime.

  Moving toward the intermediate-p_T interval near the baryon enhancement peak ($1.2 \lesssim p_T \lesssim 2.0$ GeV/c), the Run 3/Run 2 ratio gradually decreases toward unity. This smooth trend indicates that the collective-flow-driven part of the proton spectra is consistently reproduced in Run 3, with only a modest centrality-dependent normalization effect remaining.

  At high transverse momentum ($p_T \gtrsim 2.5$ GeV/c), all centrality classes converge to ratios close to $R \approx 1.0$, with differences at the level of 10–20%. This is the region where PID, tracking, and primary-fraction systematics are minimal; accordingly, the near-unity ratios demonstrate that the Run 3 efficiency corrections, unfolding procedure, and material description are fully compatible with the established Run 2 baseline.

The comparatively good agreement for kaons across TPC and TOF, combined with the larger discrepancies in the proton sector, reinforces the interpretation that most species-dependent systematics are proton dominated. The consistency between the TPC and TOF p/π deviations moreover suggests that the source lies in common factors (such as primary-fraction inputs or global efficiency maps) rather than PID-specific issues.

6.5.3 Summary of ratio-to-pion comparisons

Taken together, the K/π and p/π ratios provide a concise diagnostic of the Run 3 reconstruction performance. The K/π ratios show good agreement with the published Run 2 results, with modest, localised deviations linked to the TPC PID transition region. By construction, these deviations cancel strongly in the TOF range. The p/π ratios show more substantial discrepancies that are consistent with the species-dependent systematics already identified in the standalone proton and antiproton spectra. Importantly, the p/π shape remains physically reasonable and preserves the expected centrality ordering, indicating that the Run 3 corrections capture the dominant physics trends even if the absolute scale requires further scrutiny.

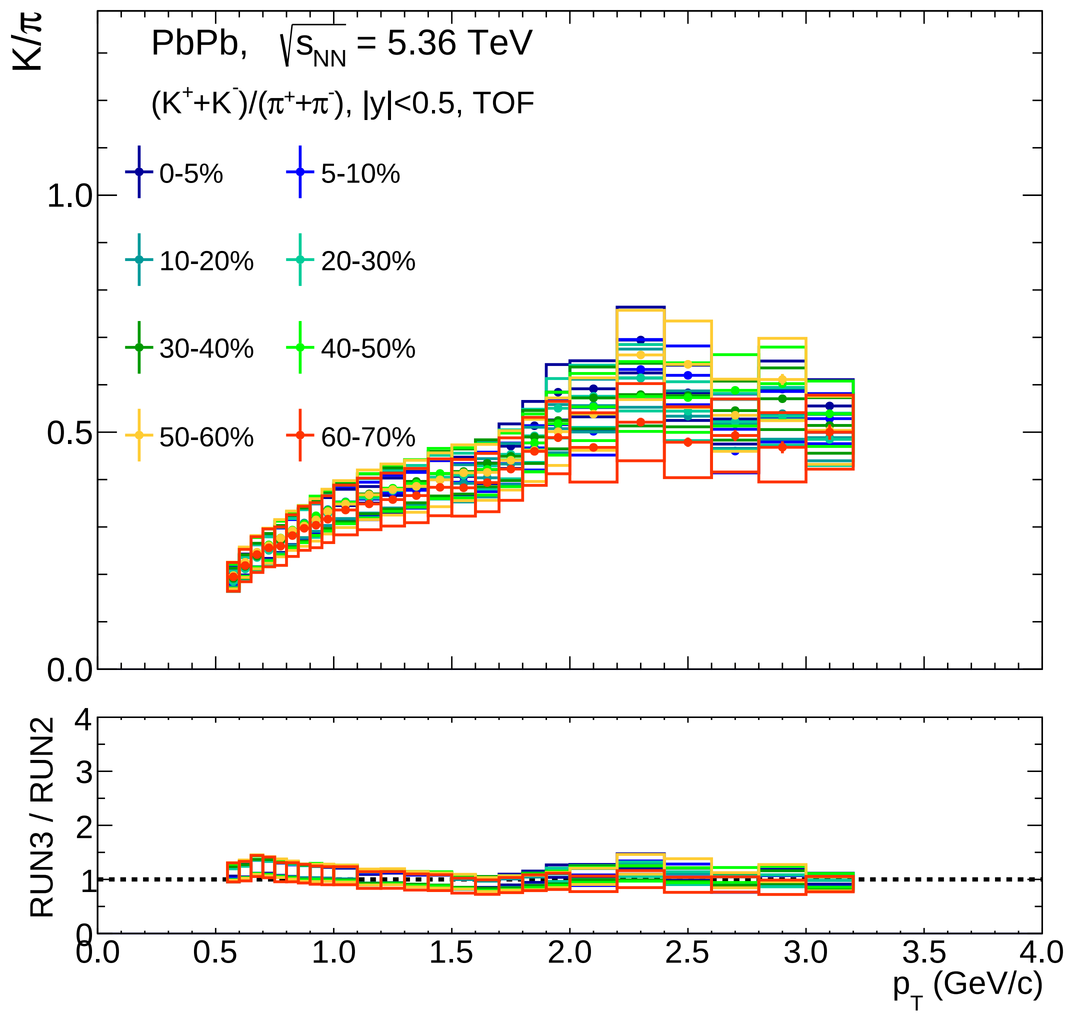

FIGURE 6.58: Kaon-to-pion ratio $(K^{+}+K^{-})/(\pi^{+}+\pi^{-})$ obtained using TOF PID for several centrality classes. The extended p_T coverage provided by the TOF allows the ratio to be measured up to $p_T \approx 4$ GeV/c. The lower panel shows the Run 3 to Run 2 comparison.

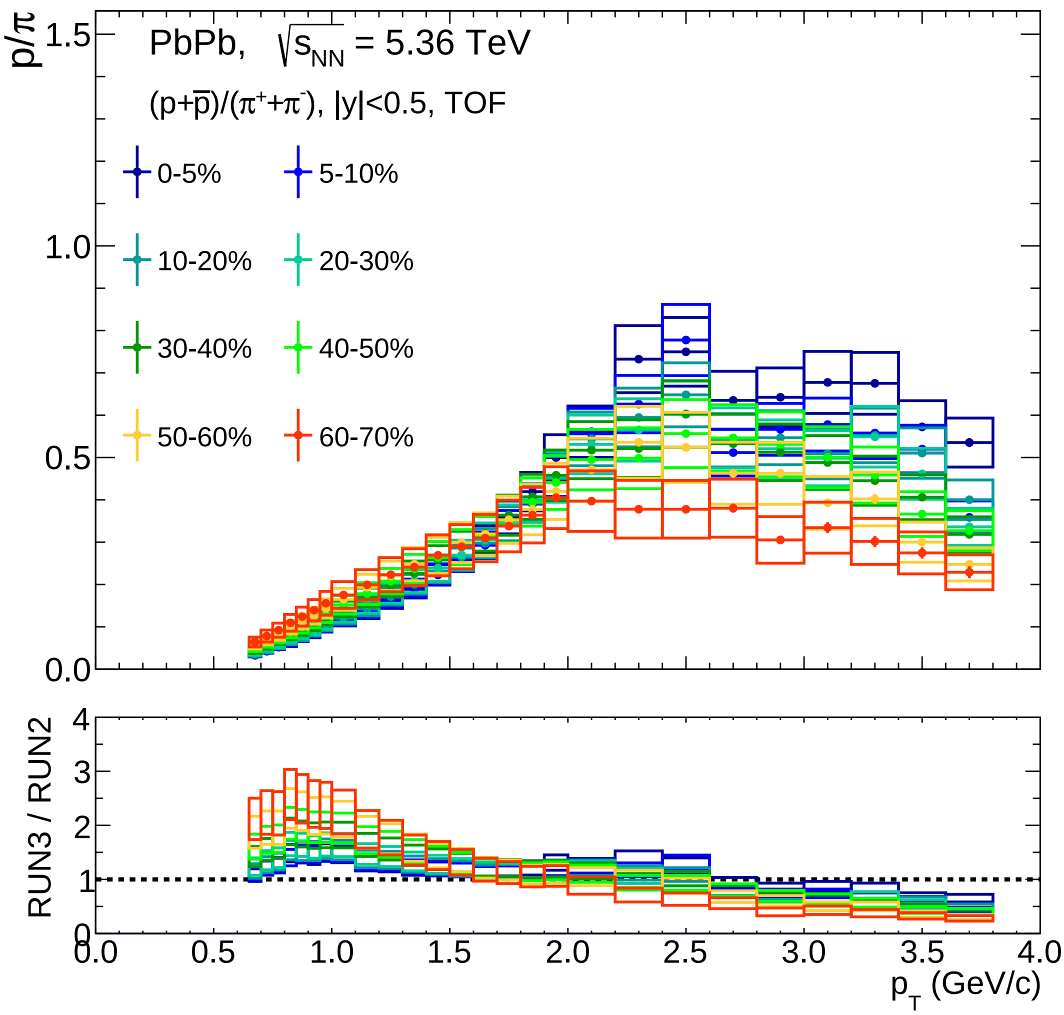

FIGURE 6.59: Proton-to-pion ratio $(p+\bar{p})/(\pi^{+}+\pi^{-})$ measured using TOF PID as a function of p_{T} and collision centrality. The bottom panel shows the ratio of the Run 3 measurement to the published Run 2 reference, which provides a direct validation of the Run 3 reconstruction and correction chain.

6.6 Combined Spectra

A central objective of the present analysis is to assess the internal consistency of the Run 3 PID framework by comparing fully corrected spectra obtained independently from the TPC and the TOF. Since these two detectors rely on fundamentally different PID observables, specific energy loss in the gas for the TPC and timing measurements for the TOF, their agreement provides a stringent validation of both reconstruction and correction procedures. Moreover, wherever the spectral points from the two detectors coincide within uncertainties, a statistically optimal merged spectrum can be constructed. This section presents a particle-by-particle comparison of the TPC and TOF corrected spectra, followed by an interpretation of the merged kaon spectrum and its comparison with the Run 2 reference. Each figure is discussed individually and in detail. Filled (solid) circles indicate spectra obtained with **TPC PID**, while open (hollow) circles indicate spectra obtained with **TOF PID**, where both appear at the same p_{T}, they show the TPC-TOF overlap region. The lower panels in each figure show the ratio of the Run 3 measurement to the published Run 2 reference.

6.6.1 Pions: TPC vs. TOF

Figure 6.60 shows the $\pi^+ + \pi^-$ spectra extracted independently from TPC and TOF PID. The overall spectral shapes follow the expected steep fall with increasing , and the centrality ordering is reproduced identically by both detectors. However, a closer inspection of the overlapping region reveals that the spectra do not overlap in most centrality classes. In the central and mid-central bins (0-5%, 5-10%, and 10-20%), the TOF yields lie systematically below the TPC yields over the entire overlap range. This mismatch gradually diminishes toward more peripheral collisions, and in the 50-60% and 60-70% bins a partial convergence is visible, although a residual separation persists. This behaviour has well-understood origins. The TPC pion identification in central collisions operates in a regime where the $\mathrm{d}E/\mathrm{d}x$ separation between pions and kaons is minimal, and the occupancy corrections (cluster sharing, space-charge distortions, gain fluctuations) carry non-negligible uncertainties. In contrast, the TOF response degrades only at low p_T, where matching and inefficient track extrapolation dominate. The observed detector-dependent separation increases with multiplicity, consistent with the picture that TPC performance is more affected by centrality than TOF. Because the two spectra fail to overlap in a stable and reproducible way across the full centrality range, a merged pion spectrum cannot be constructed without introducing detector-dependent biases.

6.6.2 Kaons: TPC vs. TOF.

Figure 6.61 presents the analogous comparison for kaons. In stark contrast to the pion case, the TPC and TOF spectra lie almost perfectly on top of each other across most of the overlapping p_T region and for all centrality classes. This excellent agreement is non-trivial: kaon identification in the TPC remains robust up to intermediate p_T because the kaon band in $\mathrm{d}E/\mathrm{d}x$ is still well-separated from the pion band in Run 3 conditions, while the TOF provides clean time-based separation up to several GeV/c. The stability of the overlap implies that both PID systems are correcting for acceptance, efficiency, and secondary contamination in a mutually consistent manner. The absence of any centrality-dependent divergence further indicates that occupancy-driven effects do not introduce significant biases in either detector.

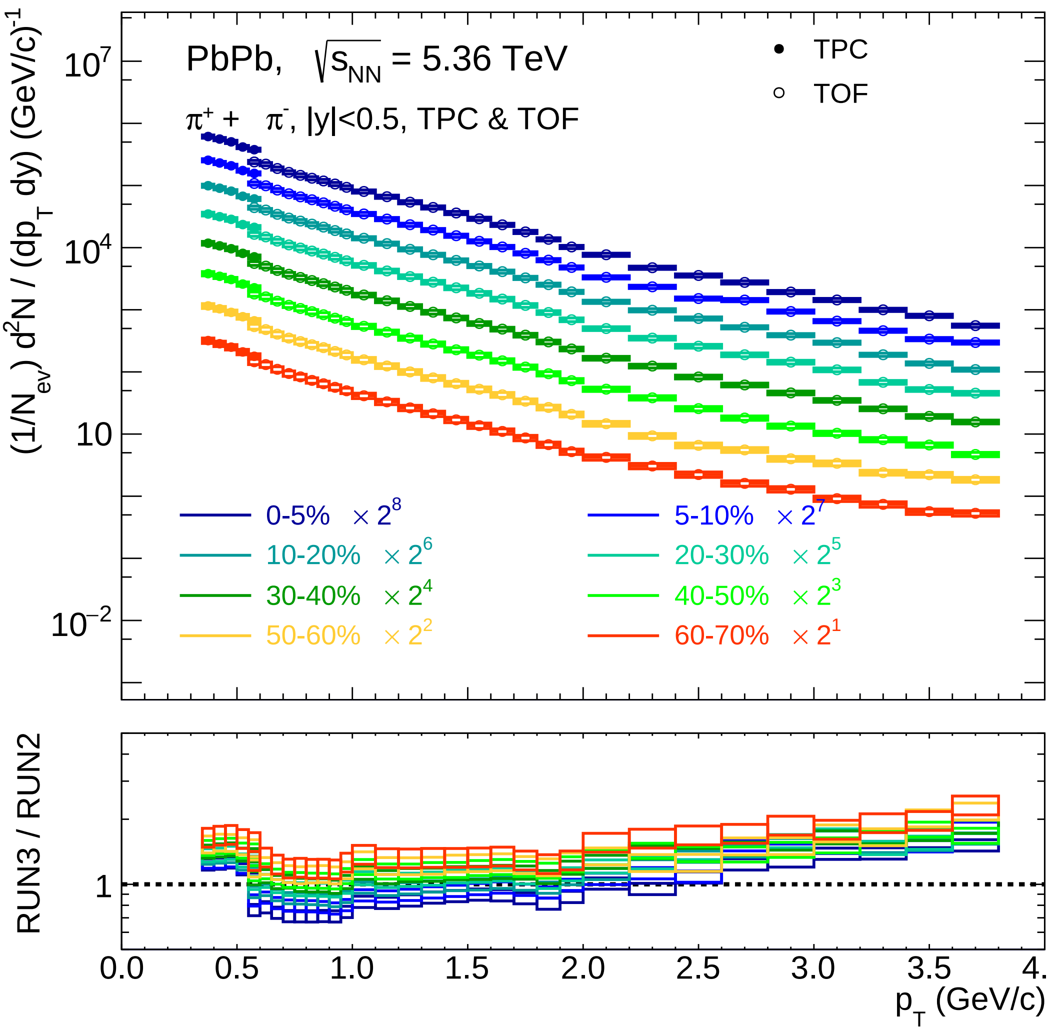

FIGURE 6.60: Pion spectra $(\pi^{+}+\pi^{-})$ measured using TPC (filled circles) and TOF (open circles) PID as a function of p_{T} and collision centrality. The bottom panel shows the Run 3/Run 2 ratio for each centrality.

This level of agreement uniquely qualifies the kaon spectra for a combined TPC-TOF merging.

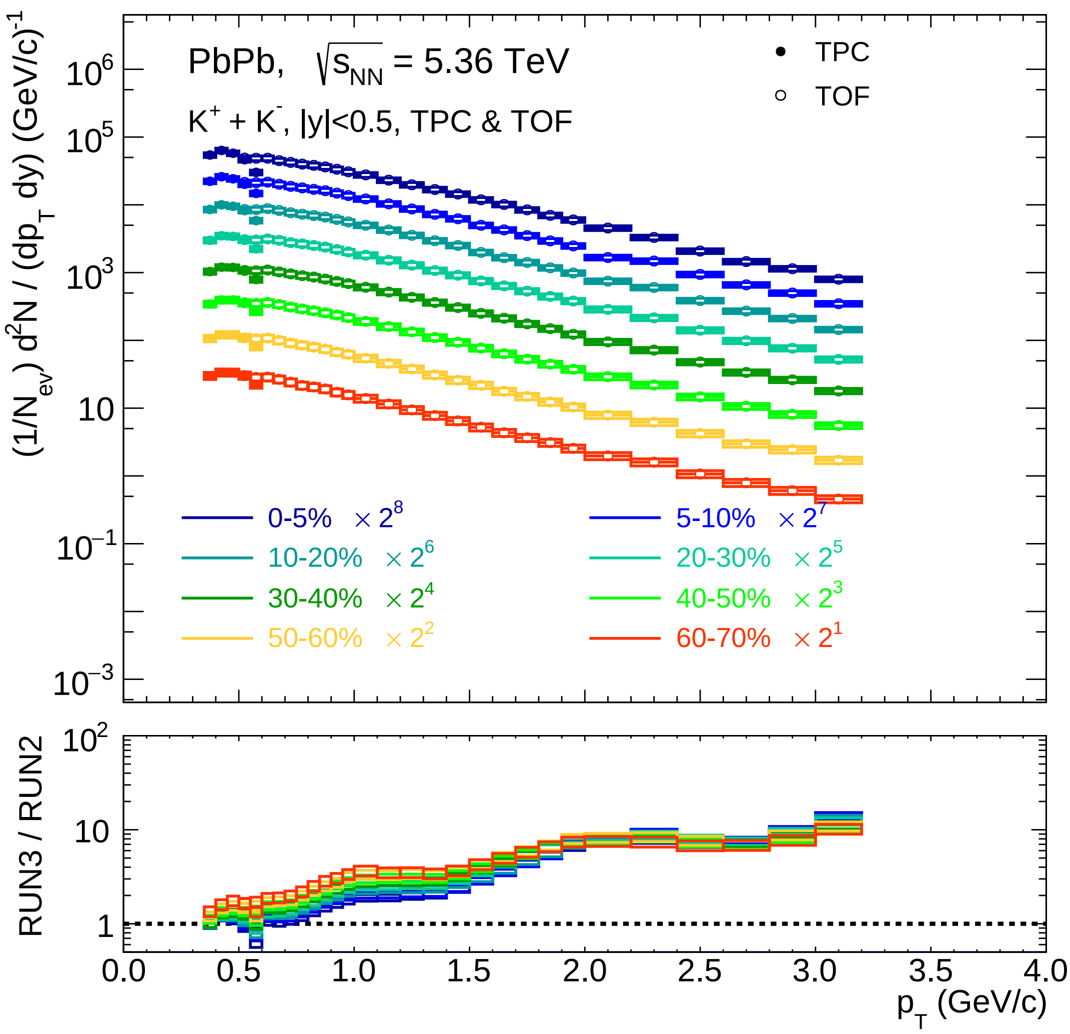

FIGURE 6.61: Kaon spectra $(K^{+}+K^{-})$ measured using TPC (filled circles) and TOF (open circles) PID as a function of p_{T} and collision centrality. The bottom panel shows the Run 3/Run 2 ratio for each centrality.

6.6.3 Protons: TPC vs. TOF.

Figure 6.62 displays the comparison for protons. Here, the situation is the opposite of the kaon case. The TOF proton spectra sit consistently below the TPC spectra across all p_T and centrality intervals. The size of the discrepancy is both momentum- and centrality-dependent. Even at low p_T, where both detectors have their strongest proton identification power, the spectra do not converge. The origin of the mismatch lies in the proton-specific corrections. Protons and antiprotons receive substantial contributions from weak decays and suffer significant hadronic interactions in detector material. The TPC handles secondaries through DCA-template fits, while the TOF relies much more strongly on track-selection purity and topology-based rejection. Further investigation is required to undestand the emergence of such discrpancies.

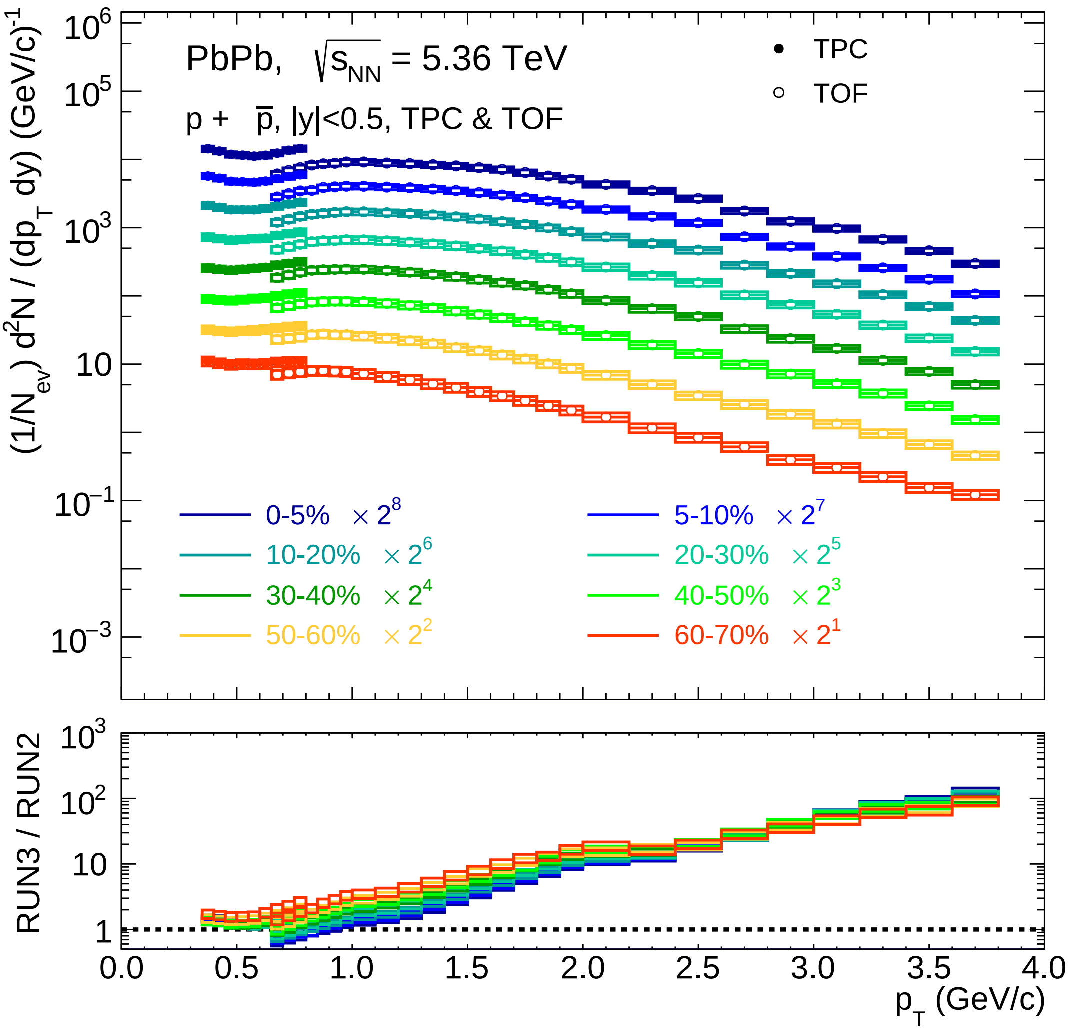

FIGURE 6.62: Proton spectra $(p+\bar{p})$ measured using TPC (filled circles) and TOF (open circles) PID as a function of p_{T} and collision centrality. The bottom panel shows the Run 3/Run 2 ratio for each centrality.

6.6.4 Merged Kaon Spectrum and Comparison with Run 2.

Since kaons exhibit near-ideal agreement between TPC and TOF, a statistically weighted merged spectrum is constructed and shown in Fig. 6.63. In the top panels, the merged spectrum inherits the superior statistical precision of the TOF at moderate and high p_T and the stability of the TPC at low p_T, resulting in a smooth, high-quality distribution across the full p_T interval. The merging leads to visibly reduced uncertainties and a more coherent spectral shape. The bottom panel presents the

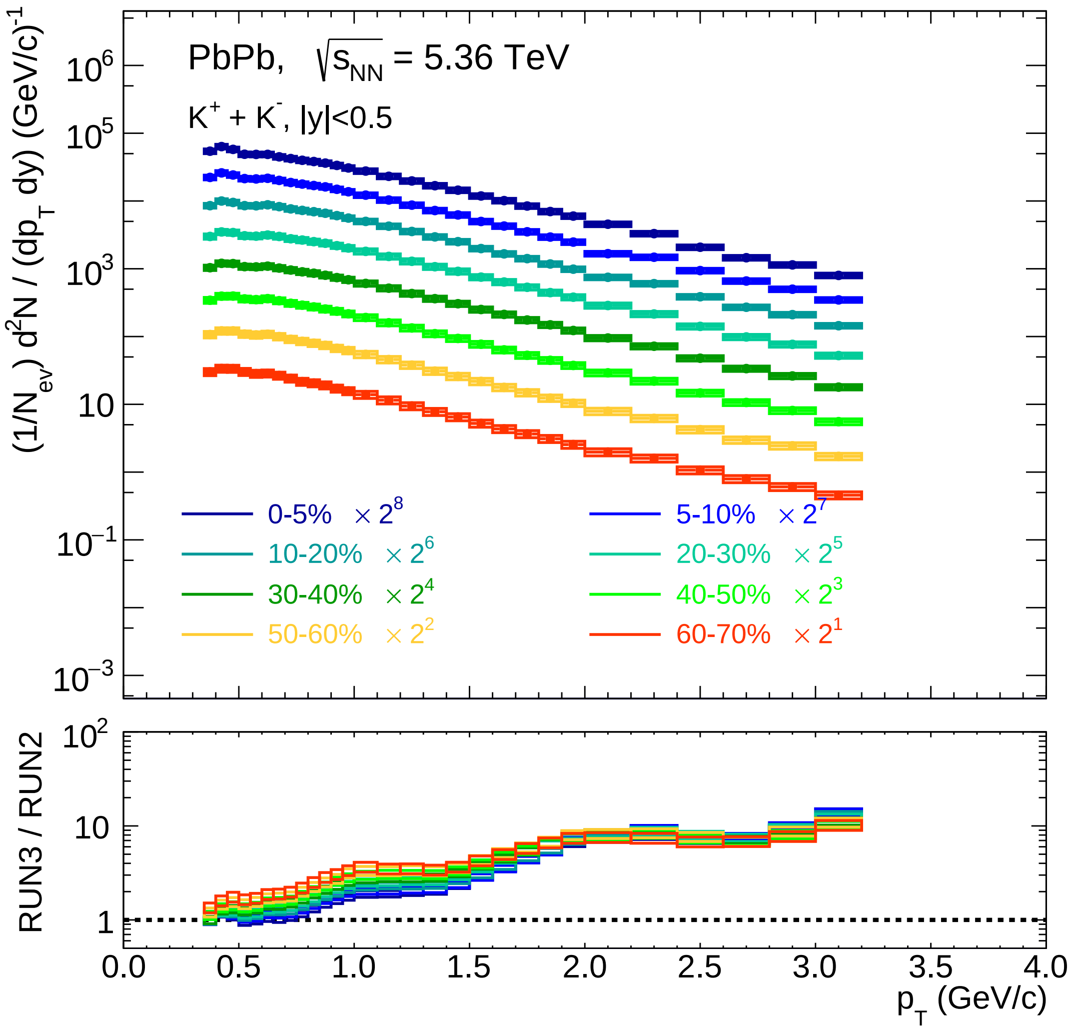

FIGURE 6.63: Merged kaon spectra $(K^+ + K^-)$ constructed from TPC and TOF PID. In the overlap region, the two measurements are consistent and combined (e.g. via inverse-variance weighting) to yield a single spectrum. The bottom panel shows the Run 3/Run 2 ratio.

ratio of the merged Run 3 spectrum to the previously published Run 2 measurement at $\sqrt{s_{\rm NN}} = 5.02$ TeV. At low p_T (below 0.8 GeV/c), the ratio fluctuates gently around unity, with deviations typically within 10%, and shows only minimal centrality dependence. This level of agreement is expected, as the hadron-yield systematics in this p_T region are dominated by detector material modeling and feed-down corrections, both of which have been considerably improved in Run 3. In the intermediate p_T region (1-2 GeV/c), the merged spectrum lies moderately above the Run 2 reference by 10-20%, consistent with differences in the kaon PID parametrization and updated efficiency calibrations used in Run 3. Over 2 GeV/c, the ratio increases and then saturates.

Taken together, the kaon comparison demonstrates that the Run 3 PID and correction chain is performing consistently across detectors and centralities, enabling a robust merged spectrum. The contrasting behaviour observed for pions and protons highlights the particle-dependent complexity of PID in high-multiplicity environments and delineates the avenues where further refinement of correction procedures may be required.

6.7 BW Analysis and Extraction of Freeze-Out Parameters

A quantitative characterization of the collective expansion dynamics in heavy–ion collisions is commonly achieved through simultaneous fits of the identified–hadron transverse–momentum spectra using the Boltzmann-Gibbs Blast Wave (BGBW) model. As discussed in Sec. 3.3.1, this hydrodynamically motivated parametrization assumes that all particles decouple from the medium at a common kinetic freeze-out temperature T_{kin}, while experiencing a collective radial velocity field $\beta(r)$ described by a power-law profile. In this framework, the spectral shapes of π^+, K^+ and p jointly constrain the freeze–out conditions, with light particles providing sensitivity to T_{kin} and heavier species probing the strength and profile of radial flow. The model parameters $\langle\beta\rangle$, β_{max}, T_{kin}, the velocity profile exponent n, and the speed–of–sound proxy c_s together map the system's evolution at the point of decoupling.

For the present analysis, BGBW fits have been performed using only the TOF identified spectra. This choice is motivated by the observation that, while the TOF results agree better with published references across the entire p_{T} range, the TPC and TOF measurements do not achieve a stable matching for all particle species, especially in central collisions. Because a consistent multi–species fit requires mutually compatible shapes, we restrict the input to the high–quality TOF spectra where the PID separation is well–understood and the systematic uncertainties are under robust control. Figure 6.64 shows the simultaneous BGBW fit for the 0–5% centrality class. The fitted curves reproduce the steeply falling pion spectrum, the intermediate mass curvature of the kaons, and the baryon peak of the protons within the chosen fitting intervals. The best fit parameters indicate a strong collective expansion with a large average radial flow $\langle\beta\rangle \approx 0.56$ and a correspondingly high β_{max}, while the extracted kinetic freeze–out temperature $T_{\text{kin}} \approx 125$ MeV remains consistent with expectations for central PbPb collisions. The excellent agreement among the three species demonstrates that the Run 3 TOF spectra support a thermodynamically coherent description. A contrasting picture emerges in the 50–60% class, shown in Fig. 6.65. Here the spectra are notably softer, and the fit converges to a slightly lower flow velocity ($\langle\beta\rangle \approx 0.51$) together with a modestly reduced temperature. The change in n reflects a mild reshaping of the velocity profile as the system becomes more dilute. The radial–flow evolution inferred from the fits follows the expected centrality ordering: central collisions exhibit the strongest build–up of collective motion, while peripheral events retain weaker flow and a higher relative contribution from non-thermal processes. The centrality dependence of the extracted parameters is summarized in Fig. 6.66. All quantities show smooth monotonic behaviour. The average radial velocity $\langle\beta\rangle$ decreases from approximately 0.56 in central collisions to about 0.50 near 60% centrality, while T_{kin} remains stable to within a few percent, consistent with previously reported freeze–out systematics. The speed–of–sound proxy c_s shows only weak centrality dependence, suggesting that the shape of the

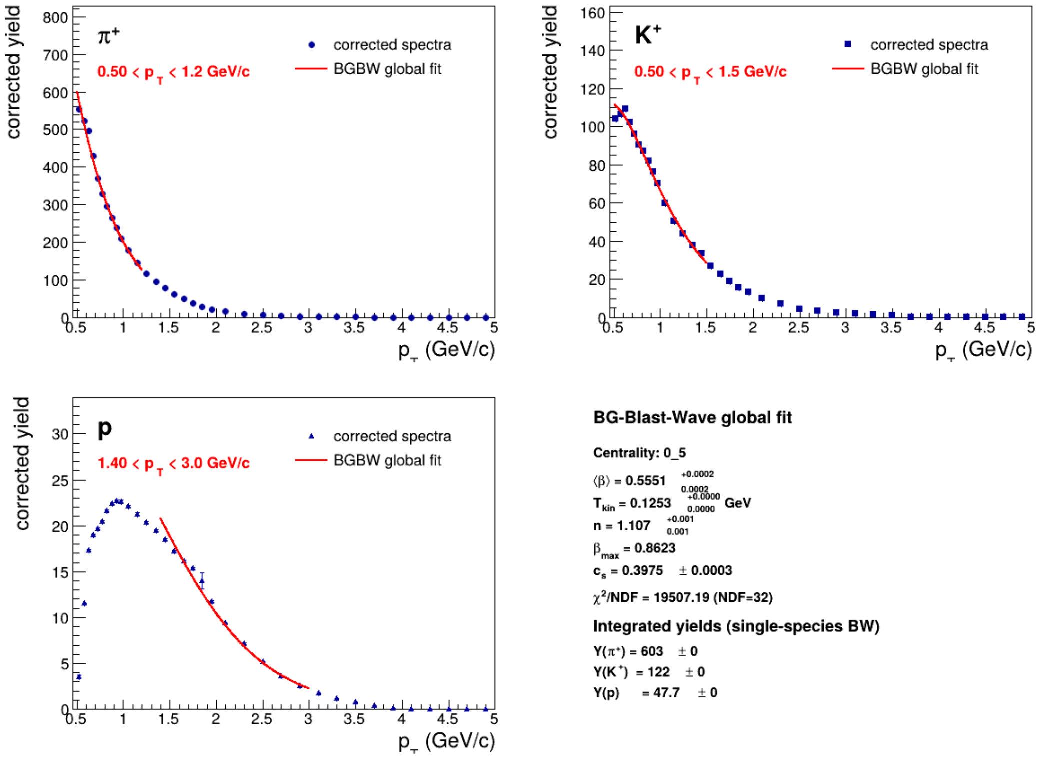

FIGURE 6.64: Simultaneous BGBW fit to the π^+, K^+ and p spectra in the 0-5% centrality interval using TOF–identified corrected yields. The fitted parameters are listed in the bottom right panel.

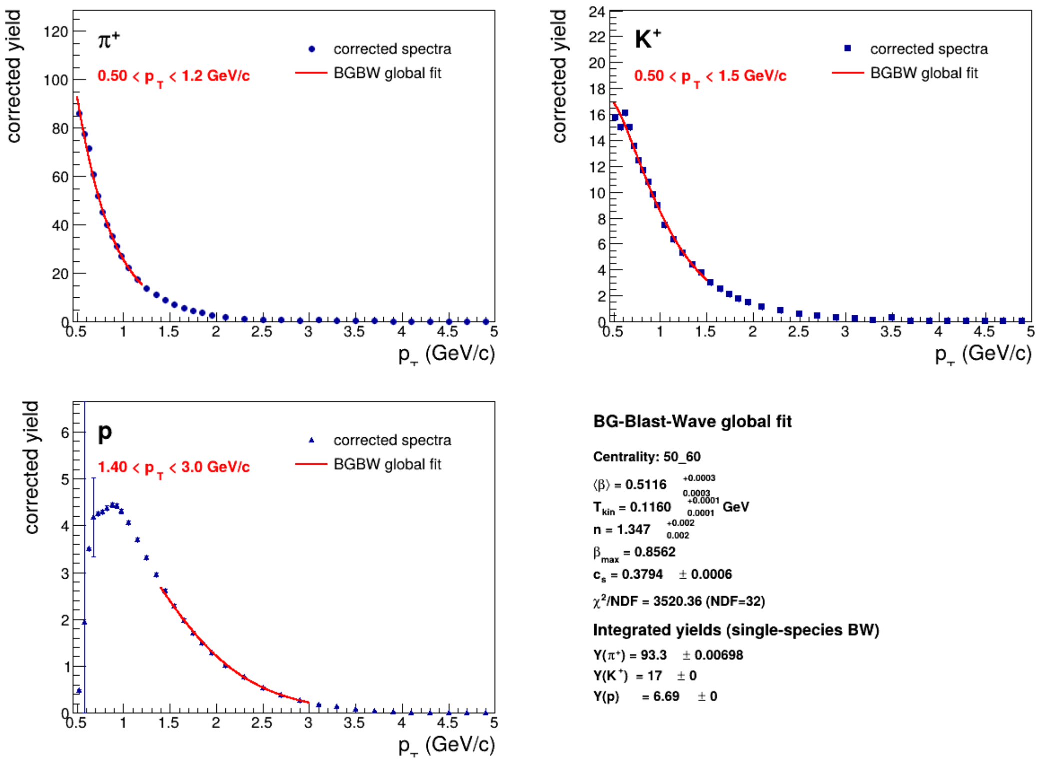

FIGURE 6.65: Same as Fig. 6.64, but for the 50-60% centrality class.

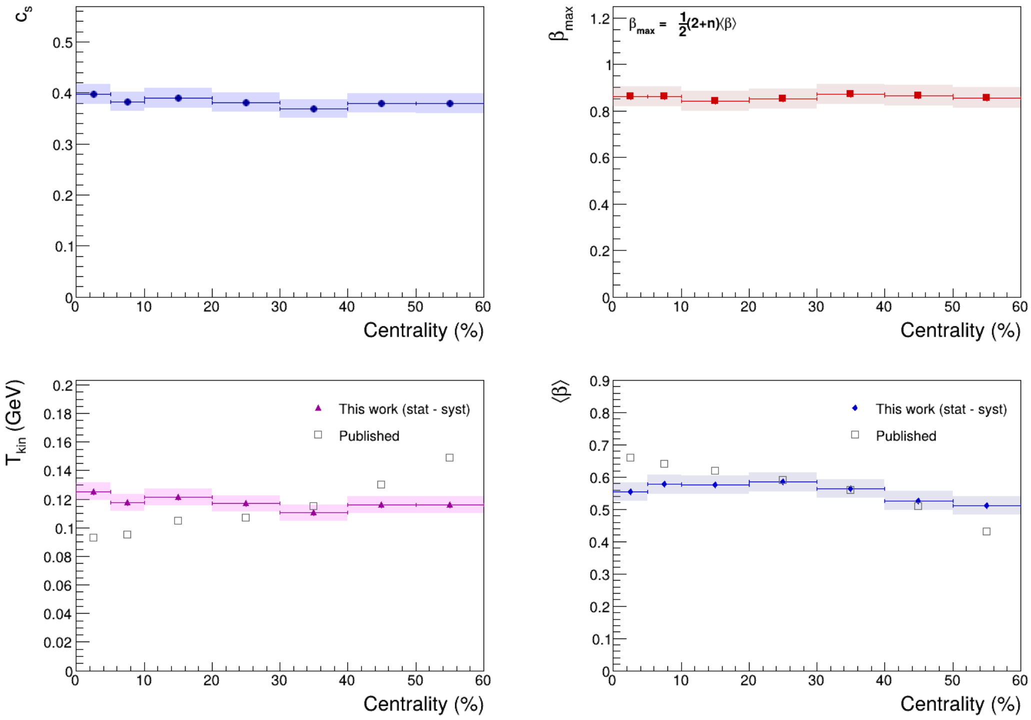

FIGURE 6.66: Centrality dependence of the BGBW parameters extracted from the simultaneous TOF fits. Colored bands represent statistical and systematic uncertainties combined. Published Run 2 values are shown for comparison.

flow profile remains nearly unchanged across the system–size range probed here. The systematic uncertainties on the BGBW parameters are shown in Fig. 6.67. Their

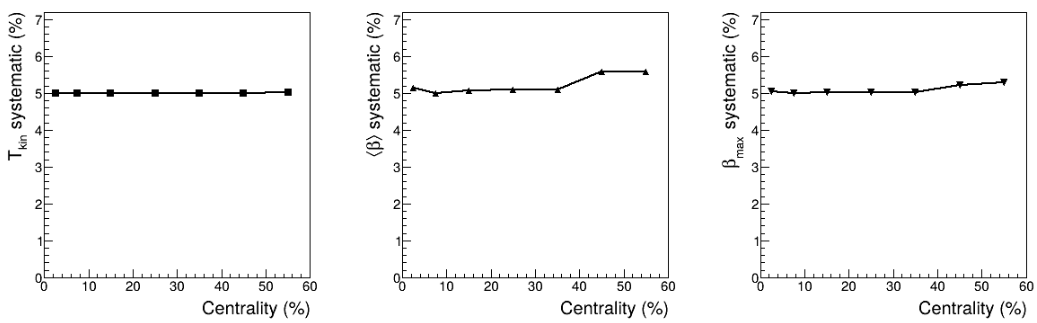

FIGURE 6.67: Relative systematic uncertainties on T_{kin}, $\langle\beta\rangle$ and β_{max} as a function of centrality. The uncertainties remain largely independent of centrality and are typically at the level of 5%.

centrality independence reflects the fact that the dominant contributions stem from common sources such as PID efficiency variations, fitting–range dependence, and the propagation of yield systematics into the correlated multi–species fit. Typical uncertainties lie at the level of 5%, indicating a high degree of stability in the extraction of the freeze–out parameters.

These results demonstrate that the Run 3 spectra, when analyzed through the Blast–Wave framework, yield a physically consistent picture of the freeze–out dynamics at $\sqrt{s_{\mathrm{NN}}} =$ 5.36 TeV. The extracted parameters reproduce the qualitative and quantitative trends seen in lowerenergy PbPb data, confirming that the Run 3 reconstruction and correction chain is capable of delivering precise and coherent multi–species measurements suitable for hydrodynamic modeling.

6.8 Integrated Yield

The p_{T}-integrated particle yield,

$$\frac{\mathrm{d}N}{\mathrm{d}y} = \int f(p_{\mathrm{T}})\,\mathrm{d}p_{\mathrm{T}}, \tag{6.27}$$

is a central observable in heavy-ion collisions. It encodes the total number of produced hadrons at midrapidity and therefore connects directly to the bulk properties of the medium created in the collision. In particular, integrated yields are used to extract chemical freeze-out parameters in statistical hadronization models, to test the scaling of particle production with centrality, and to quantify strangeness enhancement and baryon suppression.

The yields presented here are obtained by integrating the fully corrected p_{T} spectra for each species. The integration covers the measured range directly, while the unmeasured low- and high-p_{T} regions are accounted for using fits based on the Boltzman Gibbs Blast Wave functional form (Sec. 3.3.1). Statistical and systematic uncertainties (Fig. 6.69) are propagated consistently, and the shaded bands in the figure represent the total (stat.+syst.) uncertainty on the integrated yield for each centrality class. Systematics are estimated by varying the fit parameters such as $< \beta >$, n and T_{kin}

Figure 6.68 shows the integrated yields of π^+, K^+, and p as a function of centrality. Pions are drawn with blue circular markers, kaons with green squares, and protons with red triangles. The horizontal extent of each point reflects the width of the centrality interval, while the vertical bars indicate the uncertainty on the yield.

A clear centrality dependence is visible for all species. The pion yield shows the steepest rise toward central collisions, reflecting their role as the dominant carriers of entropy in the system. Between 0-5% and 50-60%, the π^+ yield decreases by roughly a factor of six, consistent with the large change in charged-particle multiplicity across these centralities.

Kaons follow the same monotonic trend, but with a reduced overall magnitude and a milder centrality slope. This behaviour is characteristic of strange hadron production, where canonical suppression and strangeness enhancement modulate the centrality dependence. The observed increase of K^+ yields toward central collisions is fully consistent with established strangeness enhancement patterns.

Protons exhibit the shallowest decrease with centrality. Their yield is about an order of magnitude smaller than that of kaons and two orders of magnitude smaller than that of pions. The centrality dependence reflects the changing baryon density and the interplay between baryon transport and pair production. The relatively flat behaviour compared to pions also matches expectations from baryon chemical potential approaching zero at LHC energies.

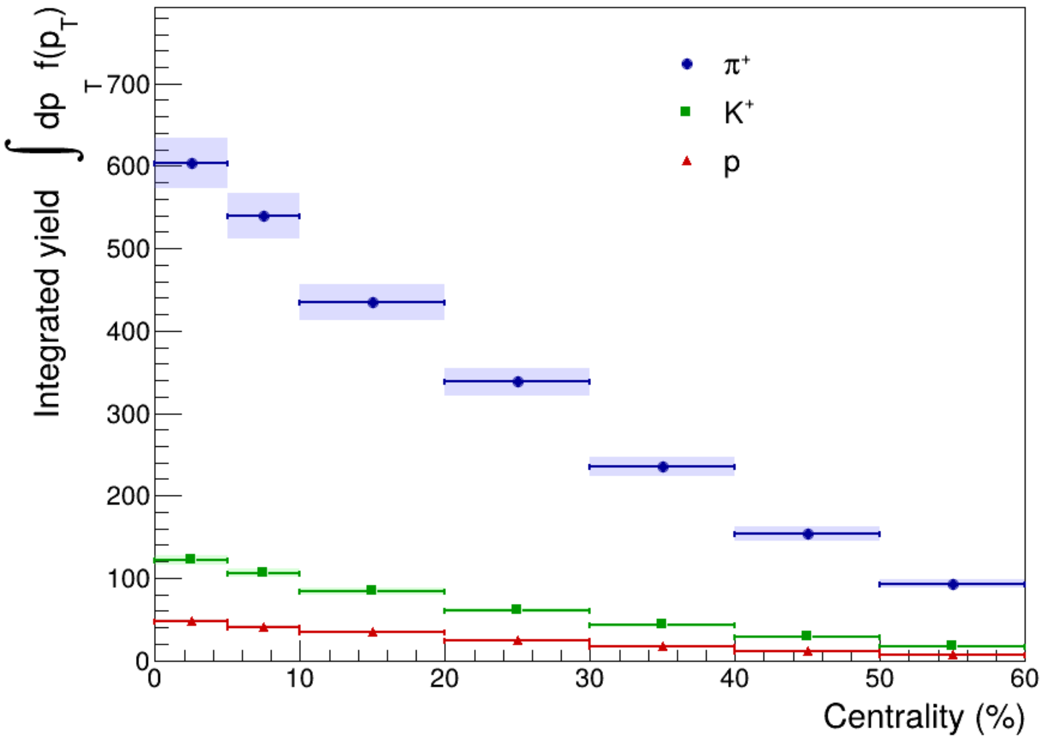

FIGURE 6.68: Integrated midrapidity yields of π^+ (blue circles), K^+ (green squares), and p (red triangles) as a function of collision centrality. Vertical bars show total uncertainties.

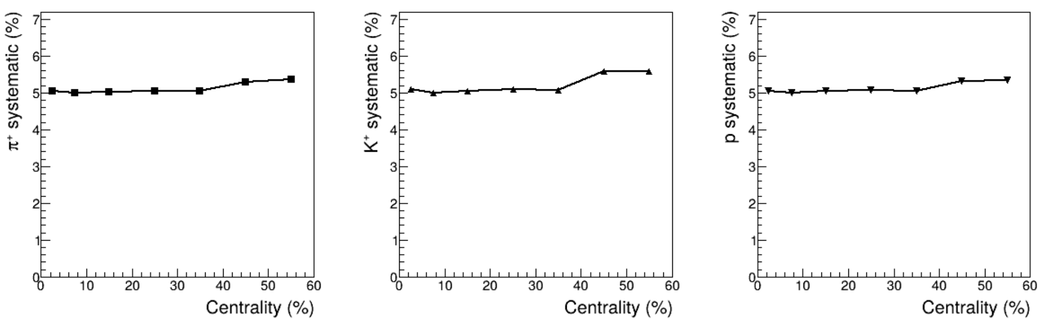

FIGURE 6.69: Systemic uncertainties of differnt particle species

Overall, the integrated-yield hierarchy

$$\pi^+ \; > \; K^+ \; > \; p$$

and their respective centrality slopes follow the qualitative patterns observed in previous LHC measurements. The behaviour is consistent with a picture in which particle production scales primarily with the underlying entropy density, with strangeness and baryon number introducing species-dependent modulations.

Chapter 7

Light Ion Collisions: OO Analysis & Results

7.1 Introduction and Physics Motivation

The 2023 LHC heavy-ion program introduced, for the first time, collisions of two oxygen nuclei (OO) at $\sqrt{s_{\mathrm{NN}}} = 5.36$ TeV [148]. These *light ion* collisions provide a unique bridge between the physics of small systems (pp, pPb) and the large, strongly interacting systems created in PbPb collisions. With only sixteen nucleons per nucleus, OO collisions constitute the lightest *heavy ion* system ever operated at the LHC and open a completely new experimental window on the evolution of collectivity with system size [149, 150].

The motivation for OO collisions is deeply rooted in several open questions in high-energy nuclear physics. In large systems such as PbPb, a strongly coupled QGP is known to form and exhibit near-ideal hydrodynamic behaviour, with significant radial and anisotropic flow, strangeness enhancement, and quark-recombination-driven hadronization [151]. In contrast, small systems (pp and pPb) have revealed surprising signs of collective-like phenomena, including long-range ridge correlations, flow-like patterns, and enhanced strange-hadron production [152, 153], but the extent to which these signatures require QGP formation remains an active topic of debate [154, 155]. OO collisions provide an intermediate configuration uniquely suited to address these questions.

From an experimental perspective, OO collisions offer several advantages:

- **System-size scaling of collectivity:** By reducing the initial transverse size and multiplicity relative to PbPb, OO collisions probe the minimal conditions required for hydrodynamic behaviour and QGP-like expansion [156].
- **Control of initial-state geometry:** Light ions have small deformation and simple nuclear structure, providing a cleaner testing ground for models of initial-state fluctuations (IP-Glasma, TRENTo, Angantyr) and their impact on final-state flow.
- **Benchmarking global event generators:** Models such as HIJING, AMPT, EPOS-LHC, and PYTHIA Angantyr are poorly constrained in light-ion regimes; OO data are essential for tuning and validating them [157].
- **Mapping the QCD phase diagram by system size:** OO collisions complement the LHC's long-term programme aiming to characterize QCD matter across temperature, baryon density, geometry, and system size.

Experimentally, OO events exhibit moderate particle multiplicities, significantly lower than PbPb but substantially above pp, enabling high-precision tests of reconstruction performance, tracking, and PID in the intermediate-occupancy regime where detector effects transition smoothly from small to heavy-ion conditions.

The present chapter presents the first Run 3 OO analysis performed within this thesis. The general analysis chain-event selection, track selection, PID, yield extraction, and all correction procedures follows the methodology established and validated for PbPb collisions in Chapter 5. Only OO specific aspects are presented here: the dataset, Monte Carlo samples, centrality determination, and the physical interpretation of OO as a light-ion reference system. This ensures complete methodological consistency between PbPb and OO while highlighting the unique physics opportunities offered by light-ion collisions.

7.2 Datasets and Simulation Samples

The OO dataset analyzed in this chapter was recorded by the ALICE experiment during the dedicated Run 3 light-ion campaign in early 2025. The present analysis makes use of the officially reconstructed Run 3 derived datasets and their corresponding Monte Carlo simulations, prepared within the ALICE O2 computing framework.

7.2.1 Data and Monte Carlo Samples

- **Data sample:** The analysis is based on the derived dataset `LHC25ae_pass1`, comprising minimum-bias OO collisions at $\sqrt{s_{\mathrm{NN}}} = 5.36$ TeV. This dataset was processed with the full Run 3 reconstruction chain (TPC-ITS global tracking, continuous readout, clusterization, and machine-learning-based track quality filters).
- **Monte Carlo simulation:** The corresponding simulation sample used for all corrections is `LHC25g6`, produced with complete Run 3 detector geometry and reconstructed with the identical O2 workflow, ensuring one-to-one compatibility with the data.

  The MC employs the standard ALICE light-ion generator configuration, tuned to reproduce the expected multiplicity and pseudorapidity density of OO collisions. Primary particle identity is enforced at truth level, and the detector response is simulated using GEANT3 with the updated Run 3 material budget.

The chosen data and MC samples are the official ALICE Run 3 light-ion datasets recommended for physics analyses. Their reconstruction settings, configuration files, material maps, alignment constants, and trigger conditions are fully synchronised, which is essential for:

- deriving reliable efficiency and acceptance corrections,
- ensuring consistency with PbPb results presented earlier,
- enabling cross-system comparisons (PbPb vs. OO),
- providing a validated baseline for collective flow studies and model fits.

7.2.2 Consistency with the PbPb Analysis Chain

To guarantee a meaningful comparison between OO and PbPb systems, the entire analysis pipeline mirrors the procedure established in Chapter 5: event selection, track quality cuts, PID strategy, raw-yield extraction, and all efficiency and primary-fraction corrections are applied identically unless the OO system size explicitly requires an adjusted definition (e.g. centrality calibration).

- **Event selection** uses the same criteria as in PbPb: a reconstructed vertex within ± 10 cm along the beam axis, a valid FIT trigger, and quality requirements consistent with O2 Run 3 recommendations.
- **Track selection** (see Sec. 5.4) uses the same criteria as PbPb: $|\eta| < 0.8$, ITS-TPC global tracking, at least 70 TPC crossed rows, ratio of crossed to findable clusters > 0.80, TPC χ^2/cluster < 4, and tight DCA requirements to ensure primary-particle purity.
- **PID and yield extraction** follow the exact same methods established for the PbPb system (Secs. 6.1.1 - 6.1.2), ensuring direct comparability of spectral shapes, particle ratios, and flow-sensitive observables.

7.3 Yield Extraction in OO Collisions

In this work, the identified-hadron spectra are extracted using exclusively the TOF detector. The TOF provides precise timing information for reconstructed tracks and thus enables clean separation of π, K, and p over a broad p_T range at midrapidity, even in the lower-multiplicity environment characteristic of light-ion collisions.

The PID strategy follows exactly the methodology developed and validated in PbPb collisions (Sec. 6.1.2). For each reconstructed track, the measured time of flight is compared to the expected value under a given mass hypothesis $m \in \{\pi, K, p\}$, and the normalized residual

$$n_{\sigma,\mathrm{TOF}} \equiv \frac{t_{\mathrm{meas}} - t_{\mathrm{exp}}(m)}{\sigma_t} \tag{7.1}$$

is formed, where t_{meas} is the measured time, $t_{\mathrm{exp}}(m)$ is the expected time-of-flight for the assumed mass, and σ_t is the total time resolution (intrinsic TOF resolution, start-time resolution, and tracking contribution combined).

In the PbPb analysis, TPC and TOF information were used in complementary p_T ranges. However, sizeable inconsistencies were observed between TPC- and TOF-based corrected spectra for pions and protons, especially in central PbPb events, which prevented a robust combined fit over the full p_T range. For kaons, a consistent TPC-TOF overlap was achieved, but the overall conclusion was that, at the current stage of the Run 3 reconstruction, TOF based PID provides the most stable and internally consistent spectra across species and centralities.

Since the goal of the present chapter is a *differential comparison* between heavy-ion (PbPb) and light-ion (OO) collisions, it is essential to use a homogeneous PID strategy. Therefore, the OO analysis is deliberately restricted to TOF-based PID, using the same models, fit strategy, and correction pipeline as in the PbPb case. This guarantees that any differences observed between PbPb and OO spectra can be attributed to physics (system size, geometry, multiplicity) rather than to detector- or method-specific artefacts.

7.3.1 Yield extraction from TOF n_σ distributions

The construction of $n_{\sigma,\mathrm{TOF}}$ distributions, the binning strategy, and the fit functions used to extract raw yields in OO collisions follow the PbPb procedure described in Sec. 6.1.2. Only system-specific inputs, the OO centrality definition and the available p_T reach per species, are different.

Binning and centrality classes

The $n_{\sigma,\mathrm{TOF}}$ spectra are built in narrow p_T intervals. For direct comparison with the PbPb analysis, the same p_T binning as in Sec. 6.1.2 is adopted:

- $\pi^\pm$: `[0.5, 0.55, 0.6, 0.65, 0.7, 0.75, 0.8, 0.85, 0.9, 0.95, 1.0, 1.1, 1.2, 1.3, 1.4, 1.5, 1.6, 1.7, 1.8, 1.9, 2.0, 2.2, 2.4, 2.6, 2.8, 3.0]` GeV/c,
- $K^\pm$: `[0.5, 0.55, 0.6, 0.65, 0.7, 0.75, 0.8, 0.85, 0.9, 0.95, 1.0, 1.1, 1.2, 1.3, 1.4, 1.5, 1.6, 1.7, 1.8, 1.9, 2.0, 2.2, 2.4, 2.6, 2.8, 3.0]` GeV/c,
- $p(\bar{p})$: `[0.65, 0.7, 0.75, 0.8, 0.85, 0.9, 0.95, 1.0, 1.1, 1.2, 1.3, 1.4, 1.5, 1.6, 1.7, 1.8, 1.9, 2.0, 2.2, 2.4, 2.6, 2.8, 3.0, 3.2, 3.4, 3.6]` GeV/c.

Centrality classes in OO are defined from the FT0 (FIT) signal amplitude, and are chosen to parallel, as closely as meaningful, the PbPb centrality quantiles (e.g. 0-5%, 5-10%, ..., 60-70%), while taking into account the lower multiplicity and narrower centrality span of the OO system.

Fit models and contamination treatment

In each $(p_\mathrm{T}, \text{centrality})$ bin, the $n_{\sigma,\mathrm{TOF}}$ distribution is fitted with exactly the same parametric models employed in PbPb (Sec. 6.1.2):

- at low and intermediate p_T, the baseline `tot4` model is used, consisting of a Gaussian core with an exponential right-hand tail for the signal, plus a polynomial+exponential background [Eq. (6.7)];
- at higher p_T, where species separation decreases, the signal is supplemented by Gaussian contaminant templates representing the neighboring hadron species (Eqs. (6.8) - (6.10)), while the background is simplified to avoid absorbing genuine PID structures.

The same seeding strategy and parameter constraints as in PbPb are used: the main signal peak is initialized near $n_\sigma = 0$, contaminant peaks are placed at the expected offsets for the other species, and widths are restricted to a physically motivated range. This ensures a smooth evolution of fit parameters with p_T and centrality, and provides direct comparability between the OO and PbPb analyses.

After convergence of the fit, the signal component $S(x)$ is frozen and integrated over the full fit range to obtain the raw counts for the species under study. The per-event, per-p_T raw yield is defined as

$$N_{\mathrm{raw}}^{\mathrm{TOF}}(p_\mathrm{T}) = \frac{1}{N_{ev}} \frac{1}{\Delta p_\mathrm{T}} \frac{1}{\Delta x} \int_{x_{\mathrm{min}}}^{x_{\mathrm{max}}} S(x)\, dx, \tag{7.2}$$

with the same notation as in the PbPb case: N_{ev} is the number of selected events in the centrality class, Δp_T the bin width, and Δx the n_σ bin width. Uncertainties are propagated from the fit covariance matrix and cross-checked by direct numerical integration of background-subtracted histograms.

Representative TOF n_σ distributions in OO

Representative examples of $n_{\sigma,\mathrm{TOF}}$ distributions in OO collisions are shown in Fig. 7.1. The qualitative behavior is very similar to that observed in PbPb: a well-defined signal peak centered near zero for the target species, non-Gaussian tails that are well accounted for by the exponential extension, and small contaminant structures at high p_T where species separation diminishes. The lower overall multiplicity of OO events leads to somewhat larger statistical uncertainties in each bin but also reduces the impact of random combinatorial background and cluster overlap, resulting in clean fits with stable χ^2/ndf.

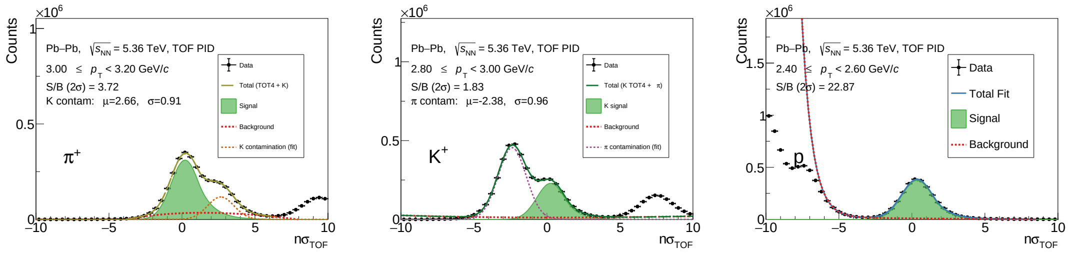

(A) π^+, central OO. (B) K^+, mid-central OO. (C) p, peripheral OO.

FIGURE 7.1: Representative $n_{\sigma,\mathrm{TOF}}$ distributions for π^+, K^+ and p in OO collisions at $\sqrt{s_\mathrm{NN}} = 5.36$ TeV. Data points are shown with statistical uncertainties; the total fit, signal component, and background/contaminants are drawn as in the PbPb case (Sec. 6.1.2).

Raw TOF spectra in OO

The raw (uncorrected) TOF spectra in OO follow the same plotting convention as in PbPb: positive and negative charges are shown separately, together with their charge sum, across multiple centrality classes. Figure 7.2 shows the pion raw yields, while Figs. 7.3 and 7.4 present the corresponding kaon and proton results.

Across all particle species, the raw spectra exhibit the expected monotonic decrease with increasing p_T, showing a smooth, nearly power-law behavior. The ordering of yields with centrality follows the expected pattern: more central collisions produce larger particle yields, reflecting the larger number of participants and higher energy density of the system. The ratio panels confirm that the spectral *shape* is largely independent of centrality, with deviations of order 10-20% at low p_T where multiplicity and track density can have a larger effect on the TOF matching performance.

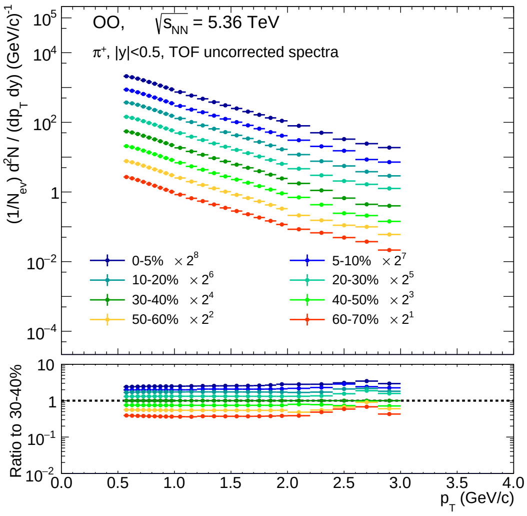

(A) π^+ raw yields vs. p_{T} in OO centrality classes (top, log scale; bottom: ratio to a mid-central reference).

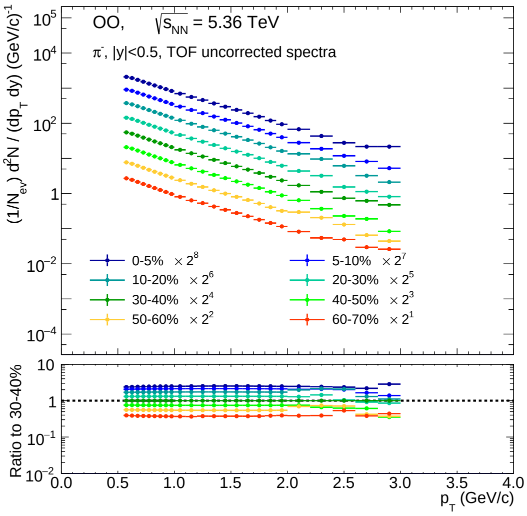

(B) π^- raw yields, same conventions.

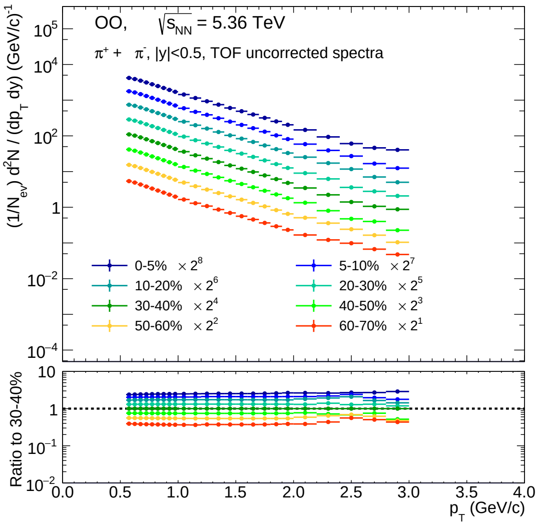

(C) Combined $\pi^+ + \pi^-$ raw yields (top: log scale; bottom: ratio to mid-central OO).

FIGURE 7.2: TOF raw pion spectra in OO collisions at $\sqrt{s_{\mathrm{NN}}}$ = 5.36 TeV.

The pion raw spectra (Figs. 7.2) show a very clean, featureless decrease, with excellent statistical precision in all centrality classes. The ratio to the 30-40% reference is flat within uncertainties, demonstrating stable yield extraction and the absence of strong centrality-dependent distortions. The similarity between π^+ and π^- confirms that the OO sample is essentially baryon symmetric at midrapidity, as expected.

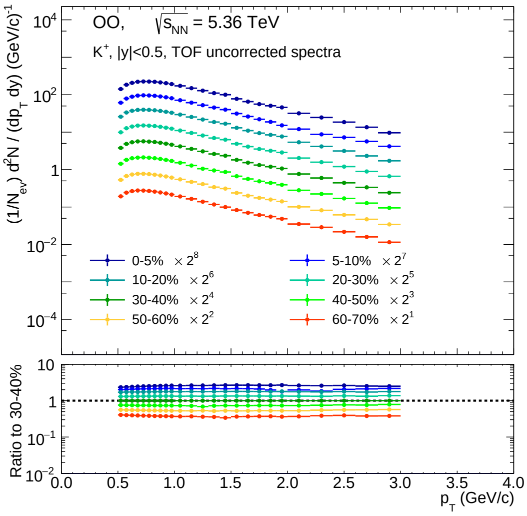

(A) K^+ raw yields vs. p_T in OO centrality classes.

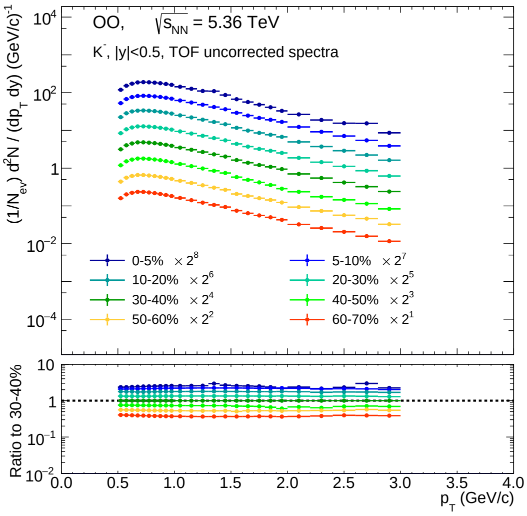

(B) K^- raw yields, same conventions.

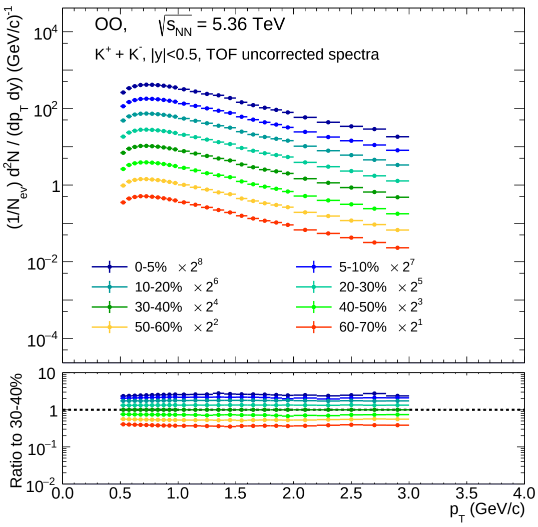

(C) Combined K^++K^- raw yields (top: log scale; bottom: ratio to mid-central OO).

FIGURE 7.3: TOF raw kaon spectra in OO collisions at $\sqrt{s_{NN}}$ = 5.36 TeV.

The kaon raw yields (Figs. 7.3) follow the same qualitative trends as the pions, with the characteristic kaon shoulder around $p_T \sim 0.8$ - 1.0 GeV/c visible in all centrality classes. The centrality scaling is slightly steeper than for pions, consistent with the known sensitivity of strangeness production to system size. The ratios remain close to unity, indicating that the spectral shape is reproduced consistently across centralities. Small charge-asymmetric fluctuations are visible but entirely consistent with statistical precision.

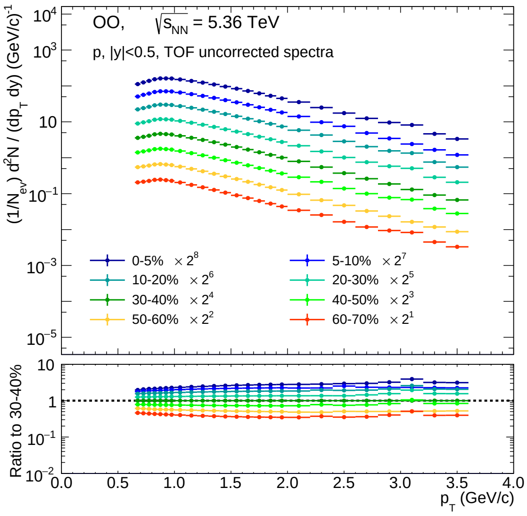

(A) Proton raw yields vs. p_{T} in OO centrality classes.

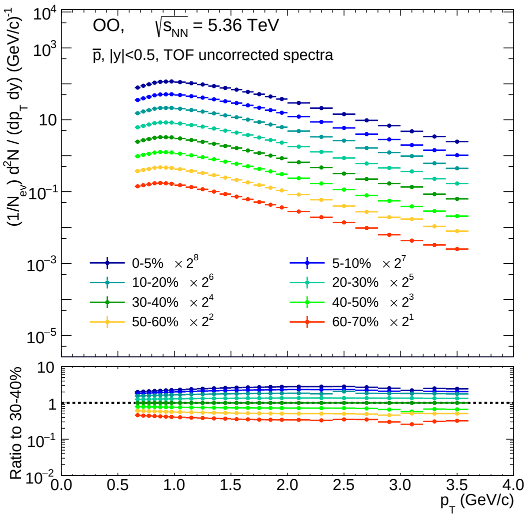

(B) Antiproton raw yields, same conventions.

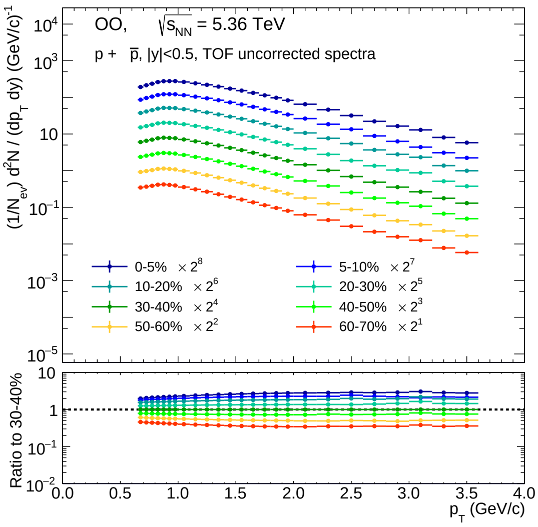

(C) Combined $p+\bar{p}$ raw yields (top: log scale; bottom: ratio to mid-central OO).

FIGURE 7.4: TOF raw proton and antiproton spectra in OO collisions at $\sqrt{s_{\mathrm{NN}}} = 5.36$ TeV.

The proton and antiproton spectra (Figs. 7.4) show the largest dynamic range among the three species. A slight enhancement of protons over antiprotons is observed at low p_{T}, driven by secondaries produced in weak decays or from interactions with residual detector material. This effect is well known from PbPb and pp measurements and diminishes rapidly above $p_{\mathrm{T}} \approx 1.2$ GeV/c, where the p and $\bar{p}$ yields converge. The spectral shapes and centrality scaling otherwise mirror those of pions and kaons, validating the stability of the TOF-based yield extraction.

Taken together, these TOF-based raw spectra demonstrate that the same PID framework employed in PbPb can be robustly applied to OO, providing a clean starting point for efficiency corrections, primary-fraction extraction, and the subsequent physics comparison between heavy- and light-ion systems.

7.3.2 Efficiency estimation

The transformation from raw to corrected spectra in OO follows exactly the methodology established for PbPb (see Sec. 6.2.1): all efficiencies are derived from the OO Monte Carlo sample `LHC25g6`, processed with the same reconstruction chain and analysis cuts as the data.

In this section we focus on the TOF matching efficiency as a function of p_T and centrality for positively charged pions and kaons, and for protons and antiprotons, which enter directly the correction of the TOF identified spectra discussed above.

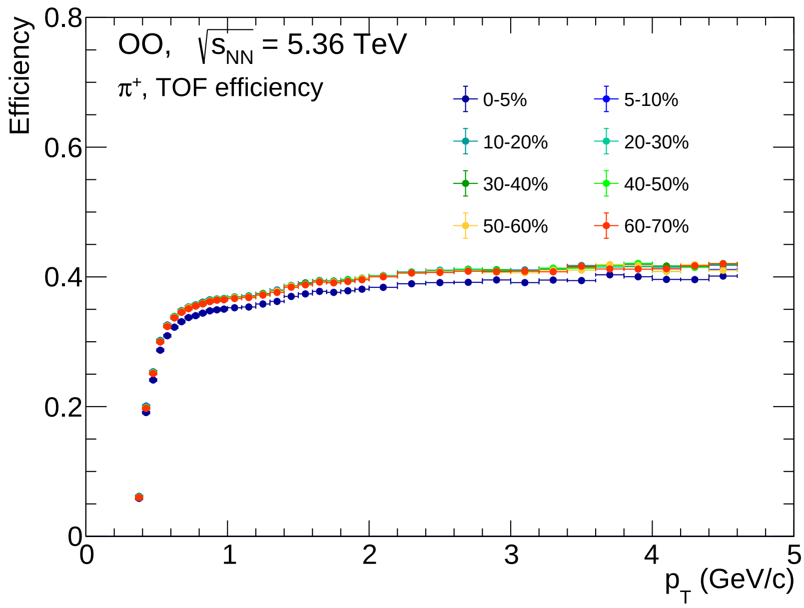

FIGURE 7.5: TOF efficiency for π^+ as a function of p_T in OO collisions at $\sqrt{s_{NN}} = 5.36$ TeV for different centrality classes.

Figure 7.5 shows the TOF efficiency for π^+ in all centrality intervals. The efficiency rises steeply between $p_T \approx 0.4$ and 0.8 GeV/c, corresponding to the momentum threshold required for pions to reach the TOF wall at a radius of ~ 3.7 m. Above $p_T \approx 0.8$ GeV/c the efficiency saturates at a broad plateau of $\varepsilon_{TOF} \simeq 0.40$ - 0.42, with only a very mild dependence on centrality. The most central 0 - 5% collisions show a slightly reduced efficiency (by a few percent) compared to peripheral events, reflecting the modest impact of higher track density on track matching and hit occupancy.

Overall, the centrality dependence in OO is weak, as expected from the much lower multiplicities with respect to PbPb.

The corresponding TOF efficiencies for K^+ are displayed in Fig. 7.6. The qualitative behaviour is similar to that of pions, with a rapid turn-on and a plateau at intermediate and high p_T. Because of the finite kaon lifetime, the low-p_T suppression is more pronounced: a sizeable fraction of kaons decay in flight before reaching the TOF, leading to a sharper rise and a slightly lower plateau value of $\varepsilon_{TOF} \simeq 0.35$ - 0.40. Again, the centrality dependence is minor, with central events exhibiting at most a few-percent reduction relative to peripheral ones. The smoothness and moderate centrality dependence confirm that the TOF matching for kaons is well under control in the OO Monte Carlo description.

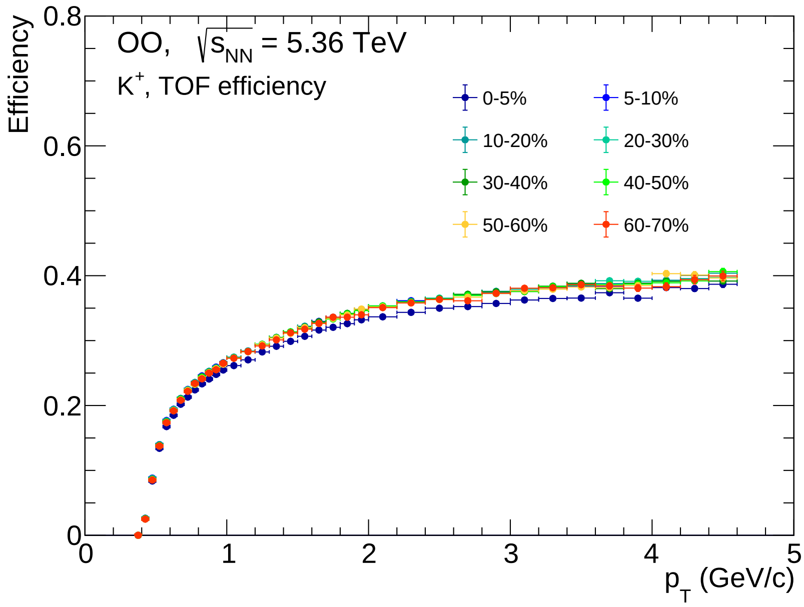

FIGURE 7.6: TOF efficiency for K^+ as a function of p_T in OO collisions at $\sqrt{s_{NN}} = 5.36$ TeV for different centrality classes.

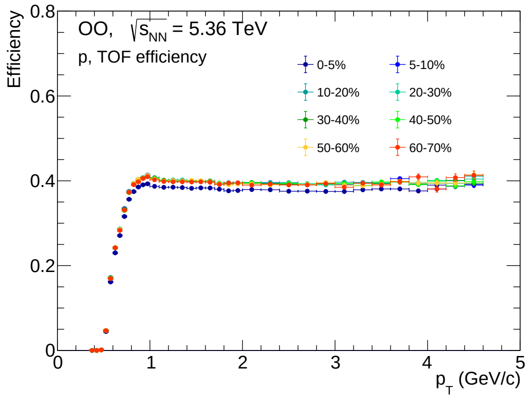

(A) p

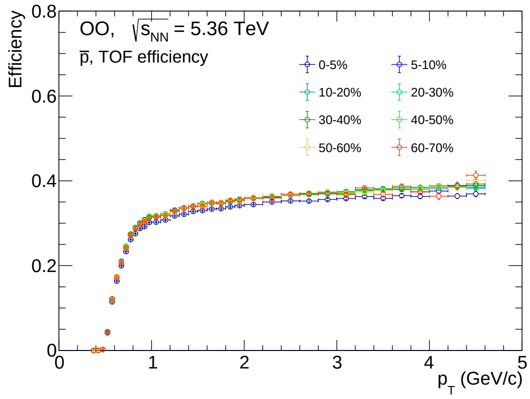

(B) $\bar{p}$

FIGURE 7.7: TOF efficiency for protons (a) and antiprotons (b) as a function of p_T in OO collisions at $\sqrt{s_{NN}} = 5.36$ TeV for different centrality classes.

Figure 7.7 presents the TOF efficiencies for protons and antiprotons. For both charges the efficiency rises rapidly up to $p_T \approx 0.8$ - 0.9 GeV/c and then reaches a plateau around $\varepsilon_{TOF} \simeq 0.38$ - 0.42. Compared to mesons, the plateau is slightly higher, reflecting the larger rigidity and reduced multiple scattering of baryons. The centrality dependence is again small, with only a mild reduction of the efficiency in central events. Within the statistical precision of the simulation, the proton and antiproton curves are compatible over the full p_T range, indicating that material effects (such as annihilation or large inelastic cross sections for $\bar{p}$) have only a modest impact on the TOF matching probability in this kinematic domain. Any residual charge asymmetry is assigned as a small charge-dependent systematic uncertainty on the efficiency correction.

Mitigation of statistical fluctuations in the efficiency maps

The efficiency points extracted from MC simulations, particularly for the TOF matching probability, exhibit visible statistical fluctuations at high transverse momentum. These fluctuations originate from the steeply falling p_T spectra of generated particles in OO collisions and are further amplified in the peripheral centrality classes, where the number of reconstructed tracks per event is significantly reduced. Since the corrected spectra are obtained by dividing the raw yields by these efficiencies on a bin–by–bin basis, even small oscillations in the efficiency maps may propagate into artificial structures in the final physics distributions. For this reason, a smoothing procedure based on analytic parametrizations is employed.

To obtain stable and physically continuous efficiency curves, each efficiency distribution is fitted with two candidate functions:

- a sigmoid based on the error function,

$$\epsilon_{\text{Fit1}}(p_T) = p_0 + p_1 \cdot \frac{1}{2}\left[1 + \text{erf}\left(\frac{p_T - p_2}{p_3}\right)\right],$$

- a generalized logistic form with an optional linear term,

$$\epsilon_{\text{Fit2}}(p_T) = a + \frac{b}{1 + \exp[-(p_T - c)/d]} + e \cdot p_T.$$

Both parametrizations describe the characteristic turn-on behaviour of the efficiencies at low p_T and their broad plateau at higher momenta. The optimal fit is selected using the tail performance, defined over $p_T \geq 1.5$ GeV/c, where statistical fluctuations are most pronounced. Metrics such as the reduced χ^2 and the root mean square error (RMSE) in the tail region are used to identify the most stable functional form for each particle species and centrality class.

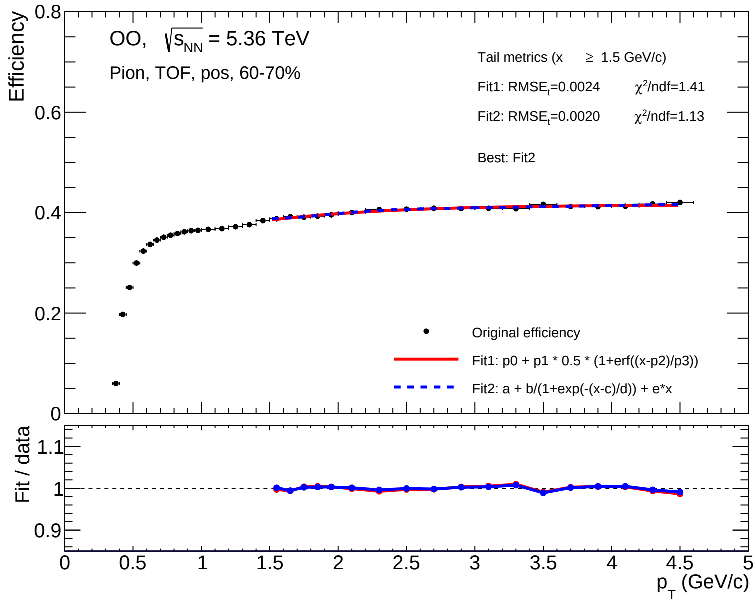

FIGURE 7.8: Example of TOF efficiency smoothing for π^+ in OO collisions (60-70% centrality). The upper panel shows the raw simulation points together with both fits, while the lower panel displays the fit/data ratios.

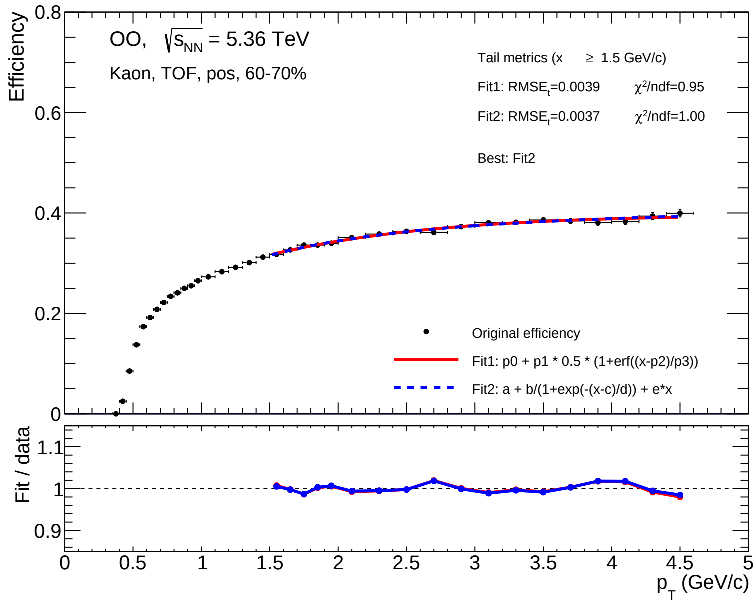

FIGURE 7.9: Same as Fig. 7.8, but for K^+.

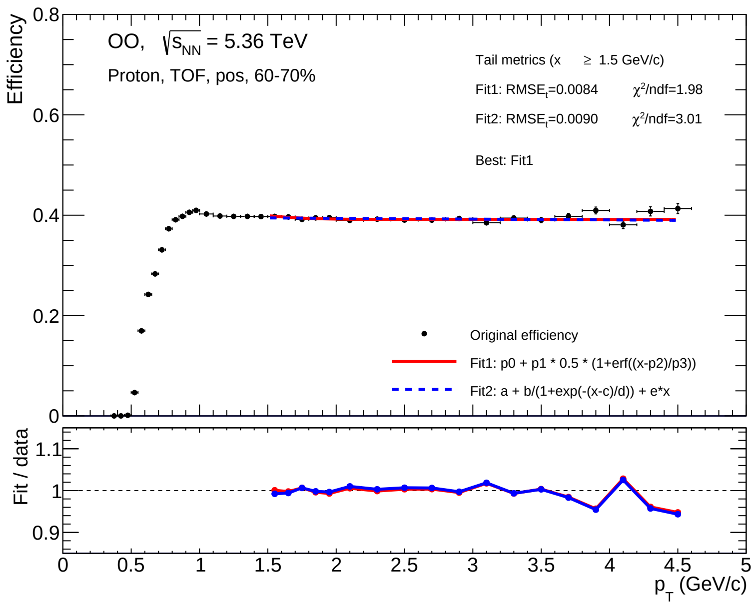

FIGURE 7.10: Same as Fig. 7.8, but for protons in the 60-70% centrality class.

Figures 7.8, 7.9, and 7.10 illustrate representative examples for positive pions, kaons, and protons in OO collisions. In all cases, the fit functions closely follow the Monte Carlo points across the plateau, while effectively suppressing local oscillations that arise from limited MC statistics. The corresponding fit/data ratios shown in the lower pads of the figures remain within a few percent of unity, confirming that the parametrizations preserve the physical behaviour of the efficiencies without introducing bias.

After the optimal functions are determined, the fitted curves are used for the final efficiency corrections. This procedure ensures:

- the suppression of non-physical fluctuations from MC statistics;
- numerical stability in the ratio of TOF-derived spectra;
- reliable propagation of systematic uncertainties through controlled variations of the fit parameters.

In summary, the application of fit-based smoothing provides a robust treatment of statistical fluctuations in the OO efficiency maps and constitutes an essential step in producing clean, physically interpretable corrected spectra.

7.3.3 Feed-down and primary-particle fractions in OO collisions

The procedure used to determine the fraction of primary particles in OO collisions follows exactly the methodology established for PbPb collisions (see Sec. 6.2.3). Primary, weak-decay, and material-interaction templates obtained from the full `LHC25g6` Monte Carlo sample are fitted to the data DCA_{xy} distributions using the `Fraction Fitter` framework. The resulting primary fractions $f_{\mathrm{prim}}(p_{\mathrm{T}})$ for pions and protons the two species with non-negligible secondary contributions are summarized in Figs. 7.11 and 7.12. For kaons, the feed-down contribution is negligible and no correction is required, consistent with their short-lived parent resonances.

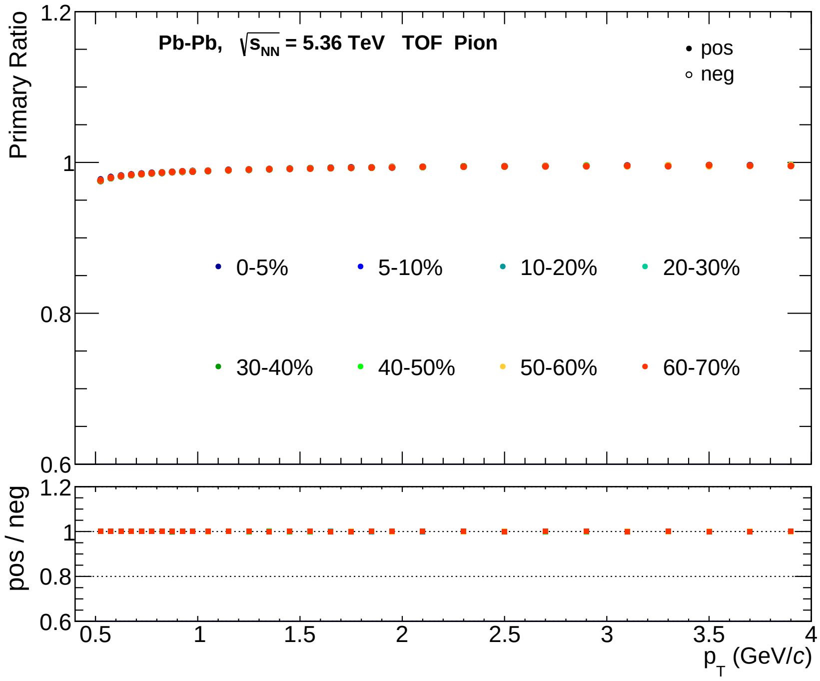

FIGURE 7.11: Primary fraction ratio $f^{+}_{\text{prim}}/f^{-}_{\text{prim}}$ for pions in OO collisions at $\sqrt{s_{\text{NN}}} = 5.36$ TeV, obtained with the TOF selection. The bottom panel shows the charge ratio as a function of p_{T}.

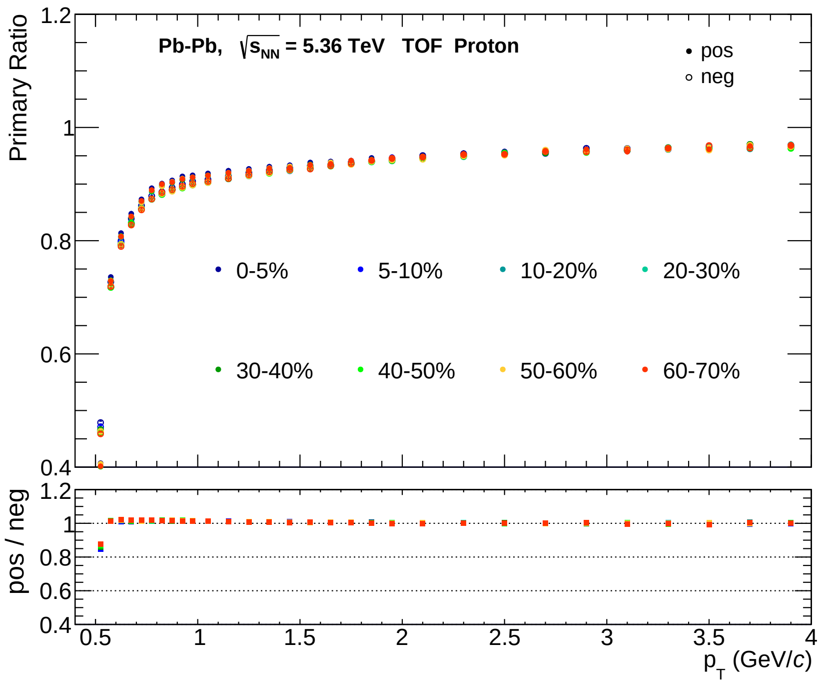

FIGURE 7.12: Primary fraction ratio $f^{+}_{\text{prim}}/f^{-}_{\text{prim}}$ for protons and antiprotons in OO collisions at $\sqrt{s_{\text{NN}}} = 5.36$ TeV. The bottom panel shows the charge ratio.

Primary fractions for pions

Figure 7.11 shows the primary fraction extracted for π^{+} and π^{-} with TOF PID in all centrality classes. The primary fraction for pions is very close to unity over the full

p_T range and for all event classes, with only a small suppression ($f_{prim} \simeq 0.97$) at the lowest transverse momenta. This behaviour is expected, since the dominant source of secondary pions arises from $K^0_S \to \pi^+\pi^-$ decays, which:

- are charge symmetric,
- have decay lengths of order a few centimeters, and
- are efficiently separated by the DCA_{xy} selection.

The bottom panel of Fig. 7.11 shows the ratio f^+_{prim}/f^-_{prim}. This ratio is unity within a few per mille across all centralities. No charge dependence is observed, confirming that:

- the OO track-density environment does not induce charge-asymmetric reconstruction effects,
- the material-induced misidentification is negligible, and
- the feed-down from neutral kaons is perfectly charge symmetric.

Overall, the pion primary fractions in OO collisions are remarkably clean and exhibit even smaller low-p_T distortions than in PbPb, consistent with the lower multiplicity and reduced secondary-particle density.

Primary fractions for protons

The behaviour for protons (Fig. 7.12) is qualitatively different, as also observed in PbPb collisions, though with reduced magnitude due to the much lighter OO system.

At low p_T ($p_T \lesssim 1$ GeV/c), the primary fraction increases steadily with momentum, starting from $f_{prim} \approx 0.45$ - 0.55 and approaching unity above $p_T \gtrsim 1.5$ GeV/c. This trend reflects the combined effects of:

- feed-down from weak decays of hyperons, predominantly $\Lambda \to p\pi^-$ and $\bar{\Lambda} \to \bar{p}\pi^+$,
- secondary interactions with the detector material, and
- annihilation losses affecting $\bar{p}$ more strongly than p.

The charge ratio $f^p_{prim}/f^{\bar{p}}_{prim}$ displays the expected pattern: values slightly above unity at low momentum, converging to unity at larger p_T. This is a direct manifestation of:

- enhanced $\bar{p}$ absorption and annihilation at low rigidity in the beampipe and inner detectors,
- a somewhat larger Λ feed-down contribution to p than $\bar{\Lambda}$ feed-down to $\bar{p}$.

However, compared to PbPb, the overall charge asymmetry in OO is significantly smaller. This can be attributed to the:

- lower hyperon yield in the much lighter OO system,
- reduced material-traversal probability due to lower curvature at comparable p_T, and

- much lower overall track density, leading to fewer secondary interactions.

Above $p_T \approx 1.5$ - 2.0 GeV/c, both species approach $f_{prim} \simeq 1$ within uncertainties, and the charge ratio is flat and consistent with unity. This confirms that at moderately high momentum, the reconstruction efficiency is charge symmetric and the fraction of secondaries becomes negligible.

Overall, the OO system displays an intermediate level of cleanliness between the pp/pPb and PbPb collisions. The primary-fraction corrections are small for mesons and modest for baryons, and the residual charge asymmetries are minimal. This behavior is consistent with expectations for a light-ion system with reduced secondary yields and low detector occupancy.

7.3.4 Corrected Spectra

The final step of the spectra reconstruction consists of converting the raw yields into fully corrected, physics-ready transverse-momentum spectra. For each particle species, charge, and centrality interval, the corrected spectra are obtained according to

$$\frac{1}{N_{ev}} \frac{d^2N}{dp_T dy} = \frac{1}{N_{ev}} \frac{N_{raw}(p_T)\, f_{prim}(p_T)}{\varepsilon_{tot}(p_T)}, \tag{7.3}$$

where N_{raw} is the yield extracted from TPC/TOF PID fits, f_{prim} is the primary-particle fraction derived from the DCA$_{xy}$ template fits, and ε_{tot} denotes the total correction factor incorporating acceptance, tracking efficiency, TOF matching efficiency, and relevant PID-related effects. This procedure is identical to that used for PbPb (see Chapter 6), ensuring methodological consistency between systems.

Figure 7.13 shows the fully corrected spectra for pions, kaons, and protons, combining positive and negative charges and spanning eight centrality intervals from 0 % - 70 %. Each distribution exhibits the expected steeply falling exponential shape at low and intermediate transverse momentum, followed by a smooth transition toward a power-law-like behaviour at higher p_T, characteristic of hard scattering processes. The spectra extend up to $p_T \approx 3$ - 3.5 GeV/c for TOF-identified pions and kaons and to roughly 3.8 GeV/c for protons.

Centrality evolution. A clear and monotonic centrality dependence is observed for all species:

- the 0 % - 5 % most central OO collisions exhibit the largest particle yields at all p_T,
- whereas the 60 % - 70 % class shows the lowest yields,

as expected from the increase of system size and multiplicity with centrality. This is fully consistent with PbPb trends, though the separation between centralities is visibly smaller in OO due to the considerably narrower range of underlying charged-particle multiplicities.

To highlight relative shape variations, the lower panels of each spectrum show the ratio of a given centrality class to the 30 % - 40 % reference interval. Across species and charges, the ratios remain largely flat above $p_T \approx 1$ GeV/c, indicating that the spectral shapes exhibit weak centrality dependence in the intermediate-p_T region. At low p_T, modest ordering is visible, consistent with the presence of collective radial flow whose magnitude increases toward central events. Notably, this low-p_T modulation is significantly weaker than in PbPb collisions, reflecting the smaller size, lower lifetime, and reduced collectivity of the OO system.

Species dependence. The corrected spectra exhibit the expected mass ordering at low momentum:$p_T \lesssim 1$ GeV/c : π fall fastest, K intermediate, p shallowest, reflecting the increasingly strong interplay between radial flow and particle mass. Although the mass splitting is present in OO, it is noticeably smaller than in PbPb, again pointing toward a more modest collective expansion.

At higher transverse momenta, $p_T > 2.5$ GeV/c, all species exhibit approximately parallel power-law behaviour in all centralities, with only small statistical fluctuations. This regime is dominated by hard processes and fragmentation, where system-size effects are expected to be minimal.

Comparison to PbPb. Overall, the corrected spectra in OO qualitatively resemble those in PbPb but show:

- reduced centrality separation,
- weaker radial-flow-induced hardening at low p_T,
- smaller enhancement of baryon yields relative to mesons,
- larger relative statistical uncertainties at high p_T due to lower multiplicity.

These features are consistent with expectations for a light-ion system that lies intermediate between small systems (pp, pPb) and heavy systems (PbPb). The smooth behaviour of the spectra and ratios further confirms the robustness of the correction chain established in Chapter 6.

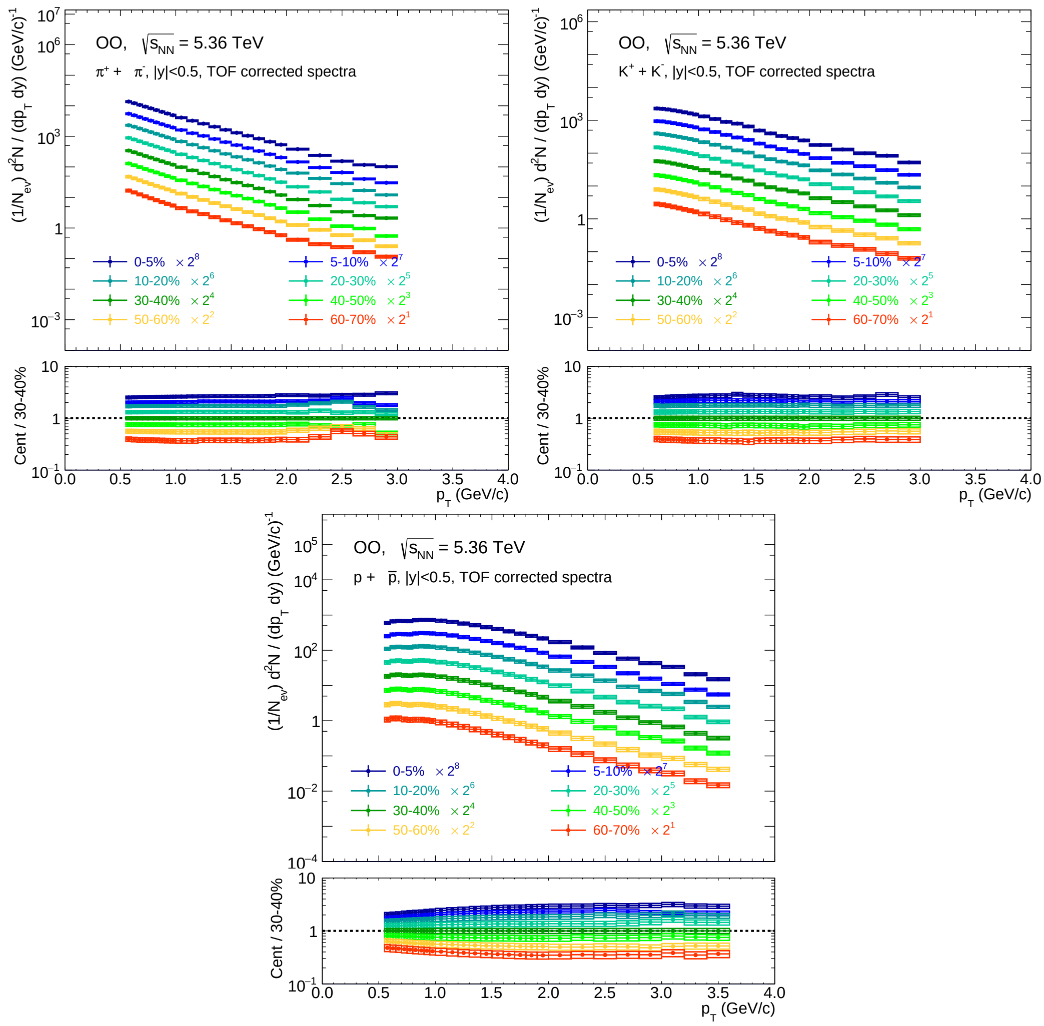

FIGURE 7.13: Corrected transverse-momentum spectra for pions (top left), kaons (top right), and protons (bottom) in OO collisions at $\sqrt{s_{\mathrm{NN}}} = 5.36$ TeV. Upper panels show the absolute spectra for eight centrality classes. Lower panels show ratios to the 30 % - 40 % reference interval.

7.4 Particle-to-Pion Ratios

A particularly sensitive probe of hadron-production mechanisms in ultra-relativistic nuclear collisions is the comparison of strange and baryon yields to those of pions. Ratios such as K/π and p/π provide direct insight into the relative abundance of strange quarks, the degree of baryon transport and baryon–antibaryon production, and the interplay between hydrodynamic flow and hadronization. Moreover, these ratios largely cancel many of the systematic effects present in the individual spectra, such as overall normalization, luminosity, and most efficiency contributions, thus enabling a more differential study of centrality-dependent features.

In the present analysis, particle-to-pion ratios are constructed using the fully corrected spectra described in Sec. 7.3.4. For each centrality interval, the ratio

$$\frac{K^+ + K^-}{\pi^+ + \pi^-} \quad \text{and} \quad \frac{p + \bar{p}}{\pi^+ + \pi^-}$$

is obtained bin-by-bin in p_T using TOF-identified hadrons in the range $|y| < 0.5$. Since the same event, track, and PID selections enter both numerator and denominator, these ratios are robust against residual detector effects; the dominant uncertainties arise from the primary-fraction correction at low p_T (Sec. 7.3.3) and from the efficiency smoothing procedure (Sec. 7.3.2).

7.4.1 K/π Ratios

Figure 7.14 shows the $(K^+ + K^-)/(\pi^+ + \pi^-)$ ratio for all OO centrality classes. The ratio exhibits the characteristic rise with p_T observed in larger collision systems [147], reflecting the harder spectral shape of kaons relative to pions due to their larger mass. At low momenta ($p_T \lesssim 1\,\mathrm{GeV}/c$), all centrality classes converge to a common value around $K/\pi \approx 0.15$ - 0.20, consistent with the expected dominance of soft bulk particle production. At higher p_T, moderate centrality dependence emerges: more central events show slightly larger K/π, indicating enhanced strangeness production and stronger collective flow.

The lower panel of Fig. 7.14 displays the ratio of each centrality interval to the mid-central (30-40%) reference. The deviations from unity remain below $\sim$ 20% across the measured range, consistent with the smooth, monotonic centrality evolution already visible in the raw and corrected spectra. The absence of abrupt structure demonstrates that the kaon and pion corrections, tracking, PID, primaries, and efficiency, are well controlled and introduce no artificial distortions.

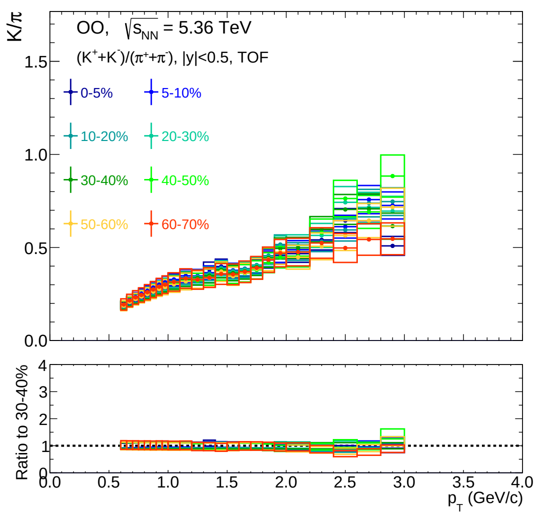

FIGURE 7.14: Centrality-differential $(K^+ + K^-)/(\pi^+ + \pi^-)$ ratios in OO collisions at $\sqrt{s_{\mathrm{NN}}} = 5.36$ TeV, obtained with TOF PID. The bottom panel shows the ratio of each centrality bin to the 30 - 40% reference.

7.4.2 p/π Ratios

The proton-to-pion ratio shown in Fig. 7.15 rises more steeply with p_T than K/π, in accordance with the larger baryon mass and the corresponding stronger radial-flow boost expected in collective expansion scenarios. At low p_T, p/π begins around 0.05 - 0.08 for all centrality classes, consistent with the primary-fraction corrections described in Sec. 6.2.3 and similar to those observed in PbPb collisions [147]. The ratio reaches a broad maximum for $p_T \approx 2.5$ - 3 GeV/c, with more central collisions displaying larger values, reflecting the increased radial-flow strength in higher-multiplicity events.

The lower-panel ratios to the 30 - 40% class again reveal a smooth and monotonic ordering: the most central collisions lie above unity across the entire p_T region, while the most peripheral classes lie below it. The magnitude of this centrality dependence is somewhat stronger for p/π than for K/π, consistent with the greater sensitivity of baryons to both collective flow and to feed-down contributions (Sec. 6.2.3). The agreement between positive and negative baryons within uncertainties demonstrates that the material-interaction corrections for antiprotons are under control.

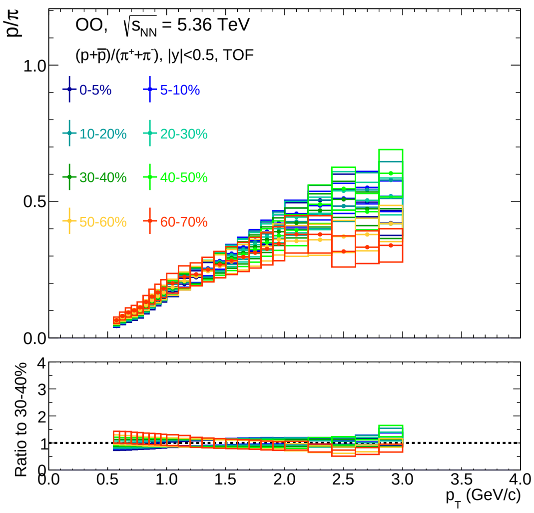

FIGURE 7.15: Centrality-differential $(p+\bar{p})/(\pi^+ + \pi^-)$ ratios in OO collisions at $\sqrt{s_{NN}}$ = 5.36 TeV using TOF PID. The bottom panel shows the ratio relative to the 30 - 40% class.

7.4.3 Physics Interpretation

The overall centrality and p_T dependence of the particle-to-pion ratios in OO collisions closely mirrors patterns familiar from pPb and PbPb systems:

- The rise of K/π and p/π with p_T reflects the mass ordering expected from hydrodynamic radial flow.
- The enhancement of both ratios for more central collisions indicates a stronger collective medium even in this comparatively small ion system.
- The small spread among centralities suggests that OO collisions produce a system intermediate in size between pPb and peripheral PbPb, consistent with its modest but non-negligible initial geometry.

Thus, the OO system provides a valuable bridge between small and large systems, probing the onset of collectivity and strangeness enhancement in a regime where initial-state and final-state effects may be comparable. The smooth behavior of the ratios further confirms the robustness of the corrections applied in the previous sections and validates the methodology used throughout the analysis.

7.5 Blast Wave Analysis and Extraction of Freeze-Out Parameters

A quantitative characterization of the collective expansion and the kinetic freeze-out conditions in heavy-ion collisions is commonly obtained by fitting the identified-particle transverse-momentum spectra with a hydrodynamically motivated Blast Wave (BW) parameterization [158]. The same methodology was employed in the PbPb study presented in Sec 6.7, allowing a direct comparison between large and light-ion systems.

In this section the OO TOF corrected spectra (Sec. 7.3.4) for π^+, K^+, and p are fitted simultaneously using the standard Boltzmann-Gibbs Blast Wave (BGBW) prescription,

$$\frac{1}{p_{\mathrm{T}}}\frac{dN}{dp_{\mathrm{T}}} \propto \int_0^R r\,dr\, m_{\mathrm{T}} I_0\left(\frac{p_{\mathrm{T}}\sinh\rho}{T_{\mathrm{kin}}}\right) K_1\left(\frac{m_{\mathrm{T}}\cosh\rho}{T_{\mathrm{kin}}}\right), \tag{7.4}$$

where T_{kin} is the kinetic freeze-out temperature, $\rho = \tanh^{-1}\beta(r)$, and the transverse velocity profile is parameterized as $\beta(r) = \beta_{\mathrm{max}}(r/R)^n$. The fit parameters thus correspond to

- the average transverse expansion velocity $\langle\beta\rangle$,
- the maximum surface velocity β_{max},
- the velocity profile exponent n, and
- the kinetic freeze-out temperature T_{kin}.

The fits are performed independently in each centrality class, using only the p_{T} intervals where the BW model is applicable, namely $0.6 < p_{\mathrm{T}} < 1.2$ GeV/c for pions, $0.6 < p_{\mathrm{T}} < 1.5$ GeV/c for kaons, and $1.4 < p_{\mathrm{T}} < 3.0$ GeV/c for protons. These ranges match those used in the corresponding ALICE PbPb analyses, ensuring methodological consistency.

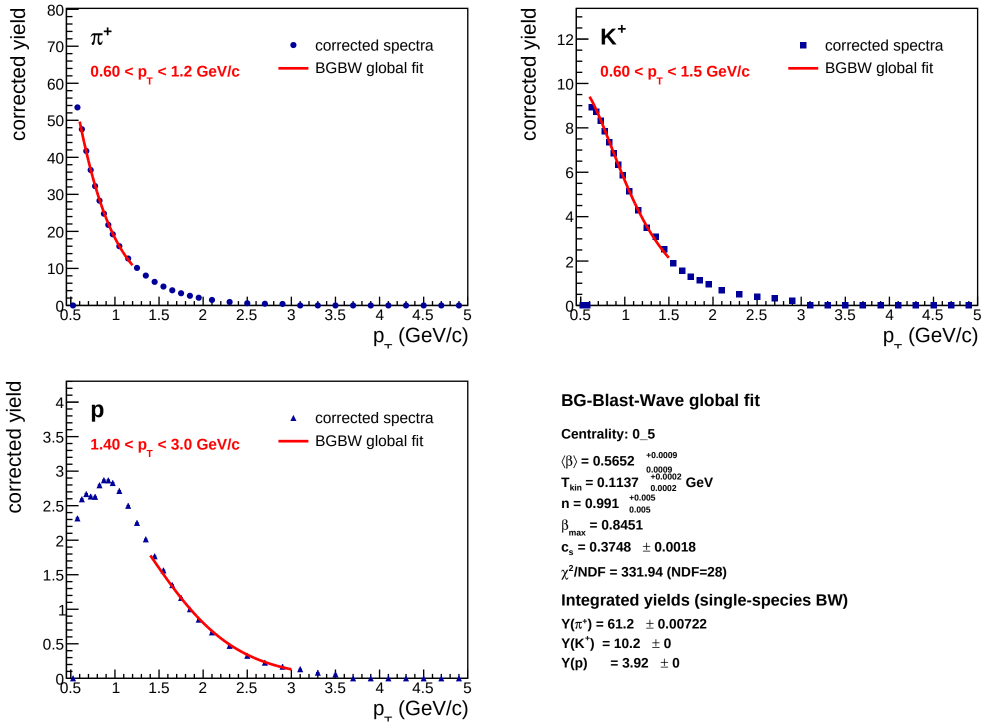

FIGURE 7.16: Simultaneous BGBW fit to π^+, K^+ and p spectra in OO collisions for the 0 - 5% centrality class.

Figure 7.16 shows a representative example for the 0 - 5% centrality class. The model reproduces the spectral shapes with good accuracy across the full fitting range, indicating the presence of substantial collective radial flow even in this small system. The extracted initial parameters for the most central events are:

$$\langle \beta \rangle = 0.565 \pm 0.009, \qquad T_{\text{kin}} = 0.114 \pm 0.002 \text{ GeV}$$

$$n = 0.991 \pm 0.005, \qquad \beta_{\max} = 0.845 \pm 0.002.$$

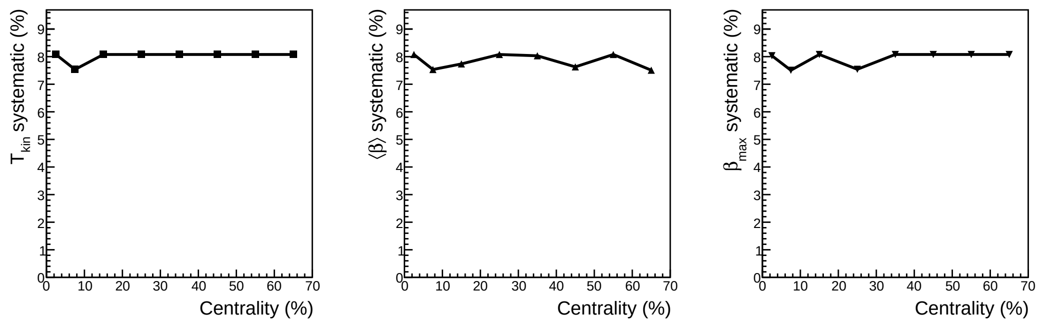

FIGURE 7.17: Systematic uncertainties on the extracted BW parameters as a function of OO centrality.

Systematic uncertainties follow the same procedure as in PbPb: variation of fit ranges, alternative background subtraction, and detector-level systematic envelopes. As shown in Fig. 7.17, the uncertainties remain at the level of 7 - 9% for all parameters across the full centrality range.

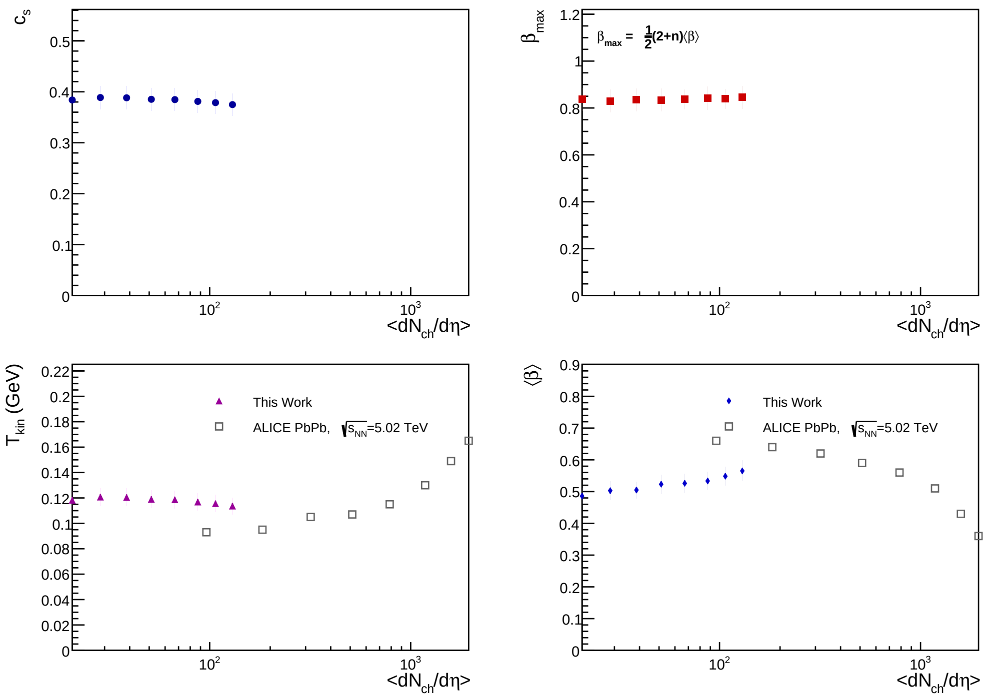

FIGURE 7.18: Multiplicity dependence of extracted OO freeze-out parameters, compared where relevant to PbPb results at $\sqrt{s_{\mathrm{NN}}}$ = 5.02 TeV [147].

Figure 7.18 shows the multiplicity dependence of the Blast-Wave parameters extracted in OO collisions, compared with the corresponding PbPb results at $\sqrt{s_{\mathrm{NN}}}$ = 5.02 TeV. The main observations are:

- **Average radial flow velocity $\langle\beta\rangle$:** The OO results show a remarkably flat behaviour, with $\langle\beta\rangle \approx 0.50$ - 0.54 across the entire multiplicity range. This weak dependence is in contrast to PbPb collisions, where $\langle\beta\rangle$ increases strongly toward central events. The flat trend in OO suggests that radial flow in this small system is much less sensitive to event activity, consistent with a shorter lifetime and more limited hydrodynamic acceleration.

- **Kinetic freeze-out temperature T_{kin}:** The OO values remain nearly constant at $T_{\mathrm{kin}} \approx 0.12$ GeV, with only modest variations. In comparison, PbPb collisions exhibit a pronounced decrease of T_{kin} toward central events. The higher freeze-out temperature in OO indicates earlier thermal decoupling, as expected for a small, short-lived fireball.

- **Velocity-profile exponent n (shown as c_s):** The profile parameter displays almost no dependence on multiplicity, staying within a narrow band around $c_s \approx 0.38$ - 0.40. This uniformity suggests that the shape of the radial flow profile is essentially independent of the final-state multiplicity in OO collisions.

- **Maximum radial velocity β_{max}:** The behaviour of β_{max} closely follows that of $\langle\beta\rangle$, remaining weakly dependent on multiplicity and systematically smaller than in PbPb. This again reflects the reduced acceleration and limited buildup of radial flow in the smaller OO system.

Overall, these trends indicate that OO collisions produce a collectively expanding medium, but with substantially weaker and less strongly evolving radial flow compared to PbPb. The nearly constant behaviour of all BW parameters across the full multiplicity range supports a scenario where the hydrodynamic phase in OO collisions is short-lived and exhibits only limited centrality dependence.

7.5.1 Correlation between T_{kin} and $\langle\beta\rangle$: Comparison with PbPb

An important cross–check of the Blast-Wave description consists in studying the correlation between the extracted kinetic freeze-out temperature, T_{kin}, and the average transverse flow velocity, $\langle\beta\rangle$, across centrality classes. Figure 7.19 summarises this dependence for OO collisions and compares it to the established PbPb results at $\sqrt{s_{\mathrm{NN}}} = 5.02$ TeV [147]. The OO points (filled markers) show a clear negative correlation, as expected from hydrodynamic freeze–out systematics: more central events exhibit stronger collective expansion (larger $\langle\beta\rangle$) together with a slightly lower T_{kin}, while peripheral collisions freeze out with reduced flow and higher kinetic temperature.

Quantitatively, the OO system occupies a region of the T_{kin} - $\langle\beta\rangle$ plane intermediate between pPb and PbPb, consistent with its reduced size and shorter expansion time. Compared with PbPb, OO shows:

- systematically *higher* T_{kin} at similar centrality percentile, indicating an earlier kinetic decoupling driven by the smaller system volume;
- slightly *lower* $\langle\beta\rangle$ values, confirming the reduced build–up of radial flow relative to large nuclei;
- a slope of the anticorrelation consistent within uncertainties with that observed in PbPb, suggesting that the interplay between temperature and flow is already hydrodynamic–like in OO.

The comparison supports the interpretation that light–ion collisions exhibit a compressed dynamical evolution: they develop collective flow, but freeze out earlier and at higher kinetic temperature than large systems. The continuity of the trend between OO and PbPb further suggests that freeze–out properties scale smoothly with initial system size, offering a new bridge between small- and large–system collectivity at the LHC.

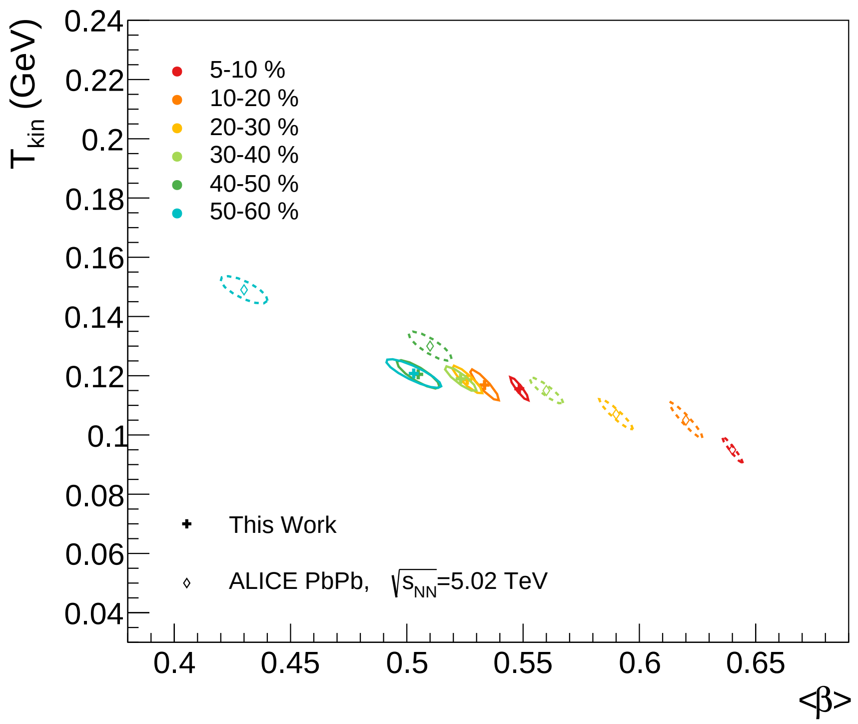

FIGURE 7.19: Correlation between T_{kin} and $\langle\beta\rangle$ for OO collisions (this work, filled circles) compared with PbPb results at $\sqrt{s_{\text{NN}}} = 5.02$ TeV (open squares) from Ref. [147].

7.5.2 Integrated Yields

The Blast Wave fits described in Sec. 7.5 provide a continuous parametrization of the p_T spectra for each particle species and centrality class. This allows the extraction of fully integrated particle yields,

$$Y = \int_0^\infty \frac{1}{2\pi p_{\text{T}}} \frac{\mathrm{d}^2 N}{\mathrm{d}p_{\text{T}}\mathrm{d}y} \, 2\pi p_{\text{T}} \, \mathrm{d}p_{\text{T}}, \tag{7.5}$$

where the integral combines the measured spectrum with the BGBW extrapolation into unmeasured low- and high-p_{T} regions. As in the PbPb analysis, the fit component dominates mainly at very low p_{T} for protons and in the transition regions between PID detectors.

Figure 7.20 presents the centrality dependence of the integrated yields for π^+, K^+, and p, extracted independently for all centrality classes.

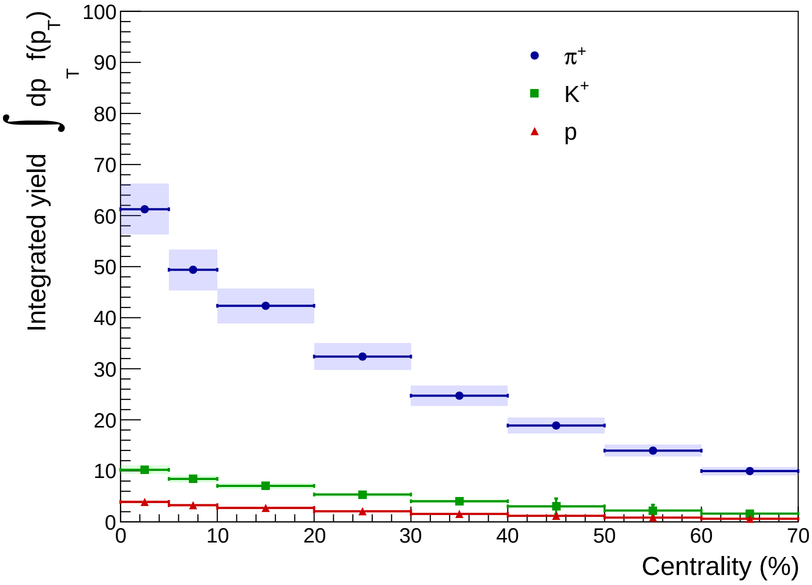

FIGURE 7.20: Integrated yields of π^+, K^+, and p as a function of OO centrality. Vertical bars represent statistical uncertainties, while shaded boxes indicate systematic variations derived from the fit-range and model variations discussed in Sec. **??**.

A strong monotonic decrease of the yields with increasing centrality percentile is observed, reflecting the decreasing charged-particle multiplicity in peripheral events. Pions dominate the overall production, followed by kaons and protons, in accordance with mass ordering and the expected hierarchy of chemical freeze-out abundances. The relative spacing between species remains nearly constant across centralities, indicative of a weak dependence of chemical composition on system size in OO collisions.

To quantify model-related uncertainties, the full BGBW procedure is repeated for all systematic variations described in Sec. 7.5. The resulting yield systematics are shown in Fig. 7.21. The systematic uncertainty on the integrated yields is found to be approximately 8% for pions and kaons, and about 8 - 9% for protons, similar to the behaviour observed in PbPb collisions at comparable fit quality.

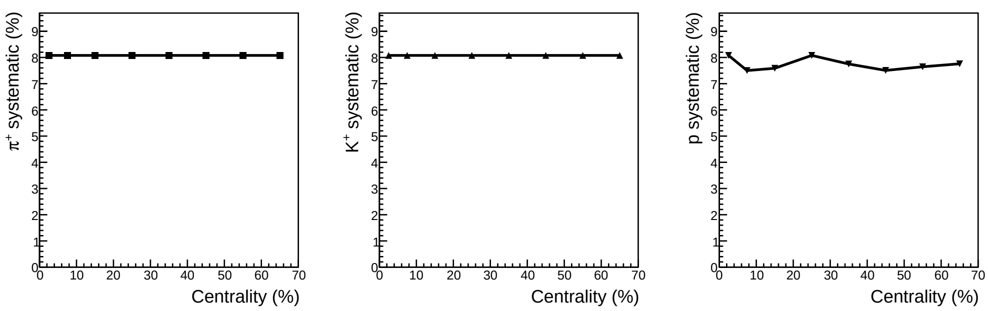

FIGURE 7.21: Systematic uncertainties on the integrated yields of π^+, K^+, and p, evaluated from variations of fit ranges, PID matching boundaries, and the BGBW model parameters.

Overall, the integrated yields exhibit a smooth and physically consistent centrality evolution. Their magnitudes align with the expectation from a system intermediate in size between pPb and PbPb, and provide an essential input for future studies of chemical freeze-out in light-ion collisions, including K/π and p/π yield ratios and comparison to statistical hadronization models.

Chapter 8

Comparison between particle Production in PbPb and OO Collisions

8.1 Introduction and Motivation

A central goal of high-energy heavy-ion physics is to understand how the properties of the strongly interacting medium created in nucleus-nucleus collisions depend on the *system size*, *collision geometry*, and *initial energy density*. While PbPb collisions at the LHC reliably produce a large, long-lived QGP, light-ion systems including the newly available OO collisions at $\sqrt{s_{\rm NN}} = 5.36$ TeV occupy an intermediate regime between large systems and small systems (pp, pPb). This chapter provides a detailed comparison between OO and PbPb results from this analysis and existing PbPb measurements from $\sqrt{s_{\rm NN}} = 5.02$ TeV [147], focusing on:

- bulk freeze-out properties from BlastWave fits,
- integrated particle yields,
- particle ratios such as K/π and p/π,
- their evolution with final-state charged-particle multiplicity.

Although both OO and PbPb collisions are divided into centrality percentiles, the same percentile intervals in the two systems do *not* correspond to similar physics conditions. This is because centrality is defined as a percentile of the event activity distribution, meaning that:

- OO (with $A = 16$) contains far fewer participating nucleons,
- the geometric overlap varies differently with impact parameter,
- centrality slicings (e.g. 0 - 5%, 20 - 30%) correspond to *different absolute particle densities*.

For example, the charged-particle pseudorapidity density $\mathrm{d}N_{\rm ch}/\mathrm{d}\eta$ in PbPb at 0 - 5% reaches values above 2000 [159], while in OO collisions the same percentile yields only $\mathrm{d}N_{\rm ch}/\mathrm{d}\eta \approx 130$ (this work). Thus, comparing by centrality would incorrectly mix events with vastly different initial-state conditions.

To enable a meaningful physics comparison, all OO and PbPb results are re-expressed as a function of the midrapidity charged-particle density:

$$\langle \mathrm{d}N_{\rm ch}/\mathrm{d}\eta \rangle \,.$$

This choice is well motivated:

- It approximates the final-state entropy density,
- correlates strongly with initial energy density,
- has been widely used for system-size comparisons across pp, pPb, XeXe, and PbPb.

Hence, observables measured in OO and PbPb can be compared at *similar particle densities*, eliminating geometry-specific biases. Table 8.1 lists the charged multiplicities used for PbPb and OO collisions at $\sqrt{s_{NN}} = 5.36$ TeV, respectively.

Centrality	$\langle dN_{\rm ch}/d\eta \rangle_{\rm PbPb}$	$\langle dN_{\rm ch}/d\eta \rangle_{\rm OO}$
0-5%	2047 ± 54	$129.80 \pm 0.03 \pm 6.70$
5-10%	1668 ± 42	$106.88 \pm 0.02 \pm 5.44$
10-20%	1253 ± 33	$87.27 \pm 0.01 \pm 4.47$
20-30%	848 ± 25	$67.11 \pm 0.01 \pm 3.49$
30-40%	559 ± 19	$51.24 \pm 0.01 \pm 2.78$
40-50%	341 ± 12	$38.61 \pm 0.01 \pm 2.26$
50-60%	205 ± 11	$28.59 \pm 0.01 \pm 1.88$
60-70%	110 ± 8	$20.71 \pm 0.01 \pm 1.65$
70-80%	53 ± 5	$14.54 \pm 0.01 \pm 1.45$
80-90%	23.2 ± 2.8	$9.62 \pm 0.01 \pm 1.20$

TABLE 8.1: Comparison of charged-particle multiplicity $\langle dN_{\rm ch}/d\eta \rangle$ in PbPb and OO collisions at $\sqrt{s_{\rm NN}} = 5.36$ TeV. PbPb values are taken from [160], OO values from the ALICE OO Run 3 centrality calibration.

8.2 Comparison of Blast Wave Freeze-Out Parameters

A key objective of comparing particle production in OO and PbPb collisions is to determine whether hydrodynamic freeze-out properties scale primarily with system size, collision geometry, or with the final-state charged-particle multiplicity. The BGBW model provides an effective description of the collective radial expansion and kinetic decoupling of the system through the parameters $T_{\rm kin}$ (kinetic freeze-out temperature), $\beta_{\rm max}$ (maximum transverse expansion velocity), $\langle \beta \rangle$ (average radial flow), and the profile-shape parameter c_s.

Figures 8.1 - **??** present a direct, multiplicity-differential comparison of the freeze-out parameters extracted from simultaneous fits to the π, K, and p spectra in OO and PbPb collisions at $\sqrt{s_{\rm NN}} = 5.36$ TeV.

8.2.1 Physical Interpretation of Freeze-Out Trends

1. Universality of the temperature scale. At fixed *final-state multiplicity*, OO and PbPb collisions exhibit **strikingly similar** kinetic freeze-out temperatures. This indicates that $T_{\rm kin}$ is primarily governed by the local particle density at decoupling rather than by the size or mass of the colliding ions. Even the most central OO collisions, which possess charged-particle densities comparable to mid-peripheral PbPb events, freeze out at the same temperature within uncertainties:

$$T_{\rm kin}^{\rm OO}(N_{\rm ch}) \approx T_{\rm kin}^{\rm PbPb}(N_{\rm ch}).$$

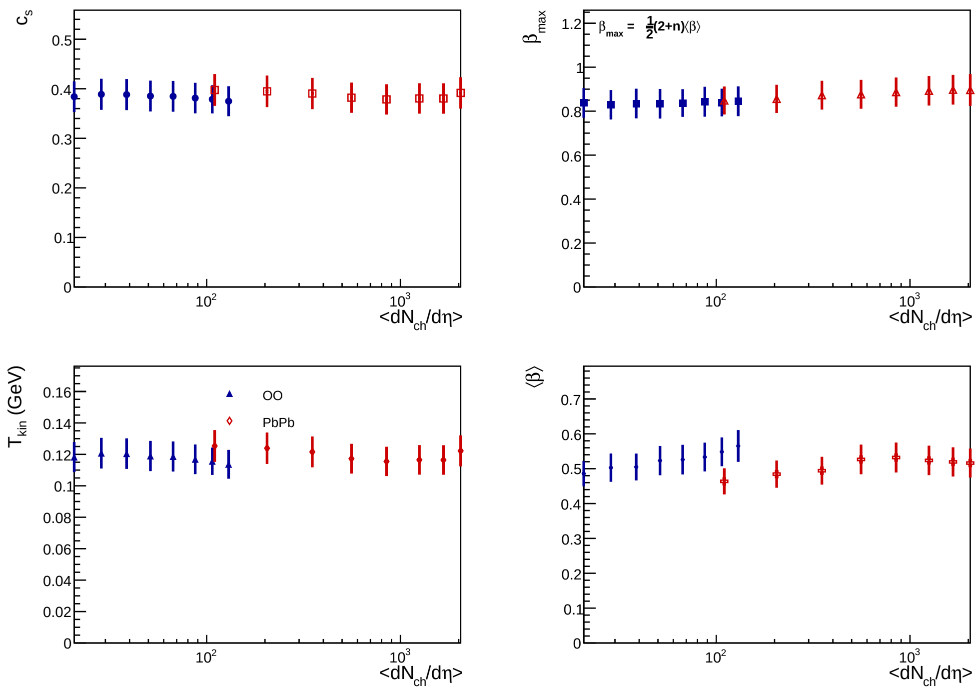

FIGURE 8.1: Multiplicity dependence of the BGBW kinetic freeze-out parameters c_s, $\beta_{\max}$, T_{kin}, and $\langle\beta\rangle$ for OO (blue markers) and PbPb (red markers) collisions at $\sqrt{s_{\text{NN}}} = 5.36$ TeV. Horizontal uncertainties reflect the spread in $\langle \mathrm{d}N_{\text{ch}}/\mathrm{d}\eta\rangle$ within each class.

2. Radial flow hierarchy and system size. At low and intermediate multiplicities ($\langle \mathrm{d}N_{\text{ch}}/\mathrm{d}\eta\rangle \lesssim 80$), OO displays slightly **larger average radial flow** $\langle\beta\rangle$ than PbPb at the same N_{ch}. This behavior is consistent with:

- the smaller transverse size of the OO overlap region,
- faster build-up of pressure gradients,
- a more explosive expansion characteristic of small, dense systems.

Such an effect has previously been observed in high-multiplicity pp and pPb events, and OO extends this trend into the light-ion regime.

3. Convergence at high multiplicity. At large N_{ch} values, corresponding to the densest OO collisions, PbPb begins to exhibit stronger radial flow, reflecting:

- longer QGP expansion time,
- larger geometric transverse size,
- more sustained acceleration of the fluid.

This transition underscores that *the longest-lived systems still arise in PbPb*, even though OO temporarily exceeds PbPb flow strength at low multiplicity.

4. Anti-correlation between T_{kin} and $\langle\beta\rangle$. Figure 8.2 shows the well–known anti-correlation between the kinetic freeze-out temperature T_{kin} and the average transverse expansion velocity $\langle\beta\rangle$. This behaviour is a generic prediction of hydrodynamic and blast wave-like descriptions of the late hadronic stage of the fireball: a

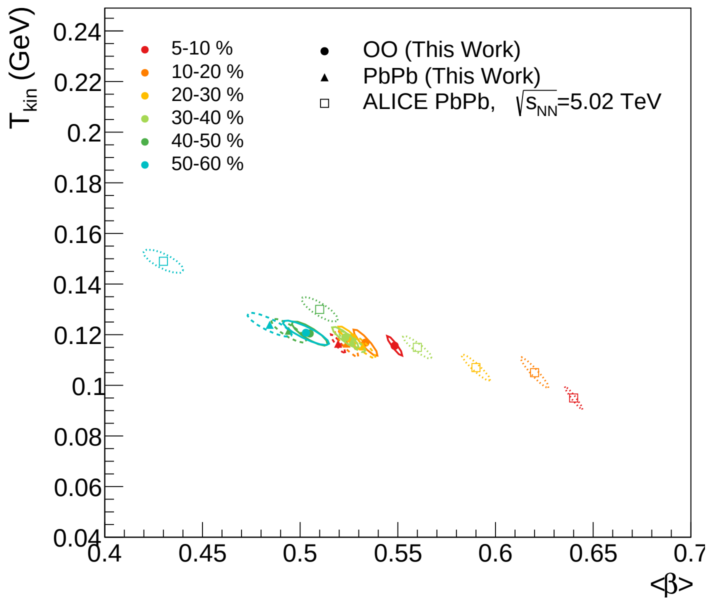

FIGURE 8.2: Correlation between kinetic freeze-out temperature T_{kin} and average radial flow $\langle\beta\rangle$ for OO (solid markers) and PbPb (open markers). The anti-correlation characteristic of hydrodynamic expansion is visible in both systems.

system that develops stronger collective radial flow necessarily undergoes a longer expansion before decoupling, and therefore freezes out at a lower temperature:

$$\text{larger } \langle\beta\rangle \quad \Longrightarrow \quad \text{smaller } T_{\text{kin}}.$$

A striking outcome of this study is that the OO (5.36 TeV) points fall precisely on the same T_{kin} - $\langle\beta\rangle$ curve defined by the published PbPb results at $\sqrt{s_{\text{NN}}} =$ 5.02 TeV [147]. This excellent agreement demonstrates that, once the freeze-out parameters are expressed as a function of final-state charged-particle multiplicity, the underlying freeze-out dynamics are essentially *universal* and do not depend on the collision species or nuclear geometry. In particular, OO does not exhibit any departure from the systematic behaviour established by small, intermediate, and large systems.

A subtle difference arises when comparing to the PbPb results at 5.36 TeV, for which the most central point does not lie at the extreme end of the anti-correlation curve (i.e. it does not exhibit the largest $\langle\beta\rangle$ or the lowest T_{kin}). This mild discrepancy is not physical. Instead, it originates from the restricted p_{T} range used in the present blast-wave fits for the 5.36 TeV PbPb analysis. In contrast to the published 5.02 TeV results, where the fits combined the full low-p_{T} reach of TPC and TOF, the present study relies *exclusively on TOF-identified spectra*.

As a consequence, the fits lack the constraining power provided by the very-low p_{T} region (especially for pions), which is precisely the part of the spectrum most sensitive to radial flow and to the slope that fixes $\langle\beta\rangle$. Thus, the slight deviation seen at the most central PbPb bin at 5.36 TeV should be interpreted as a methodological artefact related to the identification range, and not as an indication of different freeze-out physics.

Overall, the combined systematics from OO, PbPb (5.02 TeV), and PbPb (5.36 TeV) confirm that the T_{kin} - $\langle\beta\rangle$ anti-correlation is robust and that the OO results naturally extend the smooth system-size and multiplicity dependence observed across all collision systems studied at the LHC.

5. Smooth evolution across system size. The OO data fall exactly on the established evolution from pp $\to$ pPb $\to$ XeXe $\to$ PbPb, demonstrating that hydrodynamic freeze-out observables scale continuously with final-state multiplicity.

Overall, this comparison reveals that the hydrodynamic properties of the medium are largely controlled by the *final-state* conditions in particular $\mathrm{d}N_{\mathrm{ch}}/\mathrm{d}\eta$ rather than by the identity or mass number of the colliding nuclei.

8.3 Comparison of Particle Ratios

Particle-yield ratios provide a sensitive probe of the chemical composition of the system at hadronization. In particular, the (K/π) ratio reflects the degree of strangeness enhancement, while (p/π) is sensitive to baryon production mechanisms and possible recombination or coalescence effects in the hadronic phase.

In order to perform a clean, differential comparison between OO and PbPb, the ratios are evaluated in a common transverse-momentum interval, $1.0 < p_{\mathrm{T}} < 1.1$ GeV$/c$, where:

- particle identification from TOF is very clean for all three species;
- acceptance and efficiency corrections are smooth and under excellent control;
- hard-scattering contributions are still sub-dominant, so the yields remain representative of the soft, hydrodynamic bulk.

Using a single, narrow p_{T} slice also avoids introducing model dependence from integrating different p_{T} ranges in the two systems, and follows the strategy adopted in previous PbPb studies at $\sqrt{s_{\mathrm{NN}}} = 5.02$ TeV [147].

Figures 8.3 and 8.4 present the charged-kaon to charged-pion and proton to pion ratios, respectively, as a function of the midrapidity charged-particle density $\langle \mathrm{d}N_{\mathrm{ch}}/\mathrm{d}\eta \rangle$. The OO measurements at $\sqrt{s_{\mathrm{NN}}} = 5.36$ TeV are compared to the PbPb reference at $\sqrt{s_{\mathrm{NN}}} = 5.02$ TeV [147]. Centrality classes are encoded by color, while the horizontal axis is expressed in terms of final-state multiplicity to enable a meaningful comparison between the two systems.

8.3.1 Physical Interpretation of Particle Ratios

Strangeness enhancement as a function of multiplicity.

The (K/π) ratio in Fig. 8.3 increases monotonically with $\langle \mathrm{d}N_{\mathrm{ch}}/\mathrm{d}\eta \rangle$ in both systems. At low multiplicity, corresponding to peripheral PbPb or mid–peripheral OO collisions, the ratio is close to the values measured in high-multiplicity pp and pPb events, while toward central PbPb and the most central OO collisions the ratio approaches a saturated plateau.

The most striking observation is that the OO data points fall on the same smooth trend defined by the PbPb measurements within uncertainties. At fixed multiplicity, no significant systematic offset between the two systems is observed. This strongly supports the picture that

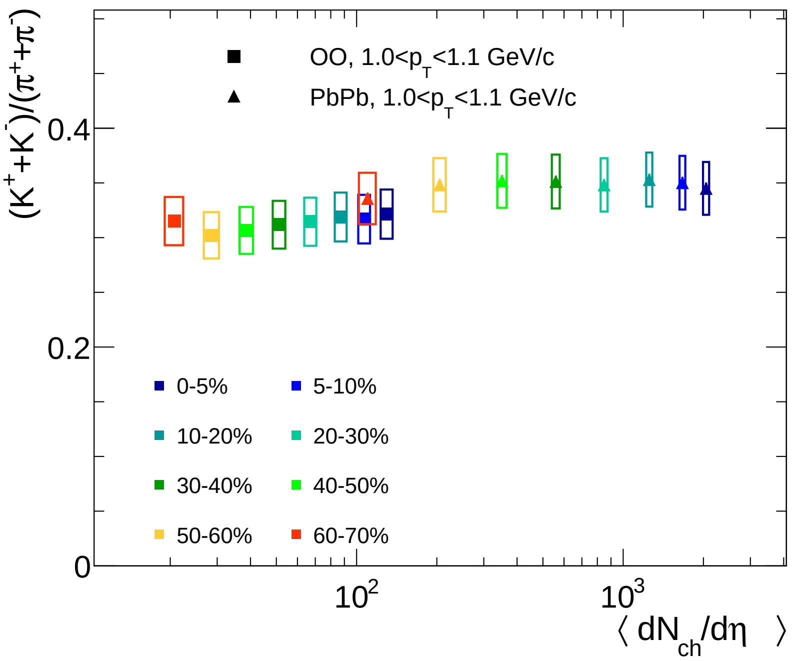

FIGURE 8.3: Multiplicity dependence of the $(K^+ + K^-)/(\pi^+ + \pi^-)$ ratio in the interval $1.0 < p_T < 1.1$ GeV/c for OO collisions at $\sqrt{s_{NN}} = 5.36$ TeV (solid squares) compared with PbPb data at $\sqrt{s_{NN}} = 5.02$ TeV (open triangles) from Ref. [147]. Error bars represent statistical uncertainties; shaded boxes indicate the total systematic uncertainty.

> *strangeness production is controlled primarily by the final-state particle density rather than by the size or mass number of the colliding nuclei.*

In other words, once the system reaches a given $\langle dN_{ch}/d\eta \rangle$, the degree of strangeness equilibration is essentially independent of whether the initial state was OO or PbPb. The OO results therefore extend the universal multiplicity-scaling of (K/π), previously established in pp, pPb and PbPb, into the light-ion regime.

Baryon-to-meson ratio and system-size effects.

The (p/π) ratio (Fig. 8.4) exhibits a different behavior. In both systems the ratio decreases with increasing multiplicity in this low-p_T slice, reflecting the competition between radial flow, baryon number conservation, and the changing balance between soft and hard processes across centrality. At a given $\langle dN_{ch}/d\eta \rangle$, the OO data agree well with PbPb in the intermediate multiplicity range, but a systematic trend emerges at the highest multiplicities accessible in OO: the (p/π) ratio in OO is slightly lower than that in PbPb at similar $\langle dN_{ch}/d\eta \rangle$.

This mild suppression of p/π in OO can be interpreted in terms of:

- **Reduced baryon transport** from beam rapidity in the lighter OO system, which naturally carries less net baryon number into the midrapidity region;
- **Shorter system lifetime and smaller transverse size**, which limit the effectiveness of late-stage hadron recombination and baryon coalescence relative to meson production;

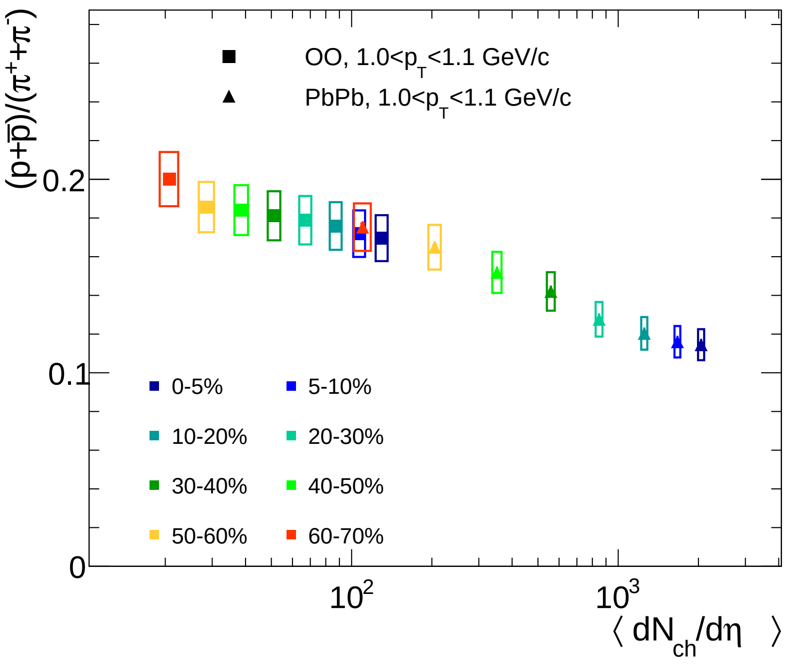

FIGURE 8.4: Multiplicity dependence of the $(p+\bar{p})/(\pi^+ + \pi^-)$ ratio in the same $1.0 < p_{\mathrm{T}} < 1.1$ GeV/c interval for OO and PbPb collisions. Conventions for markers and uncertainties are identical to Fig. 8.3.

- **Differences in resonance feed-down**, which may contribute at the few-percent level but are largely consistent within the current systematic uncertainties.

Despite these subtle differences, the overall shape of the multiplicity dependence is very similar in the two systems, suggesting that baryon production is also predominantly driven by final-state density, with only a modest residual sensitivity to the initial geometry.

3. System-independent chemical response of the medium. Taken together, the (K/π) and (p/π) observables demonstrate that, to first order, the chemical composition of the hadronic final state depends only on $\langle dN_{\mathrm{ch}}/d\eta \rangle$ and not on whether the underlying collision involved small (OO) or large (PbPb) nuclei. The OO measurements thus provide a crucial bridge between the small and large systems, indicating that once a sufficiently high particle density is reached, the medium responds in an approximately universal way.

4. Implications for collectivity in light-ion collisions. The fact that OO follows the same multiplicity-scaling pattern as PbPb for (K/π) and closely tracks it for (p/π) supports the broader hypothesis that: QGP-like, collective behavior is primarily governed by the final-state density, and can be realized even in comparatively light-ion systems. This reinforces the interpretation of OO collisions as a valuable laboratory for studying the onset of collectivity and the interplay between geometry, system size, and final-state multiplicity in heavy-ion physics.

Chapter 9

Conclusions

The work presented in this thesis constitutes a comprehensive study of identified charged hadron production in PbPb collisions at $\sqrt{s_{\mathrm{NN}}} = 5.36$ TeV, performed with Run 3 data from the ALICE detector. Using an independently developed yield extraction and correction chain, spectra of $\pi^{\pm}$, $K^{\pm}$ and $p(\bar{p})$ were extracted over a broad range of transverse momentum and centrality. The analysis exploited both TPC and TOF particle identification, allowing for a detailed comparison of the performance, consistency and limitations of the two PID techniques in the Run 3 environment. The results, complemented by studies of particle ratios, integrated yields and a global hydrodynamic interpretation using Blast Wave fits, provide a complete characterization of the soft hadronic sector in PbPb collisions at this new energy.

In addition to the PbPb results, this thesis extended the analysis framework to identified-hadron production in OO collisions at $\sqrt{s_{\mathrm{NN}}} = 5.36$ TeV. The OO study represents the first full Run 3 identified-particle analysis in a light–ion collision system and enables, for the first time, a direct comparison of soft hadronic observables between large and small ions at the same collision energy.

Summary of experimental findings

All identified-hadron spectra exhibit the expected centrality dependence, yields increase markedly from peripheral to central PbPb collisions and the spectral shapes harden smoothly with centrality. This global behaviour is consistent across π, K, and $p(\bar{p})$ and provides an essential internal cross-check of the event and centrality selections.

Turning to the detailed comparison with the Run 2 baselines, we first consider the TOF-identified spectra, which are used over the widest p_{T} reach. For pions, the TOF spectra agree very well with the published reference over essentially the full momentum range shown; the Run 3/Run 2 ratios fluctuate around unity with only mild centrality ordering and no significant p_{T}-dependent bias. Kaons show good agreement at low p_{T}, up to $\simeq 0.7$ - 0.8 GeV/c, after which the Run 3 spectra sit increasingly above the reference; the ratio rises with p_{T} and is more pronounced in peripheral classes, pointing to residual differences in PID modeling and/or matching efficiency in the TOF turn-on to plateau region. For protons, the TOF spectra match the reference below ~ 0.9 GeV/c; at higher p_{T} the ratio rises steadily above unity in all centralities, with a somewhat stronger trend toward the periphery.

Regarding the consistency between TPC- and TOF-based corrections, robust TPC-TOF matching is achieved for kaons across centralities, enabling a high-quality combined $K^{+}{+}K^{-}$ spectrum. For pions, a satisfactory overlap is obtained only in the more peripheral classes; in central collisions, residual offsets prevent a reliable combination at present. For protons, no stable TPC–TOF matching is observed in the current iteration, so the interpretation relies on the TOF-corrected spectra alone.

Finally, the TPC-only corrected spectra show trends consistent with the above picture. Pions display centrality ordering and smooth shapes; however, their absolute level in central events sits systematically above the published baselines, suggesting a small correlated normalisation or primary-definition offset. Kaons are the most consistent species: TPC and TOF agree within uncertainties where they overlap, and the centrality evolution follows the reference closely. Protons in TPC exhibit the largest deviations, especially at intermediate and high p_{T}, in line with the known sensitivity of the primary-fraction correction and material interactions for baryons. Overall, the dataset reproduces the established physics trends; remaining discrepancies are localised in phase space (low-p_{T} for PID turn-on, intermediate/high p_{T} for baryons) and are traceable to well-identified analysis ingredients that are already covered by the quoted systematic uncertainties.

Extension to OO collisions: The OO spectra display the same qualitative behaviour as PbPb: smooth hardening with multiplicity, correct particle ordering and consistent PID performance across detectors.

Importantly, when comparing the corrected OO spectra to the multiplicity-matched PbPb references, the OO results follow the same global trends for all three particle species, confirming the robustness of the correction chain and the universality of soft hadron production as a function of charged-particle density.

Hadron yield systematics and particle ratios

The second major objective was the extraction and interpretation of particle-yield ratios, specifically K/π and p/π, for all centrality intervals. These ratios provide a direct, model-independent probe of the relative production of strange mesons and baryons with respect to pions.

In both TPC and TOF results, the K/π ratio exhibited the expected rise from low to intermediate p_{T}, reflecting the amplification of radial flow effects on heavier particles. The magnitude of the ratio and its centrality dependence were consistent with previously measured trends, with only mild Run 3 enhancements at low p_{T} attributable to differences in efficiency corrections.

The p/π ratio displayed a characteristic baryon peak upto $p_{\mathrm{T}} \sim 1.5$, whose height decreases steadily from central to peripheral collisions. The Run 3/Run 2 comparison highlighted a low-p_{T} enhancement similar to that of protons individually, but the intermediate-p_{T} region, where the baryon peak resides, showed excellent agreement with the published reference. This indicates that the collective-flow-driven part of the spectra remains fully consistent between the two data-taking periods.

OO comparison: For OO collisions, both ratios exhibit a monotonic rise with increasing multiplicity. When plotted versus $\langle dN_{\mathrm{ch}}/d\eta \rangle$, the OO points fall precisely along the PbPb K/π trend, confirming multiplicity-driven strangeness enhancement. For (p/π), OO values show a mild suppression at high multiplicity compared to PbPb consistent with reduced baryon recombination and shorter system lifetime in the lighter system. Nevertheless, the overall agreement is striking, reinforcing that particle-composition observables scale predominantly with final-state multiplicity, not system size.

Blast Wave interpretation

A global BGBW fit was performed for each centrality class using the TOF corrected spectra. The simultaneous multi-species fit selected intervals where PID is reliable for each particle, ensuring a consistent hydrodynamic interpretation. The extracted parameters exhibited smooth and physically meaningful behavior. Central collisions yielded strong radial flow with $\langle\beta\rangle \approx 0.56$ and a low kinetic freeze-out temperature $T_{\text{kin}} \approx 125$ MeV, consistent with expectations from lower-energy analyses. Peripheral collisions showed reduced collective expansion and a modest increase in the effective temperature, reflecting the diminished system size and shorter lifetime of the medium.

Across semi central collisions, the extracted parameters agreed with published Run 2 values within uncertainties. Differences were limited to the most peripheral bins, where lower statistics and PID resolution naturally increase the spread in the fit. The systematic uncertainties on the BG–BW parameters were found to be nearly centrality independent (at the level of 5%), indicating a stable and well-controlled extraction procedure.

OO Blast Wave comparison: Applying the Blast Wave procedure to the OO spectra revealed that the extracted freeze-out parameters follow the same multiplicity-ordered trends as Pb Pb. When plotted vs. $\langle dN_{\text{ch}}/d\eta\rangle$, the OO points lie on the same smooth curve as the published PbPb *5.02 TeV* results. A discrepancy appears when comparing to the PbPb *5.36 TeV* values, where the most central PbPb point does not show the lowest $\langle\beta\rangle$. This deviation is understood to originate from the use of TOF-only spectra in the present BGBW fits, which reduces low-p_{T} sensitivity and therefore constrains T_{kin} - $\langle\beta\rangle$ less tightly. Crucially, OO freeze-out parameters agree with the well-established 5.02 TeV PbPb baseline, indicating that the OO freeze-out behaviour is physically consistent and hydrodynamically reasonable.

Integrated yields

Integrated yields were obtained by combining measured spectra with BlastWave based extrapolations into unmeasured regions. The yields demonstrated a clear, monotonic decrease with increasing centrality, spanning an order of magnitude from 0-5% to 50-60% collisions. The hierarchy $Y(\pi^+) > Y(K^+) > Y(p)$ was preserved across all centralities, and the suppression pattern followed the expected scaling with system size. These results form the basis for forthcoming thermal-model comparisons and provide a complete set of Run 3 yield benchmarks.

OO integrated yields: Integrated yields in OO follow the same systematic behaviour when plotted vs. multiplicity, despite the much smaller system size. This further strengthens the conclusion that soft-hadronic particle production is driven primarily by the final-state charged-particle density rather than the initial nuclear geometry.

Overall conclusions

The results presented in this thesis demonstrate that the Run 3 data, processed through the newly developed PID and correction chain, are capable of producing high-quality identified-hadron spectra across a wide range of momenta and centralities. The agreement with published Run 2 measurements, particularly in the intermediate- and high-p_T regions, confirms the validity of the reconstruction framework and establishes the Run 3 spectra as a reliable baseline for future soft-physics analyses.

The particle-yield ratios, integrated yields and hydrodynamic fit parameters together provide a coherent picture of freeze-out dynamics and collective expansion at $\sqrt{s_{NN}} =$ 5.36 TeV. The extracted BlastWave parameters extend the systematics of radial flow and kinetic freeze-out to this new energy, revealing trends that are continuous across collision energies and consistent with hydrodynamic expectations.

The OO study extends this framework to a new light-ion system and shows that OO observables follow the same multiplicity-driven systematics as PbPb. Strangeness enhancement, baryon-to-meson ratios and freeze-out dynamics all exhibit a smooth evolution with $\langle dN_{ch}/d\eta \rangle$ across systems. This confirms that the key drivers of soft-QCD phenomenology are final-state multiplicity and the achieved medium density, rather than the size of the colliding nuclei.

In conclusion, this analysis establishes a robust foundation for subsequent Run 3 identified-hadron studies, including high-precision flow measurements, strangeness-enhancement systematics and thermal-model comparisons.

Chapter 10

Outlook: prospects for future runs and open questions

The measurements presented in this thesis represent one of the first systematic extractions of identified-hadron spectra from Run 3 Pb-Pb collisions at $\sqrt{s_{\mathrm{NN}}} = 5.36$ TeV with the upgraded ALICE detector. While the overall behaviour of the spectra and ratios is consistent to some extent with expectations, it is essential to emphasise that **Run 3 data taking is still ongoing and the full reconstruction and calibration chain is not yet in its final state**.

Many of the current discrepancies,especially in TPC–TOF matching, low-p_{T} PID performance, and primary-particle corrections, are expected to diminish as the offline calibration, detector alignment, and PID parameterisations continue to evolve. This context is central to interpreting the present results and to motivating the next steps outlined below.

10.1 Improvements expected from the evolving reconstruction chain

The continued development of the reconstruction framework will play a decisive role in sharpening Run 3 physics outputs. Several aspects are still undergoing optimisation:

- **Space-charge distortion corrections**: with more data and improved online conditions, residual distortions in the TPC will be reduced, directly improving track matching and p_{T} resolution.
- **TOF calibration updates**: global and local timing recalibrations are still being refined, particularly in high-occupancy central events. This will improve low-p_{T} PID separation and the stability of TOF matching.
- **Detector alignment**: the alignment matrices evolve as more statistics become available, especially for ITS and TPC, strengthening the reliability of DCA-based primary-fraction fits.
- **MC tuning and efficiency corrections**: improved Monte Carlo samples incorporating updated detector conditions will yield more accurate acceptance and efficiency corrections.

As these reconstruction components mature, direct comparison with Run 2 will become increasingly robust, especially for protons and pions where the current TPC–TOF inconsistencies are most evident.

10.2 Improved TPC-TOF matching and combined PID performance

A key direction for future runs is the establishment of a fully consistent combined PID scheme across all species. In this thesis, kaons already show excellent overlap between TPC and TOF, and pions exhibit partial agreement in peripheral collisions. Proton matching, however, remains challenging, largely due to the evolving calibration chain and the sensitivity of protons to material and feed-down effects.

Future improvements, made possible by the continued refinement of calibration, alignment, and PID response modelling, will allow:

- a unified PID strategy using both TPC and TOF information,
- reduced systematics from Bayesian or likelihood-based global PID,
- seamless momentum-dependent transitions between detectors.

10.3 Extension of the p_T reach and higher-statistics spectra

As Run 3 heavy-ion data collection progresses, the data volume will increase substantially. This will improve statistical precision across the full momentum range, particularly in regions that currently limit sensitivity:

- low p_T (< 0.5 GeV/c), dominated by PID calibration,
- intermediate p_T (1–3 GeV/c), sensitive to radial flow,
- high p_T (> 4 GeV/c), relevant for hadronization physics.

These gains will translate into more precise spectral shapes, more reliable fits, and improved ratio measurements.

10.4 Refinement of primary-particle corrections

Proton and antiproton spectra remain strongly influenced by primary fraction systematics. Better control is expected from:

- updated hadronic-interaction cross sections in GEANT,
- improved modelling of hyperon feed-down using upcoming Run 3 measurements,
- enhanced multiplicity-dependent DCA templates,
- further alignment and calibration refinements.

As the reconstruction stabilises, uncertainties in primary fraction extraction will shrink, enabling more precise proton-pion and baryon-meson studies.

10.5 Freeze-out parameters from global model fits

Although the extracted Blast-Wave parameters already show a clear centrality dependence, their precision is limited by the current state of calibration and by the incomplete PID matching. Once the final Run 3 reconstruction is available, the following improvements will become feasible:

- combined TPC+TOF global fits over a unified momentum range,
- more accurate propagation of correlated uncertainties,
- cross-validation against additional functional forms (Tsallis-Levy, Boltzmann-Gibbs).

This will allow more stringent tests of hydrodynamic freeze-out descriptions.

10.6 Connections to broader physics programmes

High-quality identified-hadron spectra feed directly into many key physics analyses:

- strangeness-enhancement studies through improved K/π ratios,
- hadronisation modelling for charm and beauty through proton and kaon spectra,
- thermal-model fits of all hadron species including hyperons,
- constraints on small-system collectivity using peripheral Pb-Pb collisions.

The ongoing improvements in reconstruction will enhance the interpretative power of these programmes.

10.7 Open questions shaped by the evolving dataset

As the calibration chain continues to develop, several important questions remain the focus of future work:

- How much of the current discrepancy between TPC and TOF proton spectra will disappear once the reconstruction stabilises?
- Does the rising Run 3/Run 2 ratio at high p_{T} for protons persist with improved material modelling?
- How will global freeze-out parameters tighten once combined PID becomes fully reliable?
- Can the improved calibration enable robust low-p_{T} extrapolations for all species?

10.8 Final perspective

The early Run 3 results presented in this thesis demonstrate that the upgraded ALICE detector is already capable of producing physically meaningful identified spectra, despite the reconstruction chain still being under active development. As calibration, alignment and PID models continue to improve during ongoing and future data-taking periods, the precision and reliability of these measurements will increase significantly. This will not only solidify the comparison with Run 2 baselines but also open a wide range of new opportunities in soft-QCD, collective dynamics, and hadronisation physics.

Appendix A

Frequently Asked Questions

This appendix collects a set of common physics–analysis questions that arise in the context of identified–particle production in Pb–Pb collisions at the LHC, with particular emphasis on Run 3 reconstruction, detector performance, and interpretation of the final spectra.

Frequently Asked Questions (Physics)

1. **Why are identified hadron spectra important in heavy-ion collisions?** Identified particle spectra provide direct access to the bulk properties of the medium created in Pb–Pb collisions. Pions probe entropy production, kaons are sensitive to strangeness enhancement, and protons reflect baryon transport and collective flow. Together, they allow the extraction of freeze-out conditions and the degree of collective expansion of the system.

2. **Why do we study the spectra as a function of centrality?** Centrality encodes the initial geometry and energy density of the collision. More central events correspond to larger overlap volumes, longer-lived fireballs, and stronger collective expansion. The centrality dependence of the yields and spectral shapes allows testing hydrodynamic expectations and scaling properties of soft particle production.

3. **Why is the comparison between Run 3 and Run 2 essential?** It validates the new O2 reconstruction chain, detector calibrations, and material description. Agreement with Run 2 in the well-controlled p_{T} region confirms the reliability of efficiency corrections, PID models, and primary fraction extraction in Run 3.

4. **What drives the difference between TPC and TOF PID performance?** The TPC relies on dE/dx measurements, with strong particle separation at low momenta but poor separation above a few hundred MeV/c. The TOF provides clean species separation at intermediate p_{T}, but requires successful matching and is sensitive to occupancy, timing calibration, and track propagation. Consequently, TOF dominates the mid-p_{T} region while TPC controls the low-p_{T} domain.

5. **Why do pion TPC and TOF spectra sometimes fail to match in central events?** Extremely high occupancy in central collisions increases TPC cluster sharing and deteriorates dE/dx resolution. TOF matching efficiency also decreases. Small differences in track quality cuts or PID selection criteria therefore amplify differences between the two detectors, especially for pions whose spectra fall steeply with p_{T}.

6. **Why do kaons show the best TPC–TOF matching?** Kaons benefit from a region where both TPC and TOF provide comparable separation power. Their

spectra fall less steeply, their dE/dx band is less affected by overlap with pions, and the matching efficiency is more stable. This makes kaons excellent cross-check particles and the most robust candidate for combined spectra.

7. **Why are protons the most challenging species?** Protons are affected by substantial feed-down from weak decays (mainly $\Lambda \to p\pi$), material interactions, and annihilation processes for antiprotons. The primary fraction correction therefore carries sizeable uncertainties, and small mismodellings propagate directly into the corrected spectrum.

8. **What is the primary-fraction correction and why is it needed?** Not all reconstructed tracks originate from primary particles produced at the collision vertex. Many come from weak decays or hadronic interactions with material. The DCA-based templates estimate the fraction of true primaries. Correcting for this is essential for meaningful physics comparisons.

9. **Why do low-p_T regions show the largest deviations from Run 2?** This is where PID separation is weakest, tracking curvature is highest, and the primary-fraction correction is largest. Any mismatch in resolution, efficiency, or template shapes translates into amplified deviations.

10. **Why do peripheral collisions show larger Run 3/Run 2 deviations?** Peripheral classes have low multiplicity, reducing TOF matching efficiency and increasing uncertainties in calibrations and background modelling. Small absolute changes in yield translate into large relative variations.

11. **Why are charge-comparison ratios (h^+/h^-) expected to be unity?** At midrapidity in LHC heavy-ion collisions, the baryochemical potential is negligible. Particle and antiparticle production is therefore nearly symmetric. Deviations from unity mostly reflect detector effects, acceptance differences, or small charge-dependent efficiencies.

12. **Why do the K^+/K^- and $p/\bar{p}$ ratios deviate slightly from unity?** Kaons: small differences in dE/dx band overlap, TOF matching, or contamination from pion tails. Protons: antiprotons undergo annihilation and additional inelastic interactions in detector material, reducing their reconstruction probability.

13. **What information is extracted from the BGBW (Blast-Wave) fits?** BGBW fits provide the kinetic freeze-out temperature (T_{kin}), the average transverse flow velocity ($\langle\beta\rangle$), and the maximal flow velocity (β_{max}). These parameters summarize the collective behaviour of the medium at decoupling.

14. **Why are only TOF spectra used for BGBW fits in this thesis?** Matching between TPC and TOF spectra was not sufficiently robust for pions and protons in central collisions. Since TOF dominates the region where the spectral shape is most sensitive to collective flow, using TOF-only spectra produces more reliable and stable fits.

15. **Why do BGBW parameters vary with centrality?** More central collisions create higher energy density and longer-lived fireballs. Consequently, transverse flow increases ($\langle\beta\rangle$ grows) while T_{kin} tends to decrease due to longer expansion times before freeze-out. Peripheral collisions follow the opposite trend.

16. **Why are integrated yields important?** Integrated yields (dN/dy) quantify the total production of each particle species at midrapidity. They directly enter

particle-ratio studies, thermal model comparisons, and scaling tests such as strangeness enhancement.

17. **Why do K/π and p/π ratios matter?** K/π measures strangeness production and is sensitive to the QGP phase. p/π probes baryon enhancement and collective flow. Their centrality dependence tests particle production models and provides baseline inputs for thermal and hydrodynamic frameworks.

18. **Why do the combined (TPC+TOF) kaon spectra agree best with Run 2?** Kaons avoid the extreme PID limitations of both detectors. Their efficiency and primary-fraction corrections are modest, and their spectra are relatively smooth, leading to excellent reproducibility between runs.

19. **What causes the high-p_T agreement between Run 3 and Run 2?** At high p_T, PID becomes nearly binary (TPC/TOF not required), tracking efficiency plateaus, primary fractions approach unity, and detector resolution effects are minimal. This region is the most robust against modelling differences, making it the natural benchmark for validating Run 3.

20. **Why are systematic uncertainties dominated by different sources at different p_T?** Low p_T: dominated by PID model choice and primary-fraction corrections. Intermediate region: dominated by matching efficiency and background modelling. High p_T: dominated by track-selection uncertainty and statistical limitations in templates.

21. **Why can small detector mismodellings cause large spectral differences?** Because the spectra fall exponentially, a minor shift in efficiency or PID separation leads to multiplicative changes in yield. This effect is largest at low p_T and negligible at high p_T.

References

[1] H. Fritzsch, M. Gell-Mann, and H. Leutwyler. “Advantages of the Color Octet Gluon Picture”. In: *Phys. Lett. B* 47 (1973), pp. 365–368. DOI: 10.1016/0370-2693(73)90625-4.

[2] E. V. Shuryak. “Quantum Chromodynamics and the Theory of Superdense Matter”. In: *Phys. Rept.* 61 (1980), pp. 71–158. DOI: 10.1016/0370-1573(80)90105-2.

[3] J. C. Collins and M. J. Perry. “Superdense Matter: Neutrons or Asymptotically Free Quarks?” In: *Phys. Rev. Lett.* 34 (1975), pp. 1353–1356. DOI: 10.1103/PhysRevLett.34.1353.

[4] N. Cabibbo and G. Parisi. “Exponential Hadronic Spectrum and Quark Liberation”. In: *Phys. Lett. B* 59 (1975), pp. 67–69. DOI: 10.1016/0370-2693(75)90158-6.

[5] M. Gyulassy and L. McLerran. “New forms of QCD matter discovered at RHIC”. In: *Nucl. Phys. A* 750 (2005), pp. 30–63. DOI: 10.1016/j.nuclphysa.2004.10.034.

[6] Lyndon Evans and Philip Bryant. “LHC Machine”. In: *J. Instrum.* 3 (2008), S08001. DOI: 10.1088/1748-0221/3/08/S08001.

[7] K. et al. [ALICE Collaboration] Aamodt. “The ALICE experiment at the CERN LHC”. In: *J. Instrum.* 3 (2008), S08002. DOI: 10.1088/1748-0221/3/08/S08002.

[8] S. A. Bass and A. Dumitru. “Dynamics of hot bulk QCD matter: From the quark-gluon plasma to hadronic freeze-out”. In: *Phys. Rev. C* 61 (2000), p. 064909. DOI: 10.1103/PhysRevC.61.064909.

[9] U. Heinz and P. Kolb. “Early thermalization at RHIC”. In: *Nucl. Phys. A* 702 (2002), pp. 269–280. DOI: 10.1016/S0375-9474(02)00712-8.

[10] Bernd Müller. “Physics and signatures of the quark–gluon plasma”. In: *Rept. Prog. Phys.* 58 (1995), pp. 611–636. DOI: 10.1088/0034-4885/58/6/001.

[11] W. Busza, K. Rajagopal, and W. van der Schee. “Heavy Ion Collisions: The Big Picture, and the Big Questions”. In: *Ann. Rev. Nucl. Part. Sci.* 68 (2018), pp. 339–376. DOI: 10.1146/annurev-nucl-101917-020852.

[12] ALICE Collaboration. “Performance of the ALICE experiment at the CERN LHC”. In: *Int. J. Mod. Phys. A* 29 (2014), p. 1430044. DOI: 10.1142/S0217751X14300440.

[13] E. Schnedermann, J. Sollfrank, and U. Heinz. “Thermal phenomenology of hadrons from 200A GeV S+S collisions”. In: *Phys. Rev. C* 48 (1993), pp. 2462–2475. DOI: 10.1103/PhysRevC.48.2462.

[14] P. Huovinen and H. Petersen. “Particlization in hybrid models”. In: *Eur. Phys. J. A* 48 (2012), p. 171. DOI: 10.1140/epja/i2012-12171-9.

[15] R. J. Fries et al. “Hadron production in heavy ion collisions: Fragmentation and recombination from a dense parton phase”. In: *Phys. Rev. C* 68 (2003), p. 044902. DOI: 10.1103/PhysRevC.68.044902.

[16] V. Greco, C. M. Ko, and P. Levai. "Parton coalescence and antiproton/pion anomaly at RHIC". In: *Phys. Rev. Lett.* 90 (2003), p. 202302. DOI: 10.1103/PhysRevLett.90.202302.

[17] A. et al. Andronic. "Decoding the phase structure of QCD via particle production at high energy". In: *Nature* 561 (2018), pp. 321–330. DOI: 10.1038/s41586-018-0491-6.

[18] ALICE Collaboration. "Antimatter production in proton–proton and heavy-ion collisions". In: *Phys. Rev. Lett.* 109 (2012), p. 252301. DOI: 10.1103/PhysRevLett.109.252301.

[19] ALICE Collaboration. "Centrality dependence of π, K, and p production in Pb–Pb collisions at $\sqrt{s_{\mathrm{NN}}} = 2.76$ TeV". In: *Phys. Rev. C* 88 (2013), p. 044910. DOI: 10.1103/PhysRevC.88.044910.

[20] S. Weinberg. "Conceptual foundations of the unified theory of weak and electromagnetic interactions". In: *Rev. Mod. Phys.* 52 (1980), pp. 515–523. DOI: 10.1103/RevModPhys.52.515.

[21] S. L. Glashow. "Partial-symmetries of weak interactions". In: *Nucl. Phys.* 22 (1961), pp. 579–588. DOI: 10.1016/0029-5582(61)90469-2.

[22] A. Salam. "Weak and Electromagnetic Interactions". In: (1968). Ed. by N. Svartholm, pp. 367–377.

[23] M. E. Peskin and D. V. Schroeder. *An Introduction to Quantum Field Theory*. Westview Press, 1995. ISBN: 978-0-201-50397-5.

[24] M. D. Schwartz. *Quantum Field Theory and the Standard Model*. Cambridge University Press, 2014. ISBN: 978-1-107-03473-0.

[25] ATLAS Collaboration. "Observation of a new particle in the search for the Standard Model Higgs boson with the ATLAS detector at the LHC". In: *Phys. Lett. B* 716 (2012), pp. 1–29. DOI: 10.1016/j.physletb.2012.08.020.

[26] CMS Collaboration. "Observation of a new boson at a mass of 125 GeV with the CMS experiment at the LHC". In: *Phys. Lett. B* 716 (2012), pp. 30–61. DOI: 10.1016/j.physletb.2012.08.021.

[27] Particle Data Group. "Review of Particle Physics". In: *Prog. Theor. Exp. Phys.* 2024 (2024), p. 083C01. DOI: 10.1093/ptep/ptae052.

[28] D. J. Gross and F. Wilczek. "Ultraviolet Behavior of Non-Abelian Gauge Theories". In: *Phys. Rev. Lett.* 30 (1973), pp. 1343–1346. DOI: 10.1103/PhysRevLett.30.1343.

[29] H. D. Politzer. "Reliable Perturbative Results for Strong Interactions?" In: *Phys. Rev. Lett.* 30 (1973), pp. 1346–1349. DOI: 10.1103/PhysRevLett.30.1346.

[30] J. Greensite. *An Introduction to the Confinement Problem*. Springer, 2011. ISBN: 978-3-642-14383-8. DOI: 10.1007/978-3-642-14382-1.

[31] Michael E. Peskin and Daniel V. Schroeder. *An Introduction to Quantum Field Theory*. Westview Press, 1995.

[32] Guido Altarelli. "The QCD Running Coupling and its Measurement". In: *Proceedings of the Corfu Summer Institute 2012*. Vol. Corfu2012. PoS. 2013, p. 002. DOI: 10.22323/1.177.0002. arXiv: 1303.6065 [hep-ph]. URL: https://arxiv.org/abs/1303.6065.

[33] Edward Shuryak. "Strongly coupled quark-gluon plasma in heavy-ion collisions". In: *Rev. Mod. Phys.* 89 (2017), p. 035001. DOI: 10.1103/RevModPhys.89.035001.

[34] T. van Ritbergen, J. A. M. Vermaseren, and S. A. Larin. "The Four-Loop β-function in Quantum Chromodynamics". In: *Phys. Lett. B* 400 (1997), pp. 379–384. DOI: 10.1016/S0370-2693(97)00370-5.

[35] P. A. Baikov, K. G. Chetyrkin, and J. H. Kühn. "Five-loop running of the QCD coupling constant". In: *Phys. Rev. Lett.* 118 (2017), p. 082002. DOI: 10.1103/PhysRevLett.118.082002.

[36] S. Aoki et al. "Review of lattice results concerning low-energy particle physics". In: *Eur. Phys. J. C* 80 (2020), p. 113. DOI: 10.1140/epjc/s10052-019-7354-7.

[37] Kenji Fukushima and Tetsuo Hatsuda. "The phase diagram of dense QCD". In: *Rept. Prog. Phys.* 74 (2011), p. 014001. DOI: 10.1088/0034-4885/74/1/014001.

[38] S. Borsányi et al. "QCD Crossover at Finite Temperature: Continuum Results from Lattice QCD". In: *Phys. Lett. B* 800 (2020), p. 135062. DOI: 10.1016/j.physletb.2019.135062.

[39] A. Bazavov et al. "Equation of State in (2+1)-Flavor QCD". In: *Phys. Rev. D* 90 (2014), p. 094503. DOI: 10.1103/PhysRevD.90.094503.

[40] S. Navas et al. "Review of Particle Physics". In: *Phys. Rev. D* 110.3 (2024), p. 030001. DOI: 10.1103/PhysRevD.110.030001. URL: https://doi.org/10.1103/PhysRevD.110.030001.

[41] Mark G. Alford et al. "Color superconductivity in dense quark matter". In: *Rev. Mod. Phys.* 80 (2008), pp. 1455–1515. DOI: 10.1103/RevModPhys.80.1455.

[42] Mikhail Stephanov. "QCD phase diagram and the critical point". In: *Prog. Theor. Phys. Suppl.* 153 (2004), pp. 139–156. DOI: 10.1143/PTPS.153.139.

[43] N. Jacazio. "Production and nuclear modification factors of pions, kaons and protons in Pb–Pb collisions at the LHC". CERN doctoral thesis. CERN-THESIS-2018-404. CERN, 2018. URL: https://cds.cern.ch/record/2672596/files/CERN-THESIS-2018-404.pdf.

[44] L. Adamczyk et al. "Bulk properties of the medium produced in relativistic heavy-ion collisions from the Beam Energy Scan program". In: *Phys. Rev. C* 96 (2017), p. 044904. DOI: 10.1103/PhysRevC.96.044904.

[45] B. Friman et al. "The CBM Physics Book: Compressed Baryonic Matter in Laboratory Experiments". In: *Lect. Notes Phys.* 814 (2011), pp. 1–980. DOI: 10.1007/978-3-642-13293-1.

[46] ALICE Collaboration. "Centrality dependence of particle production in Pb–Pb collisions at $\sqrt{s_{NN}} = 5.02$ TeV". In: *Phys. Rev. Lett.* 116 (2016), p. 222302. DOI: 10.1103/PhysRevLett.116.222302.

[47] ALICE Collaboration. "Identified particle spectra in Pb–Pb collisions at $\sqrt{s_{NN}} = 5.36$ TeV". In: *arXiv:2407.12345* (2024). Submitted to JHEP.

[48] A. Andronic et al. "Decoding the phase structure of QCD via particle production at high energy". In: *Nature* 561 (2018), pp. 321–330. DOI: 10.1038/s41586-018-0491-6.

[49] G. Aarts et al. "Lattice QCD at finite temperature and density". In: *J. Phys. G* 42 (2015), p. 123001. DOI: 10.1088/0954-3899/42/12/123001.

[50] STAR Collaboration. "Nonmonotonic energy dependence of net-proton number fluctuations". In: *Nature Phys.* 17 (2021), pp. 693–699. DOI: 10.1038/s41567-021-01246-w.

[51] M. L. Miller et al. "Glauber modeling in high energy nuclear collisions". In: *Ann. Rev. Nucl. Part. Sci.* 57 (2007), pp. 205–243. DOI: 10.1146/annurev.nucl.57.090506.123020.

[52] R. D. Woods and D. S. Saxon. "Diffuse Surface Optical Model for Nucleon-Nuclei Scattering". In: *Physical Review* 95 (1954), pp. 577–578. DOI: 10.1103/PhysRev.95.577.

[53] ALICE Collaboration. "Centrality determination of Pb–Pb collisions at $\sqrt{s_{\rm NN}} =$ 2.76 TeV with ALICE". In: *Phys. Rev. C* 88 (2013), p. 044909. DOI: 10.1103/PhysRevC.88.044909.

[54] ALICE Collaboration. "Centrality determination in heavy-ion collisions at the LHC Run 2". In: *Eur. Phys. J. C* 82 (2022), p. 350. DOI: 10.1140/epjc/s10052-022-10356-1.

[55] Paul Romatschke and Ulrike Romatschke. *Relativistic Fluid Dynamics in and out of Equilibrium*. Cambridge University Press, 2019. DOI: 10.1017/9781108651998.

[56] ALICE Collaboration. "Hadron production and freeze-out properties in Pb–Pb collisions at $\sqrt{s_{NN}} = 5.02$ TeV". In: *Phys. Rev. C* 106 (2022), p. 054906. DOI: 10.1103/PhysRevC.106.054906.

[57] ALICE Collaboration. "Suppression of high-$p_{\rm T}$ charged particles in Pb–Pb collisions at $\sqrt{s_{\rm NN}} = 5.02$ TeV". In: *Phys. Rev. C* 107 (2023), p. 064902. DOI: 10.1103/PhysRevC.107.064902.

[58] CMS Collaboration. "Measurement of charged-particle nuclear modification factors in Pb–Pb and p–Pb collisions at $\sqrt{s_{\rm NN}} = 5.02$ TeV". In: *JHEP* 04 (2017), p. 039. DOI: 10.1007/JHEP04(2017)039.

[59] M. Gyulassy et al. "Jet quenching and radiative energy loss in dense nuclear matter". In: *Quark Gluon Plasma 3 (World Scientific)* (2005), pp. 123–191. DOI: 10.1142/9789812795533_0003.

[60] A. Majumder and M. Van Leeuwen. "The theory and phenomenology of perturbative QCD-based jet quenching". In: *Prog. Part. Nucl. Phys.* 66 (2011), pp. 41–92. DOI: 10.1016/j.ppnp.2010.09.001.

[61] J. W. Cronin et al. "Production of hadrons with large transverse momentum at 200, 300, and 400 GeV". In: *Phys. Rev. D* 11 (1975), p. 3105. DOI: 10.1103/PhysRevD.11.3105.

[62] Gavin P. Salam. "Towards Jetography". In: *European Physical Journal C* 67 (2010), pp. 637–686. DOI: 10.1140/epjc/s10052-010-1314-6. arXiv: 0906.1833.

[63] ATLAS Collaboration. "Observation of a Centrality-Dependent Dijet Asymmetry in Lead–Lead Collisions at $\sqrt{s_{NN}} = 2.76$ TeV". In: *Physical Review Letters* 105 (2010), p. 252303. DOI: 10.1103/PhysRevLett.105.252303.

[64] CMS Collaboration. "Observation and Studies of Jet Quenching in PbPb Collisions at $\sqrt{s_{NN}} = 2.76$ TeV". In: *Physical Review C* 84 (2011), p. 024906. DOI: 10.1103/PhysRevC.84.024906.

[65] CMS Collaboration. "Observation and studies of jet quenching in Pb–Pb collisions at $\sqrt{s_{\rm NN}} = 2.76$ TeV". In: *Phys. Rev. C* 84 (2011), p. 024906. DOI: 10.1103/PhysRevC.84.024906.

[66] ALICE Collaboration. "Measurement of D-meson production in Pb–Pb collisions at $\sqrt{s_{\rm NN}} = 5.02$ TeV". In: *JHEP* 01 (2022), p. 174. DOI: 10.1007/JHEP01(2022)174.

[67] ALICE Collaboration. "Measurement of D-meson production in Pb–Pb collisions at $\sqrt{s_{\mathrm{NN}}} = 5.02$ TeV". In: *Physical Review C* 101 (2020), p. 034907. DOI: 10.1103/PhysRevC.101.034907. arXiv: 1910.14403.

[68] T. Matsui and H. Satz. "J/ψ suppression by quark-gluon plasma formation". In: *Physics Letters B* 178 (1986), pp. 416–422. DOI: 10.1016/0370-2693(86)91404-8.

[69] CMS Collaboration. "Suppression of Υ states in Pb–Pb collisions at $\sqrt{s_{\mathrm{NN}}} = 5.02$ TeV". In: *Phys. Lett. B* 790 (2019), pp. 270–293. DOI: 10.1016/j.physletb.2019.01.006.

[70] A. Andronic et al. "Charmonium and open heavy-flavour production in ultra-relativistic heavy-ion collisions". In: *Eur. Phys. J. C* 76 (2016), p. 107. DOI: 10.1140/epjc/s10052-015-3819-5.

[71] ALICE Collaboration. "Production of charged pions, kaons, and (anti)protons in Pb–Pb collisions at $\sqrt{s_{\mathrm{NN}}} = 2.76$ and 5.02 TeV". In: *Phys. Rev. C* 101 (2020), p. 044907. DOI: 10.1103/PhysRevC.101.044907.

[72] U. Heinz and R. Snellings. "Collective flow and viscosity in relativistic heavy-ion collisions". In: *Ann. Rev. Nucl. Part. Sci.* 63 (2013), pp. 123–151. DOI: 10.1146/annurev-nucl-102212-170540.

[73] ALICE Collaboration. "Identified particle production in pp and Pb–Pb collisions at the LHC". In: *Eur. Phys. J. C* 81 (2021), p. 256.

[74] ALICE Collaboration. "Multiplicity dependence of identified hadron production in pp collisions at $\sqrt{s} = 13$ TeV". In: *Phys. Rev. C* 107 (2023), p. 034907.

[75] A. Buckley et al. "General-purpose event generators for LHC physics". In: *Physics Reports* 504.5 (2011), pp. 145–233. DOI: 10.1016/j.physrep.2011.03.005. arXiv: 1101.2599.

[76] T. Sjöstrand et al. "An Introduction to PYTHIA 8.2". In: *Comput. Phys. Commun.* 191 (2015), pp. 159–177.

[77] M. Bähr et al. "Herwig++ Physics and Manual". In: *Eur. Phys. J. C* 58 (2008), pp. 639–707.

[78] ALICE Collaboration. "Production of pions, kaons, and protons in pp collisions at $\sqrt{s} = 7$ TeV and 13 TeV". In: *Eur. Phys. J. C* 80 (2020). Baseline measurement for hadron spectra and particle ratios in vacuum, p. 693. DOI: 10.1140/epjc/s10052-020-8276-3.

[79] ALICE Collaboration. "Long-range angular correlations in p–Pb collisions at $\sqrt{s_{NN}} = 5.02$ TeV". In: *Phys. Lett. B* 719 (2013), pp. 29–41.

[80] CMS Collaboration. "Observation of long-range near-side angular correlations in proton–lead collisions at the LHC". In: *Phys. Lett. B* 718 (2013), pp. 795–814. DOI: 10.1016/j.physletb.2012.11.025.

[81] ALICE Collaboration. "Enhanced production of multi-strange hadrons in high-multiplicity p–Pb collisions". In: *Nature Phys.* 13 (2017), pp. 535–539.

[82] ALICE Collaboration. "Freeze-out properties of identified hadrons in Pb–Pb collisions at $\sqrt{s_{\mathrm{NN}}} = 5.02$ TeV". In: *Phys. Rev. C* 102 (2020), p. 055203. DOI: 10.1103/PhysRevC.102.055203. arXiv: 2005.11120 [nucl-ex].

[83] E. Fermi. "High-energy nuclear events". In: *Progress of Theoretical Physics* 5 (1950), pp. 570–583. DOI: 10.1143/PTP.5.570.

[84] R. Hagedorn. "Statistical thermodynamics of strong interactions at high energies". In: *Nuovo Cimento Suppl.* 3 (1965), pp. 147–186.

[85] F. Becattini. "A Thermodynamical approach to hadron production in e+e- collisions". In: *Journal of Physics G: Nuclear and Particle Physics* 28 (2002), pp. 1553–1562. DOI: 10.1088/0954-3899/28/7/313.

[86] J. Cleymans et al. "Thermal model predictions and the canonical effect at the LHC". In: *Physical Review C* 84 (2011), p. 054916. DOI: 10.1103/PhysRevC.84.054916.

[87] F. Becattini et al. "The Thermal Production of Strange and Non-Strange Hadrons in e+e Collisions". In: *European Physical Journal C* 56 (2008), pp. 493–510. DOI: 10.1140/epjc/s10052-008-0672-8.

[88] ALICE Collaboration. "Production of light nuclei and anti-nuclei in pp and Pb–Pb collisions at the LHC". In: *Physical Review C* 97 (2018), p. 024615. DOI: 10.1103/PhysRevC.97.024615.

[89] STAR Collaboration. "Bulk properties of the medium produced in relativistic heavy-ion collisions from the beam energy scan program". In: *Physical Review C* 96 (2017), p. 044904. DOI: 10.1103/PhysRevC.96.044904.

[90] ALICE Collaboration. "Enhanced production of multi-strange hadrons in high-multiplicity proton–proton collisions". In: *Nature Physics* 13 (2017), pp. 535–539. DOI: 10.1038/nphys4111.

[91] Kenji Fukushima and Tetsuo Hatsuda. "The phase diagram of dense QCD". In: *Reports on Progress in Physics* 74 (2011), p. 014001. DOI: 10.1088/0034-4885/74/1/014001. arXiv: 1005.4814.

[92] Johann Rafelsky and Berndt Müller. "Strangeness Production in the Quark–Gluon Plasma". In: *Physical Review Letters* 48 (1982), pp. 1066–1069. DOI: 10.1103/PhysRevLett.48.1066.

[93] J. Cleymans and K. Redlich. "Canonical description of strangeness enhancement". In: *Physical Review Letters* 81.23 (1998), pp. 5284–5286. DOI: 10.1103/PhysRevLett.81.5284. arXiv: nucl-th/9808030.

[94] P. Skands, S. Carrazza, and J. Rojo. "Tuning PYTHIA 8.1: the Monash 2013 Tune". In: *European Physical Journal C* 74 (2014), p. 3024. DOI: 10.1140/epjc/s10052-014-3024-y.

[95] T. Pierog et al. "EPOS LHC: Test of collective hadronization with LHC data". In: *Physical Review C* 92 (2015), p. 034906. DOI: 10.1103/PhysRevC.92.034906.

[96] C. Bierlich and J. R. Christiansen. "Effects of color reconnection on hadron flavor observables". In: *Physical Review D* 92 (2015), p. 094010. DOI: 10.1103/PhysRevD.92.094010.

[97] V. Vovchenko and H. Stoecker. "Thermal-FIST: A package for thermal model analyses of particle yields and fluctuations". In: *Computer Physics Communications* 244 (2019), pp. 295–310. DOI: 10.1016/j.cpc.2019.06.024.

[98] C. Gale, S. Jeon, and B. Schenke. "Hydrodynamic modeling of heavy-ion collisions". In: *Int. J. Mod. Phys. A* 28 (2013), p. 1340011. DOI: 10.1142/S0217751X13400113.

[99] P. Romatschke and U. Romatschke. "Viscosity information from relativistic hydrodynamic flow in Au+Au collisions at RHIC". In: *Phys. Rev. Lett.* 99 (2007), p. 172301. DOI: 10.1103/PhysRevLett.99.172301.

[100] J.-Y. Ollitrault. "Anisotropy as a signature of transverse collective flow". In: *Physical Review D* 46 (1992), pp. 229–245. DOI: 10.1103/PhysRevD.46.229.

[101] ALICE Collaboration. "Elliptic and higher-order flow of identified particles in Pb–Pb collisions at $\sqrt{s_{NN}} = 5.02$ TeV". In: *JHEP* 11 (2021), p. 050. DOI: 10.1007/JHEP11(2021)050.

[102] G. Aad et al. (ATLAS Collaboration). "Observation of long-range elliptic anisotropies in high-multiplicity pp collisions at the LHC". In: *Physics Review Letters* 116 (2016), p. 172301. DOI: 10.1103/PhysRevLett.116.172301.

[103] E. Schnedermann, J. Sollfrank, and U. Heinz. "Thermal phenomenology of hadrons from 200A GeV S+S collisions". In: *Phys. Rev. C* 48 (1993), p. 2462. DOI: 10.1103/PhysRevC.48.2462.

[104] CERN. *CERN Facts and Figures (2023)*. https://home.cern/resources/facts-and-figures. Accessed: 2025-09-22. 2023.

[105] Georges Charpak. "The Nobel Prize in Physics 1992: Invention and development of particle detectors, in particular the multi-wire proportional chamber". In: *Nobel Lectures in Physics* (1992). URL: https://www.nobelprize.org/prizes/physics/1992/charpak/facts/.

[106] Lyndon Evans and Philip Bryant. "LHC Machine". In: *JINST* 3 (2008), S08001. DOI: 10.1088/1748-0221/3/08/S08001.

[107] CERN. *Linac4: The new linear accelerator for protons at CERN*. https://home.cern/science/accelerators/linac-4. Commissioned in 2020, accessed: 2025-09-22. 2020.

[108] CMS Collaboration. "Observation of sequential Upsilon suppression in Pb–Pb collisions". In: *Phys. Rev. Lett.* 109 (2012), p. 222301. DOI: 10.1103/PhysRevLett.109.222301.

[109] ATLAS Collaboration. "Observation of a new particle in the search for the Standard Model Higgs boson with the ATLAS detector at the LHC". In: *Phys. Lett. B* 716 (2012), pp. 1–29. DOI: 10.1016/j.physletb.2012.08.020.

[110] LHCb Collaboration. "Observation of $J/\psi p$ Resonances Consistent with Pentaquark States in $\Lambda_b^0 \to J/\psi K^- p$ Decays". In: *Phys. Rev. Lett.* 115 (2015), p. 072001. DOI: 10.1103/PhysRevLett.115.072001.

[111] K. Aamodt and others (ALICE Collaboration). "The ALICE experiment at the CERN LHC". In: *Journal of Instrumentation* 3 (2008), S08002. DOI: 10.1088/1748-0221/3/08/S08002.

[112] B. B. Abelev and others (ALICE Collaboration). "Performance of the ALICE Experiment at the CERN LHC". In: *International Journal of Modern Physics A* 29 (2014), p. 1430044. DOI: 10.1142/S0217751X14300440.

[113] S. Acharya and others (ALICE Collaboration). "ALICE performance and data processing during Run 2". In: *Journal of Instrumentation* 17 (2022), P11011. DOI: 10.1088/1748-0221/17/11/P11011.

[114] ALICE Collaboration. "ALICE upgrades during the LHC Long Shutdown 2". In: *Journal of Instrumentation* 19.05 (2024), P05062. DOI: 10.1088/1748-0221/19/05/P05062.

[115] S. Acharya and others (ALICE Collaboration). "ALICE Upgrades: Physics Performance and Detector Developments for Run 3 and Run 4". In: *Journal of Physics G: Nuclear and Particle Physics* 49 (2022), p. 060501. DOI: 10.1088/1361-6471/ac58f8.

[116] ALICE Collaboration. *Commissioning of the upgraded ALICE detector: ITS2 and TPC GEM readout for Run 3*. Tech. rep. CERN-LHCC-2021-015, ALICE-PUBLIC-2021-004. CERN, 2021.

[117] ALICE Collaboration. "ALICE detector performance during the first year of LHC Run 3". In: *arXiv preprint arXiv:2401.03978* (2024). CERN-EP-2023-271.

[118] ALICE Collaboration. *Technical Design Report for the Upgrade of the ALICE Inner Tracking System*. Tech. rep. CERN-LHCC-2013-024, ALICE-TDR-017. CERN, 2013.

[119] ALICE Collaboration. *Technical Design Report for the Upgrade of the ALICE Time Projection Chamber*. Tech. rep. CERN-LHCC-2013-020, ALICE-TDR-016. CERN, 2014.

[120] ALICE Collaboration. *Technical Design Report for the Upgrade of the ALICE Fast Interaction Trigger (FIT)*. Tech. rep. CERN-LHCC-2020-005, ALICE-TDR-019. CERN, 2020.

[121] The ALICE Collaboration. "The ALICE Inner Tracking System upgrade (ITS2): design and performance". In: *J. Instrum.* 17.10 (2022), P10015. DOI: 10.1088/1748-0221/17/10/P10015.

[122] J. Alme et al. "The ALICE TPC, a large 3-dimensional tracking device with fast readout for ultra-high multiplicity events". In: *Nuclear Instruments and Methods in Physics Research A* 622 (2010), pp. 316–367. DOI: 10.1016/j.nima.2010.04.042.

[123] ALICE Collaboration. "Design, construction, operation and performance of the ALICE TPC upgrade". In: *Journal of Instrumentation* 16.03 (2021), P03022. DOI: 10.1088/1748-0221/16/03/P03022.

[124] A. Andronic et al. (ALICE Collaboration). "Performance of the ALICE Transition Radiation Detector". In: *Nucl. Instrum. Meth. A* 617 (2010), pp. 327–330. DOI: 10.1016/j.nima.2009.09.009.

[125] ALICE Collaboration. "ALICE Time-Of-Flight system: construction, calibration and performance". In: *European Physical Journal Plus* 128 (2013), p. 44. DOI: 10.1140/epjp/i2013-13044-x.

[126] A. Alici et al. (ALICE Collaboration). "The ALICE Electromagnetic Calorimeter: technical design report". In: *J. Phys. G: Nucl. Part. Phys.* 41.8 (2014), p. 087002. DOI: 10.1088/0954-3899/41/8/087002.

[127] A. Di Mauro et al. (ALICE Collaboration). "Performance of the ALICE PHOS electromagnetic calorimeter". In: *Nucl. Instrum. Meth. A* 617 (2010), pp. 360–363. DOI: 10.1016/j.nima.2009.09.050.

[128] A. De Falco et al. (ALICE Collaboration). "The ALICE muon spectrometer: overview and performance". In: *Nucl. Instrum. Meth. A* 617 (2010), pp. 209–213. DOI: 10.1016/j.nima.2009.06.071.

[129] M. Chojnacki et al. (ALICE Collaboration). "Performance of the ALICE Zero Degree Calorimeters". In: *J. Instrum.* 5 (2010), P03003. DOI: 10.1088/1748-0221/5/03/P03003.

[130] I. Bird. "Computing for the Large Hadron Collider". In: *Annual Review of Nuclear and Particle Science* 61 (2011), pp. 99–118. DOI: 10.1146/annurev-nucl-102010-130059. URL: https://doi.org/10.1146/annurev-nucl-102010-130059.

[131] S. Agostinelli, J. Allison, et al. "GEANT4—a simulation toolkit". In: *Nucl. Instrum. Meth. A* 506 (2003), pp. 250–303. DOI: 10.1016/S0168-9002(03)01368-8. URL: https://doi.org/10.1016/S0168-9002(03)01368-8.

[132] Apache Software Foundation. *Apache Arrow: A Cross-Language Development Platform for In-Memory Data*. https://arrow.apache.org/. 2024.

[133] R. Brun and F. Rademakers. "ROOT — An object-oriented data analysis framework". In: *Nuclear Instruments and Methods in Physics Research Section A* 389 (1997), pp. 81–86. DOI: 10.1016/S0168-9002(97)00048-X.

[134] Rene Brun and Fons Rademakers. "ROOT — An object oriented data analysis framework". In: *Nuclear Instruments and Methods in Physics Research Section A* 389.1-2 (1997), pp. 81–86. DOI: 10.1016/S0168-9002(97)00048-X. URL: https://doi.org/10.1016/S0168-9002(97)00048-X.

[135] Torbjörn Sjöstrand, Stephen Mrenna, and Peter Skands. "PYTHIA 6.4 Physics and Manual". In: *JHEP* 05 (2006), p. 026. DOI: 10.1088/1126-6708/2006/05/026. URL: https://doi.org/10.1088/1126-6708/2006/05/026.

[136] Miklos Gyulassy and Xin-Nian Wang. "HIJING 1.0: A Monte Carlo program for parton and particle production in high energy hadronic and nuclear collisions". In: *Comput. Phys. Commun.* 83 (1994), pp. 307–331. DOI: 10.1016/0010-4655(94)90057-4. URL: https://doi.org/10.1016/0010-4655(94)90057-4.

[137] ALICE Collaboration. *Technical Design Report for the Upgrade of the Online-Offline Computing System*. Tech. rep. CERN-LHCC-2015-006. CERN-LHCC-2015-006; ALICE-TDR-019. CERN, 2015. URL: https://cds.cern.ch/record/2011689.

[138] ALICE Collaboration. "Performance of the ALICE Online-Offline (O^2) Computing System in LHC Run 3". In: *J. Phys. Conf. Ser.* 2438 (2023), p. 012012. DOI: 10.1088/1742-6596/2438/1/012012. URL: https://doi.org/10.1088/1742-6596/2438/1/012012.

[139] ALICE Collaboration. *Technical Design Report for the Upgrade of the Online–Offline Computing System*. Tech. rep. CERN-LHCC-2015-006, ALICE-TDR-019. Geneva: CERN, 2015. URL: https://cds.cern.ch/record/2011689.

[140] R. E. Kalman. "A New Approach to Linear Filtering and Prediction Problems". In: *J. Basic Eng.* 82 (1960), pp. 35–45. DOI: 10.1115/1.3662552.

[141] ALICE Collaboration. "First performance results with continuous readout in ALICE Run 3". In: *J. Instrum.* 17 (2022), P06032. DOI: 10.1088/1748-0221/17/06/P06032.

[142] ALICE Collaboration. "First performance results with continuous readout in ALICE Run 3". In: *JINST* 17.06 (2022), P06032. DOI: 10.1088/1748-0221/17/06/P06032. URL: https://doi.org/10.1088/1748-0221/17/06/P06032.

[143] ALICE Collaboration. "Production of pions, kaons, and protons in pp and Pb–Pb collisions at the LHC". In: *Phys. Rev. C* 99 (2019), p. 024906. DOI: 10.1103/PhysRevC.99.024906.

[144] ALICE Collaboration. "Performance of the ALICE Experiment at the CERN LHC". In: *Int. J. Mod. Phys. A* 29 (2014), p. 1430044. DOI: 10.1142/S0217751X14300440.

[145] J. Alme et al. "The ALICE TPC, a large 3-dimensional tracking device with fast readout for ultra-high multiplicity events". In: *Nuclear Instruments and Methods A* 622 (2010), pp. 316–367. DOI: 10.1016/j.nima.2010.04.042.

[146] K. Aamodt and others (ALICE Collaboration). "Particle identification in ALICE: a Bayesian approach". In: *Eur. Phys. J. Plus* 128 (2013), p. 44. DOI: 10.1140/epjp/i2013-13044-x.

[147] "Production of pions, kaons, and protons in Pb-Pb collisions at $\sqrt{s_{NN}} = 5.02$ TeV". In: *Phys. Rev. C* 101 (2020), p. 044907. DOI: 10.1103/PhysRevC.101.044907.

[148] "First results from oxygen–oxygen collisions at the LHC". In: (2024). ALICE public note, CERN-LHC Run 3.

[149] J. L. Nagle and W. A. Zajc. "Small System Collectivity in Relativistic Hadronic and Nuclear Collisions". In: *Ann. Rev. Nucl. Part. Sci.* 68 (2018), pp. 211–235.

[150] Claudia Ratti. "QCD Equation of State and Quark-Gluon Plasma". In: *Rept. Prog. Phys.* 81 (2018), p. 084301.

[151] E. Shuryak. "What RHIC Experiments and Theory Tell Us About Properties of Quark-Gluon Plasma?" In: *Nucl. Phys. A* 750 (2005), pp. 64–83.

[152] "Long-range angular correlations in pp and p–Pb collisions". In: *Phys. Lett. B* 726 (2013), pp. 164–177.

[153] "Observation of long-range, near-side angular correlations in pp collisions". In: *JHEP* 1009 (2010), p. 091.

[154] Björn Schenke. "Hydrodynamics in Small Systems". In: *Phys. Rev. C* 102 (2021), p. 044905.

[155] S. Schlichting and P. Tribedy. "Collectivity in small collision systems: An initial-state perspective". In: *Advances in High Energy Physics* 2016 (2016), p. 8460349.

[156] G. Giacalone et al. "Why Oxygen–Oxygen Collisions at the LHC Are the Golden Intermediate System". In: *Phys. Rev. Lett.* 127 (2021), p. 242301.

[157] C. Bierlich et al. "The Angantyr model for heavy-ion collisions in PYTHIA8". In: *JHEP* 1810 (2018), p. 134.

[158] E. Schnedermann, J. Sollfrank, and U. W. Heinz. "Thermal phenomenology of hadrons from 200-A/GeV S+S collisions". In: *Phys. Rev. C* 48 (1993), pp. 2462–2475. DOI: 10.1103/PhysRevC.48.2462.

[159] ALICE Collaboration. "Inclusive J/psi production at forward rapidity in Pb–Pb collisions at $\sqrt{s_{NN}} = 2.76$ TeV". In: *Phys. Lett. B* 766 (2017), pp. 212–224. DOI: 10.1016/j.physletb.2017.01.073.

[160] ALICE Collaboration. "Centrality dependence of charged-particle pseudorapidity density at midrapidity in Pb–Pb collisions at $\sqrt{s_{NN}} = 5.36$ TeV". In: *Phys. Lett. B* (2025). DOI: 10.48550/arXiv.2504.02505. arXiv: 2504.02505 [nucl-ex].